Exploring gravitational-wave astrophysics: Source modelling, tests of general relativity and gravitational lensing

A Thesis

Submitted to the

Tata Institute of Fundamental Research, Mumbai

for the degree of Doctor of Philosophy

in Physics

by

Ajit Kumar Mehta

International Centre for Theoretical Sciences,

Tata Institute of Fundamental Research, Bengaluru

August 2, 2019

Final Version Submitted: November, 2019

Declaration

This thesis is a presentation of my original research work. Wherever contributions of others are involved, every effort is made to indicate this clearly, with due reference to the literature, and acknowledgement of collaborative research and discussions.

The work was done under the guidance of Professor Parameswaran Ajith, at the International Centre for Theoretical Sciences, Tata Institute of Fundamental Research, Bangalore.

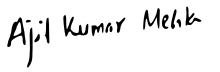

Ajit Kumar Mehta

In my capacity as supervisor of the candidate's thesis, I certify that the above statements are true to the best of my knowledge.

Parameswaran Ajith

Date: November 1, 2019

Abstract

This thesis describes three aspects of the gravitational-wave astronomy: modeling of gravitational-wave (GW) signals from binary black holes, tests of general relativity (GR) from GW observations, and astrophysical exploration using GWs, in particular, gravitational lensing of GWs. The data analysis involved in the detection of GWs and extraction of the source parameters requires computationally-efficient and theoretically accurate models of GWs. The first part of the thesis describes the modeling of higher harmonics of GWs from non-spinning quasi-circular binary black hole (BBH) systems. The second part of the thesis describes a "no-hair" test of BBHs that is based on checking the consistency between the parameters estimated from the different harmonics of the GWs and presents an example where this test might be useful, e.g., distinguishing between BHs and other (exotic) compact objects. The third part of the thesis deals with the gravitational lensing of GWs from massive objects such as galaxies. Such massive objects produce multiple "images" of a source (i.e., multiple copies of a GW signal). The thesis describes a Bayesian technique developed for identifying the multiple images of GW signals among the BBH events detectable by advanced LIGO and Virgo. The thesis also presents the results from the first search for lensing signatures in the Advanced LIGO and Virgo BBH observations during their O1 and O2 runs, which shows no strong evidence of strong gravitational lensing.

Chapter 1 presents an overview of the basic theory needed for understanding the gravitational waveforms produced by BBHs. It starts

with discussing the linearised regime of the Einstein equations where the source motions are assumed to be Newtonian and the gravity is assumed to be very weak. It then discusses the post-Newtonian (PN) theory, which corrects the Newtonian motions by taking into account the non-linearity of the Einstein equations. This theory provides a good model for the gravitational waveforms produced by BBHs during their slow inspiral. It ends with the discussion of numerical relativity (NR) theory, which provides accurate models of the post-inspiral phase (i.e., merger and ringdown phase) of the gravitational waveforms.

In chapter 2, we present an analytical inspiral-merger-ringdown waveform (IMR) model of higher harmonics of the GWs from non-spinning quasi-circular BBHs, in the frequency domain. We start with the available PN waveforms and then add some fiducial higher-order PN parameters to the amplitudes and the phases of the waveforms to capture the merger dynamics, i.e., when the black holes (BHs) are moving very near to each other. The post-merger dynamics (i.e., ringdown) is modeled by taking information from the waveforms predicted by BH perturbation theory. The fiducial parameters appearing in the model are fixed by calibrating the model with a set of hybrid waveforms, which are made by matching NR waveforms with the PN waveforms. We asses the accuracy of our model with a different set of hybrid waveforms and show that they are highly faithful towards them with mismatches $< 0.04\%$.

In chapter 3, we discuss a test of BBHs that we developed using our IMR waveforms containing higher harmonics. This is based on inferring the intrinsic parameters of BBHs from the different harmonics of the GWs and checking for the consistency between them. In GR, the multi-harmonic structure of GWs is uniquely determined by the intrinsic parameters, such as masses and spins of the black holes. Thus any inconsistency between different harmonics would point to either a departure from GR, or the non-black hole nature of the compact objects. Using our test, we demonstrate that it might be

possible to distinguish BHs from the other compact objects.

In chapter 4, we present an overview of gravitational lensing theory. We describe how a massive object (a gravitational lens) affects the propagation of GWs. We show that the gravitational lensing can lead to the formations of multiple images of a source which reach the observers at different times. For transient GW source like BBHs, this implies that multiple GW events can be observed, from the same source. We describe different kinds of lenses and their lensing properties, e.g., the number of images formed, the typical time delay between the images, their magnifications, etc. In chapter 5, we present a Bayesian method to identify the multiply imaged GW signals among the BBH events detectable by advanced LIGO and Virgo. We find that a small fraction ($\sim$ 0.5%) of the BBH events detectable by Advanced LIGO and Virgo will be strongly lensed. Using simulated lensed and unlensed BBH merger events, we demonstrate how and with what efficiency our method can distinguish images of strongly lensed merger events from unlensed events. We finally present the results from the first search for lensing signatures in the Advance LIGO and Virgo BBH observations during their O1 and O2 runs. We show that there is no strong evidence of strong gravitational lensing.

Contents

1 An introduction to the physics of gravitational waves

This chapter will give a brief introduction to the gravitational wave physics. Starting from the Einstein equations of general relativity which describes the dynamics of gravity, we will see how gravitational waves naturally arise from the weak-field limit. We will discuss in detail a particular kind of gravitational wave source, i.e., binary compact objects. In the subsequent sections, we will go through the tools that have been developed to solve Einstein equations beyond the weak-field limit.

The material presented in this chapter is based on standard theory of gravitational waves. For a longer discussion, see for e.g., [87, 103].

1.1 *Gravitational waves*

In 1905, Albert Einstein formulated the special theory of relativity which postulates two things: 1) The speed of light is same in all inertial frames of reference, 2) The local measurement of physical quantities is independent of a chosen inertial frame. These two postulates together imply that space and time can no longer be separated from each other, i.e., time becomes a coordinate like spatial coordinates, and together they form a four-dimensional manifold called *spacetime*. This means that there is no notion of absolute time coordinate (as is assumed in Newtonian gravity), i.e., time runs differently in different inertial frames. In this sense, Newtonian gravity is incompatible with the special theory of relativity because Newton's law of gravitation

defines a force between two distant bodies at a given instant in time. This requires a unique notion of simultaneity, which conflicts with the very principle of the special theory of relativity. Otherwise, the Newtonian gravitational force between two bodies will be measured differently in different inertial frames.

In 1915, Einstein formulated a relativistic theory of gravity known as *general theory of relativity* [1] which respects the principle of general covariance, i.e., no coordinate system is preferred at all, in contrast to special theory of relativity, where the physical quantities are invariant only in a certain class of transformation known as Poincare transformation, i.e., under translation, rotation and boosts. This means that in general relativity, we can work in any coordinate system that we like, e.g., one can always construct a freely falling frame of reference associated with a freely falling observer. Any physical experiment carried out in such a freely falling frame will give the same results as a similar experiment done in the absence of gravitational fields. The physical effect of gravity starts showing up only when we look at the geodesics of two nearby particles.

[1] We will instead use "general relativity." elsewhere.

General relativity describes gravity as the change in the geometry (i.e., the metric, which determines the distance between the two infinitesimally separated events) of the spacetime due to the presence of matter-energy distribution in the spacetime itself. In other words, matter curves the spacetime. This is expressed through the *Einstein field equations* [2]:

$$G_{\alpha\beta} = 8\pi T_{\alpha\beta}, \tag{1.1}$$

[2] Throughout this thesis, we would be working in natural units: $G = c = 1$, unless we explicitly specify. Here G is Newton's gravitational constant, and c is the speed of light in vacuum. In these units $1M_\odot \simeq 5 \times 10^{-6}$s $\simeq 1.5$km

where the left hand side represents the geometry of spacetime while the right hand side represents the matter-energy content of it. Mathematically, $G_{\alpha\beta} := R_{\alpha\beta} - \frac{1}{2} g_{\alpha\beta} R$, where $g_{\alpha\beta}$ is the metric of the spacetime. $R_{\alpha\beta}$ is the trace of Riemann tensor $R_{\alpha\beta\gamma\delta}$ which is a function of metric $g_{\alpha\beta}$ and involves first and second derivatives of it. The

particular combination $R_{\alpha\beta} - \frac{1}{2} g_{\alpha\beta} R$ is divergenceless, i.e.,

$$\nabla^{\alpha} G_{\alpha\beta} = 0, \tag{1.2}$$

where ∇_{α} is a natural generalisation of partial derivative in the flat spacetime to the curved spacetime. $T_{\alpha\beta}$ is known as stress-energy tensor, because it is constructed by combining the energy density, momentum density and the stress tensor of a material body (as defined in the Newtonian physics). From the definition itself, one can show that the stress energy tensor is covariantly conserved [3], i.e.,

[3] Analogous to the conservation law $\partial^{\alpha} T_{\alpha\beta} = 0$, in the flat spacetime.

$$\nabla^{\alpha} T_{\alpha\beta} = 0. \tag{1.3}$$

Einstein equations (Eq. 1.1) make sure that this requirement is fulfilled. The conservation law in the Eq. 1.3 determines the equations of motion for the matter in the curved spacetime.

For a given matter-energy distribution (i.e., $T_{\alpha\beta}$), Eq. 1.1 could, in principle, be solved. As of now, there exist only a few exact solutions of Eq. 1.1, among which are Schwarzschild metric and Kerr metric [4]. The Schwarzschild black hole metric is described by just one parameter, its mass while the Kerr black hole metric is described by two parameters, its mass and the angular momentum. The exact analytical solution of Einstein equations for the time evolution of a generic two-body system, such as, two black holes in a bound orbit, is still an open problem in general relativity. In the coming sections of this chapter, we, however, will go through some approximate methods that have been developed to deal with such systems.

[4] They correspond to Schwarzschild black hole and Kerr black hole, respectively.

First of all, let us understand the behaviour of Einstein field equations in the case where the curvature produced by the sources is very small, i.e., when the metric of the curved spacetime deviates by a just little amount from that of the flat spacetime. Mathematically,

$$g_{\alpha\beta} = \eta_{\alpha\beta} + h_{\alpha\beta}, \tag{1.4}$$

where,

$$|h_{\alpha\beta}| \ll 1. \tag{1.5}$$

and $\eta_{\alpha\beta}$ is the metric of flat spacetime expressed in Cartesian coordinates where the modulus of each matrix element is 1. Computing the Einstein tensor $G_{\alpha\beta}$ and keeping the terms up to only first order in $h_{\alpha\beta}$ (linearised gravity regime), the Einstein field equations 1.1 reduce to

$$\Box \bar{h}_{\alpha\beta} = -16\pi T_{\alpha\beta}, \tag{1.6}$$

where $\bar{h}_{\alpha\beta}$ is the trace-reversed form of $h_{\alpha\beta}$. Note that, this particular form of Eq. 1.6 is valid only in a specialised coordinate system known as Lorenz gauge which is constructed by using up the gauge degrees of freedom in general relativity. In this gauge, $\bar{h}_{\alpha\beta}$ has zero divergence which helps cast Einstein equations in the above form. Notice however that, outside the source, $T_{\alpha\beta} = 0$ [5], for which Eq. 1.6 becomes

[5] Assuming that the source is localised in the space.

$$\left(-\frac{\partial^2}{\partial t^2} + \nabla^2 \right) \bar{h}_{\alpha\beta} = 0 \qquad \text{(Vacuum equations).} \tag{1.7}$$

This is a wave equation in three spatial directions. The solution is

$$\bar{h}_{\alpha\beta} = A_{\alpha\beta} \exp(i k_\mu k^\mu), \tag{1.8}$$

where k_μ represents the direction of propagation of the gravitational wave. Since $h_{\alpha\beta}$ is a symmetric tensor, it has 10 independent components. However, Lorenz gauge condition imposes four conditions on them which means that we have only six independent components. Furthermore, Lorenz gauge is not uniquely fixed, i.e., there is residual gauge degrees of freedom which preserves the Lorenz gauge. This further imposes four conditions on the six components, implying that $\bar{h}_{\alpha\beta}$ actually has only two independent degrees of freedom. This can be independently verified by computing the components of Riemann tensor which is a gauge independent quantity in lin-

earised gravity. In short, the Lorenz gauge choice makes the metric perturbation look like a transverse wave while the residual gauge degrees are used to make $\bar{h}_{\alpha\beta}$ traceless and purely spatial. We refer this gauge as transverse-traceless (TT) gauge. For a wave travelling along z-direction, $\bar{h}_{\alpha\beta}$ can be written as

$$(\bar{h}^{\rm TT}_{\alpha\beta}) = \begin{bmatrix} 0 & 0 & 0 & 0 \\ 0 & A^{\rm TT}_{xx} & A^{\rm TT}_{xy} & 0 \\ 0 & A^{\rm TT}_{xy} & -A^{\rm TT}_{xx} & 0 \\ 0 & 0 & 0 & 0 \end{bmatrix} \exp(ikz - i\omega t), \tag{1.9}$$

where $\omega = k$. The two independent components, $\bar{h}^{\rm TT}_{xx}$ and $\bar{h}^{\rm TT}_{xy}$ correspond to the two polarisation states of gravitational waves, denoted as h_+ and $h_\times$, respectively.

We saw that the vacuum Einstein equations predict wave-like solutions which can propagate out to the asymptotic infinity. Thus it would be interesting to ask whether an observer sitting at the asymptotic infinity would be able to detect these waves. This is related to asking whether gravitational waves have any physical effects on the bodies (or observers) they pass through. Let us take a system composed of two test particles at rest and separated in x-direction by a distance L. In TT gauge, one can show that the coordinates of free test particles do not change with time [6] even if there is a gravitational wave propagating along the z-axis. However, the *proper distance* (s) between them does change and up to linear order in $\bar{h}^{\rm TT}_{xx}$ can be given by

$$s \simeq L\big[1 + \frac{1}{2}\bar{h}^{\rm TT}_{xx}\big], \tag{1.10}$$

alternatively, the change in the proper length L,

$$\Delta L \simeq L\big[1 + \frac{1}{2}A^{\rm TT}_{xx} cos(\omega t)\big]. \tag{1.11}$$

This means that the proper distance between the test particles will oscillate with time if there is a gravitational wave passing through. Now consider these two test particles as the mirrors and a light beam

[6] Note that if they are not free, then the coordinates will change, e.g., for the end points of a rigid ruler. In other words, an object can not have rigid walls in TT gauge.

is allowed to travel back and forth between them. The time taken by the light to make a round trip depends on the proper distance between them. The change in the proper distance in the presence of gravitational waves implies that that the gravitational waves can be detected by measuring the round trip time between the mirrors. The interferometric gravitational wave detectors like LIGO and Virgo are based on the very same principle. Experimentalists, however, prefer to work in the so-called *proper detector frame*, i.e., a sufficiently small region of space around a chosen origin of the detector system. Mathematically, the size of the detector (L) should be much smaller than the reduced wavelength of the gravitational waves, i.e., $L \ll \lambda\!\!\!^{-}$. In this frame, the metric can be taken to be flat even in the presence of gravitational waves. The geodesic deviation equation between a test mass at origin and another one at some distance from it is given by

$$\ddot{\xi}^i = \frac{1}{2}\ddot{h}^{\mathrm{TT}}_{ij}\xi^j, \tag{1.12}$$

where ξ is the separation vector between the test masses. With respect to the origin, this is analogous to a *Newtonian force* acting on a point particle of mass m:

$$F_i = \frac{m}{2}\ddot{h}^{\mathrm{TT}}_{ij}\xi^j. \tag{1.13}$$

Thus, in the proper detector frame, the response of a detector to gravitational waves can be treated solely within the Newtonian physics. Also,

$$\partial_i F_i = \frac{m}{2}\ddot{h}^{\mathrm{TT}}_{ij}\delta_{ij}. \tag{1.14}$$

and since h^{TT}_{ij} is traceless, the divergence of the force vanishes, i.e., $\nabla \cdot \mathbf{F} = 0$. This implies that $\mathbf{F}$ can be represented pictorially by its field lines in the detector plane. At each point in the plane, the lines go in the direction of the force and their density provides the strength of the force ($|\mathbf{F}|$). The zero divergence of the force implies that there are no sources nor sinks for the field lines, analogous to magnetic

fields in electrodynamics. The field lines for h_+ and $h_\times$ polarization of gravitational waves passing through a ring of particles centered on the origin of the detector take shape corresponding to $+$ and $\times$ sign, respectively. This is the reason behind the names of the polarisations.

1.2 *Generation of gravitational waves*

Eq 1.7 represents the case when we are in a region far away from the source, known as the far-field zone. Here, we have plane wave solutions, but the values of amplitudes and phases are completely unknown. We can fix them by solving Einstein equations near the source (called near zone) which produces it. In the presence of matter, the Einstein equations in Lorenz gauge are

$$\Box \bar{h}^{\alpha\beta} = -16\pi T^{\alpha\beta}, \tag{1.15}$$

where $\bar{h}_{\alpha\beta}$ is the trace-reversed metric perturbation. Since $\Box$ is the flat space operator, the solution to Eq 1.15 is

$$\bar{h}^{\alpha\beta}(t, \boldsymbol{x}) = 4 \int \frac{T^{\alpha\beta}(t - ||\boldsymbol{x} - \boldsymbol{x}'||, \boldsymbol{x}')}{||\boldsymbol{x} - \boldsymbol{x}'||} d^3\boldsymbol{x}'. \tag{1.16}$$

We will solve Eq. 1.16 in both far region and near region assuming that the source is moving slowly. An important point to note is that the Lorenz gauge, i.e., $\dfrac{\partial \bar{h}^{\alpha\beta}}{\partial x^\alpha} = 0$ implies the conservation laws,

$$\frac{\partial T^{\alpha\beta}}{\partial x^\alpha} = 0. \tag{1.17}$$

One can directly see this using Eq. 1.15.

1.2.0.1 *Far zone*

In this region, the point at which we want to compute the field is at a distance (r) much greater than the gravitational-wave wavelength [7] (λ). This means that, for a source of size R,

$$R \ll \lambda \ll r. \tag{1.18}$$

[7] Later we will see that, for a source moving at a speed v, the gravitational wave produced by it, has the wavelength, $\lambda \sim \frac{c}{v} R$. Thus, a non-relativistic source ($v \ll c$) implies $R \ll \lambda$.

In the far-field approximation then, the quantity $||\boldsymbol{x} - \boldsymbol{x}'|| \simeq r$ would not vary significantly across the source and hence can be taken out of the integral in the Eq. 1.16. Furthermore, the slow motion assumption of the source allows us to approximate $t - ||\boldsymbol{x} - \boldsymbol{x}'|| \approx t - r$, in other words, the relative retardation effect between two points of the source can be neglected [8]. With these valid approximations, Eq. 1.16 can be written as

[8] Relaxing this approximation would lead to multipole expansion of the source, i.e., the expansion of $T^{\alpha\beta}(t - ||\boldsymbol{x} - \boldsymbol{x}'||)$ in $\boldsymbol{x}'$ around $T^{\alpha\beta}(t - ||\boldsymbol{x}||)$.

$$\bar{h}^{\alpha\beta}(t, \boldsymbol{x}) \simeq \frac{4}{r} \int T^{\alpha\beta}(t - r, \boldsymbol{x}') d^3\boldsymbol{x}'. \tag{1.19}$$

In the far-field region, we can work in TT gauge where only spatial components of the metric are non-vanishing. Hence, we can work with only the spatial components,

$$\bar{h}^{ij}(t, \boldsymbol{x}) \simeq \frac{4}{r} \int T^{ij}(t - r, \boldsymbol{x}') d^3\boldsymbol{x}'. \tag{1.20}$$

Using conservation equations 1.17, we can show that the spatial component of the stress-energy momentum tensor T^{ij} is related to the time-time component by

$$T^{ij} = \frac{1}{2} \frac{\partial^2}{\partial t^2} (x^i x^j T^{00}) \quad + \quad \text{boundary terms of integral.} \tag{1.21}$$

Eq. 1.20 can then be written as

$$\bar{h}^{ij}(t, \boldsymbol{x}) \simeq \frac{2}{r} \frac{\partial^2}{\partial t^2} \int (x'^i x'^j T^{00})(t - r, \boldsymbol{x}') d^3\boldsymbol{x}'. \tag{1.22}$$

Defining, what is called *quadrupole moment tensor* by,

$$I^{ij}(t) = \int (x^i x^j T^{00})(t, \boldsymbol{x}) d^3\boldsymbol{x}. \tag{1.23}$$

the solution then takes the form,

$$\bar{h}^{ij}(t, \boldsymbol{x}) \simeq \frac{2}{r} \frac{\partial^2}{\partial t^2} I^{ij}(t - r). \tag{1.24}$$

With the constants G and c, this looks

$$\bar{h}^{ij}(t, \boldsymbol{x}) \simeq \frac{2G}{rc^4} \frac{\partial^2}{\partial t^2} I^{ij}(t - r/c). \tag{1.25}$$

Note that not all of the spatial components are physical. We can see this by projecting $\bar{h}^{ij}$ into TT gauge which will select out only the physical degrees of freedom. We proceed as follows: given the direction of propagation of the gravitational waves ($\boldsymbol{n}$), we construct a transverse projection operator

$$P_{ij} = \delta_{ij} - \hat{n}_i \hat{n}_j, \tag{1.26}$$

where $\hat{n}_i = x^i / r$ is the unit vector. This operator projects a vector into a plane orthogonal to the direction of propagation of gravitational waves. Using P_{ij}, we construct a projection tensor that can be used to project any second rank symmetric tensor into TT gauge,

$$\Lambda_{ij,kl}(\hat{n}) = P_{ik} P_{jl} - \frac{1}{2} P_{ij} P_{kl}. \tag{1.27}$$

Then, for a plane wave solution in Lorenz gauge [9], the corresponding solution in TT gauge is

$$\bar{h}^{\mathrm{TT}}_{ij} = \Lambda_{ij,kl} \bar{h}_{kl}, \tag{1.28}$$

and by construction, the right hand side of Eq. 1.28 is transverse and traceless in (i, j).

[9] Note that, it's important to start with Lorenz gauge, otherwise the fact that $\Box \bar{h}_{ij} = 0$ no longer holds and TT projection will not work.

1.2.0.2 *Near-field zone*

Near-field zone describes the dynamics of the source. This is defined as a region of spacetime in which a point at distance r from the source satisfies the following condition:

$$R \ll r \ll \lambda. \tag{1.29}$$

Since we are working with slow motion source in weak gravity, the source dynamics can be described by Newtonian mechanics. The equation of motion of the source is then described by the Newtonian potential,

$$\Phi = -\frac{1}{2}c^4 h^{00} = -\frac{1}{2}c^4\left(\bar{h}^{00} + c^{-2}\delta_{ij}\bar{h}^{ij}\right). \tag{1.30}$$

For a given energy momentum tensor ($T^{\mu\nu}$), the solution to this potential is [10]

$$\Phi(t,\boldsymbol{x}) = -G\int \frac{T^{00}(t,\boldsymbol{x'}) + c^{-2}\delta_{ij}T^{ij}(t,\boldsymbol{x'})}{||\boldsymbol{x}-\boldsymbol{x'}||}d^3\boldsymbol{x'}. \tag{1.31}$$

We can neglect the term $\delta_{ij}T^{ij}$ which represents the internal stresses in the source, because this is suppressed by a factor $\frac{1}{c^2}$ in Newtonian limit and is thus much smaller than the mass energy density c^2T^{00}. We then have,

$$\Phi(t,\boldsymbol{x}) = -G\int \frac{T^{00}(t,\boldsymbol{x'})}{||\boldsymbol{x}-\boldsymbol{x'}||}d^3\boldsymbol{x'}. \tag{1.32}$$

We can write a perturbative solution for the potential by expanding $||\boldsymbol{x}-\boldsymbol{x'}||^{-1}$ in powers of $1/r$,

$$\Phi(t,\boldsymbol{x}) = -G\left[\frac{M}{r} + \frac{D_i x^i}{r^3} + \frac{3}{2}\frac{I\!\!I_{ij}x^i x^j}{r^5} + \cdots\right], \tag{1.33}$$

where,

$$M := \int T^{00}(\boldsymbol{x})d^3\boldsymbol{x} \tag{1.34}$$

$$D := \int x^i T^{00}(\boldsymbol{x})d^3\boldsymbol{x} \tag{1.35}$$

$$I\!\!I_{ij} := \int \left(x^i x^j - \frac{1}{3}r^2\delta_{ij}\right)T^{00}(\boldsymbol{x})d^3\boldsymbol{x}. \tag{1.36}$$

We can set the origin of the coordinate system at the centre of the mass which remains fixed in time for Newtonian motions. Thus, in the centre of mass coordinates, the dipole moment of the source (D^i) can be set to zero for all time. Note that, $I\!\!I_{ij}^{\mathrm{TT}} = I_{ij}^{\mathrm{TT}}$, because they differ from each other only by the trace which, in TT gauge, is anyway zero. From Eq. 1.25, we see that far-field solution i.e.,

[10] We have ignored the retardation effects, which is a valid assumption in near zone.

the gravitational waves, is related to the near zone solution, i.e., the Newtonian potential (given in terms of I^{ij})

$$h_{ij}^{\mathrm{TT}} \simeq \frac{2G}{rc^4}\frac{\partial^2}{\partial t^2} I^{ij}(t - r/c). \tag{1.37}$$

1.2.1 *Gravitational wave luminosity*

The energy momentum tensor associated with gravitational waves is given by the expression

$$t_{\mu\nu} = \frac{c^4}{32\pi G}\langle \partial_\mu h_{\alpha\beta} \partial_\nu h^{\alpha\beta} \rangle. \tag{1.38}$$

[11] and the conservation laws, when taking the effect of gravitational waves on the background spacetime, modifies to

$$\bar{D}^\mu (\bar{T}_{\mu\nu} + t_{\mu\nu}) = 0, \tag{1.39}$$

where the $\bar{D}^\mu$ is the covariant derivative w.r.t the background curvature and $\bar{T}_{\mu\nu}$ is the matter energy density [12]. Far from the source, this reduces to

$$\partial^\mu t_{\mu\nu} = 0 \tag{1.40}$$

In TT gauge, the energy density carried by gravitational waves would be given by

$$t^{00} = \frac{c^2}{32\pi G}\langle \dot{h}_{ij}^{\mathrm{TT}} \dot{h}_{ij}^{\mathrm{TT}} \rangle, \tag{1.41}$$

where the dot represents the partial derivative w.r.t the time [13]

Using the Eq. 1.40, we can show that the gravitational wave flux, i.e., the amount of energy passing through an area dA of a spherical surface surrounding the source at a large distance r, is given by

$$\frac{dE}{dtdA} = -\frac{c^3}{32\pi G}\langle \dot{h}_{ij}^{\mathrm{TT}} \dot{h}_{ij}^{\mathrm{TT}} \rangle. \tag{1.42}$$

In terms of gravitational wave amplitudes [14],

$$\frac{dE}{dtdA} = -\frac{c^3}{32\pi G}\langle \dot{h}_{+}^2 + \dot{h}_{\times}^2 \rangle. \tag{1.43}$$

[11] The notation $\langle\rangle$ represents an average over many wavelengths of gravitational waves. In general relativity, there is no notion of unique local gravitational energy. The reason is that one can always choose to work in a local inertial frame where it would vanish. In other words, gravitational waves can not be confined locally. Finding an expression for the energy carried by gravitational waves requires decomposing the total metric into a background metric (smooth) and the metric perturbation, $h_{\mu\nu}$ (highly oscillating). Averaging procedure gives a way for such a decomposition. $t_{\mu\nu}$ obtained this way is an invariant quantity, i.e., its value does not depend on a chosen coordinate system. Thus we can replace $h_{\alpha\beta}$ by the physical modes h_{ij}^{TT} in TT gauge.

[12] Eq. 1.39 shows that there is an exchange of energy and momentum between matter and gravitational waves.

[13] For a plane gravitational wave propagating along the z-direction, the only non-vanishing components are t^{03} and t^{00} and are related to each other by $t^{03} = -c^{-1}t^{00}$.

[14] For a plane wave, $h_{ij}^{\mathrm{TT}} = h_{+}e_{ij}^{+} + h_{\times}e_{ij}^{\times}$, where e_{ij}^{+} and $e_{ij}^{\times}$ are the two polarization tensors, which depend on the direction of propagation.

Using Eq. 1.37, we can write the gravitational wave flux directly in terms of the source moments,

$$\frac{dE}{dtdA} = -\frac{G}{8\pi c^5 r^2}\langle \dddot{I}^{ij}_{\rm TT}\dddot{I}^{\rm TT}_{ij}\rangle. \tag{1.44}$$

Thus the energy radiated per unit solid angle at the source is

$$\frac{dE}{dtd\Omega} = -\frac{G}{8\pi c^5}\langle \dddot{I}^{\rm TT}_{ij}\dddot{I}^{ij}_{\rm TT}\rangle. \tag{1.45}$$

To find the gravitational wave luminosity, i.e., the total energy emitted by the source per unit time, we would need to integrate over all solid angles. This gives

$$L_{\rm GW} = -\frac{dE}{dt} = \frac{1}{5}\frac{G}{c^5}\langle \dddot{I}_{ij}\dddot{I}^{ij}\rangle. \tag{1.46}$$

1.2.2 *Radiation reaction*

When a system radiates gravitational waves, it loses its energy as a consequence of energy conservation. This means that the system would feel a back reaction because it loses its energy. In general, a body experiences a force as a result of its own gravitational field, known as *self-force*. This has a contribution from both the conservative and non-conservative (gravitational radiation) part of the gravitational field. In general relativity, it is this force that ensures that bodies move on the geodesics of spacetime where the gravitational fields of bodies are also included.

To describe the source dynamics fully, we must know the form of radiation reaction force. In general, its computation is difficult. However, for weakly gravitating and slowly moving bodies we can find it by enforcing the energy conservation. By definition, the work done by the radiation reaction force ($\boldsymbol{F}^{\rm RR}$) on a body should be equal to the negative of the power radiated by it in the gravitational waves, i.e.,

$$\int \boldsymbol{F}^{\rm RR}\cdot\mathbf{v}dt = -\frac{1}{5}\frac{G}{c^5}\int \dddot{I}_{ij}\dddot{I}^{ij}dt, \tag{1.47}$$

where the integral is to be performed over a many gravitational wave

cycles. From this, we can show that, the radiation reaction force on the body with mass m [15], is given by

[15] Assuming that the body can be treated as a point particle.

$$F_j^{\mathrm{RR}} = -\frac{2}{5}\frac{G}{c^5} m x^i \frac{d^5 I_{ij}}{dt^5}, \tag{1.48}$$

where $\boldsymbol{x}$ is the position of the body. The associated potential for this force such that, $\boldsymbol{F}^{\mathrm{RR}} = -\nabla\Phi^{\mathrm{RR}}$, is

$$\Phi^{\mathrm{RR}} = \frac{1}{5}\frac{G}{c^5} x^i x^j \frac{d^5 I_{ij}}{dt^5}. \tag{1.49}$$

In short, the equations of motion of a system should be obtained from a potential which is the sum of the Newtonian potential and the radiation reaction potential. The former gives the conservative dynamics of the system while the later includes the effect of the energy loss by the system in gravitational waves.

It is easy to show that a body moving under this radiation reaction force, will lose the angular momentum too. This fact can then be used to find a formula for the angular momentum carried by the gravitational waves. The rate of change of angular momentum of a point particle due to the force $\boldsymbol{F}^{\mathrm{RR}}$ acting on it is

$$\frac{d\boldsymbol{J}}{dt} = \boldsymbol{x} \times \boldsymbol{F}^{\mathrm{RR}}, \tag{1.50}$$

which after a few steps of computations gives

$$\frac{dJ_i}{dt} = -\frac{2}{5}\frac{G}{c^5}\epsilon_{ijk}\langle \dddot{I}^k_l \ddot{I}^{lj} \rangle. \tag{1.51}$$

The R.H.S term represents the angular momentum carried by the gravitational waves.

1.3 *Gravitational wave source: binary system*

Let us now apply the tools developed in the earlier section to compute the gravitational waves from a particular kind of source, the binary system. Throughout the thesis, we will mainly be interested

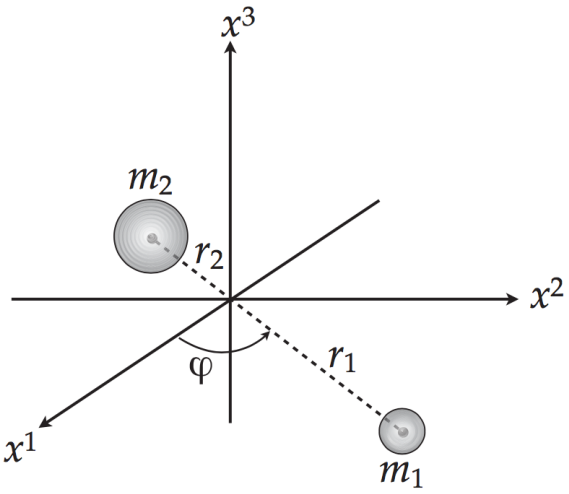

Figure 1.1: A binary system with two point masses in $x^1 - x^2$ plane encircling each other [87].

in computing the gravitational waves from such systems.

Consider a system consisting of two-point particles with masses m_1 and m_2 orbiting each other (see Fig. 1.1). We assume that the orbit is circular. We choose to work in the center of mass coordinates. Let us say; there is an observer at a distance r from the center of the binary plane forming an angle i with the axis (x^3) of the orbital plane. Since we assume Newtonian dynamics of the system, the orbital angular momentum direction (x^3) will not change with time, i.e., the plane of binary will remain fixed.

We compute the quadrupole moment tensor for this system and put in Eq. 1.25. This gives us the two polarizations of gravitational waves as follows [16],

$$h_+ = -\frac{2G\mu}{c^2 r}(1+\cos^2 i)\left(\frac{v}{c}\right)^2 \cos(2\varphi) \tag{1.52}$$

$$h_\times = -\frac{2G\mu}{c^2 r} 2\cos i \left(\frac{v}{c}\right)^2 \sin(2\varphi), \tag{1.53}$$

where $\varphi = \omega_{orb} t$ and ω_{orb} is the orbital frequency of the system. The other parameters are defined below:

$$\mu = \frac{m_1 m_2}{M}; \qquad M = m_1 + m_2 \tag{1.54}$$

$$v = (GM\omega_{orb})^{1/3}. \tag{1.55}$$

[16] It is easy to compute the quadrupole moment tensor in the binary frame itself with coordinates chosen as shown in the Fig. 1.1 and it turns out that the metric perturbation tensor 1.25 already has a form that we want it to have in TT gauge. Hence one can directly read off the polarizations. This metric tensor can then be transformed to any other coordinate system attached to the binary plane, e.g. the one whose axis is inclined at an angle i with respect to the orbital angular momentum of the binary system.

We see that the gravitational wave generated by such a system has a frequency twice the orbital frequency, i.e., $\omega_{\rm GW} = 2\pi f = 2\omega_{orb}$. The energy lost by the system in gravitational waves has to come from its orbital energy itself. This means that the orbit will decay with time which will cause the orbital frequency and amplitude both to increase. To understand this mathematically, we first compute the luminosity (the energy lost by the system) using the Eq. 1.46 (which requires the third time derivative of quadrupole moment tensor)

$$L_{\rm GW} = \frac{32}{5}\frac{c^5}{G}\eta^2\Big(\frac{v}{c}\Big)^{10}, \tag{1.56}$$

where $\eta = \mu/M$ is called the *symmetric mass ratio*. The orbital energy of the system is simply the sum of the kinetic energy of the individual particles plus their gravitational interaction potential energy. They combine to give,

$$E = -\frac{1}{2}\mu v^2. \tag{1.57}$$

Since $L_{\rm GW} = -dE/dt$, we have

$$\frac{d(v/c)}{dt} = \frac{32\eta}{5}\frac{c^3}{GM}\Big(\frac{v}{c}\Big)^9. \tag{1.58}$$

This gives the evolution of the orbital frequency ω_{orb} with time as a consequence of the back reaction which the system feels due to the gravitational wave radiation. Let us investigate this a bit more.

First of all, we would like to know the time that binary takes to coalesce starting from some initial orbital velocity/frequency (v_0), so that it would give us a feel about the length of time duration of the gravitational waves being produced. Using Eq. 1.58, we can write

$$\int_{v_0/c}^{\infty}\frac{d(v/c)}{(v/c)^9} = \frac{32\eta}{5}\frac{c^3}{GM}\int_0^{\tau_c} dt, \tag{1.59}$$

where τ_c is called the *time until coalescence*. Upon integration we get,

$$\tau_c = \frac{5}{256\eta}\frac{GM}{c^3}\Big(\frac{v_0}{c}\Big)^{-8}. \tag{1.60}$$

The important quantity for the gravitational wave data analysis [17] is

[17] The tools required for gravitational wave detection and subsequent investigations.

the phase evolution of the binary due to the loss in orbital energy and angular momentum. Let us define two useful quantities, the *energy function* $\mathcal{E}(v)$ and the *flux function* $\mathcal{F}(v)$ as

$$\mathcal{E}(v) := \frac{E(v) - Mc^2}{Mc^2} \tag{1.61}$$

$$\mathcal{F}(v) := \frac{G}{c^5} L_{\rm GW}(v). \tag{1.62}$$

For our system, they become

$$\mathcal{E} = -\frac{1}{2}\eta\left(\frac{v}{c}\right)^2, \tag{1.63}$$

$$\mathcal{F} = \frac{32}{5}\eta^2\left(\frac{v}{c}\right)^{10}. \tag{1.64}$$

Using $L_{\rm GW} = -dE/dt$, we can write

$$\frac{dt}{dv} = -\frac{GM}{c^3}\frac{1}{\mathcal{F}}\frac{d\mathcal{E}}{dv}. \tag{1.65}$$

Let us take t_c as the time of coalescence [18]. Then the time corresponding to a given orbital velocity v can be found by

[18] Note that this is not the time until coalescence τ_c, rather, it represents the time at which the coalescence takes place.

$$t(v) = t_c + \frac{GM}{c^3}\int_v^{v_c}\frac{1}{\mathcal{F}}\frac{d\mathcal{E}}{dv}dv, \tag{1.66}$$

where v_c is the velocity at the time t_c. The orbital phase as a function of orbital velocity/frequency can be easily computed by

$$\frac{d\varphi}{dv} = \frac{d\varphi}{dt}\frac{dt}{dv} = -\left(\frac{v}{c}\right)^3\frac{1}{\mathcal{F}}\frac{d\mathcal{E}}{dv}, \tag{1.67}$$

which gives

$$\varphi(v) = \varphi_c + \int_v^{v_c}\left(\frac{v}{c}\right)^3\frac{1}{\mathcal{F}}\frac{d\mathcal{E}}{dv}dv. \tag{1.68}$$

The gravitational waveform in Eq. 1.74 can be now completely parametrized by $v = (GM\omega_{orb})^{1/3}$, where f is gravitational wave frequency, as

$$h_+(t(v)) = -\frac{2G\mu}{c^2 r}(1+\cos^2 i)\left(\frac{v}{c}\right)^2\cos 2\varphi(v) \tag{1.69}$$

$$h_\times(t(v)) = -\frac{2G\mu}{c^2 r}2\cos i\left(\frac{v}{c}\right)^2\sin 2\varphi(v), \tag{1.70}$$

Where $t(v)$ and $\varphi(v)$ are given by Eq. 1.66 and 1.68, respectively.

Note that v is directly related to the gravitational wave frequency as $v = (\pi GMf)^{1/3}$, since $f = 2\omega_{orb}/2\pi$. The frequency evolution can be computed by

$$\frac{df}{dt} = \frac{df}{dv}\frac{dv}{dt} = \frac{96}{5}\pi^{8/3}\eta\left(\frac{GM}{c^3}\right)^{5/3} f^{11/3}. \tag{1.71}$$

Introducing a quantity known as the *chirp mass*, $\mathcal{M} = \eta^{3/5}M = \mu^{3/5}M^{2/5} = (m1_1m_2)^{3/5}(m_1+m_2)^{-1/5}$, we can write the frequency evolution as

$$\frac{df}{dt} = \frac{96}{5}\pi^{8/3}\left(\frac{G\mathcal{M}}{c^3}\right)^{5/3} f^{11/3}. \tag{1.72}$$

This shows that the frequency evolution depends on just the chirp mass and not on any other combination of component masses. In fact, we can show that, the entire gravitational waveform has the mass dependence only through the chirp mass [19] as expressed below

[19] Note that this is true only for Newtonian limit of gravity, i.e., where the gravity is weak and particles are moving slowly.

$$h_+(t) = -\frac{G\mathcal{M}}{c^2 r}\frac{1+\cos^2 i}{2}\left(\frac{c^3(t_c-t)}{5G\mathcal{M}}\right)^{-1/4}\cos\left[2\phi_c - 2\left(\frac{c^3(t_c-t)}{5G\mathcal{M}}\right)^{5/8}\right] \tag{1.73}$$

$$h_\times(t) = -\frac{G\mathcal{M}}{c^2 r}\cos i\left(\frac{c^3(t_c-t)}{5G\mathcal{M}}\right)^{-1/4}\sin\left[2\phi_c - 2\left(\frac{c^3(t_c-t)}{5G\mathcal{M}}\right)^{5/8}\right]. \tag{1.74}$$

1.4 *Post-Newtonian theory*

In the previous section we discussed the generation and propagation of gravitational waves in weak field limit of Einstein equations with sources following Newtonian dynamics, i.e., linearised gravity regime. For example, we discussed the production of gravitational waves from a binary system where the component objects were moving slowly and were assumed to be the weak source of gravity. However, when the system is highly relativistic or strongly gravitating, this approximation will no longer be valid and one should consider going beyond the Newtonian limit. *Post-Newtonian* (PN)

theory, as the name itself suggests, deals with systems that are moving with moderate velocities and thus gives relativistic corrections to the equations of motion of bodies, in orders of their velocity. While *Numerical relativity* (NR), discussed in next section, is an approach to directly solve Einstein equations without resorting to any approximations.

A system with mass M and size R produces the gravitational field, GM/c^2R. We call this system a weak source of gravity if $GM/c^2R \ll 1$. If the system is self-gravitating, the virial theorem implies that $GM/c^2R \sim v^2/c^2$. This means that for weak self-gravitating sources, the internal motions within the system are small. Post-Newtonian theory expands the equations of motion in the powers of v^2/c^2 (or simply $1/c^2$). A full treatment of post-Newtonian theory not just provides the corrections to the equation of motion but also gives the general relativistic (non-linear interactions of gravitational field itself) corrections to the gravitational field in orders of GM/c^2R (or simply in orders of G). In this sense, the linearised theory considers the leading order term in G (i.e., the term of $\mathcal{O}(h^2)$ was neglected). Our aim here is to compute gravitational waveforms produced by inspiralling binaries to a very high order in v^2/c^2 using PN theory. This is motivated by the fact that a very accurate prediction of gravitational wave signals is required to extract them from the experimental data.

Before we proceed to the details, the whole problem of computing gravitational waves from a system with typical velocity v and size R [20], can be summarised as following [21]: the near zone for such a system extends up to a radius $\mathcal{R} \gg R$. The PN formalism is used to find the gravitational field in the region, $r < \mathcal{R}$. While in the region, $\mathcal{R} < r < \infty$, PN formalism breaks down and a different formalism known as *post-Minkowskian* expansion is used to compute the gravitational field. In fact, the post-Minkowskian formalism is applicable in the whole region outside the source where the matter stress-energy tensor vanishes. Thus, there is an overlapping region $R < r < \mathcal{R}$

[20] We assume that $v/c \ll 1$.

[21] There have been developed different approaches for solving this problem. Here we outline the steps used in Blanchet-Damour approach.

where both formalisms are valid. The idea is then to match these two solutions in the overlapping region. This allows us to express the gravitational waveforms in terms of source parameters.

1.4.1 *post-Newtonian expansion of Einstein equations*

Let us first discuss how to find the lowest order correction [22] to the equations of the motion of a source.

[22] Called as 1PN correction to the Newtonian equations of motion.

Ou aim is to expand Einstein equations in some small parameter. Here, we introduce

$$\epsilon \sim (R_s/R)^{1/2} \sim v/c, \tag{1.75}$$

where $R_s = 2GM/c^2$. Since source components are assumed to be moving slowly, we have $\epsilon \ll 1$. We also assume that the source is weakly stressed [23], i.e., $|T^{ij}|/T^{00} = \mathcal{O}(\epsilon^2)$. We now expand the metric and the stress energy tensor components in the powers of ϵ as follows [24]:

[23] For a fluid with pressure p and energy density ρ, this would imply $p/\rho = \mathcal{O}(\epsilon^2)$.

[24] If we neglect the gravitational radiation for time being, then a closed system must be invariant under time reversal, because there will not any non-conservative forces acting on it. This means that physical quantities such as, the line element (ds^2) must also be invariant. Then by definition, under time reversal, g_{00} and g_{ij} become even while g_{0i} becomes odd (because with it comes the term dt which is already odd).

$$\begin{aligned} g_{00} &= -1 + {}^{(2)}g_{00} + {}^{(4)}g_{00} + {}^{(6)}g_{00} + \cdots \\ g_{0i} &= \epsilon\ {}^{(3)}g_{0i} + \epsilon\ {}^{(5)}g_{0i} + \cdots \\ g_{ij} &= \epsilon^2\ \delta_{ij} + \epsilon^2\ {}^{(2)}g_{ij} + \epsilon^2\ {}^{(4)}g_{ij} + \cdots, \end{aligned} \tag{1.76}$$

and

$$\begin{aligned} T^{00} &= {}^{(0)}T^{00} + {}^{(2)}T^{00} + \cdots \\ T^{0i} &= {}^{(1)}T^{0i} + {}^{(3)}T^{0i} + \cdots \\ T^{ij} &= {}^{(2)}T^{ij} + {}^{(4)}T^{ij} + \cdots, \end{aligned} \tag{1.77}$$

where ${}^{(n)}g_{\mu\nu}$ represents the term of order ϵ^n in the expansion of $g_{\mu\nu}$. Note that we have included appropriate powers of ϵ in g_{0i} and g_{ij} expansion just to keep count of relative order of each term needed to be computed to work consistently to a given order in ϵ [25]. For example, if g_{00} is to be computed up to a order ϵ^n then one has to compute g_{0i} up to a order ϵ^{n-1} and g_{ij} up to a order ϵ^{n-2}.

[25] By inspecting Einstein equations, one finds that compared to g_{00}, g_{0i} starts at $\mathcal{O}(\epsilon)$ while g_{ij} at $\mathcal{O}(\epsilon^2)$.

We plug in these expansions in the Einstein equations and equate the terms of the same order in ϵ. However, in doing so, we would require to take into account of the fact that for non-relativistic sources, the time derivatives of the metric (e.g., ${}^{(n)}g_{\mu\nu}$) is smaller than the spatial derivatives by a factor of $\mathcal{O}(\epsilon)$, i.e,

$$\frac{\partial}{\partial t} = \mathcal{O}(\epsilon)\frac{\partial}{\partial x^i}, \tag{1.78}$$

and whenever the d'Alembertian operator appears, it should be replaced by

$$\Box = -\frac{1}{c^2}\frac{\partial^2}{\partial t^2} + \boldsymbol{\nabla^2} = [1 + \mathcal{O}(\epsilon^2)]\boldsymbol{\nabla^2}. \tag{1.79}$$

Or in other words, the retardation effects are assumed to be small in the post-Newtonian theory. This means that any retarded quantity $F(t - r/c)$ (e.g., the metric components, ${}^{(n)}g_{\mu\nu}$) can be reconstructed from its expansion for small retardation $r/c \ll t$ [26]

$$F(t - r/c) = F(t) - \frac{r}{c}\dot{F}(t) + \frac{r^2}{2c^2}\ddot{F}(t) + \cdots . \tag{1.80}$$

This also means that in the case of small retardation effects, we can express any retarded function in terms of instantaneous functions. Furthermore, $\partial/\partial t \sim \omega$, where ω is a typical frequency of radiation emitted. Since $\omega/c = 1/\lambda\!\!\!^{-}$, Eq. 1.80 is actually an expansion in $r/\lambda\!\!\!^{-}$. Thus post-Newtonian expansion would be valid only in region $r \ll \lambda\!\!\!^{-}$, which is precisely the definition of near zone. As it turns out, post-Newtonian theory can not simply be used in the region $r \gg \lambda\!\!\!^{-}$ otherwise it would lead to divergences. One must adopt a new approach to compute gravitational field in the far region (radiation zone).

We now insert the expansions in Eq. 1.76 and Eq. 1.77 in Einstein equations. By computing the equation of motion of the source, we see that the Newtonian dynamics can be recovered with $g_{00} = -1 + {}^{(2)}g_{00}$, $g_{0i} = 0$ and $g_{ij} = 0$ [27]. Thus the terms ${}^{(4)}g_{00}$, ${}^{(3)}g_{0i}$ and ${}^{(2)}g_{ij}$ are expected to give the first post-Newtonian correction to the

[26] The truncation of the series depends on the post-Newtonian order required in the problem.

[27] This is only true when we want to compute equation of motion of non-relativistic particles which is the case in our problem. However, for relativistic particles, we will also have contribution from ${}^{(2)}g_{ij}$ at the leading order only. For non-relativistic particles, ${}^{(2)}g_{ij}$ contribution gets suppressed by $\mathcal{O}(\nu)$ in the equation of motion.

equation of motion while the higher order expansions in the metric would provide the higher order post-Newtonian corrections. Let us work out the first post-Newtonian (1PN) correction to the equation of motion of the source.

1.4.2 *First post-Newtonian order*

It is better to choose a gauge from the beginning itself because a right gauge can simplify the equations a lot. We choose what is called harmonic gauge [28]

$$\partial_\mu(\sqrt{-g}g^{\mu\nu}) = 0. \tag{1.82}$$

[28] Actually in this gauge, the coordinates satisfy

$$\partial_\mu(\sqrt{-g}g^{\mu\nu}\partial_\nu)x^\rho = 0, \tag{1.81}$$

and this is called harmonic condition.

Inserting the Eq. 1.76 and Eq. 1.77 in Einstein equations, we find that, ${}^{(2)}g_{00}$ indeed describes Newtonian equations

$$\boldsymbol{\nabla^2}[{}^{(2)}g_{00}] = -\frac{8\pi G}{c^4}\ {}^{(0)}T^{00}, \tag{1.83}$$

while

$$\begin{aligned}
\boldsymbol{\nabla^2}[{}^{(2)}g_{ij}] &= -\frac{8\pi G}{c^4}\delta_{ij}\ {}^{(0)}T^{00} \\
\boldsymbol{\nabla^2}[{}^{(3)}g_{0i}] &= \frac{16\pi G}{c^4}\delta_{ij}\ {}^{(1)}T^{0i} \\
\boldsymbol{\nabla^2}[{}^{(4)}g_{00}] &= \partial_0^2[{}^{(2)}g_{00}] + {}^{(2)}g_{ij}\partial_i\partial_j[{}^{(2)}g_{00}] - \partial_i[{}^{(2)}g_{00}]\partial_i[{}^{(2)}g_{00}] \\
&\quad - \frac{8\pi G}{c^4}\left\{{}^{(2)}T^{00} + {}^{(2)}T^{ii} - 2\,{}^{(0)}g_{00}\,{}^{(0)}T^{00}\right\},
\end{aligned} \tag{1.84}$$

describes the 1PN correction to the metric.

Eq. 1.83 can be seen as Newton's law with the replacement, ${}^{(2)}g_{00} = -2\phi$, where $U = -c^2\phi$ is the Newton's potential. The solution is

$$\phi(t,\boldsymbol{x}) = -\frac{G}{c^4}\int d^3\boldsymbol{x'}\,\frac{{}^{(0)}T^{00}(t,\boldsymbol{x'})}{|\boldsymbol{x}-\boldsymbol{x'}|}. \tag{1.85}$$

Solutions to the Eq. 1.84 turn out to be

$$\begin{aligned}
g_{00} &= -1 + \frac{2}{c^2}V - \frac{2}{c^4}V^2 + \mathcal{O}\Big(\frac{1}{c^6}\Big) \\
g_{0i} &= -\frac{4}{c^3}V_i + \mathcal{O}\Big(\frac{1}{c^5}\Big) \\
g_{ij} &= \delta_{ij}\Big(1 + \frac{2}{c^2}V\Big) + \mathcal{O}\Big(\frac{1}{c^4}\Big),
\end{aligned} \tag{1.86}$$

where V and V_i are retarded integrals of stress energy tensor of the source [29],

$$V(t,\boldsymbol{x}) = G\int d^3\boldsymbol{x'}\frac{1}{|\boldsymbol{x}-\boldsymbol{x'}|}\sigma(t-|\boldsymbol{x}-\boldsymbol{x'}|/c,\boldsymbol{x'}), \tag{1.87}$$

and

$$V_i(t,\boldsymbol{x}) = G\int d^3\boldsymbol{x'}\frac{1}{|\boldsymbol{x}-\boldsymbol{x'}|}\sigma_i(t-|\boldsymbol{x}-\boldsymbol{x'}|/c,\boldsymbol{x'}), \tag{1.88}$$

where $\sigma = \frac{1}{c^2}\left[{}^{(0)}T^{00} + {}^{(2)}T^{00} + {}^{(2)}T^{ii}\right]$ and $\sigma_i = \frac{1}{c}\left[{}^{(1)}T^{0i}\right]$.

Now that we have the near zone metric at 1PN order, we can compute the equations of motion of a particle of mass m that moves in this metric. This can be found by extremizing the action written in this curved background

$$\begin{aligned} S &= -mc\int dt\left(-g_{\mu\nu}\frac{dx^\mu}{dt}\frac{dx^\nu}{dt}\right)^{1/2} \\ &= -mc^2\int dt\left(-g_{00}-2g_{0i}\frac{v^i}{c}-g_{ij}\frac{v^iv^j}{c^2}\right)^{1/2}. \end{aligned} \tag{1.89}$$

Let us compute the 1PN correction to the metric for a binary system with point masses (particles). The stress energy momentum tensor for a set of point-like particles with mass m_a moving along the trajectory $\boldsymbol{x_a}(a=1,2)$ is defined by

$$T^{\mu\nu} = \frac{1}{\sqrt{-g}}\sum_a \gamma_a m_a\frac{dx^\mu}{dt}\frac{dx^\nu}{dt}\delta^{(3)}(\boldsymbol{x}-\boldsymbol{x_a}(t)), \tag{1.90}$$

where x_a^μ are the coordinates for $\boldsymbol{x_a}(t)$. If we neglect the self-force [30], then the metric felt by a particle is due to stress energy momentum tensors of others. Thus the action can be divided into two parts $S = S_1 + S_2$, where for example, S_1 is due to the metric produced by the second particle. The stress energy momentum tensor for S_1 is

ity in this case is not a problem. The reason is that the PN solution will be matched with the post-Minkowskian solution in the overlapping region. In post-Minkowskian expansion, however, choosing no-incoming radiation at spatial infinity is allowed because its validity region extends up to spatial infinity.

[30] This can not be neglected if radiation reaction effects are being taken into account. However, we will see that this occurs at high post-Newtonian orders.

then,

$$
\begin{aligned}
{}^{(0)}T^{00}(t,\boldsymbol{x}) &= m_2 c^2 \delta^{(3)}(\boldsymbol{x}-\boldsymbol{x_2}(t)) \\
{}^{(2)}T^{00}(t,\boldsymbol{x}) &= m_2\left(\frac{1}{2}v_2^2+2\phi c^2\right)\delta^{(3)}(\boldsymbol{x}-\boldsymbol{x_2}(t)) \\
{}^{(1)}T^{0i}(t,\boldsymbol{x}) &= m_2 c v_2^i \delta^{(3)}(\boldsymbol{x}-\boldsymbol{x_2}(t)) \\
{}^{(2)}T^{ij}(t,\boldsymbol{x}) &= m_2 v_2^i v_2^j \delta^{(3)}(\boldsymbol{x}-\boldsymbol{x_2}(t)),
\end{aligned}
\tag{1.91}
$$

where ϕ is the potential produced by the second particle (see Eq. 1.85). Similarly, we can write for the first particle. From the total action, we can extract the Lagrangian for the binary system. We get, $L = L_0 + 1/c^2 L_2$, where

$$
L_0 = \frac{1}{2}m_1 v_1^2 + \frac{1}{2}m_2 v_2^2 + \frac{G m_1 m_2}{r}, \tag{1.92}
$$

and

$$
\begin{aligned}
L_2 = &\frac{1}{8}m_1 v_1^4 + \frac{1}{8}m_2 v_2^4 \\
&+ \frac{G m_1 m_2}{2r}\Big[3(v_1^2+v_2^2) - 7\boldsymbol{v_1}\cdot\boldsymbol{v_2} - (\hat{\boldsymbol{x}}\cdot\boldsymbol{v_1})(\hat{\boldsymbol{x}}\cdot\boldsymbol{v_2}) - \frac{G(m_1+m_2)}{r}\Big],
\end{aligned}
\tag{1.93}
$$

where $\boldsymbol{x}$ denotes the separation vector between the two point particles with $r = |\boldsymbol{x}|$ and $\hat{x} = \boldsymbol{x}/r$. The equations of motions can be found from Euler-Lagrange equations

$$
\frac{d}{dt}\frac{\partial L}{\partial v_a^i} = \frac{\partial L}{\partial x_a^i}, \tag{1.94}
$$

where $a = (1,2)$. It has the following form:

$$
\frac{d^2 x^i}{dt^2} = -\frac{GM}{r^2}\left\{\hat{x}^i\left[1+\mathcal{O}(\epsilon^2)\right] + \hat{v}^i\mathcal{O}(\epsilon^2)\right\}, \tag{1.95}
$$

where M is the total mass. We can see that the leading order term is the Newton's force, which was expected and $\mathcal{O}(\epsilon^2)$ terms give the first post-Newtonian corrections to the equations of motion [31].

So far, we have neglected the gravitational radiation to keep things simple. However, before we proceed to a systematic post-Newtonian

[31] The $\mathcal{O}(\epsilon^2)$ correction in the equations of motion leads to the periastron advance of the orbit, e.g., the orbit of mercury around the sun.

expansion where the radiation reaction effect will automatically be taken care of, we should pause for a moment and think of what would happen to the equations of motions if the gravitational radiation is to be also included. First of all, our assumption that g_{00} will have a contribution from only even powers of velocity and similarly for other components, will break down. This is because the radiation breaks the time-reversal symmetry. Thus g_{00} might as well contain odd powers of velocity.

From linearised gravity, we know that the power radiated by a self-gravitating system with typical velocity v is $P \sim GM^2v^6/(c^5r^2)$, where M denotes the mass scale of the system and r its typical size. Furthermore, the virial theorem implies that the total energy of the system is $E_{tot} = -(1/2)Mv^2$. From the energy conservation, $dE/dt = -P$, we get,

$$\frac{dv}{dt} \sim \frac{GM}{r^2}\left(\frac{v}{c}\right)^5. \tag{1.96}$$

Thus we expect the radiation reaction effects to occur at $\mathcal{O}(\epsilon^5)$ in the equations of motion. Hence, we expect the equations of motion to look like,

$$\begin{aligned}\frac{d^2x^i}{dt^2} = -\frac{GM}{r^2}\Big\{&\hat{x}^i\left[1 + \mathcal{O}(\epsilon^2) + \mathcal{O}(\epsilon^4) + \mathcal{O}(\epsilon^5) + \mathcal{O}(\epsilon^6) + \cdots\right] \\ &+ \hat{v}^i\left[\mathcal{O}(\epsilon^2) + \mathcal{O}(\epsilon^4) + \mathcal{O}(\epsilon^5) + \mathcal{O}(\epsilon^6) + \cdots\right]\Big\}.\end{aligned} \tag{1.97}$$

Note that there are no $\mathcal{O}(\epsilon^3)$ terms, because no PN correction leads to this power of velocity.

1.4.3 The relaxed Einstein equations

A particular convenient formulation of Einstein equations (called relaxed Einstein equations) useful for systematic post-Newtonian expansion is given by

$$\mathrm{h}^{\alpha\beta} \equiv (-g)^{-1/2}g^{\alpha\beta} - \eta^{\alpha\beta}. \tag{1.98}$$

Note that this is just an another way of writing the same metric [32]. There is no assumption involved here [33]. Again we start by choosing the harmonic gauge,

$$\partial_\beta \mathrm{h}^{\alpha\beta} = 0. \tag{1.99}$$

In this gauge the Einstein equations take the form,

$$\Box \mathrm{h}^{\alpha\beta} = \frac{16\pi G}{c^4}\tau^{\alpha\beta}, \tag{1.100}$$

where $\Box \equiv -\partial^2/\partial t^2 + \nabla^2$ is the usual d'Alembertian operator in flat spacetime [34] and the quantity appearing in the right hand side is

$$\tau^{\alpha\beta} \equiv (-g)T^{\alpha\beta} + \frac{c^4}{16\pi G}\Lambda^{\alpha\beta}, \tag{1.101}$$

where $T^{\alpha\beta}$ is the matter stress energy tensor while $\Lambda^{\alpha\beta}$ is independent of the matter variables and is given by

$$\Lambda^{\alpha\beta} = \frac{16\pi G}{c^4}(-g)t^{\alpha\beta}_{\mathrm{LL}} + (\partial_\nu \mathrm{h}^{\alpha\mu}\partial_\mu \mathrm{h}^{\alpha\nu} - \mathrm{h}^{\mu\nu}\partial_\mu\partial_\nu \mathrm{h}^{\alpha\beta}), \tag{1.102}$$

$t^{\alpha\beta}_{\mathrm{LL}}$ is called Landau-Lifshitz energy momentum pseudotensor, which is highly non-linear in $\mathrm{h}_{\mu\nu}$. Eq. 1.98 and Eq. 1.99 together are completely equivalent to the Einstein equations in Eq. 1.1 and Eq. 1.3. The gauge condition in Eq. 1.99 leads to the conservation law and hence provides the equation of motion for the matter variables

$$\partial_\beta \tau^{\alpha\beta} = 0. \tag{1.103}$$

Mathematically it makes perfect sense to solve Eq. 1.100 first without requiring the gauge condition (Eq. 1.99) to be satisfied, i.e., without requiring the matter variables to follow their equations of motions. This allows us to write an expression for the solutions and then we impose the gauge condition on them [35]. With no-incoming boundary condition the solutions to Eq. 1.100 are given by

$$\mathrm{h}^{\alpha\beta}(t, \boldsymbol{x}) = -\frac{4G}{c^4}\int d^3x' \frac{\tau^{\alpha\beta}(t - |\boldsymbol{x} - \boldsymbol{x'}|)}{|\boldsymbol{x} - \boldsymbol{x'}|}. \tag{1.104}$$

[32] However, we should note that there is a non-linear relation between the $\mathrm{h}^{\alpha\beta}$ and $g^{\alpha\beta}$.

[33] The notation $\mathrm{h}^{\alpha\beta}$ is also different from the linearised gravity $h^{\alpha\beta}$. However, one can show that, in linearised gravity limit, $\mathrm{h}^{\alpha\beta}$ reduce to $\bar{h}_{\alpha\beta}$ except for an overall sign. Also, $(-g)^{-1/2}g^{\alpha\beta}$ is called "gothic metric".

[34] Actually, this is the benefit of recasting Einstein equations in the relaxed form, i.e., we know how to deal with the d'Alembertian operator.

[35] The Eq 1.100 are called relaxed equations because of the very reason that we have relaxed the condition that particles have to follow their equations of motion.

Since $\tau^{\alpha\beta}$ is a functional of $h^{\alpha\beta}$ and its derivatives, it is extremely difficult to find an exact solution to Eq. 1.104. The key idea is then to resort to approximation methods, e.g., solving this in near and far zone separately. Let us briefly discuss these methods in the following.

1.4.4 Post-Minkowskian expansion outside the source

In the region outside the source, $R < r < \infty$, the matter stress energy tensor ($T^{\alpha\beta}$) vanishes. Since we are interested in weak sources, Einstein equations Eq. 1.1 suggest that the metric will not deviate much from the flat spacetime ($\eta_{\alpha\beta}$). The correction to the flat metric should be given as an expansion in R_s/r, where $R_s = 2Gm/c^2$, with m being the mass scale of the system. We will simply write this as an expansion in G. We thus write

$$(-g)^{-1/2}g^{\alpha\beta} = \eta^{\alpha\beta} + Gh_1^{\alpha\beta} + G^2h_2^{\alpha\beta} + \cdots . \tag{1.105}$$

This means,

$$h^{\alpha\beta} = \sum_{n=1}^{\infty} G^n h_n^{\alpha\beta}. \tag{1.106}$$

Putting this ansatz in the relaxed Einstein equations, Eq. 1.100 with $T^{\alpha\beta} = 0$, gives a form which looks like the following:

$$\Box h^{\alpha\beta} = \Lambda^{\alpha\beta}, \tag{1.107}$$

where $\Lambda^{\alpha\beta}$ contains all possible powers of $h_{\mu\nu}$. We now equate the terms of same order in G. We find that, to linear order in G,

$$\Box h_1^{\alpha\beta} = 0. \tag{1.108}$$

This is because the $\Lambda^{\alpha\beta}$ contain terms starting from quadratic in $h_1^{\alpha\beta}$. And to higher orders, we find,

$$\Box h_2^{\alpha\beta} = N^{\alpha\beta}[h_1, h_1], \tag{1.109}$$

and so on [36]. The general n-th order equation can be written as

$$\Box \mathrm{h}_n^{\alpha\beta} = \Lambda_n^{\alpha\beta}[\mathrm{h}_1, \mathrm{h}_2, \ldots, \mathrm{h}_{n-1}]. \tag{1.110}$$

We should remember that all this is valid only in the region $r > R$.

The Eq. 1.108 represents the linearised gravity limit. The most general solution to this equation is given in terms of retarded multipolar waves,

$$\mathrm{h}_1^{\alpha\beta} = \sum_{l=0}^{\infty} \partial_L \left[\frac{1}{r} K_L^{\alpha\beta}(t - r/c) \right], \tag{1.111}$$

where $K_L^{\alpha\beta} \equiv K^{\alpha\beta}_{i_1 i_2, \ldots, i_l}$ are traceless and symmetric with respect to $i_1 i_2, \ldots, i_l$. We now impose the gauge condition, Eq. 1.99 on this solution. This reduces the number of independent components of $\mathrm{h}_1^{\alpha\beta}$ from 10 to 6 and the most general solution in the outer region of source becomes

$$\mathrm{h}_1^{\alpha\beta} = k_1^{\alpha\beta} + \partial^\alpha \varphi_1^\beta + \partial^\beta \varphi_1^\alpha - \eta^{\alpha\beta} \partial_\mu \varphi_1^\mu. \tag{1.112}$$

It turns out that $k_1^{\alpha\beta}$ are fully described by a set of symmetric and traceless (STF) tensors $I_L(u)$ and $J_L(u)$, with u being the retarded time. They are called mass type and current type, respectively. The φ_1^β are fully described by four STF tensors $W_L(u)$, $X_L(u)$, $Y_L(u)$ and $Z_L(u)$.

The idea is now to plug the solution of linearised, Eq. 1.112, in the right hand side of the Eq. 1.109 and solve for h_2. One can go on doing this till we achieve our required order in G.

Note that the multipole moments $(I_L, J_L, W_L, X_L, Y_L, Z_L)$ that characterize the gravitational field outside the source (i.e., the vacuum Einstein equations) are freely specifiable variables, i.e., they have not yet been related to the source properties. This would be possible only after we find the solution in the near zone.

[36] $N^{\alpha\beta}$ just represents a function quadratic in $\mathrm{h}^{\alpha\beta}$.

1.4.5 *Post-Newtonian expansion in the near region*

We have already derived the first post-Newtonian correction to the metric in the section 1.4.2 (see Eq. 1.86). Our aim here is to expand this to get higher order corrections. The post-Newtonian expansion of $h^{\mu\nu}$ is,

$$h^{\mu\nu} = \sum_{n=2}^{\infty} \frac{1}{c^n} {}^{(n)}h^{\mu\nu}, \tag{1.113}$$

[37] Note that the expansion starts from $n = -2$, because $\tau^{\mu\nu}$ has the dimension of ρc^2.

and for the effective stress energy momentum tensor [37], we similarly write,

$$\tau^{\mu\nu} = \sum_{n=-2}^{\infty} {}^{(n)}\tau^{\mu\nu}. \tag{1.114}$$

Plugging this in the relaxed Einstein equations, Eq. 1.100, and keeping the terms with same powers of c, gives a recursive set of equations,

$$\nabla^2 \left[{}^{(n)}h^{\mu\nu}\right] = 16\pi G \left[{}^{(n-4)}\tau^{\mu\nu}\right] + \partial_t^2 \left[{}^{(n-2)}h^{\mu\nu}\right]. \tag{1.115}$$

These equations can be solved iteratively [38]. The solutions, of course, have to described in terms of instantaneous potentials (sourced by matter stress energy tensor) . We can further expand these functions in the powers of R/r, where R is the size of the source, to get the multipolar post-Newtonian expansion, in the region outside the source (called exterior near zone) [39]. For example, the expansion of $|\boldsymbol{x} - \boldsymbol{x'}|$ around $\boldsymbol{x'}$ in the Eq. 1.87 and Eq. 1.88 will give the multipolar expansion of the potentials V and V_i.

[38] There are a few technical details that we will not discuss here, e.g, a naive poisson integration gives divergent results because the boundary condition at spatial infinity for the field can not taken to be vanishing.

[39] Note that post-Newtonian expansion is valid in the region $0 < r < \mathcal{R}$.

1.4.6 *Matching of the solutions*

To make the matching possible in the intermediate region $R < r < \mathcal{R}$, each term of the multipolar post-Minkowskian expansion can be further expanded in post-Newtonian way, i.e., in powers of v/c. It turns out that the n-th term of post-Minkowskian expansion has the

following PN orders

$$\mathrm{h}_n^{00} = \mathcal{O}\Big(\frac{1}{c^{2n}}\Big), \quad \mathrm{h}_n^{0i} = \mathcal{O}\Big(\frac{1}{c^{2n+1}}\Big), \quad \mathrm{h}_n^{ij} = \mathcal{O}\Big(\frac{1}{c^{2n}}\Big). \tag{1.116}$$

This suggests that if we want to compute the corrections to the Newtonian metric at 2PN order, i.e., keeping the term up to $\mathcal{O}\Big(\frac{1}{c^4}\Big)$ in the metric, then we would need to compute h_n up to $n = 3$ (see, Eq. 1.113). In other words, we will have to iterate the linearised solution h_1 twice. It is now possible to compare the two solutions at each PN order. The comparison will allow us to express the multipole moments $(I_L, \ldots, Z_L)$ in terms of stress energy tensor of the source.

We must note that the key idea in this whole formalism is the existence of an overlapping region which, however, is not guaranteed. Let us investigate this. We had said that for a system of size R with $v \ll c$, the near region extends up to the distance $r < \mathcal{R}$, where $\mathcal{R} \gg R$. The PN expansion is valid until $r < \mathcal{R}$ [40] and break down at distances, $r \sim \lambda\!\!\!^{-} \sim (c/v)R$. From linearised gravity theory, we know that the higher multipole moments of the source produce gravitational waves at higher frequencies, e.g., n-th order multipole produces radiation with a set of frequencies ranging from source frequency ω_s to a maximum frequency $n\omega_s$. In PN expansion, n-th order term contains the multipoles of up to order $\sim n$ producing radiation with frequencies up to $\sim n\omega_s$. This means that the reduced wavelength will now be $\lambda\!\!\!^{-} = \mathcal{O}\Big(\frac{1}{n}\Big)\lambda\!\!\!^{-}_0$, where $\lambda\!\!\!^{-}_0 \sim (v/c)R$. Thus, when n becomes larger than $\mathcal{O}\Big(\frac{c}{v}\Big)$, the condition $\lambda\!\!\!^{-} \gg R$ will no longer hold, implying that the matching region will not exist for arbitrarily large PN order. This suggests that we can compute gravitational waves only up to a PN order $\sim \mathcal{O}(c/v)$.

[40] Remember that, $\mathcal{R}$ is of the order of the reduced wavelength ($\lambda\!\!\!^{-}$) of the gravitational wave.

1.4.7 *Radiative field at infinity*

In the subsection 1.4.4, we discussed the solution outside the source. The gravitational waves can then be extracted from the solution at the future null infinity [41], where we expect them to be found. Let

[41] This means, at spatial infinity $r \to \infty$ with $u = t - r/c$ fixed.

us choose what is called *radiative coordinate system* at the future null infinity [42], i.e., $X^\mu = (T, \boldsymbol{X})$ with $R = |\boldsymbol{X}|$ and $U = T - R/c$. In this coordinate system the n-th term of the post-Minkowskian expansion is given by

$$H_n^{\mu\nu} = \sum_{k=1}^{\infty} K^{\mu\nu}_{L,(k,n)}(U)\frac{\hat{N}_L}{R^k}, \tag{1.117}$$

where $\boldsymbol{N} = \boldsymbol{X}/R$ is unit radial direction [43]. For gravitational waves, we need to select only the $1/R$ part of H_{ij}. The physical components can be extracted by projecting it into TT gauge using the Lambda tensor $\Lambda_{ij,kl}$ (see, Eq. 1.27). The result is,

$$\begin{aligned} H_{ij}^{\rm TT}(U,\boldsymbol{N}) =& \frac{4G}{c^2R}\Lambda_{ij,ab}\sum_{l=2}^{\infty}\frac{1}{c^l l!}\Bigg\{N_{L-2}U_{abL-2}(U) \\ &- \frac{2l}{c(l+1)}N_{cL-2}\epsilon_{cd(a}V_{b)dL-2}(U)\Bigg\}, \end{aligned} \tag{1.118}$$

where we have introduced two sets of STF tensors $U_L(U)$ and $V_L(U)$. They are called radiative multipole moments and describe the gravitational waves at future null infinity. We need to connect the radiative moments to the source multipole moments, in order to describe the gravitational waves in terms of the source parameters. Notice that, to lowest order in post-Minkowskian expansion (linearised theory) [44], there is no difference between harmonic coordinates and radiative coordinates. Thus $1/R$ term in the radiative coordinates is simply given by the $1/r$ terms of Eq. 1.112. We find that the radiative moments satisfy the following relations:

$$U_L(U) = I_L^{(l)}(U), \qquad V_L(U) = J_L^{(l)}(U). \tag{1.119}$$

This means that, to lowest order, the radiative moments U_L and V_L are given by the l-th time derivative of the source multipole moments I_L and J_L, respectively [45], e.g. by second derivative of mass quadrupole moment, by third derivative of mass octupole moment and so on.

As usual, we can consistently iterate this to get higher-order corrections to the radiative moments. This will provide us the grav-

[42] One can choose any other coordinate system as well. However, it turns out that most of the coordinate systems involve logarithmic terms and thus not suitable for dealing with the radiation.

[43] Note that R is not the size of the system as used earlier.

[44] That is, $\mathrm{h}^{ij} = G\mathrm{h}_1^{ij}$ (see, Eq. 1.112).

[45] This is the same result one gets from the linearised theory. We have thus reproduced the result.

itational waves at the required PN order. The power radiated by gravitational waves can then be computed using Eq. 1.42.

1.4.8 *Radiation from inspiraling compact binaries*

Let us now compute the gravitational waves from inspiraling compact binaries [46]. In section 1.3, we saw that such systems produce "chirp" like gravitational waveforms, i.e., the amplitude and frequency gradually increase with time. Here we will compute the PN corrections to the gravitational waveforms. The PN computations are valid only in what is called inspiral phase, i.e., where the component objects are far apart and thus move slowly enough. However, when they come close to each other, their speeds become significantly high and make the PN computations fail. This is called the late inspiral phase, which is followed by the *merger phase* where they finally plunge into each other. In the case of black hole binaries, the resulting system is a deformed black hole which settles down into a stable rotating black hole (Kerr black hole) by radiating the asymmetries into gravitational waves. Thus the coalescence of compact binaries can be divided into three phases: inspiral, merger and ringdown. The ringdown refers to the phase after the merger. We will discuss the methods developed to deal with merger and ringdown phases in the following sections.

[46] More specifically, black hole binaries.

For the time being, we are interested in computing the gravitational waveforms produced by compact binaries during their inspiral phase where post-Newtonian theory is applicable.

1.4.9 3.5 *PN equations of motion*

For a binary system made of two point particles, the equation of motion in the centre of mass coordinate has the following form:

$$\frac{dv^i}{dt} = -\frac{Gm}{r^2}\left[(1+\mathcal{A})\frac{x^i}{r} + \mathcal{B}v^i\right] + \mathcal{O}\left(\frac{1}{c^8}\right). \tag{1.120}$$

It has two terms: one proportional to the relative separation x^i and other to the relative velocity v^i. Finding $\mathcal{A}$ and $\mathcal{B}$ for a generic orbit is really difficult task. However, for binaries moving in the circular orbits, it turns out to be relatively easier [47]. For such binary systems, the equations of motions have been computed to 3.5PN orders, which is

[47] We also neglect the spins of the components objects.

$$\frac{dv^i}{dt} = -\omega_s^2 x^i - \zeta v^i, \tag{1.121}$$

where

$$\begin{aligned}\omega_s^2 =& \frac{Gm}{r^3}\left\{1 + (-3+\eta)\gamma + \left(6 + \frac{41}{6}\eta + \eta^2\right)\gamma^2 \right.\\ &\left. + \left[-10 + \left(22log(r/r'_0 - \frac{75707}{840} + \frac{41}{64}\pi^2)\right)\eta + \frac{19}{2}\eta^2 + \eta^3\right]\gamma^3\right\}\\ &+ \mathcal{O}\left(\frac{1}{c^8}\right),\end{aligned} \tag{1.122}$$

and

$$\zeta = \frac{32}{5}\frac{G^3 m^3 \eta}{c^5 r^4} + \mathcal{O}\left(\frac{1}{c^7}\right). \tag{1.123}$$

Here η is the symmetric mass ratio of the binary system (see, Eq. 1.56) and $\gamma = Gm/rc^2$ is the post-Newtonian expansion parameter [48]. The first term in Eq. 1.122 is simply the Kepler's law and other terms represent the PN correction to the Newtonian dynamics. In Eq. 1.121, the velocity-dependent term is due to the radiation reaction and Eq. 1.123 provides 2.5PN radiation reaction term, ($\mathcal{O}(1/c^5)$) that appears in the equation of motion.

[48] Note that for self-gravitating system, $\gamma = \frac{Gm}{rc^2} \sim \mathcal{O}(v^2/c^2)$.

The 3.5PN expansion of the energy of the circular orbit is,

$$\begin{aligned}E =& -\frac{\mu c^2 x}{2}\left\{1 + \left(-\frac{3}{4} - \frac{1}{12}\eta\right)x + \left(-\frac{27}{8} + \frac{19}{8}\eta - \frac{1}{24}\eta^2\right)x^2 \right.\\ &\left. + \left[-\frac{675}{64} + \left(\frac{34445}{576} - \frac{205}{96}\pi^2\right)\eta - \frac{155}{96}\eta^2 - \frac{35}{5184}\eta^3\right]x^3\right\}\\ &+ \mathcal{O}\left(\frac{1}{c^8}\right),\end{aligned} \tag{1.124}$$

where $x = \left(\frac{Gm\omega_s}{c^3}\right)^{2/3}$ is a dimensionless variable. Note that this is a physical quantity and is thus measurable. While the parameter γ is a gauge-dependent quantity as this depends on the separation r between the objects which of course is a coordinate dependent quantity. Thus, a physical observable expressed in γ might contain coordinate dependent terms, e.g., r'_0 in Eq. 1.122. However, when we re-express the observables (e.g., the orbital energy, gravitational wave flux, etc.) in the parameter x, the coordinate dependent terms go away.

1.4.10 Energy flux and orbital phase to 3.5*PN order*

The energy flux carried by gravitational waves produced by a non-spinning quasi-circular binary system has been also computed up to 3.5PN order. The power radiated can then be computed by averaging over the full sky,

$$\begin{aligned}
P_{gw} =& \frac{32c^5}{5G}\eta^2 x^5 \Bigg\{ 1 + \left(-\frac{1247}{336} - \frac{35}{12}\eta \right) x + 4\pi x^{3/2} \\
&+ \left(-\frac{44711}{9072} + \frac{9271}{504}\eta + \frac{65}{18}\eta^2 \right) x^2 \\
&+ \left(-\frac{8191}{672} - \frac{583}{24}\eta \right) \pi x^{5/2} \\
&+ \Bigg[\frac{6643739519}{69854400} + \frac{16}{3}\pi^2 - \frac{1712}{105}C - \frac{856}{105}\log(16x) \\
&+ \left(-\frac{134543}{7776} + \frac{41}{48}\pi^2 \right)\eta - \frac{94403}{3024}\eta^2 - \frac{775}{324}\eta^3 \Bigg] x^3 \\
&+ \left(-\frac{16285}{504} + \frac{214745}{1728}\eta + \frac{193385}{3024}\eta^2 \right) \pi x^{7/2} + \mathcal{O}\left(\frac{1}{c^8}\right) \Bigg\},
\end{aligned} \tag{1.125}$$

where $C = 0.577\ldots$ is the Euler-Mascheroni constant. The limit $\eta \to 0$ corresponds to a test particle moving in the background of a massive object. This falls under the regime of black hole perturbation theory, which we will discuss later, allows to compute the power radiated in gravitational waves up to 5.5PN order. It turns out that there is an excellent agreement between these two computations

up to 3.5PN order, up to which PN computation is available. This provides a remarkable consistency check for the PN computation.

Given the the PN expansions of orbital energy and the energy flux, one can easily find the orbital phase evolution by integrating the energy balance equation,

$$\frac{dE}{dt} = -P_{gw} \Rightarrow \frac{dE}{dx}\frac{dx}{dt} = -P_{gw}. \tag{1.126}$$

From this, we can compute the orbital frequency (ω_s) as a function of time and the phase evolution can be computed by $d\phi/dt = \omega_s$. Alternatively, we can also write

$$\frac{dt}{dx} = -\frac{dE}{dx}\Big/ P_{gw}, \tag{1.127}$$

and

$$\frac{d\varphi}{dx} = \omega_s \frac{dt}{dx}. \tag{1.128}$$

This will give us the parametric solution to the phase, $\{t(x), \varphi(x)\}$. We call this ***TaylorT2*** time-domain approximate. One might as well wish to first Taylor expand the polynomials in the Eq. 1.127 and keep the terms up to required PN orders. This would give some other approximate. One can also solve numerically the coupled equations, Eq. 1.127 and Eq. 1.128. Asking that which approximate is better, would really depend on the level of accuracy required in the problem.

1.4.11 3PN polarisation waveforms

Using Eq. 1.123 and Eq. 1.128, we can compute the time derivatives of the various source moments which are required to compute the polarization waveforms (Eq. 1.118). For an observer located at some distance, r, from the origin of the coordinate system attached to the binary making an angle, ι, with the $z-$axis (orbital axis) and ϕ with the $x-$axis, the polarization waveforms h_+ and $h_\times$ (presently known

up to 3PN) are given by,

$$h_{+,\times}(t) = \frac{2G\mu x}{c^2 r}\Bigg\{ H^{(0)}_{+,\times} + x^{1/2} H^{(1/2)}_{+,\times} + x H^{(1)}_{+,\times} + x^{3/2} H^{(3/2)}_{+,\times} + x^2 H^{(2)}_{+,\times} + x^{5/2} H^{(5/2)}_{+,\times} + x^3 H^{(3)}_{+,\times} + \mathcal{O}\left(\frac{1}{c^7}\right)\Bigg\}. \tag{1.129}$$

The leading term are,

$$\begin{aligned} H^{(0)}_{+}(t) &= -(1+\cos^2\iota)\cos 2\psi(t), \\ H^{(0)}_{\times}(t) &= -2\cos\iota \sin 2\psi(t), \end{aligned} \tag{1.130}$$

where ψ is given in terms of the orbital phase φ [49] as

$$\psi(t) = \varphi(t) - \frac{2Gm\omega_s}{c^3}\log\left(\frac{\omega_s}{\omega_0}\right). \tag{1.131}$$

Here ω_0 is a constant frequency which can be chosen as per convenience [50]. As expected, we see that, the leading order terms are simply the linearised theory results, i.e., gravitational waveforms produced by the second time derivative of quadrupole moments of the source. However, $\psi(t)$ here denotes the full 3.5PN phase [51]. For very small values of x, the higher order corrections (e.g., $x^{1/2}H^{(1/2)}$, $xH^{(1)}$, etc.) to the amplitudes $H^{(0)}_{+,\times}$ can be neglected, because, in the limit $x \to 0$, they vanish. However, for moderate values of x, a first few corrections can be important, keeping which would produce modulations in the amplitude of the Newtonian chirp signal.

[49] The initial phase ϕ is absorbed into the orbital phase $\varphi(t)$.

[50] We can choose this as the entry frequency of an interferometric detector.

[51] One may not choose to take full 3.5PN order for the phase to work consistently at the leading order, i.e., 0PN. However, one can show that up to 2PN order, the orbital phase $\varphi(t)$ diverges in the limit $x \to 0$. Only terms starting from 2.5PN order gives the finite limit. Thus for gravitational data analysis purposes, one must keep the corrections to the orbital phase at least up to 2.5PN.

1.4.12 *Mode decomposition of gravitational waveforms*

The full waveform in the Eq. 1.129 can also be written in an expansion of spin-2 weighted spherical harmonic basis functions [52],

$$h_+ - ih_\times = \sum_{\ell=2}^{\infty}\sum_{m=-\ell}^{\ell} Y^{-2}_{\ell m}(\iota,\phi) h_{\ell m}, \tag{1.132}$$

where the complex modes $h_{\ell m}$ can be computed by [53]

$$h_{\ell m} := \int Y^{*-2}_{\ell m}(\iota,\phi)(h_+ - ih_\times) d\Omega, \tag{1.133}$$

[52] We will come back to this again when we discuss numerical relativity.

[53] This is an old way of computing $h_{\ell m}$. The better way would be to directly relate them with the radiative multipole moments U_L and V_L by relating first the STF tensor N_L with spherical harmonics $Y^{-2}_{\ell m}$.

and satisfy (for non-spinning binary systems),

$$h_{\ell,m} = (-1)^{\ell} h^{*}_{\ell,-m}. \tag{1.134}$$

The spin-s weighted spherical harmonic basis functions, $Y^{-s}_{\ell m}$, can be found in the literature [87].

Using the Eq. 1.133, we can find the complex modes, $h_{\ell m}(t)$, to the PN order we want. A few modes up to the 1PN order are given below,

$$\begin{aligned}
h_{22} &= -8\sqrt{\frac{\pi}{5}}\frac{G\mu}{c^2 r}\mathrm{e}^{-2i\varphi}x\left[1-\left(\frac{107}{42}-\frac{55}{42}\eta\right)x\right]+\mathcal{O}\left(\frac{1}{c^5}\right)\\
h_{21} &= -i\frac{8}{3}\sqrt{\frac{\pi}{5}}\frac{G\mu}{c^2 r}\frac{\delta m}{M}\mathrm{e}^{-i\varphi}x^{3/2}+\mathcal{O}\left(\frac{1}{c^5}\right)\\
h_{33} &= 3i\sqrt{\frac{6\pi}{7}}\frac{G\mu}{c^2 r}\frac{\delta m}{M}\mathrm{e}^{-3i\varphi}x^{3/2}+\mathcal{O}\left(\frac{1}{c^5}\right)\\
h_{32} &= -\frac{8}{3}\sqrt{\frac{\pi}{7}}\frac{G\mu}{c^2 r}\mathrm{e}^{-2i\varphi}(1-3\eta)x^2+\mathcal{O}\left(\frac{1}{c^6}\right)\\
h_{44} &= \frac{64}{9}\sqrt{\frac{\pi}{7}}\frac{G\mu}{c^2 r}\mathrm{e}^{-4i\varphi}(1-3\eta)x^2+\mathcal{O}\left(\frac{1}{c^6}\right),
\end{aligned} \tag{1.135}$$

where $\delta m := m_1 - m_2$ with the convention that the first object is always heavier than the second one. We see that the h_{22} mode has the lowest power in x and hence is called the dominant mode. This is also called *quadrupole* mode [54], because the first term appearing in h_{22} is sourced by the quadrupole moment of the binary system. In the literature, the other modes are either called higher modes or sub-dominant modes or non-quadrupole modes.

[54] Including $h_{2,-2}$ mode.

1.4.13 *Frequency structure of gravitational waveforms*

Let us now look at the frequency structure of the full gravitational waveforms given by Eq. 1.129 or Eq. 1.132. This can be done analytically using what is called *stationary phase approximation* [55], which requires that the change in the amplitude is much smaller than the change in the phase of the waveform. This condition is well satisfied by the inspiral (PN) waveforms. Here, we restrict ourselves to

[55] Phys. Rev. D, Vol. 62, 084036, Page No., 14

the leading order term in Eq. 1.129 [56]. The Fourier transform of the restricted waveform is given by

$$\tilde{h}_+(f) = \left(\frac{5}{6}\right)^{1/2} \frac{1}{2\pi^{2/3}} \frac{c}{r} \left(\frac{G\mathcal{M}}{c^3}\right)^{5/6} f^{-7/6}\, e^{i\Psi_+(f)}\, \frac{1+\cos^2\iota}{2}, \tag{1.136}$$

where

$$\Psi_+(f) = 2\pi f(t_* + r/c) - \varphi(t_*) - \pi/4, \tag{1.137}$$

with φ being the orbital phase of the binary and t_* is given by the condition,

$$2\pi f = \frac{d\varphi}{dt}\Big|_{t=t_*} \Rightarrow f = F(t_*), \tag{1.138}$$

i.e., the largest contribution to the Fourier component $\tilde{h}_+(f)$ comes from the the time when the orbital frequency $F(t)$ becomes equal to the Fourier frequency f. The polarisation waveform, $\tilde{h}_\times(f)$ is obtained by simply replacing $(1+\cos^2\iota)/2$ by $\cos\iota$ and with $\Psi_\times = \Psi_+ + \pi/2$ in the Eq. 1.136.

Similarly, We can compute the Fourier transform of the higher modes (or higher PN corrections). The important point to note is that the stationary point ($t_*^{\ell m}$) for a ℓm mode is now given by

$$f = mF(t_*^{\ell m}) \Rightarrow F(t_*^{\ell m}) = f/m. \tag{1.139}$$

This means that for a given Fourier frequency, say, the initial frequency of a interferometric detector f_0, the contribution of the different modes to $\tilde{h}_{+,\times}(f_0)$ come from the different times of the orbital evolution.

[56] Or equivalently, only the dominant $(2,2$ and $2,-2)$ mode in Eq. 1.132 are being taken. For this reason, this is also called "restricted" waveform approximation.

1.5 *Numerical relativity*

In the previous section, we dealt with the case when the gravity was weak. For self-gravitating systems, this also means that the source motions were assumed to be small. However, if that is not the case, then the PN theory might not give accurate results. This is because, in strong gravity regime, the full non-linear structure of the Einstein

equations starts playing the role, e.g., during the merger of the binary black holes. In *numerical relativity*, one solves the Einstein equations numerically. Initially, there were many challenges to developing numerical methods to evolve Einstein equations, but now people have succeeded in this. Here, we will discuss the basic ideas used in numerical relativity and will see some results of the binary black hole simulations.

Any correct theory of nature must posses the initial value formulation, i.e., given the initial conditions, the dynamical variables must be uniquely evolved in time. For example, in Newtonian dynamics, once we specify the initial positions and momenta of the particles, the theory uniquely predicts the time evolution of the positions and momenta of the particles. Similar thing happens in Electrodynamics. Analogously, we also expect Einstein equations to posses the initial value formulation, if it has to represent a correct theory of gravity. It turns out that it does admit a well posed initial value formulation [57]. This is shown by decomposing Einstein equations in a set of time evolution equations and a set of initial value equations, analogous to what is done in electrodynamics. This decomposition also becomes a suitable choice for solving Einstein equations on computers. Here, we are mainly interested in evolving Einstein equations for the coalescence of compact binary objects, such as, binary black holes, etc.

[57] There is a precise mathematical definition of being "well posed", but physically it means that "small changes" in the initial data should produce correspondingly "small changes" in the solution.

1.5.1 *The* $3+1$ *decomposition of spacetime*

Let us take a $4-$dimensional spacetime manifold M with the metric $g_{\mu\nu}$. We assume that the spacetime $(M, g_{\mu\nu})$ can be foliated by a set of three dimensional surfaces Σ_t, where t is the time coordinate [58] of our coordinate system. The dual vector $(1-$form$)$ associated with the time coordinate t is,

$$\Omega_\alpha = \nabla_\alpha t = [1, 0, 0, 0]. \tag{1.140}$$

[58] Note that, it does not have to be the time coordinate itself. One can instead choose any scalar function. However, the equations we are interested in, get simplified a lot if we choose the label parameter as the coordinate time itself.

Let us assume that the norm of this dual vector is $-\alpha^{-2}$ [59], i.e.,

[59] This is called lapse function. We will discuss the reason behind it later.

$$||\mathbf{\Omega}|| = g^{\alpha\beta}\nabla_\alpha t \nabla_\beta t = -\frac{1}{\alpha^2}. \tag{1.141}$$

We then find the normalised dual vector,

$$n_\alpha = -\alpha\Omega_\alpha = [-\alpha, 0, 0, 0]. \tag{1.142}$$

The unit normal to the hypersurface Σ_t is defined by

$$n^\alpha = g^{\alpha\beta}n_\beta. \tag{1.143}$$

We can see that n^α is a time-like vector, i.e.,

$$n^\alpha n_\alpha = -1. \tag{1.144}$$

We can think of n^α as the $4-$velocity of a "normal" observer whose worldline is always normal to the hypersurface Σ_t. The induced metric on this hypersurface can then be given by

$$\gamma_{\alpha\beta} = g_{\alpha\beta} + n_\alpha n_\beta. \tag{1.145}$$

We can check that $\gamma_{\alpha\beta}$ is purely spatial, i.e., resides in Σ_t. This just means that it has no component along n^α,

$$n^\alpha \gamma_{\alpha\beta} = n^\beta - n^\beta = 0. \tag{1.146}$$

Thus $\gamma_{\alpha\beta}$ is a projector tensor that projects out any $4-$vector lying along n^α. Furthermore, we construct a projector using $\gamma_{\alpha\beta}$ that projects any $4-$vector lying in M into the Σ_t,

$$\gamma^\alpha_\beta = g^\alpha_\beta + n^\alpha n_\beta = \delta^\alpha_\beta + n^\alpha n_\beta. \tag{1.147}$$

We can check that, for a given 4-dimensional vector v^α, $\gamma^\alpha_\beta v^\beta$ is purely a spatial, i.e., resides in Σ_t. This can be used to project any higher rank tensor also, e.g.,

$$\perp T_{\alpha\beta} = \gamma^\mu_\alpha \gamma^\nu_\beta T_{\mu\nu}, \tag{1.148}$$

where $\perp$ denotes the projection into the spatial hypersurface Σ_t. Similarly, we would like to define a projector that projects a given 4−dimensional vector along the normal vector n^α. This can simply be given by

$$N^\beta_\alpha = -n^\alpha n_\beta = \delta^\alpha_\beta - \gamma^\alpha_\beta. \tag{1.149}$$

It is now possible to write a given tensor as a sum of its spatial part and its time-like part. For example,

$$v^\alpha = \delta^\alpha_\beta v^\beta = (\gamma^\alpha_\beta + N^\beta_\alpha)v^\beta = \perp v^\alpha - n^\alpha(n_\beta v^\beta). \tag{1.150}$$

From the spatial metric $\gamma_{\alpha\beta}$, we can compute the 3−dimensional covariant derivative and Riemann tensor $\left(R^\alpha_{\beta\gamma\delta}\right)$. Our aim is basically to write Einstein equations in terms of these three dimensional quantities. This would require us to decompose 4−dimensional Riemann tensor $\left({}^{(4)}R^\alpha_{\beta\gamma\delta}\right)$ into spatial tensors. However, this decomposition will certainly not contain all the information encoded in ${}^{(4)}R^\alpha_{\beta\gamma\delta}$, simply because the later also contains the time derivatives (because it lives in M), while the 3−dimensional Riemann tensor is a purely spatial quantity, i.e., can be computed from only spatial derivatives of $\gamma_{\alpha\beta}$. The thing to note is that, $R^\alpha_{\beta\gamma\delta}$ just tells us about the intrinsic geometry of the spatial hypersurface. It does not tell us how the hypersurface is embedded in M. The idea is that if we foliate a spacetime M by a stack of 3−surfaces and we want to get all the information that are there in the full metric $g_{\alpha\beta}$, then one must also specify how these 3−surfaces are embedded in M in addition to the intrinsic metric $\gamma_{\alpha\beta}$. The quantity that characterises the embedding is called the *extrinsic curvatue*.

1.5.2 *Extrinsic curvature*

The extrinsic curvature is defined as

$$K_{\alpha\beta} = -\gamma^\mu_\alpha \gamma^\nu_\beta \nabla_\mu n_\nu, \tag{1.151}$$

i.e., it represents the symmetric projection of the gradient of the normal vector n^α into the hypersurface Σ_t. Thus by construction, it is purely spatial [60]. Physically, this tells us how the normal vector n^α changes if we parallel transport it to a infinitesimally nearby point. Since the normal vectors are, by definition, normalised at all points in M, they can only differ by the direction in which they are pointing. Thus, the extrinsic curvature gives us the information about how much the direction of the normal vector changes from a given point in Σ_t to a some other point on the same hypersurface. This means that the extrinsic curvature can be used to find the rate at which the hypersurface deforms as it moves in the time. Later we will show that the extrinsic curvature $K_{\alpha\beta}$ is actually related to the first time derivative of the spatial metric $\gamma_{\alpha\beta}$. We can thus think of $(\gamma_{\alpha\beta}, K_{\alpha\beta})$ as an analogue of the position and velocity in Newtonian mechanics.

[60] However, since it involves the normal vector which is actually a $4-$dimensional vector, it measures the curvature of the spatial hypersurface as embedded in the spacetime.

To get the time evolution equations for Einstein equations, we need to the first decide on the direction of the time evolution along which they are to be evolved. Shall we evolve along the normal vector n^α or some other direction? First of all, the natural time flow direction should be αn^α, not just n^α. Because the former has unit dot product with the hypersurface dual vector Ω_α [61]. However, if we add a spatial shift vector β^α to it, i.e.,

[61] The dot product is, $\alpha n^\alpha \Omega_\alpha = \alpha g^{\alpha\beta}(-\alpha\Omega_\beta)\Omega_\alpha = 1$.

$$t^\alpha = \alpha n^\alpha + \beta^\alpha, \tag{1.152}$$

also has unit dot product with Ω_α [62]. Thus we should take the normal vector t^α as the direction of the time evolution. We can also understand it mathematically as follows: an infinitesimal change in the coordinate time t if we move along the normal vector t^α is, $dt = t^\alpha \nabla_\alpha t = 1$ and thus has the same value at all points of hypersurface Σ_t. This means that if we move along the vector t^α, we can label the hypersurface at $t = constant$ as Σ_t and the hypersurface at $t + dt = constant$ as Σ_{t+dt}, which is not possible with using the vector n^α. Consequently, all infinitesimal vectors $t^\alpha dt$ originating on

[62] Because, β^α is a spatial vector.

Σ_t will end on the same hypersurface Σ_{t+dt}, not on some other hypersurfaces. Also, the choice in the Eq. 1.152 for the time evolution direction makes sure that the coordinate positions do not change during the evolution from Σ_t to Σ_{t+dt} [63]. The shift vector β^α then measures how much coordinates have moved while going from Σ_t to Σ_{t+dt} with respect to the normal vector t^α.

[63] Otherwise $dt = 1$ condition will not hold.

We can now compute the spacetime metric $g_{\mu\nu}$,

$$\begin{aligned} g_{00} &= g_{\mu\nu} t^\mu t^\nu = (\gamma_{\mu\nu} - n_\mu n_{nu})(\alpha n^\mu + \beta^\mu)(\alpha n^\nu + \beta^\nu) = \gamma_{ij}\beta_i\beta_j - \alpha^2 \\ g_{0j} &= g_{\mu j} t^\mu = \gamma_{\mu j}(\alpha n^\mu + \beta^\mu) = \beta_j \\ g_{ij} &= \gamma_{ij}. \end{aligned} \tag{1.153}$$

And therefore the proper interval,

$$ds^2 = -\alpha^2 dt^2 + \gamma_{ij}(dx^i + \beta^i dt)(dx^j + \beta^j dt). \tag{1.154}$$

We can see that the lapse function α measures the proper time elapsed between the spatial hypersurface Σ_t and Σ_{t+dt} and hence the name, lapse function. The lapse function and the shift vector give the time evolution of the coordinates and hence are purely the gauge degrees of freedom. One can choose them as per convenience [64]. This just represents the coordinate freedom in general relativity. The Eq. 1.154 is known as $3+1$ decomposition of spacetime.

[64] For example, since the lapse function α depends both on t and on x, we can choose it in such a way that it has different behaviour at the different point of spacetime, e.g., in the case of binary black holes evolution, there would be singularities, which can be avoided by choosing an appropriate α.

1.5.3 *The $3+1$ decomposition of Einstein equations*

Using the definition of $K_{\alpha\beta}$ itself, we can show that it can be written as

$$2K_{\alpha\beta} = -\nabla_\alpha n_\beta - \nabla_\beta n_\alpha - n^\mu \nabla_\mu \gamma_{\alpha\beta}. \tag{1.155}$$

This can be simply re-expressed as

$$\frac{\partial \gamma_{ij}}{\partial t} = -2\alpha K_{ij} + D_i\beta_j + D_j\beta_i, \tag{1.156}$$

where D_i is the covariant derivative associated with spatial metric γ_{ij}. This is related to the four dimensional covariant derivative ∇ as,

$$D_\alpha w^\beta = \gamma^\mu_\alpha \gamma^\beta_\nu \nabla_\mu w^\nu, \tag{1.157}$$

where $\boldsymbol{w}$ is a $4-$dimensional vector. Given this, we can easily decompose the $4-$dimensional Riemann tensor in to its spatial part and time-like part (which will involve the extrinsic curvature) [65].

[65] Note that the Riemann tensor is computed from the action of covariant derivatives.

Now, the decomposition of the Einstein equations can be done. One finds the following equations,

$$\begin{aligned} G_{\mu\nu} n^\mu n^\nu &= \frac{8\pi G}{c^4} T_{\mu\nu} n^\mu n^\nu = \frac{8\pi G}{c^2}\rho \\ G_{\mu\nu} \gamma^\mu_\alpha n^\nu &= \frac{8\pi G}{c^4} T_{\mu\nu} \gamma^\mu_\alpha n^\nu = -\frac{8\pi G}{c^3} j_\alpha \\ G_{\mu\nu} \gamma^\mu_\alpha \gamma^\nu_\beta &= \frac{8\pi G}{c^4} T_{\mu\nu} \gamma^\mu_\alpha \gamma^\nu_\beta = \frac{8\pi G}{c^4} S_{\alpha\beta}. \end{aligned} \tag{1.158}$$

$$\frac{\partial \gamma_{ij}}{\partial t} = -2\alpha K_{ij} + D_i \beta_j + D_j \beta_i, \tag{1.159}$$

$$\begin{aligned} \frac{\partial K_{ij}}{\partial t} =& \alpha \left\{ R_{ij} - 2K_{ik}K^k_j + K K_{ij} - \frac{8\pi G}{c^4}\left[\frac{1}{2}\rho c^2 \gamma_{ij} + S_{ij} - \frac{1}{2}\gamma_{ij} S \right] \right\} \\ & - D_i D_j \alpha + \beta^k D_k K_{ij} + K_{kj} D_i \beta^k + K_{ik} D_j \beta^k, \end{aligned} \tag{1.160}$$

along with two *constraint equations*: first the Hamiltonian constraint equation

$$R + K^2 - K_{ij}K^{ij} = \frac{16\pi G}{c^2}\rho, \tag{1.161}$$

and second the momentum constraint equation

$$\gamma^{jk}(D_j K_{ik} - D_i K_{jk}) = \frac{8\pi G}{c^3} j_i, \tag{1.162}$$

where R_{ij} is $3-$dimensional Ricci tensor and $R = \gamma^{ij} R_{ij}$, $K = \gamma^{ij} K_{ij}$ and $S = \gamma^{ij} S_{ij}$. Note that $\rho c^2 := n^\mu n^\nu T_{\mu\nu}$ is the matter density. Similarly, $j_\alpha c$ is the current density and $S_{\alpha\beta}$ is the matter stress tensor.

Once we choose the lapse function and shift vector, we can pro-

ceed to solve the coupled first-order partial differential equations (Eq. 1.159 and Eq. 1.160). However, we would first need to solve the constraint equations, Eq. 1.161 and Eq. 1.162, for a given initial value of (γ_{ij}, K_{ij}). It can be easily shown that Einstein equations make sure that once constraint equations are satisfied on some initial hypersurface, it will continue to do so on spatial hypersurfaces at later times during the evolution. The evolution equations combined with the constraint equations are called $3+1$ form of Einstein equations.

1.5.4 Numerical integration of $3+1$ *Einstein equations*

It turns out the $3+1$ equations are not suitable for numerical integration. The reason is that, the $3+1$ evolution equations do not form a symmetric hyperbolic set of equations for which the numerical stability is known. For hyperbolic equations, the solutions are wave-like and propagate at a finite speed. Moreover, if there is a slight perturbation in the initial data (i.e., in solving constraint equations), the effect of it reaches to generic point (grid point on the computer) only after a finite time. On the other hand, in an elliptic and parabolic set of equations, any slight perturbation in the initial data would cause an instantaneous effect on the whole of the domain. In practice, the numerical codes are always prone to some errors, such as truncation errors. This leads to the generation of "constraint-violating modes", i.e., the solutions to the time evolution equations will not satisfy the constraint equations. In recent years, a significant amount of effort has thus gone into the development of the formulations of the Einstein equations, different from the standard $3+1$ equations that keep under control the growth of these "constraint-violating modes". Two main formulations have been developed. One is the Baumgarte-Shapiro-Shibata-Nakamura (BSSN) formalism [66] which is actually a variant of standard $3+1$ decomposition and other defers completely from the standard $3+1$ approach and is based on a generalization of harmonic coordinates [67].

[66] Baumgarte-Shapiro-Shibata-Nakamura(1987,1995,1999)

[67] Frans Pretorius, 2005

1.5.5 Constructing initial data

Let us discuss how to solve the constraint equations, once the initial data is specified. We know that the dynamical quantities are γ_{ij} and K_{ij}. They have thus 12 independent components to be solved for and we have only four constraint equations. This means that we will have 8 undetermined components. Furthermore, we also have four gauge degrees of freedom associated with choosing a coordinate system. This reduces the undetermined components to four (2 for γ_{ij} and 2 for K_{ij}). Thus, we have just 4 freely specifiable components. However, the question is, which four components of the γ_{ij} and K_{ij} are freely specifiable and which four components are to be constrained using constraint equations Eq. 1.161 and Eq. 1.162 [68]. If we choose one over others, then this will bring asymmetry among the components of γ_{ij} and K_{ij}. There is, however, one mathematical trick that can be used to overcome this problem. The trick is to use the conformal transformation, i.e., to choose γ_{ij} as a conformally flat metric,

[68] Note that, after removing the coordinate degrees of freedom, we have just 8 components to worry about.

$$\gamma_{ij} = \Omega^2 \delta_{ij}, \tag{1.163}$$

where Ω is the conformal factor. Now we can solve for Ω using the constraint equations. Notice that now there is no partiality among the components of the spatial metric γ_{ij}, because we are choosing a background metric (here δ_{ij}) where we are specifying all of the components at once. The three dimensional Ricci scalar is,

$$R = \Omega^{-2}\big[-4\nabla^2 \ln\Omega - 2(\nabla \ln\Omega)\cdot(\nabla\ \ln\Omega)\big]. \tag{1.164}$$

The most frequently used conformal factor is $\Omega = \psi^2$, which implies, $\gamma_{ij} = \psi^4 \delta_{ij}$. Then the Ricci scalar becomes

$$R = -8\psi^{-5}\nabla^2\psi. \tag{1.165}$$

Let us say we want to construct an initial data for a static black hole [69]. The extrinsic curvature K_{ij} for a static spacetime vanishes,

[69] Schwarzschild black hole.

which means that we have to just solve the Hamiltonian constraint equation (Eq. 1.161),

$$\nabla^2\psi = -\psi^5\frac{2\pi G}{c^2}\rho. \tag{1.166}$$

Outside the matter, this gives us the Laplace equation in ψ,

$$\nabla^2\psi = 0, \tag{1.167}$$

whose solution for a system of particles (static black holes in our case) is

$$\psi(\boldsymbol{x}) = 1 + \frac{1}{2}\sum_A \frac{Gm_A}{c^2||\boldsymbol{x} - \boldsymbol{x}_A||}. \tag{1.168}$$

However, for systems like two black holes orbiting each other in circular orbits, one would have to solve the momentum constraint too along with the Hamiltonian constraint.

1.5.6 Extraction of gravitational waves

Finally, the gravitational waves can be extracted at the edge of our numerical grids [70]. We know that the gravitational waves have a very simple form in TT gauge. On the other hand, numerical simulation is performed in some other gauge (e.g., harmonic gauge). Thus, it would be wise to extract the waves directly from the Riemann tensor itself. We proceed as follows: First of all, we choose a set of four linearly independent vectors [71]. For the time being, let us denote them by,

$$z_a^\mu = (l^\mu, q^\mu, m^\mu, \bar{m}^\mu), \tag{1.169}$$

where a labels the four-vector. We demand these vectors to be null, i.e.,

$$g_{\mu\nu}l^\mu l^\nu = g_{\mu\nu}q^\mu q^\nu = g_{\mu\nu}m^\mu m^\nu = g_{\mu\nu}\bar{m}^\mu\bar{m}^\nu = 0, \tag{1.170}$$

with the condition that

$$g_{\mu\nu}m^\mu\bar{m}^\nu = 1, \qquad g_{\mu\nu}l^\mu q^\nu = -1, \tag{1.171}$$

[70] Because they only make sense at the far distances from the source.

[71] So that they form a basis for the spacetime. They can be chosen as per convenience. We would need to project the Riemann tensor on these vectors to extract the waves.

and other scalar products to be zero. This is then called a null tetrad system. In this tetrad, the spacetime metric can be expressed as

$$g^{\mu\nu} = m^{\mu}\bar{m}^{\nu} + m^{\nu}\bar{m}^{\mu} - l^{\mu}q^{\nu} - l^{\nu}q^{\mu}. \tag{1.172}$$

1.5.7 *The Weyl tensor*

Weyl tensor is defined as the trace free part of the 4−dimensional Riemann tensor,

$$\begin{aligned} C_{\mu\nu\rho\sigma} =& R_{\mu\nu\rho\sigma} - \frac{1}{2}(g_{\mu\rho}R_{\nu\sigma} - g_{\mu\sigma}R_{\nu\rho} - g_{\nu\rho}R_{\mu\sigma} + g_{\nu\sigma}R_{\mu\rho}) \\ &+ \frac{1}{6}R(g_{\mu\rho}g_{\nu\sigma} - g_{\mu\sigma}g_{\nu\rho}). \end{aligned} \tag{1.173}$$

We can check that the trace of $C_{\mu\nu\rho\sigma}$ (i.e., contraction of any pair of its indices) vanishes. By construction, it has the same symmetries as the Riemann tensor. Weyl tensor has a special property that under conformal scaling of the metric, i.e.,

$$g_{\mu\nu}(x) \to g'_{\mu\nu}(x) = \mathrm{e}^{2\phi(x)}g_{\mu\nu}(x), \tag{1.174}$$

this transforms as

$$C_{\mu\nu\rho\sigma}(x) \to C'_{\mu\nu\rho\sigma}(x) = \mathrm{e}^{2\phi(x)}C_{\mu\nu\rho\sigma}(x), \tag{1.175}$$

where $\phi(\boldsymbol{x})$ is an arbitrary function [72]. As a corollary, if the Weyl tensor vanishes in a coordinate system, then the metric in that coordinate system can be always written as

[72] Thus Weyl tensor is also called conformal tensor.

$$g_{\mu\nu}(\boldsymbol{x}) = \exp\{2\phi(\boldsymbol{x})\}\eta_{\mu\nu}, \tag{1.176}$$

and the converse is also true.

Projection of the Weyl tensor onto the null tetrad gives the follow-

ing scalars,

$$\begin{aligned}
\mathbf{\Psi}_0 &= C_{\mu\nu\rho\sigma} l^\mu m^\nu l^\rho m^\sigma \\
\mathbf{\Psi}_1 &= C_{\mu\nu\rho\sigma} l^\mu q^\nu l^\rho m^\sigma \\
\mathbf{\Psi}_2 &= C_{\mu\nu\rho\sigma} l^\mu q^\nu l (l^\rho q^\sigma + m^\rho \bar{m}^\sigma) \\
\mathbf{\Psi}_3 &= C_{\mu\nu\rho\sigma} q^\mu l^\nu q^\rho \bar{m}^\sigma \\
\mathbf{\Psi}_4 &= C_{\mu\nu\rho\sigma} q^\mu \bar{m}^\nu q^\rho \bar{m}^\sigma .
\end{aligned} \tag{1.177}$$

These scalars encode the different physical effects. To see that, let us choose the radiative null tetrad which is suitable for extracting the waves at asymptotically large distance from the source (r),

$$\begin{aligned}
l^\mu &= \frac{1}{\sqrt{2}}(n^\mu + r^\mu) \\
q^\mu &= \frac{1}{\sqrt{2}}(n^\mu - r^\mu),
\end{aligned} \tag{1.178}$$

where $n^\mu = (-1, 0, 0, 0)$ is the unit normal to the constant time hypersurface Σ_t at the distance r and $r^\mu = (0, 1, 0, 0)$ is the radial unit vector. While m^μ can be chosen as

$$m^\mu = \frac{1}{\sqrt{2}}(0, \hat{\phi} - i\hat{\theta}), \tag{1.179}$$

where $\hat{\theta} = (0, 1, 0)$ and $\hat{\phi} = (0, 0, 1)$ are $3-$dimensional spatial unit vectors on Σ_t. $\bar{m}^\mu$ is just the complex conjugate of m^μ. In this null tetrad, we can show that,

$$\mathbf{\Psi}_4 = \ddot{h}_+ - i\ddot{h}_\times . \tag{1.180}$$

Thus Weyl scalar $\mathbf{\Psi}_4$ is the one which encodes all the informations about the gravitational waves. Other Weyl scalars either vanish or contain the non-radiative components of Riemann tensor, in which, of course, we are not interested.

In numerical relativity, one usually measures $\mathbf{\Psi}_4$ at a finite extraction radius. This might introduce errors. We must, therefore, estimate the errors arising due to the finite extraction radius. This can be done by comparing the results at various extraction radii.

Another important point to note about $\mathbf{\Psi}_4$ is that, under the rotation of our axes by an angle 2ψ around the direction of propagation, it transforms as

$$\mathbf{\Psi}_4 \to \mathrm{e}^{-2i\psi}\mathbf{\Psi}_4. \tag{1.181}$$

The same property is followed by the spherical harmonics $Y^{(s)}_{lm}(\theta,\phi)$ with $s = -2$ under the rotation. Thus $\mathbf{\Psi}_4$ can be expanded in the spherical harmonics,

$$\mathbf{\Psi}_4(t,\boldsymbol{x}) = \sum_{\ell=2}^{\infty}\sum_{m=-\ell}^{m=\ell} \mathbf{\Psi}_4^{\ell m}(t,r)Y^{(-2)}_{lm}(\theta,\phi). \tag{1.182}$$

Note that there are no terms for $\ell < 2$, because $Y^{(s)}_{\ell m}$ vanish for $\ell < |s|$. We can similarly expand the waveform, i.e.,

$$h_+ - ih_\times = \sum_{\ell=2}^{\infty}\sum_{m=-\ell}^{m=\ell} h_{\ell m}(t,r)Y^{(-2)}_{lm}(\theta,\phi), \tag{1.183}$$

where $h_{\ell m}(t,r)$ are computed by integrating $\mathbf{\Psi}_4^{\ell m}(t,r)$ twice with respect to time.

1.5.8 An example of a binary black holes simulation

Fig. 1.2 shows an example of a binary black holes simulation based on the BSSN formulation of the Einstein equations. It shows the three phases of the waveform, i.e., the inspiral, merger and ringdown. We see that both amplitude and the frequency increase slowly during the early inspiral phase, but start increasing steeply from the late inspiral phase until they merge. The important point to note is that the total energy radiated in the gravitational waves is $\sim 4\%$ of the total mass of the binary and the most of the energy is radiated during the merger phase.

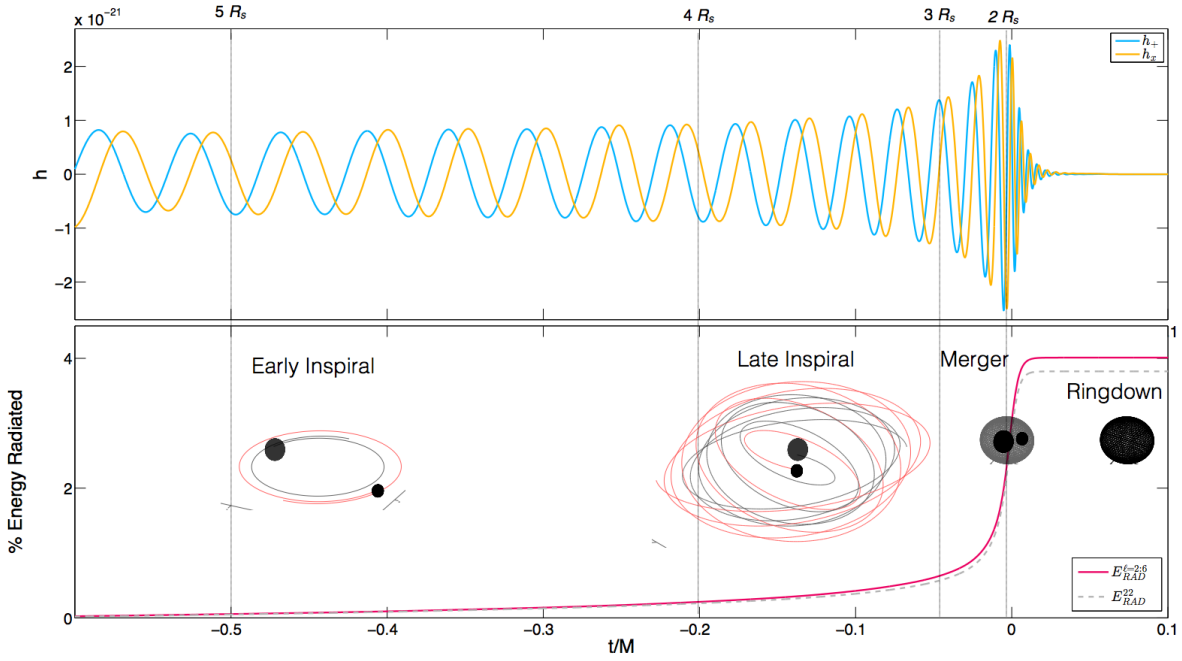

Figure 1.2: The top plot shows the two polarisations h_+ and $h_\times$ as the function of time, for non-spinning equal mass black hole binary with unit total mass. The bottom plots shows the accumulated fraction of total mass radiated in $(2, \pm 2)$ mode and all the modes from $\ell = 2 : 6$ and $m = -\ell : \ell$, in the percentage of the total mass of the binary. We can see that the energy radiated in the subdominant modes is almost negligible compared to the $(2, \pm 2)$ mode for a nearly equal mass binary. Here, R_s is the Schwarzschild radius of the individual black hole. Note that, the unit of M $(= GM/c^3)$ is second. $t = 0$ corresponds to the peak of the amplitude of the waveform [www.einstein.gatech.edu].

1.6 *Organization of the thesis*

The thesis is organised as follows: In chapter 2, we present an analytical waveform family describing GWs from the inspiral, merger and ringdown of non-spinning black-hole binaries including the effect of several non-quadrupole modes [$(\ell = 2, m = \pm 1), (\ell = 3, m = \pm 3), (\ell = 4, m = \pm 4)$, $(\ell = 3, m = \pm 2)$, $(\ell = 4, m = \pm 3)$ apart from the leading quadrupole mode, $(\ell = 2, m = \pm 2)$]. We first construct spin-weighted spherical harmonics modes of *hybrid* waveforms by matching numerical-relativity simulations (with mass ratio $1 - 10$) describing the late inspiral, merger and ringdown of the binary with post-Newtonian/effective-one-body waveforms describing the early inspiral. The analytical waveform family is constructed in frequency domain by modeling the Fourier transform of the hybrid waveforms making use of analytical functions inspired by perturbative calculations. We also develop a method for accurately modeling the effect of "mode mixing", which is exhibited by $(\ell = 3, m = \pm 2)$ and

($\ell = 4, m = \pm 3$) modes. The resulting highly accurate, ready-to-use waveforms are highly faithful (unfaithfulness $\simeq 10^{-4} - 10^{-2}$) for observation of GWs from non-spinning black hole binaries and are extremely inexpensive to generate. We use this analytical waveform family to formulate a consistency test between the different modes (harmonics) of gravitational waves from BBHs. The black-hole "no-hair" theorem in GR asserts that, gravitational radiation (*quasi-normal modes*) from a perturbed Kerr black hole is uniquely determined by its mass and spin. Thus, the spectrum of quasi-normal mode frequencies have to be all consistent with the same value of the mass and spin. Similarly, the gravitational radiation from a coalescing binary black hole system is uniquely determined by a small number of parameters (masses and spins of the black holes and orbital parameters). Thus, consistency between different spherical harmonic modes of the radiation is a powerful test that the observed system is a binary black hole predicted by GR. In chapter 3, we formulate such a test, develop a Bayesian implementation, demonstrate its performance on simulated data and investigate the possibility of performing such a test using previous and upcoming gravitational wave observations. Chapter 4 provides an introduction to the theory of gravitational lensing (GL). GL of EM waves is a well known phenomenon, where EM waves get deflected off their paths due to presence of a massive object (lens). The gravitational bending of light was among the first observational tests of GR. GWs undergo GL in the same way. When the mass scale of the lens is large as compared to the wavelength, GL magnifies/de-magnifies the GW signals without affecting their frequency profiles. Thus sources could be detected from higher redshifts which were otherwise not detectable. GL also produces multiple images of a source (strong lensing), which reach the GW detector at different times. Based on the rate of GW detections by Advanced LIGO and Virgo, we expect these detectors to observe hundreds of binary black hole mergers as they achieve their design sensitivities (within a few years). A small fraction of them can un-

dergo strong gravitational lensing by intervening galaxies, resulting in multiple images of the same signal. In chapter 5, we develop a Bayesian inference technique to identify pairs of strongly lensed images among hundreds of binary black hole events, and demonstrate its performance using simulated GW observations. We also search for signatures of strong gravitational lensing in the binary black hole events detected by Advanced LIGO and Virgo during their first two observational runs. We find no compelling evidence of strong lensing signature in the observed gravitational wave signals. However, as the sensitivities of gravitational wave detectors improve in the future, detecting lensed events may become quite likely.

2 Inspiral-Merger-Ringdown Gravitational Waveforms for Non-Spinning Black Hole Binaries

LIGO's recent observations of gravitational waves (GWs) from coalescing binary black hole systems [22, 13] mark the beginning of a new branch of astronomy. Based on the observed rate of GW signals, a large number of merger events can be expected in upcoming observing runs of Advanced LIGO and Virgo [24, 21], providing us a unique opportunity to constrain the mass and spin distribution of binary black holes, to infer their astrophysical formation channels and to probe the true nature of extreme gravity.

The most sensitive GW detection pipelines use the technique of matched filtering to detect GW signals from binary black holes [139, 107], which involves cross-correlating the data with theoretical templates of expected signals. Post detection, the physical and astrophysical properties of the GW source are inferred by comparing the data with theoretical signal templates, by means of Bayesian inference [146]. Tests of general relativity (GR) using GW observations also involves comparing the data with GR templates, to investigate the consistency of the observation with the prediction of GR [23]. Thus, accurate theoretical models of the expected signals are an essential input for GW astronomy.

Theoretical templates describing the gravitational waveforms from the inspiral, merger and ringdown of binary black holes have been computed in the recent years by combining perturbative calculations in GR with large-scale numerical relativity simulations [49, 50, 134, 46, 112, 111, 113, 64, 65, 66, 29, 27, 117, 81, 90, 84]. Most of these waveform families aim to model only the leading (quadrupole; $\ell = 2, m = \pm 2$) modes of the gravitational radiation. Indeed, careful investigations suggested that the systematic errors introduced by neglecting subdominant (non-quadrupole) modes in the parameter estimation of the LIGO events are negligible [20]. Due to the near "face-on" orientations of the binaries and moderate mass ratios, the effect of subdominant modes was negligible in the observed signals – the systematic errors introduced by neglecting the subdominant modes were well within the statistical errors [20]. However, for binaries with large mass ratios or high inclination angles or large signal-to-noise ratios, the systematic errors can dominate the statistical errors, biasing our inference of the physical and astrophysical properties of the source (see, e.g., [144, 52, 142]). In addition, including the effect of subdominant modes can improve the precision with which source parameters can be extracted, due to the increased information content in the templates (see, e.g., [123, 140, 33, 138, 32, 80, 96, 110]), potentially improving the accuracy of various observational tests of GR [108, 93].

In this chapter we present an analytical waveform family describing GW signals from the inspiral, merger and ringdown of non-spinning black-hole binaries. These waveforms are constructed by combining perturbative calculations in GR with numerical-relativity (NR) waveforms in the "phenomenological" approach presented in a series of papers in the past [30, 29, 27, 117, 26, 81, 90, 84, 102]. This frequency domain, closed form waveform family has excellent agreement (faithfulness > 0.996) with "target" waveforms including subdominant modes, for binaries with mass ratio up to 10. Target waveforms including subdominant modes (with $\ell \leq 4, m \neq 0$) have

been constructed by matching NR simulations describing the late inspiral, merger and ringdown of the binary with post-Newtonian (PN)/effective-one-body waveforms describing the early inspiral. Our highly accurate, ready-to-use, analytical waveforms are both effectual and faithful for observation of GWs from non-spinning black hole binaries and are extremely inexpensive to generate.

The material presented in this chapter is based on the articles [94, 104].

2.1 *The waveform model*

As we discussed in Eq. 1.132 and Eq. 1.183, for a gravitational wave travelling along the direction (ι, φ_0) in the source frame, the polarizations $h_+(t)$ and $h_\times(t)$ can be expanded in terms of the spin -2 weighted spherical harmonics as

$$h_+(t) - ih_\times(t) = \sum_{\ell=2}^{\infty} \sum_{m=-\ell}^{\ell} Y^{-2}_{\ell m}(\iota, \varphi_0)\, h_{\ell m}(t). \tag{2.1}$$

The spherical harmonic modes $h_{\ell m}(t)$ are purely functions of the intrinsic parameters of the system (such as the masses and spins of the binary), while all the angular dependence is captured by the spherical harmonic basis functions $Y^{-2}_{\ell m}(\iota, \varphi_0)$. Here, by convention, the polar angle ι is measured with respect to the orbital angular momentum of the binary. From the PN inspiral waveforms in Eq. 1.135 we can see that the leading contribution to $h(t; \iota, \varphi_0)$ comes from the quadrupolar ($\ell = 2, m = \pm 2$) modes. The relative contributions of various subdominant (nonquadrupole) modes, however, depend on the symmetries of the system. For non-spinning binaries, Eq. 1.135 suggests that the subdominant modes with the largest amplitudes are $(\ell = 3, m = 3), (\ell = 4, m = 4)$, $(\ell = 2, m = 1)$ and $(\ell = 3, m = 2)$. This observation seems to hold through the merger regime (described by NR waveforms) as well. Thus, in this chapter we focus on the modeling of these subdominant modes [1], apart from the dominant quadrupole modes. Note that, due to the sym-

[1] Including $(\ell = 4, m = 3)$ mode. We will explain a slightly later why we also include this mode.

Simulation ID	q	$M\omega_{\rm orb}$	e	# orbits
Fitting				
SXS:BBH:0198	1.20	0.015	2.0×10^{-4}	20.7
SXS:BBH:0201	2.32	0.016	1.4×10^{-4}	20.0
SXS:BBH:0200	3.27	0.017	4.1×10^{-4}	20.1
SXS:BBH:0182	4.00	0.020	6.8×10^{-5}	15.6
SXS:BBH:0297	6.50	0.021	5.9×10^{-5}	19.7
SXS:BBH:0063	8.00	0.019	2.8×10^{-4}	25.8
SXS:BBH:0301	9.00	0.023	5.7×10^{-5}	18.9
SXS:BBH:0185	9.99	0.021	2.9×10^{-4}	24.9
Verification				
SXS:BBH:0066	1.00	0.012	6.4×10^{-5}	28.1
SXS:BBH:0184	2.00	0.018	7.6×10^{-5}	15.6
SXS:BBH:0183	3.00	0.019	6.3×10^{-5}	15.6
SXS:BBH:0182	4.00	0.020	6.8×10^{-5}	15.6
SXS:BBH:0187	5.04	0.019	5.0×10^{-5}	19.2
SXS:BBH:0181	6.00	0.017	7.9×10^{-5}	26.5
SXS:BBH:0298	7.00	0.021	4.0×10^{-4}	19.7
SXS:BBH:0063	8.00	0.019	2.8×10^{-4}	25.8
SXS:BBH:0301	9.00	0.023	5.7×10^{-5}	18.9
SXS:BBH:0185	9.99	0.021	2.9×10^{-4}	24.9

Table 2.1: Summary of the parameters of the NR waveforms used in this chapter: $q \equiv m_1/m_2$ is the mass ratio of the binary, $M\omega_{\rm orb}$ is the orbital frequency after the junk radiation and e is the residual eccentricity. The waveforms listed under the title *Fitting* are used to produce the analytical fits described in Section 2.2.1 while those listed under the title *Verification* are used for assessing the faithfulness of the analytical model in Section 2.4.

metry of non-spinning binaries, where the orbital motion is fully restricted to a fixed plane, the negative m modes are related to positive m modes by a complex conjugation. That is $h_{\ell -m} = (-1)^{\ell} h^{*}_{\ell m}$ [91]. Also, the $m = 0$ modes are comprised of the nonlinear memory in the waveform, which has only negligible effect in GW detection and parameter estimation. It is also challenging to accurately extract this non-oscillatory signal from NR simulations [73, 115]. Thus, only $m > 0$ modes are considered in this chapter.

In this chapter, we construct an analytical waveform family in the Fourier domain, that describes the the subdominant modes ($\ell m = 33, 44, 21, 32, 43$) apart from the dominant 22 mode of the GW polarizations from non-spinning black hole binaries. We will first discuss the modeling of ($\ell m = 22, 33, 44, 21$) modes and then the remaining ($\ell m = 32, 43$) modes. The reason is that the modes 32 and 43 have a more complicated behavior in their post-merger part of the waveforms [2] due to an effect known as *mode mixing*. As a consequence, they posses some unusual bumps in the post-merger part

[2] Unlike other modes which we model.

which make it difficult to model them accurately. Thus we take a slightly different route for modeling of these two modes. As GW observations are entering a regime of precision astronomy, such as precision tests of general relativity (GR) [19, 77, 106, 67], modeling of such subtle effects in the waveforms becomes important.

2.2 *Construction of hybrid waveforms*

We start by constructing the spherical harmonic modes of *hybrid* waveforms by combining PN and NR waveforms in a region where both calculations are believed to be accurate.

PN inspiral waveforms (e.g., see Eq. 1.135), scaled to unit total mass and unit distance, can be written as

$$h^{\rm PN}_{\ell m}(t) = 2\,\eta\,v^2\,\sqrt{\frac{16\pi}{5}}\,H_{\ell m}\,e^{-i\,m\,\varphi_{\rm orb}(t)}, \tag{2.2}$$

where $\eta = m_1 m_2/M^2$ is the symmetric mass ratio and $M = m_1 + m_2$ is the total mass of the binary, $v = (M\omega_{\rm orb})^{1/3}$ is the PN expansion parameter, $\omega_{\rm orb} = d\varphi_{\rm orb}/dt$ is the orbital frequency and $\varphi_{\rm orb}$ is the orbital phase. The PN mode amplitudes $H_{\ell m}$ are currently computed up to 3PN [3] accuracy by [45, 91, 31, 43] while the 3.5PN orbital phase $\varphi_{\rm orb}(t)$ can be computed in the adiabatic approximation using inputs given in [44] and references therein.

[3] The dominant, 22 mode inspiral model that we use here is actually 3.5PN accurate [74].

In order to improve the accuracy of the inspiral waveforms, we compute the phase evolution of the inspiral part from the 22 mode of the effective-one-body (EOB) waveforms calibrated to NR simulations (SEOBNRv4 [46]). Hence our inspiral waveforms are given by

$$h^{\rm PN}_{\ell m}(t) = 2\eta v^2\sqrt{\frac{16\pi}{5}}\,H_{\ell m}\,e^{-i\,m\varphi_{\rm EOB22}(t)/2}, \tag{2.3}$$

where $\varphi_{\rm EOB22}$ is the phase of the 22 mode of the SEOBNRv4 waveform. Note that, for $m = 2$ modes, $H_{\ell m}$ contains imaginary terms at order 2.5PN and above, which can be absorbed into the phase. However, since this correction appears at order 5PN and above in the

phase, we neglect these corrections and use $|H_{\ell m}|$ instead of $H_{\ell m}$ for the $m = 2$ modes.

Hybrid waveforms containing all the relevant modes ($\ell \leq 4, 1 \leq m \leq \ell$) are constructed by matching NR modes $h^{\rm NR}_{\ell m}(t)$ with PN modes $h^{\rm PN}_{\ell m}(t)$ with the same intrinsic binary parameters. The PN waveforms are matched with NR by a least square fit over two rotations[4] on the NR waveform and the time-difference between NR and PN waveforms over an appropriately chosen matching interval (t_1, t_2), where the NR and PN calculations are believed to be accurate.

$$\min_{t_0,\varphi_0,\psi} \int_{t_1}^{t_2} dt \sum_{\ell,m} \left| h^{\rm NR}_{\ell m}(t - t_0)\, e^{i(m\varphi_0+\psi)} - h^{\rm PN}_{\ell m}(t) \right|. \qquad (2.4)$$

[4] These two rotations are necessary due to the freedom in choosing the frame with respect to which the NR and PN waveforms are decomposed into spherical harmonics modes. In general three Euler rotations (ι, φ_0, ψ) can be performed between the two frames. However, one angle (ι) is fixed by the choice of aligning the z axis along the direction of the total angular momentum of the binary [144, 53].

The hybrid waveforms are constructed by combining the NR waveform with the "best matched" PN waveform in the following way:

$$h^{\rm hyb}_{\ell m}(t) \equiv \tau(t)\, h^{\rm NR}_{\ell m}(t - t'_0)\, e^{i(m\varphi'_0+\psi')} + [1 - \tau(t)]\, h^{\rm PN}_{\ell m}(t), \qquad (2.5)$$

where t'_0, φ'_0 and ψ' are the values of t_0, φ_0 and ψ that minimizes the difference δ between PN and NR waveforms. Above, $\tau(t)$ is a weighting function defined by:

$$\tau(t) \equiv \begin{cases} 0 & \text{if } t < t_1 \\ \frac{t-t_1}{t_2-t_1} & \text{if } t_1 \leq t < t_2 \\ 1 & \text{if } t_2 \leq t. \end{cases} \qquad (2.6)$$

Our hybrid waveforms include spherical harmonic modes up to $\ell = 4$ and $m = -\ell$ to ℓ in this analysis, except the $m = 0$ modes. We use a subset of these hybrid waveforms for constructing the analytical waveforms in the Fourier domain and to test the faithfulness of the analytical waveforms. The NR waveforms that were used to construct the hybrids are listed in Table 2.1. Note that, although the analytical waveforms only model the $22, 33, 44, 21$ modes, their faithfulness is established by computing their mismatches with hybrids

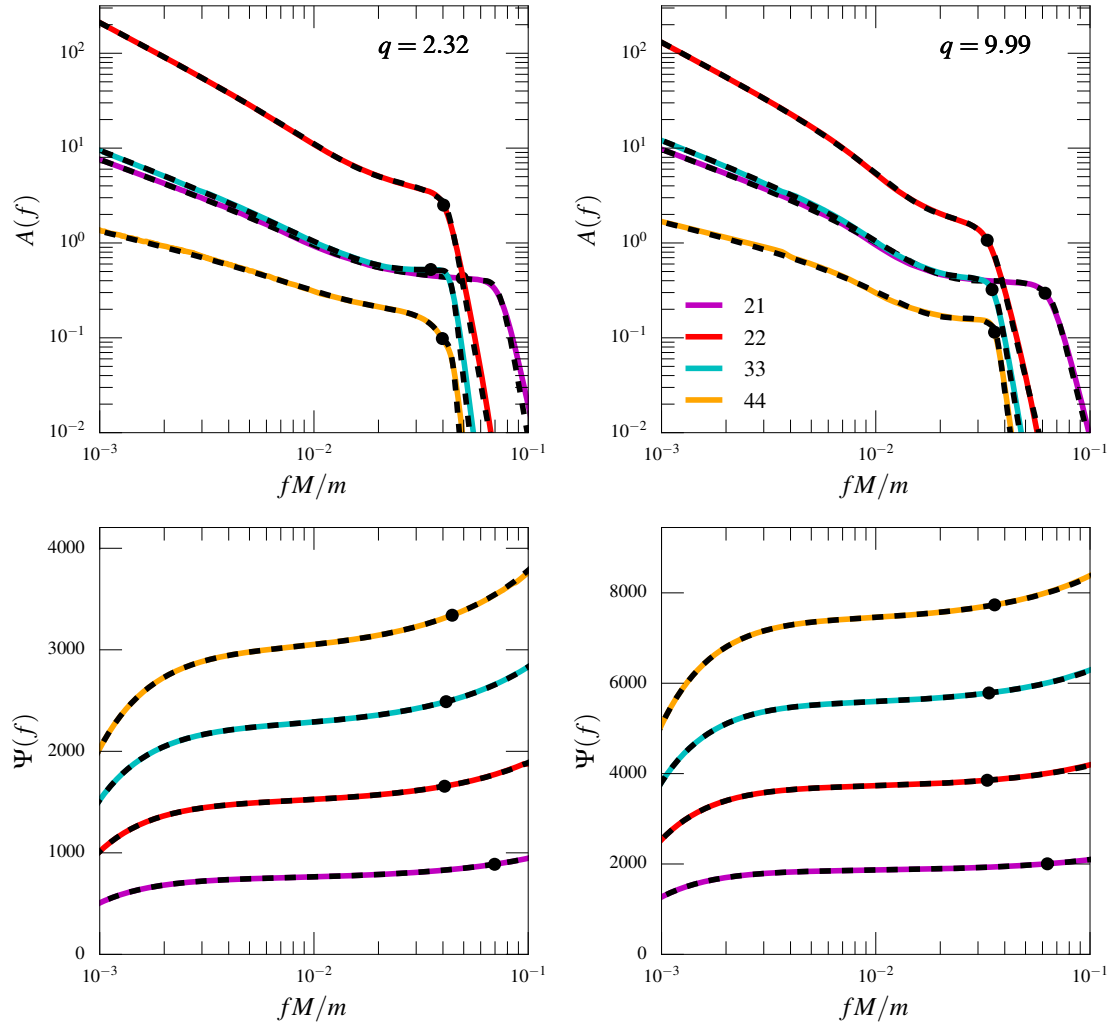

Figure 2.1: Comparison between the amplitude (top panels) and phase (bottom panels) of the hybrids and analytical waveforms for selected mass ratios $q = 2.32$ (left panels) and $q = 9.99$ (right panels). In each plot, the solid lines correspond to hybrid waveforms for different modes and the dashed lines correspond to the analytical waveforms for the same mode. The legends show the ℓm value for different modes. The black dots show the transition frequency ($f^{\rm A}_{\ell m}$ and $f^{\rm P}_{\ell m}$) from the inspiral-merger to the ringdown part of the phenomenological amplitude and phase models.

containing all the modes up to $\ell = 4$, except the $m = 0$ modes.

2.2.1 *Construction of the analytical waveform model*

In this section, we construct an analytical model for the Fourier transform $h_{\ell m}(f)$ of the real part of $h_{\ell m}(t)$ for the 22, 33, 44, 21 modes. Due to the symmetry of the non-spinning binaries, the Fourier transform of the imaginary part of $h_{\ell m}(t)$ can be computed by adding a phase shift of $\pi/2$ to $h_{\ell m}(f)$ (see Appendix A.3). Writing this in terms of a Fourier domain amplitude and phase

$$h_{\ell m}(f) = A_{\ell m}(f)\, e^{\mathrm{i}\Psi_{\ell m}(f)}, \tag{2.7}$$

our phenomenological model for the amplitude of each mode is the following:

$$A_{\ell m}(f) = \begin{cases} A^{\rm IM}_{\ell m}(f);\ f < f^{\rm A}_{\ell m} \\ \\ A^{\rm RD}_{\ell m}(f);\ f \geq f^{\rm A}_{\ell m}. \end{cases} \tag{2.8}$$

The Fourier frequencies below the matching frequency $f^{\rm A}_{\ell m}$ roughly correspond to the inspiral-merger stages of the signal, while the frequencies above $f^{\rm A}_{\ell m}$ roughly corresponds to the ringdown stage. The amplitude model for the inspiral-merger part is given by

$$A^{\rm IM}_{\ell m}(f) = A^{\rm PN}_{\ell m}(f) \left(1 + \sum_{k=0}^{k=1} \left(\alpha_{k,\,\ell m} + \alpha^{L}_{k,\,\ell m} \ln v_f\right) v_f^{k+8}\right), \tag{2.9}$$

where $v_f = (2\pi M f/m)^{1/3}$ and $A^{\rm PN}_{\ell m}(f)$ is the Padé resummed version of the 3.5PN (3PN) amplitude of 22 (33, 44, 21) mode in the Fourier domain (see Appendix A.1). The Padé resummed version of the PN amplitude was employed to provide a better agreement with the late inspiral part of the hybrid amplitude. The inspiral-merger amplitude is modeled as the product of a Padè resummed PN amplitude and another function that mimics a PN-like expansion. Such a form allows the resulting function to include very higher order terms, thus providing better fits to the late inspiral and merger part of the hybrid amplitude [5]. Above, $\alpha_{k,\,\ell m}$, $\alpha^{L}_{k,\,\ell m}$ and $f^{\rm A}_{\ell m}$ are phenomenological parameters whose values are determined from fits with numerical Fourier transforms of the hybrid waveforms.

[5] This idea is similar in spirit to the "factorized resummed amplitude" for effective one body waveforms proposed by [65].

The ringdown amplitude is modeled from the Fourier transform of a damped sinusoid, which is exponentially damped to mimic the high-frequency fall of the NR waveforms in the Fourier domain. That is,

$$A^{\rm RD}_{\ell m}(f) = w_{\ell m}\, e^{-\lambda_{\ell m} f}\ \left|\mathcal{B}_{\ell m}(f)\right|, \tag{2.10}$$

where $\mathcal{B}_{\ell m}(f)$ is the Fourier transform of the $\ell, m, n = 0$ quasi-normal mode of a Kerr black hole with mass M_f and dimensionless spin

a_f [39], determined from initial masses:

$$\mathcal{B}_{\ell m}(f) = \frac{\sigma_{\ell m} - i\, f}{f_{\ell m}^2 + (\sigma_{\ell m} - i\, f)^2}. \tag{2.11}$$

The frequencies $f_{\ell m}$ and $\sigma_{\ell m}$ are the real and imaginary parts of the $\ell, m, n = 0$ quasi-normal mode frequency $\Omega_{\ell m 0} = 2\pi\,(f_{\ell m} + \mathrm{i}\,\sigma_{\ell m})$. The phenomenological parameters $\lambda_{\ell m}$ in Eq.(2.10) are determined from fits with numerical Fourier transforms of the hybrid waveforms, while $w_{\ell m}$ is a normalization constant to make the amplitudes continuous at the merger-ringdown matching frequency $f_{\ell m}^{\mathrm{A}}$. The mass M_f and spin a_f of the final black hole are computed from the masses m_1 and m_2 of the initial black holes, using fitting formulae calibrated to NR simulations. For this work, we use the fitting formulae given by [111].

Our analytical model for the phase of the Fourier domain waveform reads

$$\Psi_{\ell m}(f) = \begin{cases} \Psi_{\ell m}^{\mathrm{IM}}(f) & ;\ f < f_{\ell m}^{\mathrm{P}} \\ \\ \Psi_{\ell m}^{\mathrm{RD}}(f) & ;\ f \geq f_{\ell m}^{\mathrm{P}} \end{cases}$$

where the phase model for the inspiral-merger part of each mode takes the following form:

$$\Psi_{\ell m}^{\mathrm{IM}}(f) = \Psi_{\ell m}^{\mathrm{PN}}(f) + \sum_{k=0}^{k=4} (\beta_{k,\,\ell m} + \beta_{k,\,\ell m}^{\mathrm{L}}\, \ln v_f + \beta_{k,\,\ell m}^{\mathrm{L2}}\, \ln^2 v_f)\, v_f^{k+8}, \tag{2.12}$$

where $\Psi_{\ell m}^{\mathrm{PN}}(f)$ is the PN phasing of the ℓm mode, while the higher order phenomenological coefficients $\beta_{k,\,\ell m}$, $\beta_{k,\,\ell m}^{\mathrm{L}}$, $\beta_{k,\,\ell m}^{\mathrm{L2}}$ are determined from fits against the phase of hybrid waveforms. This particular phenomenological ansatz is motivated from the PN expansion of the frequency domain GW phasing of the inspiral waveforms in the test particle limit (see, e.g., [143]).

For the ringdown part of the phase we simply attach the phase of Fourier transform $\mathcal{B}_{\ell m}(f)$ of the $\ell, m, n = 0$ quasi-normal mode at a

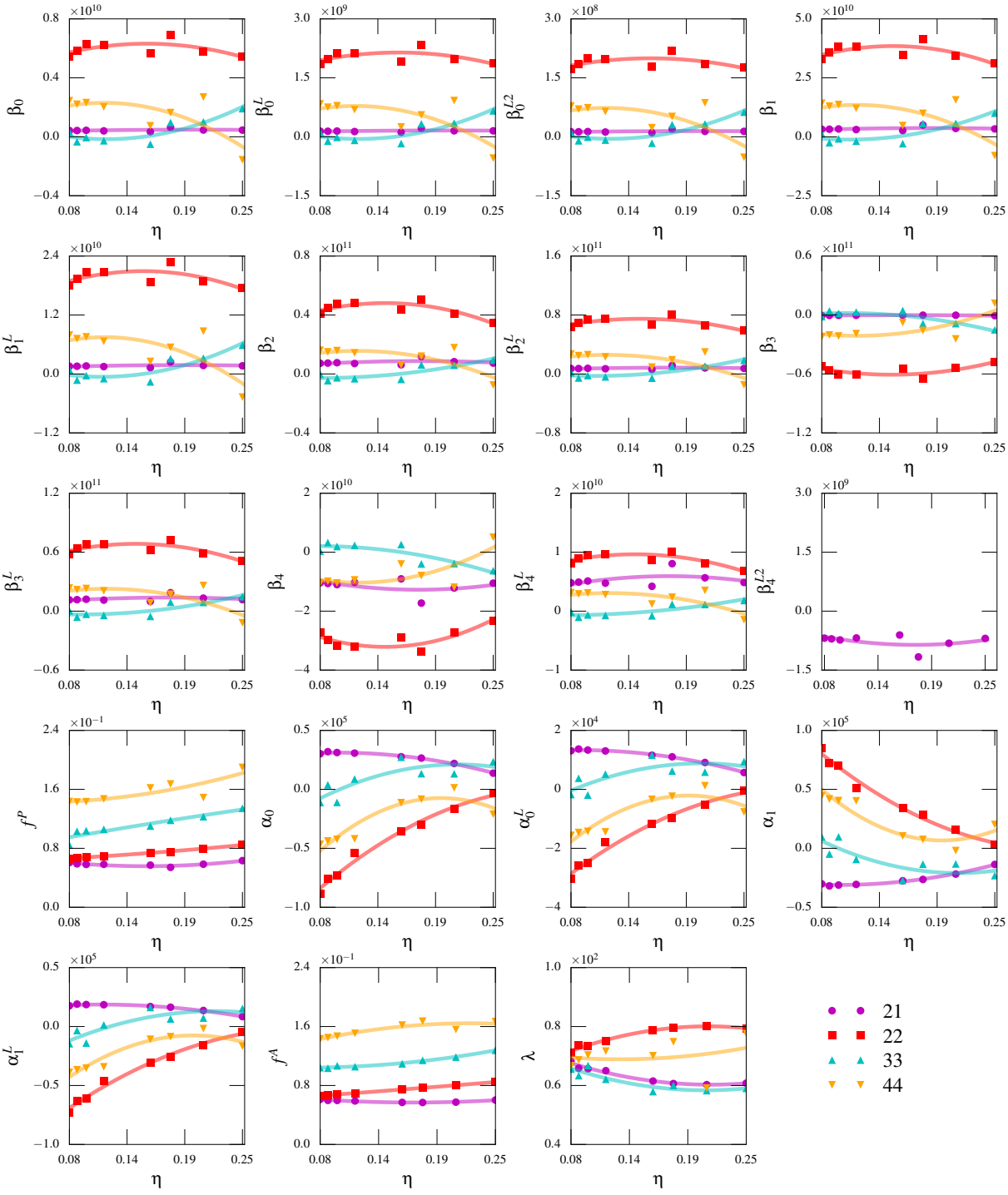

Figure 2.2: The estimated values of the phenomenological parameters describing the analytical waveforms, plotted against the symmetric mass ratio η. Different markers correspond to different modes. Also plotted are the fits given by Eqs. (2.28).

transition frequency $f^{\rm P}_{\ell m}$. Thus, our ringdown phase model reads

$$\Psi^{\rm RD}_{\ell m}(f) = 2\pi f t^{\rm P}_{\ell m} + \phi^{\rm P}_{\ell m} + \arctan\, \mathcal{B}_{\ell m}(f), \qquad (2.13)$$

where $t^{\rm P}_{\ell m}$ and $\phi^{\rm P}_{\ell m}$ are computed by matching two phases ($\Psi^{\rm IM}_{\ell m}$ and $\Psi^{\rm RD}_{\ell m}$) and their first derivative at the matching frequency $f^{\rm P}_{\ell m}$. Fig-

ure 2.1 provides a comparison of the amplitude and phase of the numerical Fourier transform of the hybrid waveforms, along with the analytical fits given by Eqs. (2.8) and (2.12).

Finally, the phenomenological parameters describing the analytical model are represented as quadratic functions of the symmetric mass ratio η

$$\begin{aligned}
\alpha_{i,\ell m} &= a_{i,\ell m} + b_{i,\ell m}\,\eta + c_{i,\ell m}\,\eta^2\,, \\
\alpha^{\rm L}_{i,\ell m} &= a^{\rm L}_{i,\ell m} + b^{\rm L}_{i,\ell m}\,\eta + c^{\rm L}_{i,\ell m}\,\eta^2\,, \\
\beta_{k,\ell m} &= a_{k,\ell m} + b_{k,\ell m}\,\eta + c_{k,\ell m}\,\eta^2\,, \\
\beta^{\rm L}_{k,\ell m} &= a^{\rm L}_{k,\ell m} + b^{\rm L}_{k,\ell m}\,\eta + c^{\rm L}_{k,\ell m}\,\eta^2\,, \\
\beta^{\rm L2}_{j,\ell m} &= a^{\rm L2}_{j,\ell m} + b^{\rm L2}_{j,\ell m}\,\eta + c^{\rm L2}_{j,\ell m}\,\eta^2\,, \\
\lambda_{\ell m} &= (\breve{a}_{\ell m} + \breve{b}_{\ell m}\,\eta + \breve{c}_{\ell m}\,\eta^2)\,, \\
f^{\rm A}_{\ell m} &= (a^{\rm A}_{\ell m} + b^{\rm A}_{\ell m}\,\eta + c^{\rm A}_{\ell m}\,\eta^2)\,/M, \\
f^{\rm P}_{\ell m} &= (a^{\rm P}_{\ell m} + b^{\rm P}_{\ell m}\,\eta + c^{\rm P}_{\ell m}\,\eta^2)\,/M\,.
\end{aligned} \tag{2.14}$$

where the index i runs from 0 to 1, k runs from 0 to 4 and j is 0 except for 21 mode (j=0,1). Figure 2.2 shows the values of the phenomenological parameters estimated from the hybrid waveforms, as well as the fits described by Eq. (2.28).

2.3 *Modeling of* 32 *and* 43 *modes*

Figure 2.3 shows the amplitude (solid lines in left panel) and instantaneous frequency (solid lines in right panel) of the second time derivative of different spherical harmonic modes of the hybrid waveforms with mass ratio $q = 4$ [6]. We can see that the 32 and 43 modes have some bumps in the post-merger regime ($t > 0$). The unusual behavior of these modes is attributed to what is known as *mode-mixing*, where multiple *spheroidal* harmonic modes are getting mixed in one *spherical* harmonic mode. The prime cause of the mode mixing is the mismatch between the angular basis that is used in NR simulations to extract waveforms (spherical harmonics) and the one

[6] We consider the second time derivative of $\hbar$ (i.e., the Weyl scalar ψ_4) here instead of $\hbar$ itself in order to give a cleaner illustration. If we make the same plot using $\hbar$, we find additional oscillations, even in modes that are not expected to have significant mode mixing. These oscillations appear to be due primarily to additional constant and linear terms in $\hbar$ that are removed by taking the time derivatives. Taking a single time derivative of $\hbar$ (i.e., considering the Bondi news) removes most of the oscillations, but taking a second time derivative removes some remaining oscillations. Since we are concerned with removing the mode mixing in the frequency domain, where the time derivatives correspond to a multiplicative factor, there is nothing lost in illustrating the mode mixing removal in the time domain using ψ_4.

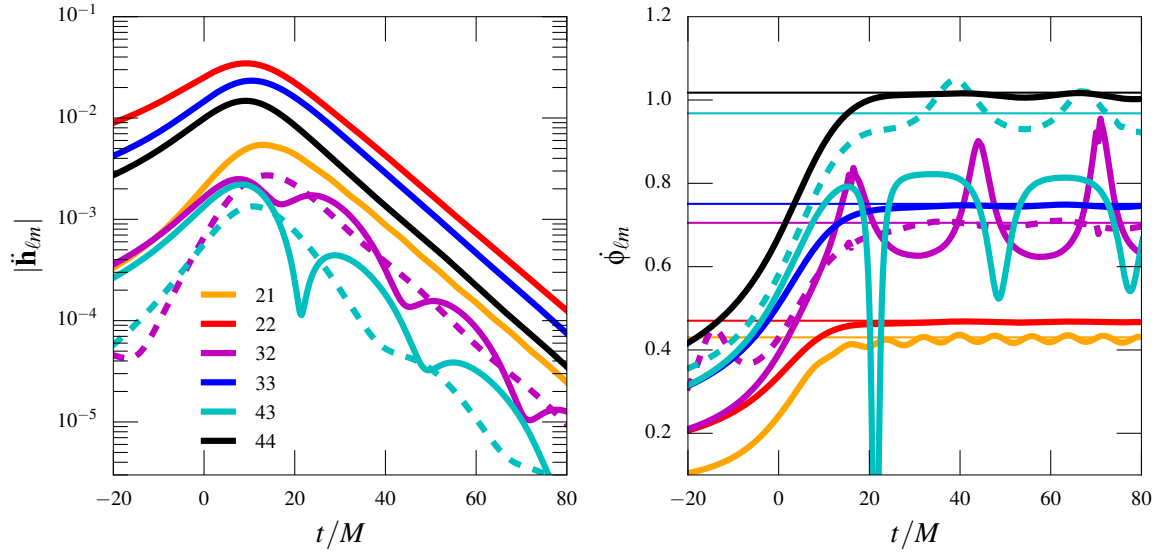

Figure 2.3: *Left panel:* Amplitude of the second time derivative of different spherical harmonic modes ${}^{\mathrm{Y}}\ddot{h}_{\ell m}(t)$ (solid lines) from a nonspinning binary with mass ratio $q = 4$. Time $t = 0$ corresponds to the peak amplitude of 22 mode. Note the oscillations in the 32 and 43 modes for $t > 0$, due to the mixing of multiple spheroidal harmonic modes. The dashed lines show the amplitude of the second time derivative of the *spheroidal* harmonic modes ${}^{\mathrm{S}}\ddot{h}_{\ell m 0}(t)$ for $\ell m \in \{32, 43\}$ constructed using the prescription presented in Sec. 2.3.1, which are better behaved in the ringdown regime ($t > 0$). *Right panel:* The instantaneous frequency $\dot{\phi}_{\ell m}(t)$ of the second time derivatives of the spherical (solid lines) and spheroidal (dashed lines) modes. The horizontal lines show the quasi-normal-mode frequencies of different modes. Note that the 32 and 43 spherical harmonic modes' frequencies (solid lines) do not approach the corresponding quasi-normal-mode frequencies, while the spheroidal harmonic modes' frequencies (dashed lines) do.

that is used to separate the Teukolsky equations in Kerr black hole perturbation theory (spheroidal harmonics) [89].

The mixing of multiple spheroidal harmonic modes creates multiple frequencies in the ringdown waveform that makes it hard to model them using simple analytical functions. Figure 2.4 shows an example of the Fourier domain amplitude $|{}^{\mathrm{Y}}\tilde{h}^{\mathrm{R}}_{\ell m}(f)|$ of different hybrid modes — note the non-monotonic behavior seen in the higher frequencies of the 32 and 43 modes. Our approach is thus to subtract the effect of mode mixing from these modes which allows us to model these "unmixed" modes using methods that we used for $22, 33, 44, 21$ modes in previous section, and then reintroduce the effects of mode mixing to obtain the final model.

2.3.1 *Removal of mode mixing from the 32 and 43 modes*

The binary merger produces a perturbed black hole which settles into a stationary Kerr black hole. Teukolsky's solution for GWs from a perturbed Kerr black hole has a natural decomposition in spin -2 weighted *spheroidal* harmonics, $S_{\ell mn} \equiv S_{\ell m}(a_f \omega_{\ell mn})$ associated with quasinormal mode (QNM) frequencies $\omega_{\ell mn}$, where $M_f a_f$ is the spin angular momentum of the final black hole (of mass M_f). See, e.g., [38] for information about the properties of these functions.

Thus, GW polarizations from the ringdown can be written as

$$h(t;\iota,\varphi_0) = \sum_{\ell'\geq 2}\sum_{|m|\leq\ell'}\sum_{n\geq 0} S_{\ell' mn}(\iota,\varphi_0)\ {}^{\mathrm{S}}h_{\ell' mn}(t). \tag{2.15}$$

Here the overtone index n measures the magnitude of the imaginary part of the quasinormal mode frequencies $\omega_{\ell mn}$. Note that the spheroidal harmonic basis functions $S_{\ell' mn}$ can be expressed in terms of (spin -2 weighted) spherical harmonics $Y_{\ell m}$ as

$$S_{\ell' mn} = \sum_{\ell\geq|m|} \mu^*_{m\ell\ell' n} Y_{\ell m}, \tag{2.16}$$

where $\mu_{m\ell\ell' n}$ are mixing coefficients which can be computed simply using the fits provided by Berti and Klein [37] (there are more complicated fits given in [100]) and the star denotes the complex conjugate [7] . By inserting this expansion in Eq. (2.15), we have

$$h(t;\iota,\varphi_0) = \sum_{\ell'\geq 2}\sum_{|m|\leq\ell'}\sum_{n\geq 0}\sum_{\ell\geq|m|} \mu^*_{m\ell\ell' n} Y_{\ell m}(\iota,\varphi)\ {}^{\mathrm{S}}h_{\ell' mn}(t). \tag{2.17}$$

Comparing this with Eq. 1.132, we get

$${}^{\mathrm{Y}}h_{\ell m}(t) = \sum_{\ell'\geq|m|}\sum_{n\geq 0} {}^{\mathrm{S}}h_{\ell' mn}(t)\,\mu^*_{m\ell\ell' n}. \tag{2.18}$$

Thus, spherical harmonic modes of the hybrid waveforms can be written in terms of the spheroidal harmonic modes. From inspection of the different spherical harmonic modes of the NR data, we get an understanding of the relative amplitudes of these modes (see, e.g., Fig. 1 in both [111] and [59]). We thus make the following approximations when removing the mode mixing:

- The amplitudes of the higher spheroidal overtones are negligible because their damping times are factors of $\gtrsim 3$ smaller than those of the leading overtone $n = 0$. Hence we will only consider mixing from the leading overtone.

- For $\ell = m$ spherical modes, the mixing contribution from any mode except the $\ell\ell 0$ spheroidal mode is negligible.

[7] We actually substitute $\mu_{m\ell\ell' n} \to (-1)^{\ell+\ell'}\mu_{m\ell\ell' n}$, where the prefactor corrects for the difference in the sign convention for spin-weighted spherical harmonics that we use—the same convention as [28], which is also the one used in the SpEC code [1]—and the one used by Berti and Klein. There is an additional factor of $(-1)^m$ that we neglect, as it is fixed for each mode we consider (including its mixed modes).

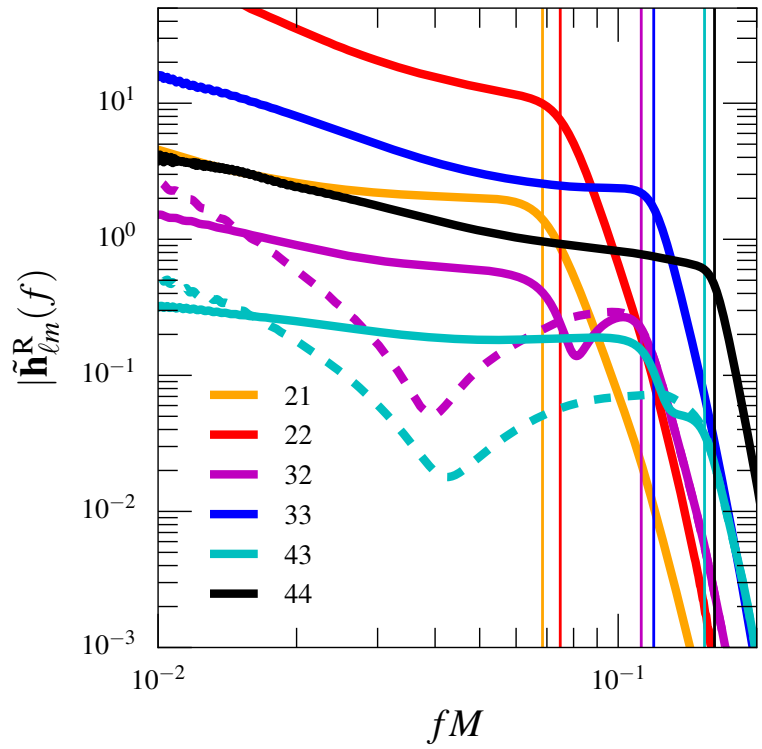

Figure 2.4: Fourier domain amplitude $|\tilde{h}^{\mathrm{R}}_{\ell m}(f)|$ of the spherical (solid) and spheroidal (dashed) harmonic modes from a nonspinning binary with mass ratio $q = 4$. The vertical line with the corresponding color represents $f^{\mathrm{QNM}}_{\ell m}$.

- For a general ℓm spherical mode, contribution from spheroidal modes with $\ell' > \ell$ is negligible, since the higher mode amplitudes are much smaller than the $\ell m 0$ spheroidal mode, and they are also multiplied by the mixing coefficient which is already small.

As a result of these approximations, a particular ℓm spherical mode will have contribution from spheroidal modes $\ell' m 0$ with $\ell' \leq \ell$ (and the obvious restriction of $\ell' \geq |m|$). We thus have

$$ {}^{\mathrm{Y}}h_{\ell m}(t) \simeq \sum_{\ell' \leq \ell} {}^{\mathrm{S}}h_{\ell' m 0}(t)\, \mu^{*}_{m \ell \ell' 0}. \tag{2.19} $$

To determine the spheroidal modes ${}^{\mathrm{S}}h_{\ell' m 0}(t)$ from the spherical modes ${}^{\mathrm{Y}}h_{\ell m}(t)$, we observe that it is a perfectly determined system of coupled equations when we consider different ℓm spherical modes. To be specific, we compute the following spheroidal modes: [8]

[8] The same procedure also works for modes with $m \leq \ell - 2$ that have three or more spheroidal modes mixed into the spherical mode in our approximation, e.g., the 42 mode studied in [137]. However, this mode has a small enough amplitude that we do not include it in the present study.

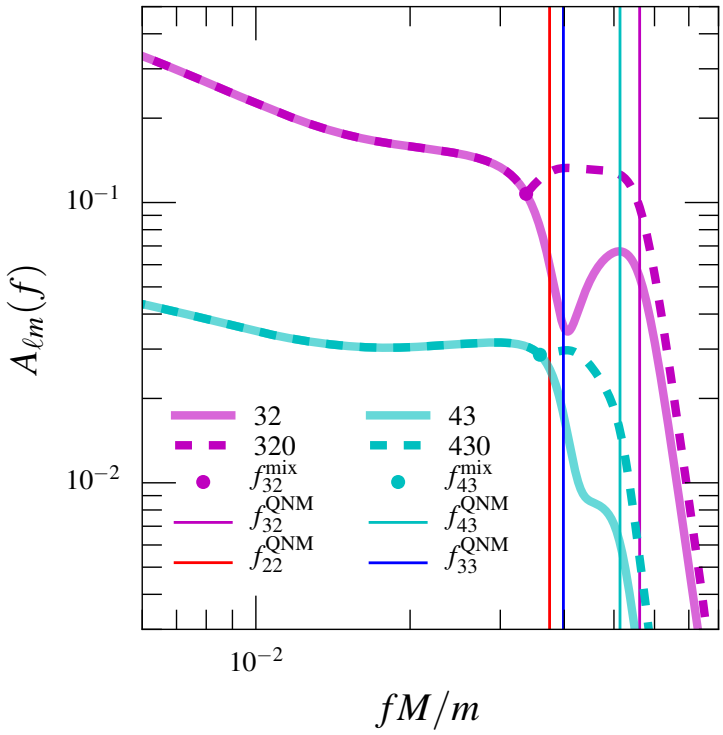

Figure 2.5: The amplitude of mixed and unmixed modes as a function of frequency for mass ratio $q = 4$. The dashed lines represent the amplitude of unmixed modes. The 43 mode has been scaled appropriately to avoid overlap with the 32 mode.

$$ {}^{\rm S}h_{320}(t) \simeq \frac{{}^{\rm Y}h_{32}(t) - {}^{\rm Y}h_{22}(t)\mu^*_{2320}/\mu^*_{2220}}{\mu^*_{2330}}, \tag{2.20a} $$

$$ {}^{\rm S}h_{430}(t) \simeq \frac{{}^{\rm Y}h_{43}(t) - {}^{\rm Y}h_{33}(t)\mu^*_{3430}/\mu^*_{3330}}{\mu^*_{3440}}. \tag{2.20b} $$

These spheroidal harmonic modes for a binary with $q = 4$ are shown as dashed lines in Fig. 2.3 (as discussed there, we plot the second time derivatives to give a cleaner illustration). It can be seen that the amplitude oscillations seen in the spherical modes (solid lines) are largely absent in the spheroidal modes (dashed lines). In addition, the instantaneous frequency (right panel) of the spheroidal modes approaches the corresponding quasi-normal-mode frequency.

We can also convert Eqs. (2.20) into the frequency domain, so that we can remove the mode mixing from the frequency domain waveforms. Here we want to compute the Fourier transforms of the real and imaginary parts separately, since in this nonprecessing case we can focus on just modeling the real part, and the imaginary part can be obtained from the real part by a phase shift of $\pi/2$. However, we

give the expression for the imaginary part as well, for completeness. A straightforward calculation, i.e., taking the real and imaginary parts of Eq. (2.20a) and expressing them in the frequency domain, gives us the following form for the 32 mode:

$$\begin{aligned} {}^{\mathrm{S}}\tilde{h}^{\mathrm{R}}_{320}(f) &\simeq (\alpha_1 \mu^{\mathrm{R}}_{2330} - \alpha_2 \mu^{\mathrm{I}}_{2330})/|\mu_{2330}|^2, \\ {}^{\mathrm{S}}\tilde{h}^{\mathrm{I}}_{320}(f) &\simeq (\alpha_2 \mu^{\mathrm{R}}_{2330} + \alpha_1 \mu^{\mathrm{I}}_{2330})/|\mu_{2330}|^2, \end{aligned} \tag{2.21}$$

where

$$\begin{aligned} \alpha_1 &:= {}^{\mathrm{Y}}\tilde{h}^{\mathrm{R}}_{32}(f) - \left({}^{\mathrm{Y}}\tilde{h}^{\mathrm{R}}_{22}(f)\rho^{\mathrm{R}}_{2320} + {}^{\mathrm{Y}}\tilde{h}^{\mathrm{I}}_{22}(f)\rho^{\mathrm{I}}_{2320} \right), \\ \alpha_2 &:= {}^{\mathrm{Y}}\tilde{h}^{\mathrm{I}}_{32}(f) + \left({}^{\mathrm{Y}}\tilde{h}^{\mathrm{R}}_{22}(f)\rho^{\mathrm{I}}_{2320} - {}^{\mathrm{Y}}\tilde{h}^{\mathrm{I}}_{22}(f)\rho^{\mathrm{R}}_{2320} \right). \end{aligned} \tag{2.22}$$

Here $\rho_{2320} := \mu_{2320}/\mu_{2220}$ and ${}^{\mathrm{Y}}\tilde{h}^{\mathrm{R}}_{\ell m}(f)$, ${}^{\mathrm{Y}}\tilde{h}^{\mathrm{I}}_{\ell m}(f)$ are the Fourier transforms of the real and imaginary parts of ${}^{\mathrm{Y}}h_{\ell m}(t)$, respectively. The expressions for the 43 mode are analogous.

The amplitude $|{}^{\mathrm{Y}}\tilde{h}^{\mathrm{R}}_{\ell m}(f)|$ in the Fourier domain is shown for the 32 and 43 modes in Fig. 2.5 (lighter shades). There are clearly two features in the 32 mode at close to the QNM frequencies of the 320 and 220 modes and similarly for the 43 mode. Now the "unmixed" modes are constructed as follows:

$$A^{\mathrm{U}}_{\ell m}(f) := \begin{cases} |{}^{\mathrm{Y}}\tilde{h}^{\mathrm{R}}_{\ell m}(f)|, & f < f^{\mathrm{mix}}_{\ell m}, \\ w^{\mathrm{U}}_{\ell m}|{}^{\mathrm{S}}\tilde{h}^{\mathrm{R}}_{\ell m 0}(f)|, & f \geq f^{\mathrm{mix}}_{\ell m}, \end{cases} \tag{2.23a}$$

$$\Psi^{\mathrm{U}}_{\ell m}(f) := \begin{cases} \arg({}^{\mathrm{Y}}\tilde{h}^{\mathrm{R}}_{\ell m}(f)), & f < f^{\mathrm{mix}}_{\ell m}, \\ \phi^{\mathrm{U}}_{\ell m} + \arg({}^{\mathrm{S}}\tilde{h}^{\mathrm{R}}_{\ell m 0}(f)), & f \geq f^{\mathrm{mix}}_{\ell m}, \end{cases} \tag{2.23b}$$

where $A^{\mathrm{U}}_{\ell m}(f)$ and $\Psi^{\mathrm{U}}_{\ell m}(f)$ represent the amplitude and phase of the unmixed modes respectively, while $f^{\mathrm{mix}}_{\ell m}$ is a transition frequency. The parameters $w^{\mathrm{U}}_{\ell m}$ and $\phi^{\mathrm{U}}_{\ell m}$ are determined by demanding the continuity of the amplitude and phase at $f^{\mathrm{mix}}_{\ell m}$, respectively.

To determine $f^{\mathrm{mix}}_{\ell m}$, we note that the bump in the amplitude of a certain ℓm spherical harmonic mode due to the mixing of the $(\ell - 1)m$ mode always appears at frequencies slightly below the ℓm

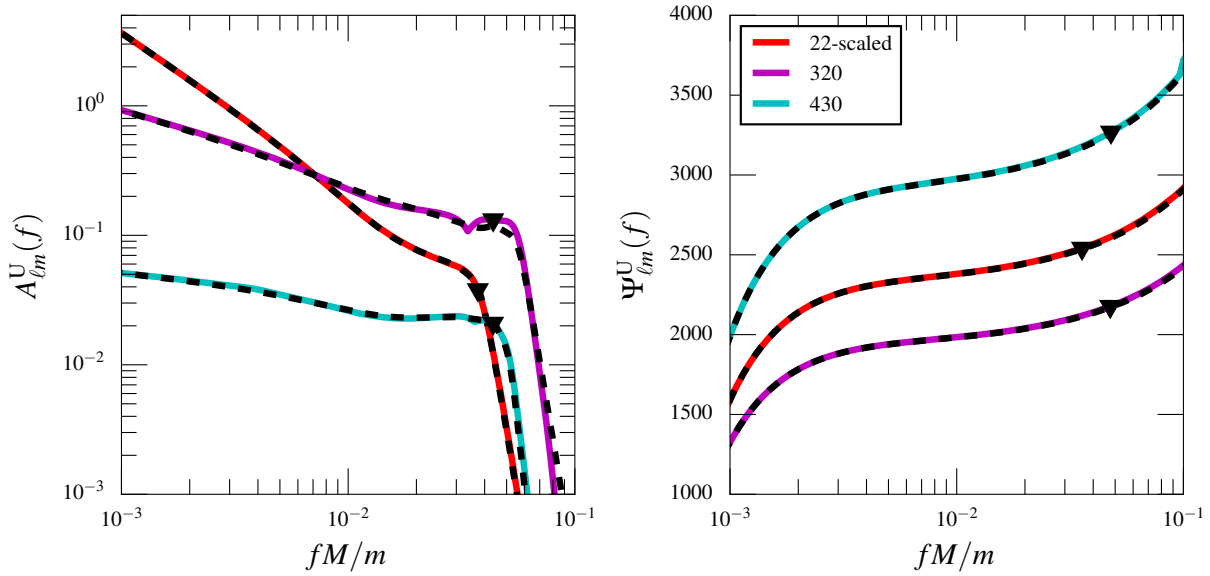

Figure 2.6: Comparison between the amplitude (left panel) and phase (right panel) of the unmixed modes for the hybrid and analytical model waveforms for mass ratio $q = 4$. In each plot, the solid lines correspond to the unmixed modes and the dashed lines correspond to the analytical model waveforms for the same mode. The black triangles represent the transition frequency from inspiral-merger to ringdown as defined in Eqs. (2.8) and (2.12), i.e., $f^{\rm A}_{\ell m}$ and $f^{\rm P}_{\ell m}$. The amplitude and phase of the 22 mode have been scaled appropriately to make them fit inside the figure.

mode's dominant QNM frequency $f^{\rm QNM}_{\ell m}$. When $f^{\rm mix}_{\ell m}$ is allowed to be a free parameter, it becomes degenerate with the model parameters [Eq. (2.28)] and thus makes the model fail, i.e., the parameters appearing in Eq. (2.28) do not have a simple dependence on η. We find that fixing $f^{\rm mix}_{\ell m} = 0.9 f^{\rm QNM}_{\ell m}$ gives good agreement of the model parameters with quadratic functions of η. In Fig. 2.5, we also plot the unmixed modes (dashed lines). The bumps in the amplitudes of the spherical harmonic modes due to mode mixing are significantly suppressed in the unmixed modes.

2.3.2 *Construction of the analytical waveform model*

To construct models for the amplitude $A^{\rm U}_{\ell m}(f)$ and phase $\Psi^{\rm U}_{\ell m}(f)$, $\ell m \in \{32, 43\}$, we follow exactly the same procedure as in section 2.2.1. Here again, the imaginary part of the unmixed mode (in the time domain) is related to the real part by a phase shift of $\pi/2$, due to the symmetry of nonprecessing binaries. Hence, we only model the Fourier transform of the real part. The amplitude

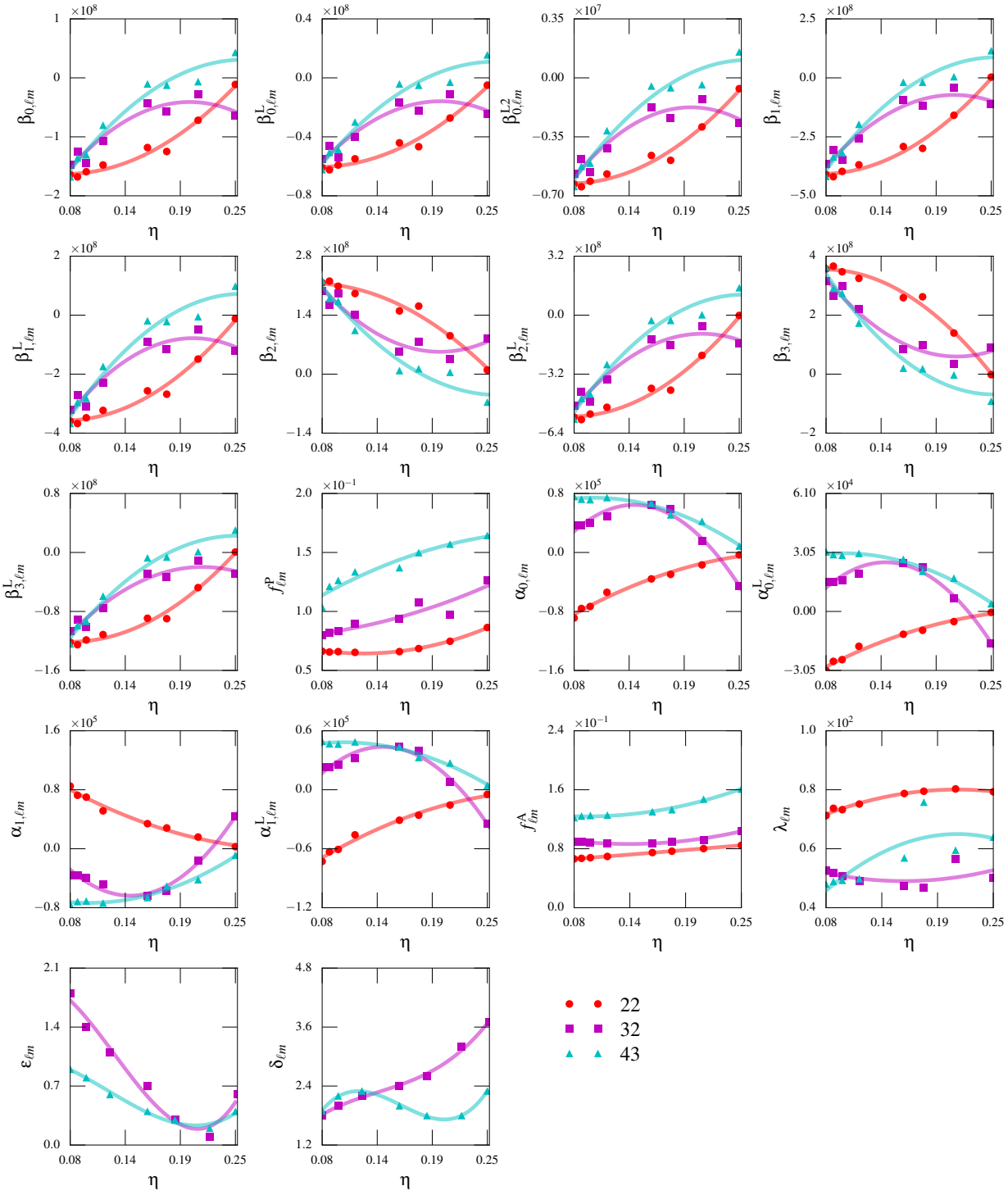

Figure 2.7: The estimated values of the phenomenological parameters describing the analytical model waveforms, plotted against the symmetric mass ratio η.

model is thus

$$A^{\mathrm{U,\,mod}}_{\ell m}(f) = \begin{cases} A^{\mathrm{IM}}_{\ell m}(f), & f < f^{\mathrm{A}}_{\ell m}, \\ A^{\mathrm{RD}}_{\ell m}(f), & f \geq f^{\mathrm{A}}_{\ell m}, \end{cases} \tag{2.24}$$

where $f^{\rm A}_{\ell m}$ denotes the transition frequency from the inspiral-merger part of the waveform to the ringdown in the amplitude. The inspiral-merger part is modelled as

$$A^{\rm IM}_{\ell m}(f) = A^{\rm PN}_{\ell m}(f)\left[1+\sum_{k=0}^{k=1}\left(\alpha_{k,\,\ell m}+\alpha^{\rm L}_{k,\,\ell m}\,\ln v_f\right)v_f^{k+8}\right], \qquad (2.25)$$

where $v_f = (2\pi M f/m)^{1/3}$ and $A^{\rm PN}_{\ell m}(f)$ is the Padé resummed version of the Fourier domain 3PN amplitude of the 32 and 43 modes. The Fourier domain amplitude is obtained using the stationary phase approximation as in [141], starting from the time-domain PN results in [45]. We use P^0_4 and P^0_3 Padé approximants for the 32 and 43 modes, respectively, similar to our treatment of the other modes in [104]. The modeling of $A^{\rm RD}_{\ell m}(f)$ exactly follows Eq. 2.10.

Similarly, for the phase model we have

$$\Psi^{\rm U,\,mod}_{\ell m}(f) = \begin{cases}\Psi^{\rm IM}_{\ell m}(f), & f < f^{\rm P}_{\ell m},\\ \Psi^{\rm RD}_{\ell m}(f), & f \geq f^{\rm P}_{\ell m},\end{cases} \qquad (2.26)$$

$$\Psi^{\rm IM}_{\ell m}(f) = \Psi^{\rm PN}_{\ell m}(f) + \sum_{k=0}^{k=3}(\beta_{k,\,\ell m} + \beta^{\rm L}_{k,\,\ell m}\,\ln v_f + \beta^{\rm L2}_{k,\,\ell m}\,\ln^2 v_f)\,v_f^{k+8}, \qquad (2.27)$$

where $\Psi^{\rm PN}_{\ell m}(f)$ is the PN phasing of the ℓm mode and $f^{\rm P}_{\ell m}$ denotes the transition frequency from the inspiral-merger part of the waveform to the ringdown in the phase. The ringdown part of the phase is modelled as in Eq. 2.13.

As before, the phenomenological parameters appearing in the analytical models (for the 32 and 43 modes) are represented as quadratic

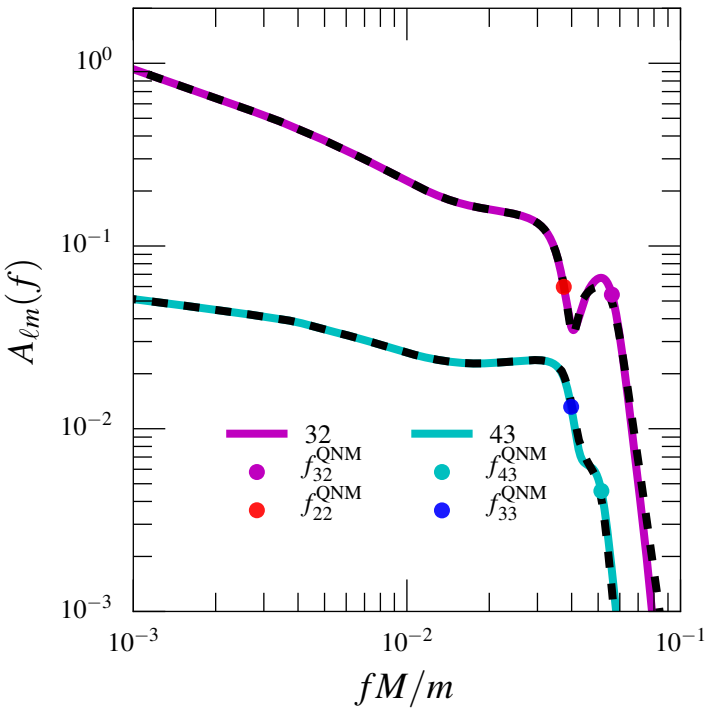

Figure 2.8: Comparison of the amplitude of the mixed modes for a mass ratio $q = 4$, showing the hybrid (solid lines) and analytical model (dashed lines).

functions of the symmetric mass ratio η:

$$
\begin{aligned}
\alpha_{i,\ell m} &= a^{\alpha}_{i,\ell m} + b^{\alpha}_{i,\ell m}\,\eta + c^{\alpha}_{i,\ell m}\,\eta^2\,,\\
\alpha^{\rm L}_{i,\ell m} &= a^{\alpha,{\rm L}}_{i,\ell m} + b^{\alpha,{\rm L}}_{i,\ell m}\,\eta + c^{\alpha,{\rm L}}_{i,\ell m}\,\eta^2\,,\\
\beta_{k,\ell m} &= a^{\beta}_{k,\ell m} + b^{\beta}_{k,\ell m}\,\eta + c^{\beta}_{k,\ell m}\,\eta^2\,,\\
\beta^{\rm L}_{k,\ell m} &= a^{\beta,{\rm L}}_{k,\ell m} + b^{\beta,{\rm L}}_{k,\ell m}\,\eta + c^{\beta,{\rm L}}_{k,\ell m}\,\eta^2\,,\\
\beta^{\rm L2}_{0,\ell m} &= a^{\beta,{\rm L2}}_{0,\ell m} + b^{\beta,{\rm L2}}_{0,\ell m}\,\eta + c^{\beta,{\rm L2}}_{0,\ell m}\,\eta^2\,,\\
\lambda_{\ell m} &= \breve{a}_{\ell m} + \breve{b}_{\ell m}\,\eta + \breve{c}_{\ell m}\,\eta^2\,,\\
f^{\rm X}_{\ell m} &= \left(a^{\rm X}_{\ell m} + b^{\rm X}_{\ell m}\,\eta + c^{\rm X}_{\ell m}\,\eta^2\right)/M,
\end{aligned}
\tag{2.28}
$$

where the index i runs from 0 to 1 and k runs from 0 to 3, while $X \in \{A, P\}$. We also refit the phase of the 22 mode using the smaller number of coefficients given in (2.12); the fit in [104] has the same form, except that the sum extends up to $k = 4$ instead of $k = 3$. We use this refit since it improves the 22 mode's overlap with high mass ratio hybrid waveforms. Figure 2.6 provides a comparison of the amplitudes and phases of the unmixed modes in the Fourier domain with the analytical fits given by Eqs. (2.8) and (2.12). Figure 2.7 shows

the values of the phenomenological parameters estimated from the hybrid waveforms, as well as the fits given in Eq. (2.28).[9]

[9] We find that quadratic polynomials in η provide sufficiently accurate fits in terms of mismatches. Hence we do not consider higher order fits, even though there appears to be some substructure that would require a higher-order polynomial to fit (Fig. 2.7). It is possible that some of the structure seen in the 32 and 43 modes' coefficients for η close to 0.25 is related to the fact that the mode mixing removal does not work as well for $q < 3$, as discussed below.

2.3.3 *Adding the mode mixing contribution into unmixed modes*

Having constructed analytical models for the amplitude and phase of unmixed modes, we need to add the mode mixing contribution back into this model in order to get the analytical model for the amplitude and phase of the spherical harmonic modes ${}^{\rm Y}\tilde{h}^{\rm R}_{\ell m}(f)$. This is done as follows: We denote the (Fourier domain) model waveform by

$$ {}^{\rm Y}\tilde{h}^{\rm mod}_{\ell m}(f) := A^{\rm U,\,mod}_{\ell m}(f)\; e^{\,{\rm i}\,\Psi^{\rm U,\,mod}_{\ell m}(f)}, \tag{2.29} $$

where $A^{\rm U,\,mod}_{\ell m}(f)$ and $\Psi^{\rm U,\,mod}_{\ell m}(f)$ are given by Eqs. (2.8) and (2.12). We then write

$$ \begin{aligned} {}^{\rm M}\tilde{h}^{\rm R,\,mod}_{32}(f) = {}&{}^{\rm Y}\tilde{h}^{\rm R,\,mod}_{22}(f)\rho^{\rm R}_{2320} - {}^{\rm Y}\tilde{h}^{\rm I,\,mod}_{22}(f)\rho^{\rm I}_{2320} \\ &+ {}^{\rm U}\tilde{h}^{\rm R,\,mod}_{320}(f)\mu^{\rm R}_{2330} - {}^{\rm U}\tilde{h}^{\rm I,\,mod}_{320}(f)\mu^{\rm I}_{2330}, \end{aligned} \tag{2.30} $$

where

$$ {}^{\rm U}\tilde{h}^{\rm mod}_{320}(f) := \varepsilon_{32}\,{}^{\rm Y}\tilde{h}^{\rm mod}_{\ell m}(f)\; e^{\,{\rm i}\,\delta_{32}\pi}. \tag{2.31} $$

The expressions for the 43 mode are analogous.

Here we have introduced two free parameters, $\varepsilon_{\ell m}$ and $\delta_{\ell m}$, corresponding to the amplitude ratio and phase difference at $f^{\rm mix}_{\ell m}$. We fit these parameters by minimizing the mismatch of ${}^{\rm M}\tilde{h}^{\rm R}_{32}(f)$ with the corresponding hybrid mode. They are represented as cubic functions of the symmetric mass ratio; we find similar functional behavior when we compute the amplitude ratio and phase difference between mixed (spherical) and spheroidal modes [Eq. (2.21)] at $f^{\rm mix}_{\ell m}$. Specifically,

$$ \begin{aligned} \varepsilon_{\ell m} &= a^{\varepsilon}_{\ell m} + b^{\varepsilon}_{\ell m}\,\eta + c^{\varepsilon}_{\ell m}\,\eta^2 + d^{\varepsilon}_{\ell m}\,\eta^3, \\ \delta_{\ell m} &= a^{\delta}_{\ell m} + b^{\delta}_{\ell m}\,\eta + c^{\delta}_{\ell m}\,\eta^2 + d^{\delta}_{\ell m}\,\eta^3, \end{aligned} \tag{2.32} $$

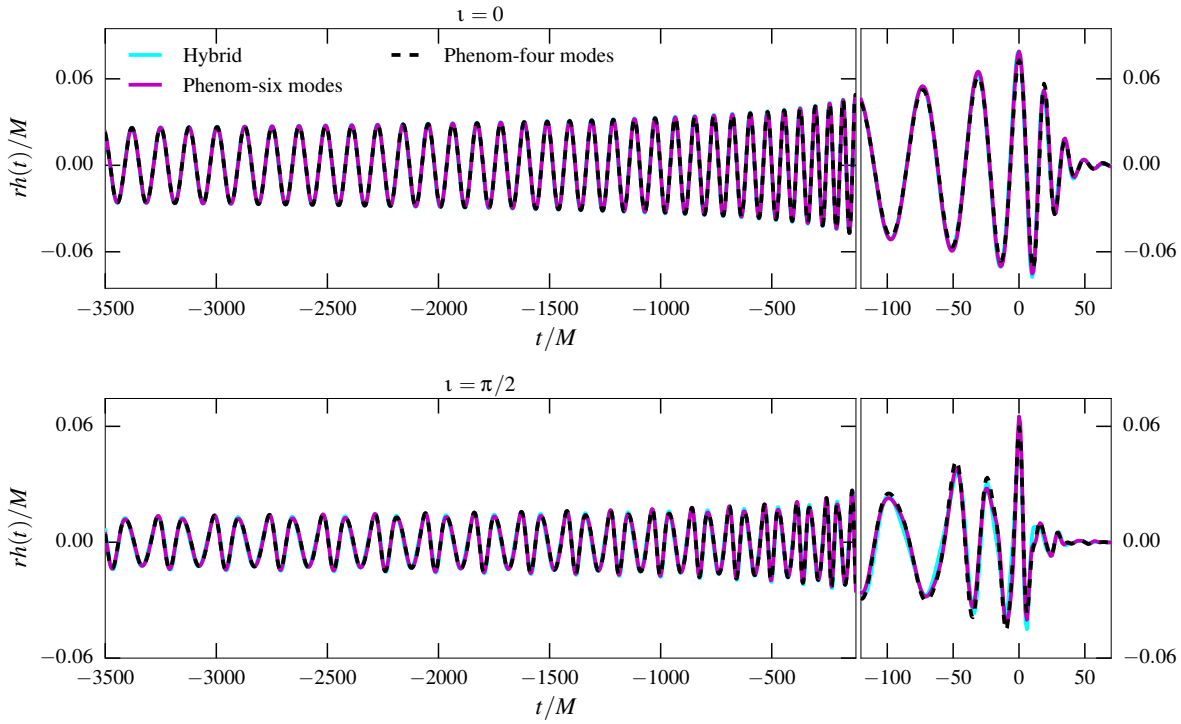

Figure 2.9: Comparison between hybrid waveforms and our analytical phenomenological waveforms for a binary with mass ratio $q = 10$. Hybrid waveforms are constructed using all the modes with $\ell \leq 4$, except the $m = 0$ modes. Phenomenological waveforms are constructed by taking the (discrete) inverse Fourier transform of the analytical model waveforms in the Fourier domain. The top panel corresponds to a "face-on" binary (inclination angle $\iota = 0$) while the bottom panel corresponds to an "edge-on" binary ($\iota = \pi/2$). The two phenomenological waveforms correspond to the current model with and without the 32 and 43 modes.

where $\ell m \in \{32, 43\}$. The fits for parameters $\varepsilon_{\ell m}$ and $\delta_{\ell m}$ are shown in the Fig. 2.7.

The amplitude and phase of the complete model for ${}^{\mathrm{Y}}\tilde{h}^{\mathrm{R}}_{\ell m}(f)$ for the mixed modes (32 and 43) are finally constructed as follows:

$$A_{\ell m}(f) = \begin{cases} |{}^{\mathrm{Y}}\tilde{h}^{\mathrm{R,\,mod}}_{\ell m}(f)|, & f < f^{\mathrm{mix}}_{\ell m}, \\ w^{\mathrm{M}}_{\ell m} |{}^{\mathrm{M}}\tilde{h}^{\mathrm{R,\,mod}}_{\ell m}(f)|, & f \geq f^{\mathrm{mix}}_{\ell m}, \end{cases} \tag{2.33a}$$

$$\Psi_{\ell m}(f) = \begin{cases} \arg({}^{\mathrm{Y}}\tilde{h}^{\mathrm{R,\,mod}}_{\ell m}(f)), & f < f^{\mathrm{mix}}_{\ell m}, \\ \phi^{\mathrm{M}}_{\ell m} + \arg({}^{\mathrm{M}}\tilde{h}^{\mathrm{R,\,mod}}_{\ell m}(f)), & f \geq f^{\mathrm{mix}}_{\ell m}. \end{cases} \tag{2.33b}$$

The parameters $w^{\mathrm{M}}_{\ell m}$ and $\phi^{\mathrm{M}}_{\ell m}$ ensure the continuity of amplitude and phase at $f^{\mathrm{mix}}_{\ell m}$, respectively. We compare the results of the final model for the spherical harmonics with the hybrids in Fig. 2.8.

So far, we have used $q = 4$ for all our illustrations. We chose this mass ratio to give a clean illustration in a case where the higher modes are relatively prominent and the mode mixing is still fairly large. (The mode mixing decreases as the mass ratio increases for nonspinning binary black holes, as the final spin decreases with increasing mass ratio.) We find that the mode mixing removal is less

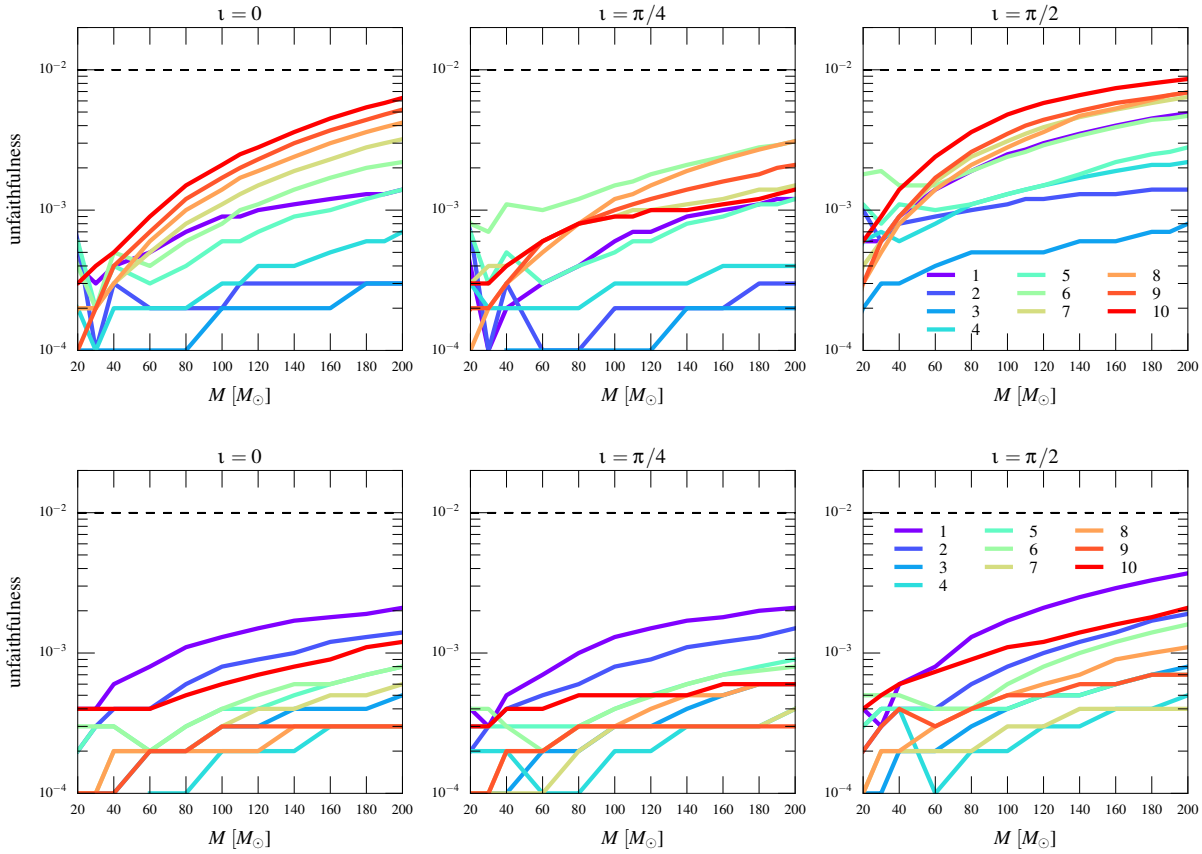

Figure 2.10: The unfaithfulness (mismatch) of the analytical model waveform family towards hybrid waveforms for inclination angle $\iota = \pi/2$. The analytical model waveform family in the top panel contains only the 22, 33, 44, and 21 modes while in the bottom panel the mixed modes we model here are also included, i.e., also the 32 and 43 modes. The horizontal axes report the total mass of the binary and different curves correspond to different mass ratios q (shown in the legend). Horizontal black dashed lines correspond to a mismatch of 1%. The overlaps are computed assuming the design power spectrum of Advanced LIGO (in the "high-power, zero-detuning" configuration), assuming a low-frequency cutoff of 20 Hz. We do not consider a smaller low-frequency cutoff or smaller total masses due to computational difficulties with constructing hybrid waveforms starting from lower dimensionless frequencies.

effective for smaller mass ratios, for reasons that we do not understand. Nevertheless, we still find that our model provides an accurate representation of the waveforms in these cases, as is shown by the match calculations below. We give illustrations of the mode mixing removal and the accuracy of the model for $q = 2.32$ in Appendix A.5.

2.4 *Assessing the accuracy of the analytical model*

We now assess the accuracy of our model by computing mismatches with a set of 10 hybrid waveforms used to validate the model (which only share 4 waveforms—primarily high mass-ratio ones—with the set of 8 waveforms that are used to construct the model; see table 2.1). The overlaps are computed assuming the design power spectrum of Advanced LIGO (in the "high-power, zero-detuning" configuration [4]), [10] assuming a low-frequency cutoff of 20 Hz, for a range of total masses.

[10] This noise curve has recently been updated slightly with newer predictions for the thermal noise [5]. We use the older version.

Figure 2.9 shows the comparison of our waveform model in the time domain against the hybrid waveforms for two cases, firstly when the model waveforms contain only four modes, i.e., 22, 33, 44, and 21, and secondly when it also includes the 32 and 43 modes in addition to the four modes mentioned before. The hybrid waveforms contain all modes with $\ell \leq 4$, except for the $m = 0$ modes, which are small and not well-resolved in the NR simulations. We see that the inclusion of the two additional modes improves the agreement between the hybrid and phenomenological waveforms. Additionally, comparing with Fig. 3 in [104], we see the improvement in the face-on case due to the refit of the 22 mode, as well as the inclusion of the 32 mode; the 43 mode does not contribute for a face-on binary.

While Fig. 2.9 only shows qualitative agreement between the phenomenological and hybrid waveforms, Fig. 2.10 shows the mismatch plots. The top panel plots show the mismatch (unfaithfulness) between the hybrid waveforms and the case where the model waveforms contain only four modes for various inclination angles. The bottom panel plots show the mismatch after including the 32 and 43 modes in the model waveforms for the same inclination angles. We see that for high mass ratio waveforms, the maximum mismatch reduces from 1% to 0.2% for the highest inclination angle $\iota = \pi/2$. However, mismatches are even lower ($\sim 0.05\%$) for other inclination angles. The lower mass ratio cases are almost unaffected, though they show a little improvement. This is expected, because the contribution of higher modes is significant for high mass ratio and inclination angles.

We also show the improvement in the accuracy of the model for the 22 mode alone for higher mass ratios in Fig. 2.11. This comes from a refit of this mode's phase. Unfortunately, this improvement for higher mass ratios comes at the cost of a somewhat larger mismatch for mass ratios of 1 and 2. Future work will consider improvements to the structure of the model to improve the mismatch for small mass ratios.

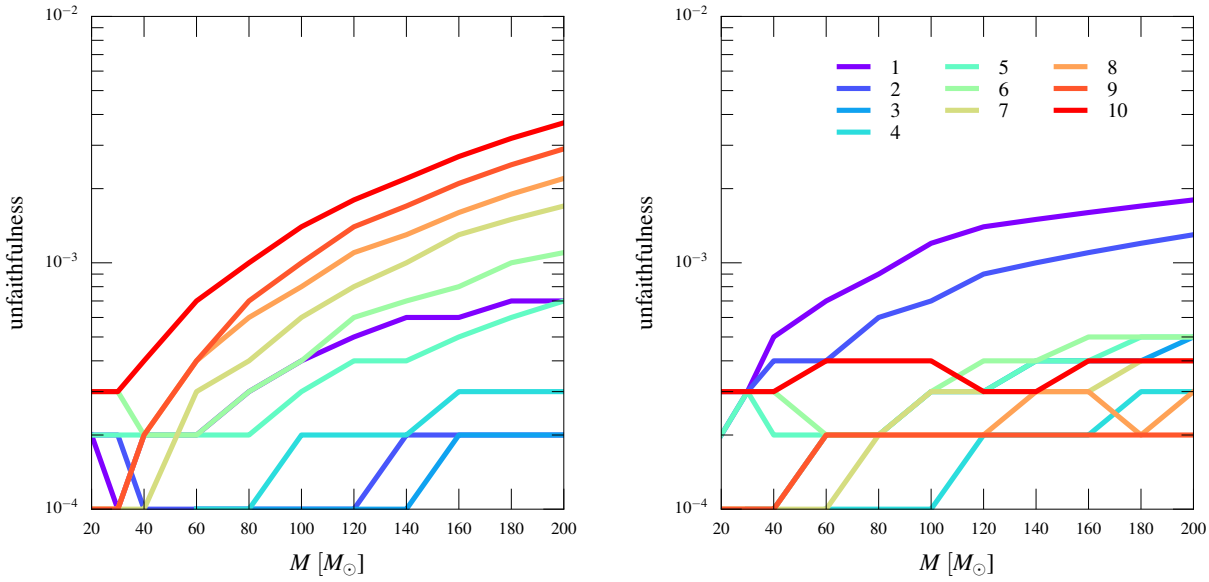

Figure 2.11: The unfaithfulness (mismatch) of the analytical model waveform 22 mode against the hybrid 22 mode. The left plot shows the mismatch for the previous phenomenological 22 mode and right plot shows the mismatch for the current phenomenological 22 mode which has been remodeled. The horizontal axes report the total mass of the binary and different curves correspond to different mass ratios q (shown in the legend). We can see a significant improvement in the mismatch for high mass ratio waveforms in the right-hand plot.

2.5 *Summary and Conclusions*

In this chapter, we presented an analytical family of frequency-domain waveforms describing the GW signals from non-spinning black-hole binaries, including some of the leading subdominant modes of the radiation ($\ell m = 21, 33, 44, 32, 43$), apart from the dominant ($\ell m = 22$) mode. The construction of these analytical waveforms involves two major steps: 1) the construction of a set of hybrid waveforms by combining the spherical harmonic modes of PN and NR waveforms corresponding to a limited set of mass ratios $1 \leq q \leq 10$, 2) representing the numerical Fourier transform of the hybrid waveforms by a suitable set of analytical functions which allow us to interpolate these waveforms smoothly over the parameter space. In particular, the modes 32 and 43 exhibit the effects of mode-mixing, i.e., having multiple spheroidal harmonic ringdown modes mixed into a single spherical harmonic mode. This leads to bumps in the ringdown part of the waveform. We have introduced a simple way of approximately extracting the unmixed (spheroidal harmonic) modes. We then model these unmixed modes using the method used for the other modes in [104]. We then reinstate the mode mixing using

the models for the unmixed modes to obtain the final model for the spherical harmonic modes. We also refit our model for the dominant 22 mode to improve its accuracy for large mass ratios. The analytical gravitational waveforms that are constructed in this way are highly faithful (mismatch < 0.04%) to our target hybrid waveforms that include all the modes up to $\ell = 4$ (except the $m = 0$ modes).

The Fourier domain amplitude of our phenomenological waveforms contain a inspiral-merger part that is smoothly matched to the ringdown part. The inspiral-merger amplitude is modeled as the product of a Padè resummed version of the Fourier domain PN amplitude and another function that mimics a PN-like expansion whose coefficients are determined by fitting against the Fourier-domain amplitude of the hybrid waveforms. The ringdown part is modeled as the Fourier transform of a time-symmetric damped sinusoid, which is exponentially damped to mimic the high-frequency fall of the NR waveforms in Fourier domain. Similarly, the Fourier domain phase is modeled as a PN-like series including the known coefficients from PN theory till 3.5PN order, while the higher order "pseudo-PN" terms are determined by fitting against the hybrid waveforms. The resulting waveforms are also computationally inexpensive to generate, allowing their direct implementation in GW searches and parameter estimation. As GW observations are becoming precision probes of physics and astrophysics, accuracy requirements on GW templates can only grow.

3 A "No-Hair" Test for Binary Black Holes

One of the remarkable predictions of general relativity (GR) is that a stationary black hole can be fully described by a small number of parameters — its mass, spin angular momentum and electric charge [85, 86, 54]. As a consequence of this "no-hair" theorem, frequencies of the gravitational radiation (*quasi-normal modes* [147, 116, 55]) from a perturbed black hole is fully determined by these parameters. Astrophysical black holes are not expected to possess significant electric charge; hence, different quasi-normal modes have to be consistent with the same value of the mass and spin. Thus, the consistency between multiple quasi-normal modes provides a test of the "no-hair" theorem for stationary, isolated black holes [70]. Similarly, the dynamics and gravitational radiation from a binary black hole (BBH) system are uniquely determined by a small number of parameters (masses and spins of the black holes and orbital parameters), and hence different spherical harmonic modes of the radiation have to be consistent with the same values of this small set of parameters. Thus, the consistency between different modes of the observed signal is a powerful test that the radiation emanated from a BBH. Inconsistency between different modes would point to either a departure from GR, or the non-black hole nature of the compact objects.

Coalescence of binaries composed of chargeless black holes would produce a perturbed Kerr black hole as the remnant, and the late time gravitational-wave (GW) signal is described by a spectrum of

quasi-normal modes (see, e.g. [51]). While the relatively simple structure of quasi-normal modes has been known from black-hole perturbation theory for a long time (see, e.g., [39] for a review), the radiation from the full inspiral, merger and ringdown have a much more complex structure. Fortunately, recent numerical-relativity simulations, together with high-order analytical calculations, have enabled us to accurately model several subdominant multipoles of the radiation [111, 101, 104]. This allows us to formulate a powerful test of the consistency of the GW signal with a BBH waveform in GR, based on the consistency of different multipoles of the radiation. While the relatively low signal-to-noise ratios (SNRs) of the ringdown signals makes the measurement of multiple quasi-normal modes extremely difficult using the current generation of GW detectors [40], we show that the test proposed in this chapter can be performed using GW detections expected in the next few years, because it makes use of the full inspiral-merger-ringdown signal.

The material presented in this chapter is based on the article [67].

3.1 *Method*

In practice it is difficult to extract different multipoles of the radiation from the GW observation of a single BBH system — all we measure is a particular linear combination of the modes. Thus, our strategy, developed below, is to introduce extra parameters that describe inconsistency between different modes and to constrain them using a Bayesian framework. This is similar in spirit to the tests of the "no-hair" theorem using quasi-normal modes, developed in [79, 105].

As discussed in Eq. 1.132, the two polarizations $h_+(t)$ and $h_\times(t)$ of gravitational radiation in GR can be written as,

$$h(t;\mathbf{n},\lambda) = \frac{1}{d_L}\sum_{\ell=2}^{\infty}\sum_{m=-\ell}^{\ell} Y^{-2}_{\ell m}(\mathbf{n})\, h_{\ell m}(t;\lambda), \tag{3.1}$$

where $h(t) := h_+(t) - i\,h_\times(t)$ and $Y^{-2}_{\ell m}$ are the basis functions of spin -2 spherical harmonics, $\mathbf{n} := \{\iota, \varphi_0\}$ define the direction of radia-

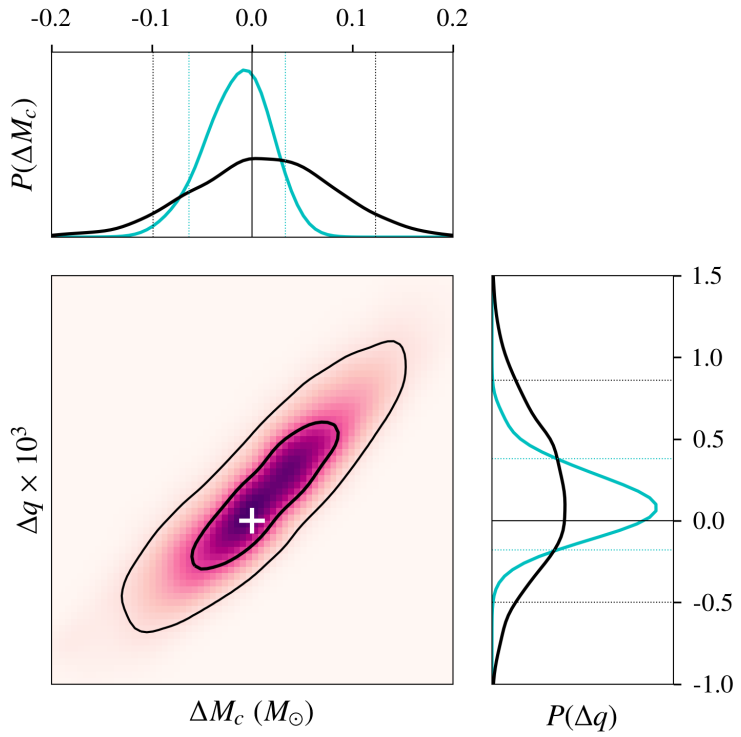

Figure 3.1: The thick (thin) contours show the 50% (90%) credible regions in the joint posteriors of two parameters ΔM_c and Δq (difference in the chirp mass M_c and mass ratio q estimated from the quadrupole vs non-quadrupole modes) from a simulated BBH signal. Black histograms on the side panels show the marginalized posteriors in ΔM_c and Δq, while the cyan histograms show the 1-dimensional posteriors in ΔM_c and Δq estimated from the data by introducing only one variation (say, ΔM_c) at a time, keeping the other fixed (say, $\Delta q = 0$). It can be seen that the posteriors are fully consistent with the GR prediction of $\Delta M_c = \Delta q = 0$ (shown by a "+" sign in the center panel and by thin black lines in side panels). In the side panels, the dotted lines mark the 90% credible regions. The simulated GR signal corresponds to a BBH system with total mass $M = 80 M_\odot$, mass ratio $q = 1/9$ and inclination angle $\iota = 60^\circ$ observed by a single Advanced LIGO detector with an optimal SNR of 25.

tion in the source frame, d_L is the luminosity distance to the binary, and $h_{lm}(t;\lambda)$ are the spherical harmonic modes of the waveform, which are completely described by the intrinsic parameters λ of the system. We assume that the black holes are non-spinning and the binary to be quasi-circular. Hence λ consists of only the masses m_1 and m_2 of the black holes (it is more convenient to describe the system in terms of the *chirp mass* $M_c := (m_1 m_2)^{3/5}/(m_1+m_2)^{1/5}$ and mass ratio $q = m_2/m_1 \leq 1$). In GR, the gravitational radiation is dominated by the quadrupole modes ($\ell = 2, m = \pm 2$); however non-quadrupole modes can make an appreciable contribution if the black holes have significantly unequal masses. The set of intrinsic parameters $\lambda := \{M_c, q\}$ completely determines the multipolar structure (i.e., spherical harmonic modes) of the waveform $h_{lm}(t)$.

In order to formulate a consistency test between different multipoles, we rewrite Eq. (3.1) by splitting the contributions from the dominant ($\ell = 2, m = \pm 2$) mode of gravitational radiation, and the

sub-dominant (higher order) modes

$$\begin{aligned} h(t;\mathbf{n},\lambda,\Delta\lambda) &= \sum_{m=\pm 2} Y^{-2}_{2m}(\mathbf{n})\, h_{2m}(t,\lambda) \\ &+ \sum_{\text{H.O.M}} Y^{-2}_{\ell m}(\mathbf{n})\, h_{\ell m}(t,\lambda+\Delta\lambda) \end{aligned} \tag{3.2}$$

where the sum in the second term on the RHS is just over the higher-order modes. Note that we allow a possibility of inconsistency between the dominant mode and higher order modes by introducing a deviation $\Delta\lambda := \{\Delta M_c, \Delta q\}$ in the set of intrinsic parameters that describe the higher order modes. For BBHs in GR, $\Delta\lambda = 0$.

An interferometric GW detector observes a linear combination of the two polarizations $h_+(t)$ and $h_\times(t)$, given by

$$h(t) = F_+(\theta,\phi,\psi)\, h_+(t-t_0) + F_\times(\theta,\phi,\psi)\, h_\times(t-t_0), \tag{3.3}$$

where F_+ and $F_\times$ are the antenna pattern functions of the GW detector, t_0 is the time of arrival of the signal at the detector, and $(\theta,\phi),\psi$ define the sky position and polarisation angle of the GW source, respectively. For coalescing BBH systems in quasi-circular orbits, the observed signal $h(t)$ is described by a set of *intrinsic* parameters $\lambda = \{M_c, q\}$ and *extrinsic* parameters $\theta := \{t_0, \iota, \varphi_0, d_L, \theta, \phi, \psi\}$ in GR. In addition to the parameters that describe signals in GR, we introduce a set of parameters $\Delta\lambda$ describing difference between the intrinsic parameters used to generate the dominant and subdominant modes. The combined set of parameters is denoted as $\boldsymbol{\xi} = \{\lambda, \theta, \Delta\lambda\}$.

The data $d(t) = n(t) + h(t)$ contains the observed signal $h(t)$ given in Eq. (3.3) along with noise $n(t)$, which is modeled as a stationary Gaussian random process. Given data d and assuming a particular model of the waveform given in (3.2) as our hypothesis H, we can compute the posterior distribution of the set of parameters $\boldsymbol{\xi}$ making use of the Bayes theorem:

$$P(\boldsymbol{\xi} \mid d, H) = \frac{P(\boldsymbol{\xi} \mid H)\, P(d \mid \boldsymbol{\xi}, H)}{P(d \mid H)}. \tag{3.4}$$

The *posterior* probability density $P(\vec{\xi} \mid d, H)$ that the data contains a signal with parameters $\vec{\xi}$ is determined by the *prior* probability distribution $P(\vec{\xi} \mid H)$ and the *likelihood* $P(d \mid \vec{\xi}, H)$ that the data contains a signal described by parameters $\vec{\xi}$; $P(d \mid H)$ is a normalization constant, called the *evidence*. For stationary Gaussian noise with power spectral density $S_n(f)$, the likelihood can be written as:

$$P(d \mid \vec{\xi}, H) = \exp\left[-\frac{1}{2}\int_{f_{\rm low}}^{f_{\rm high}} \frac{|\tilde{d}(f) - \tilde{h}(f; \vec{\xi}, H)|^2}{S_n(f)} df\right] \tag{3.5}$$

where $f_{\rm low}$ and $f_{\rm high}$ define the sensitivity bandwidth of the detector, while $\tilde{d}(f)$ and $\tilde{h}(f)$ are the Fourier transforms of $d(t)$ and $h(t)$, respectively.

We estimate the posterior of $\vec{\xi}$ by stochastically sampling the likelihood function over the entire parameter space of interest. In this work, we use the `emcee` [75] package, a Python implementation of the stochastic sampling algorithm proposed by [78] [1]. From the posterior distribution $P(\vec{\xi} \mid d, H)$ of the full parameter set, we construct the posterior distribution $P(\Delta\lambda \mid d, H)$ of the set of parameters $\Delta\lambda := \{\Delta M_c, \Delta q\}$ describing deviation from the GR prediction of a BBH signal, by marginalizing the posterior over all other parameters $\{\lambda, \theta\}$. If the data is consistent with a BBH signal in GR, we expect $P(\Delta\lambda \mid d, H)$ to be consistent with zero.

[1] We have compared the posterior distributions obtained from our `emcee` based code with that from the Nested-Sampling based LALInferenceNest code [145] that is part of the LIGO Algorithm Library (LAL) software suite [2]. Posteriors obtained from simulated GR waveforms containing only the dominant ($\ell = 2, m = \pm 2$) modes observed by a single detector are in good agreement.

3.2 *Simulations using BBH waveforms in GR*

We now demonstrate this test on simulated GW observations of BBH signals predicted in GR. We employ the recent inspiral-merger-ringdown waveform model proposed by [104], which provide accurate Fourier-domain models of the following spherical harmonic modes $h_{\ell m}(f)$ of the expected GW signals from non-spinning BBHs: $(\ell = 2, m = \pm 2)$, $(\ell = 2, m = \pm 1)$, $(\ell = 3, m = \pm 3)$, $(\ell = 4, m = \pm 4)$. (The other spherical harmonic modes that are neglected only introduce an inaccuracy (mismatch) of less than 1% in the waveforms [104]). GW observations are simulated making use of Eqs. (3.1)

and (3.3). For estimating the parameters, we assume the likelihood function given in Eq. (3.5), with noise power spectral density anticipated in Advanced LIGO's "high-power, zero-detuning" configuration [122]. We consider binaries with total mass $M := m_1 + m_2$ in the range $40M_\odot$ – $200\ M_\odot$ with mass ratio $q := m_2/m_1$ in the range $1/9$ – 1, with varying inclination angles ι (angle between the orbital angular momentum of the binary and the line of sight).

We perform the test by introducing variations in the higher order modes, as in Eq.(3.2). The higher-order modes $h_{\ell m}(f;\lambda + \Delta\lambda)$ are generated by introducing an extra parameter $\Delta\lambda$ while the quadrupole-modes $h_{2\pm2}(f;\lambda)$ are generated by using the standard set of parameters λ in GR. We make two choices for the deviation parameter $\Delta\lambda$: First, by introducing *one* deviation parameter at a time; i.e., $\Delta\lambda = \Delta M_c$ or $\Delta\lambda = \Delta q$. Second, by introducing a concurrent deviation in *two* parameters $\Delta\lambda = \{\Delta M_c, \Delta q\}$. We show in Fig. 3.1 the results of the tests performed by varying either one parameter or two parameters, for a binary with total mass $M = 80M_\odot$, mass ratio $q = 1/9$, inclination angle $\iota = 60^\circ$ producing an SNR of 25 (SNR in higher modes is ~ 10). We see that the posterior probability density for the parameters Δq and ΔM_c are consistent with zero as in GR. As expected, the width of the posterior is smaller when only one deviation parameter is allowed to vary at a time (either ΔM_c or Δq). Figures 3.2 and 3.3 show the 90% credible regions of the posteriors of the deviation parameters for the case of binaries with different masses, mass ratios and inclination angles. For all cases SNR is 25, and either ΔM_c or Δq is introduced at a time. This shows that binaries with large mass ratios ($q < 1/2$) and inclination angles ($\iota > 60^\circ$) will allow precision tests of the GR predictions, reaching statistical uncertainties $< 10^{-2}$ for $\Delta M_c/M_c$ and Δq.

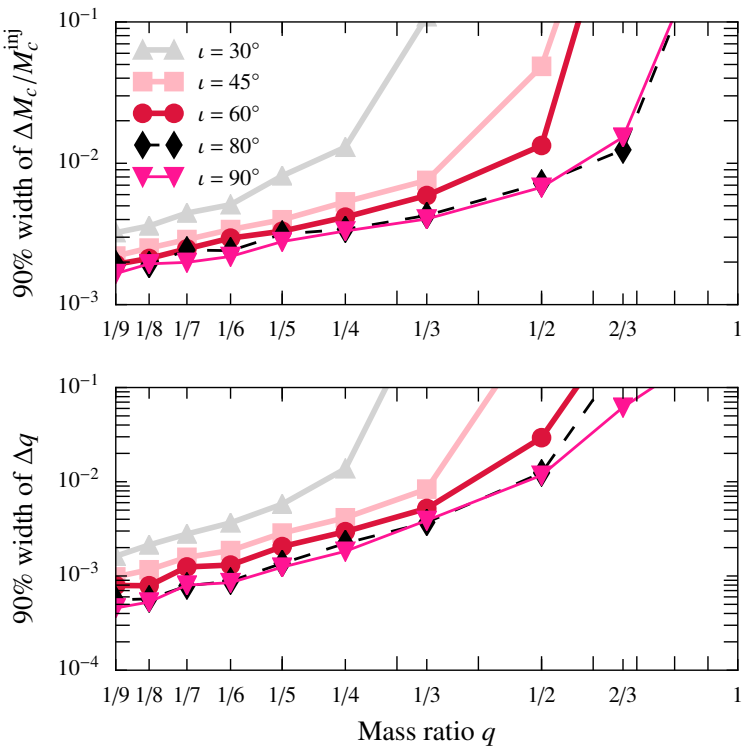

Figure 3.2: The figure shows the width of the 90% credible region of ΔM_c and Δq for binaries with different mass ratios q (horizontal axis) and inclination angles ι (legends). All binaries have a total mass $40M_\odot$. Best constraints are provided by binaries with high mass ratios and/or large inclination angles.

3·3 *Simulations using non-BBH waveforms*

If the multipole structure of the GW signal is sufficiently different from that of BBHs in GR (either when the underlying theory is different from GR or when the binary contains compact objects other than black holes), then this test should be able to identity this difference. We demonstrate this by performing the test on a simulated GW signal from a black hole-neutron star binary with mass ratio 1/6 from the numerical-relativity waveform catalog of the SXS collaboration [3]. We rescale this waveform to a total mass of $M = 120M_\odot$ and use it as a proxy for GW signals from a binary consisting of at least one non-black hole compact object [2]. Figure 3.4 shows the posteriors of the deviation parameters ΔM_c and Δq estimated from a simulated observation containing this signal, which are *inconsistent* with the GR prediction of BBHs. The Figure also shows the results of the test applied on a numerical relativity waveform from a BBH system with

[2] Note that the rescaled signal will not correspond to a black hole-neutron star binary, as $m_2 \simeq 17M_\odot$ is much larger than the maximum mass of a neutron star. However, we use this as a proxy for GW signals produced by a binary containing an exotic compact object.

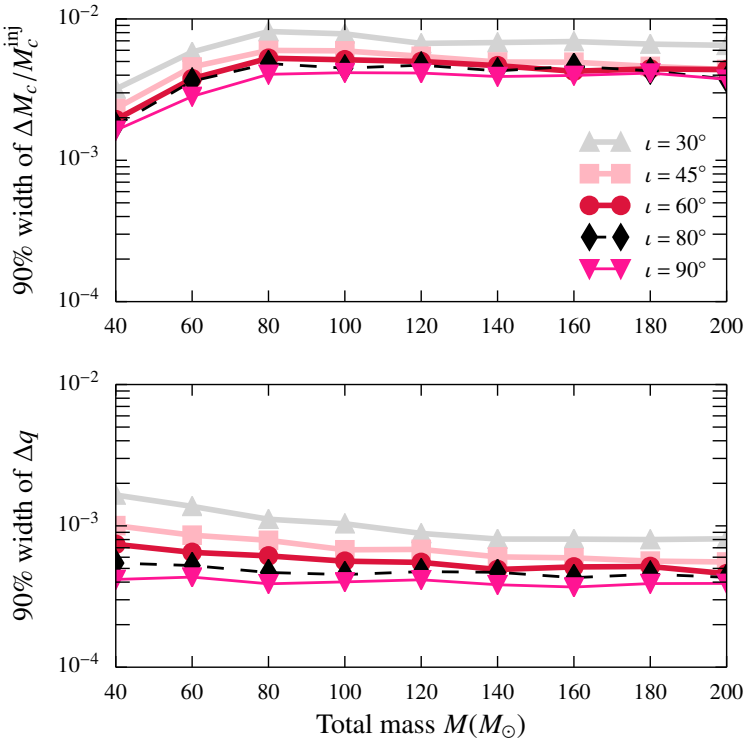

Figure 3.3: Same as Fig. 3.2, except that the horizontal axis reports the total mass M. All binaries correspond to a mass ratio $q = 1/9$.

same parameters, which shows consistency with $\Delta M_c = \Delta q = 0$. The simulated signals correspond to binaries with inclination angle $\iota = 90°$, producing SNR of 50 in Advanced LIGO.

3·4 *Astrophysical prospects*

Recent observations of GW signals from merging binaries of black holes [11, 12, 21, 14, 15, 16, 18] and neutron stars [17] by LIGO and Virgo have enabled the first tests of GR in the highly relativistic regime [23, 21, 14, 15, 16]. However, the test proposed in this chapter requires the observation of GW signals where the subdominant modes can be observed with appreciable SNR. These modes are excited predominantly for binaries with large mass ratios. Also, due to the radiation pattern, radiation from binaries with highly inclined orbits will contain appreciable contribution from subdominant modes. Hence binaries with large mass ratios ($q \lesssim 1/2$) and inclined orientations ($\iota \gtrsim 60°$) are particularly suitable sources for performing

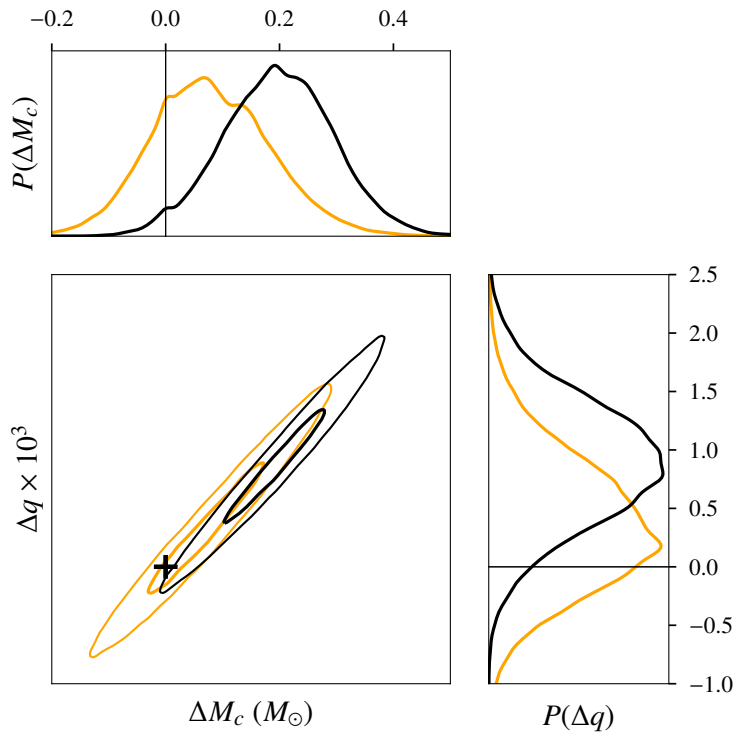

Figure 3.4: Black contours show the posterior distributions of ΔM_c and Δq (similar to Fig 3.1) estimated from a simulated GW signal from a binary containing at least one compact object other than a black hole. The signal was produced by rescaling a numerical relativity waveform from a neutron star-black hole binary with mass ratio 1/6 to a total mass of $120M_\odot$ (inclination angle $\iota = 90°$, producing SNR of 50 in Advanced LIGO). Note that the posteriors are inconsistent with a BBH system in GR ($\Delta M_c = \Delta q = 0$, marked by a "+" sign, is outside the 90% credible region). The orange contours show the posteriors estimated from a numerical relativity waveform from a BBH system with same parameters, which show consistency with $\Delta M_c = \Delta q = 0$.

the test described in this chapter. Consequently, we do not expect the test to be effective for GW signals observed by LIGO and Virgo during their first two observational runs, for which mass ratios are less than 2 and inclinations are close to being face-on/face-off [18]. The detection rate of binaries with large mass ratios depends on the astrophysical merger rate of such binaries, which is currently uncertain, while the detection rate of binaries with large inclination angle is related to the same with small inclination angles by a simple geometric factor.

Here we investigate the prospect of performing the proposed test on BBH events that Advanced LIGO and Virgo could observe over the next few years. We simulate populations of BBHs based on reasonable astrophysical assumptions, and examine the distributions of the mass ratio and inclination angle of detectable signals. In particular, we simulate binaries with two astrophysically motivated mass distributions in the source-frame [9]:

1. Component masses following a power-law $p(m_{1,2}) = m_{1,2}^{-1}$ with $m_1, m_2 \geq 5M_\odot$ and $m_1 + m_2 \leq 100M_\odot$.

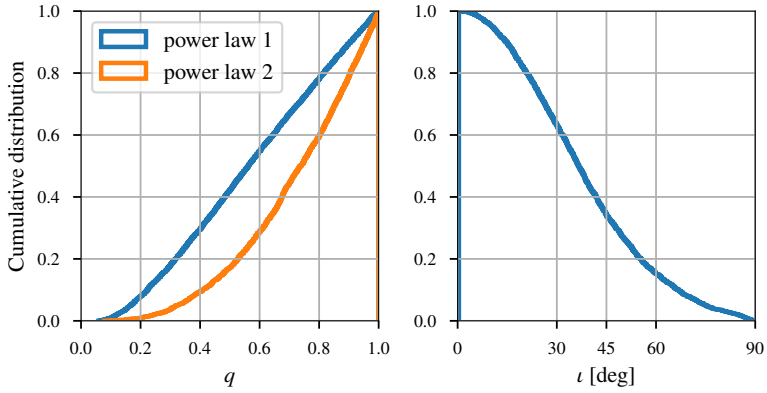

Figure 3.5: Projected cumulative distribution of the mass ratio q (left) and inclination angle ι (right) of simulated BBHs that are detectable by Advanced LIGO, based on our assumed component mass distribution. The two distributions in the left plot corresponds to two assumed distributions of the component masses (see text).

2. Power-law $p(m_1) = m_1^{-2.35}$ on the mass of the larger black hole, with the smaller mass distributed uniformly in q and with $5M_\odot \leq m_1 + m_2 \leq 100M_\odot$.

In both cases, binaries are distributed uniformly in the sky with isotropic orientations. The distribution of the mergers in redshift is chosen according to the prescription given in [69]. The cosmological redshift on the GW signals can be absorbed by a rescaling of the masses $m_{1,2}(1+z)$ where z is the redshift. From the simulated events, we compute the SNR expected in Advanced LIGO and apply an SNR threshold for detection (the probability distributions are independent of the exact value of the SNR threshold). The cumulative distribution of the mass ratio q and inclination angle ι of binaries crossing the detection threshold is plotted in Fig. 3.5. It can be seen that $\sim 20-40\%$ of the detectable binaries will have a mass ratio greater than 2, out of which $\sim 15\%$ will be observed with inclination angle greater than 60°. Thus, only a few percent of the observed systems are likely to have large mass ratios ($q < 1/2$) and inclined orbits ($\iota > 60^\circ$). However, since Advanced LIGO and Virgo are expected to observe hundreds of BBH mergers over the next few years [9], we conclude that the proposed test could be performed when detectors reach their design sensitivity over the next few years, if not sooner. Indeed, the precision of such tests will depend on the SNR of the observed signals. While the earlier examples that we studied assume

a rather high SNR of 25, we show in Fig. 3.6 that interesting statistical constraints on the deviation parameters can be expected even for modest SNRs, such as 10 or 12.

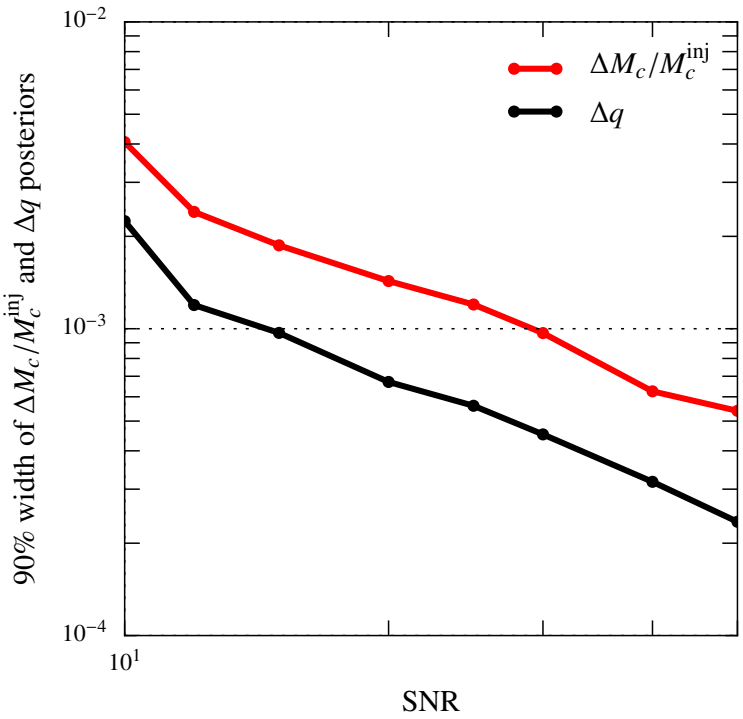

Figure 3.6: The width of the 90% credible region of the posteriors of ΔM_c and Δq as a function of the optimal SNR of the signal in a single Advanced LIGO detector. The simulated GR signal corresponds to a BBH system with total mass $M = 80 M_\odot$, mass ratio $q = 1/9$ and inclination angle $\iota = 60^\circ$ (same as Fig. 3.1).

3·5 *Conclusions and future work*

In this chapter, we proposed a new method to test the consistency of an observed GW signal with a BBH system predicted by GR. The test relies on the fact that the multipolar structure of the radiated GW signal from a BBH system in quasi-circular orbit is uniquely determined in GR by the masses and spins of the black holes and no other parameters. Thus, if we estimate the parameters of the binary from different spherical harmonic modes of the observed signal independently, those estimates will have to be consistent with one another. Any inconsistency between the different estimates will point to a deviation from GR or to the non-black hole nature of the compact objects. We have used Bayesian parameter inference to identify po-

tential deviations from GR predictions, using simulated GW signals. We provided the first estimates of the expected precision of such tests that can be performed using GW observations of BBHs anticipated by Advanced LIGO and Virgo in the next few years.

The specific implementation of the test presented in this chapter checks for the consistency of the masses (and spins, in the case of spinning binaries) estimated from the quadrupole/non-quadruple modes. If we have enough SNR to distinguish different modes, we can introduce deviation parameters for each mode (say, $\Delta M_c^{\ell m}$ and $\Delta q^{\ell m}$). This is analogous to checking the consistency of different quasi-normal mode frequencies, as the frequency evolution of the binary is determined by these intrinsic parameters. In addition, one could also check the consistency of the amplitudes of different modes, by introducing extra parameters describing deviations from the predicted amplitudes. While this would expand the scope of this test, in general, introducing more parameters would increase the statistical uncertainties, due to correlations between different parameters.

We have assumed, for simplicity, that the component black holes of the binary have negligible spins. Nevertheless, the method can be easily generalized to the case of binaries consisting of spinning black holes. We have also neglected the systematic errors due to inaccuracies in waveform modeling and detector calibration; these need to be understood before implementing the test on real observations. We aim these investigations for future work.

4 Gravitational Lensing Theory

This chapter will discuss the gravitational lensing of gravitational waves [92, 103, 133]. This is related to the study of the propagation of the gravitational waves in the curved spacetime. Understanding the effect of the gravitational waves on the background spacetime allows us to find an expression for the energy carried by them. We here, however, ask the opposite question, i.e., how does the background object affect the propagation of the gravitational waves, having assumed that the gravitational waves have a negligible contribution to the background curvature. We will see that the background object (called *lens*) can bend the trajectories of the gravitational waves (and the electromagnetic waves) in such a way that the multiple trajectories can make their way to the observer, i.e., we might be able to see the multiple images of a source [1]. For transient gravitational wave sources, this implies that multiple gravitational wave events can be observed, from the same source. For lensing by galaxies, the time delay between the images can range from minutes to months, depending on the mass of the lens.

[1] This phenomenon is called strong lensing and the corresponding lens object is called a strong lens, e.g., galaxies can act as the gravitational lens.

The rough plan of this chapter is as follows: we will first discuss the general case of lensing, i.e., the wave-optics limit of the gravitational lensing and then discuss how to transition into the geometric optics limit, in which we are mainly interested. We will compute the lensing effect on gravitational waves from some of the lens models, such as point masses and spherical mass distributions. We will end this chapter by discussing in detail the lensing phenomenon by elliptical mass distributions, which are expected to be good models

for the galaxy lenses [2]. In the next chapter, we will discuss how to identify such lensed pairs of images from a set of LIGO-Virgo binary black holes merger detections.

The material presented in this chapter is based on standard theory of gravitational lensing. For a longer discussion, see for e.g., [92, 103, 133].

4.1 *Propagation of Gravitational Waves in Curved Spacetime*

Consider a small perturbation field $h_{\mu\nu}$ in the background spacetime metric $\bar{g}_{\mu\nu}$, so that

$$g_{\mu\nu} = \bar{g}_{\mu\nu} + h_{\mu\nu} \tag{4.1}$$

Let us assume that the typical scale over which the background spacetime $\bar{g}_{\mu\nu}$ varies is L_B. We further assume that the typical amplitude of $h_{\mu\nu}$ is h and $h \ll 1$ [3]. From Einstein equations, we find that,

$$h \ll \lambda\!\!\!^{-}/L_B \ll 1 \tag{4.2}$$

where $\lambda\!\!\!^{-}$ is the typical wavelength of the perturbation $h_{\mu\nu}$. We, thus, have two expansion parameters, h and $\lambda\!\!\!^{-}/L_B$ [4]. We choose a gauge such that,

$$\bar{D}^{\nu}\bar{h}_{\mu\nu} = 0 \tag{4.4}$$

where $\bar{D}^{\mu}$ is the covariant derivative compatible with background metric $\bar{g}_{\mu\nu}$ and $\bar{h}_{\mu\nu} = h_{\mu\nu} - \frac{1}{2}\bar{g}_{\mu\nu}h$, where $h = \bar{g}^{\mu\nu}h_{\mu\nu}$.

We will restrict ourselves to only linear order in h. We find that, outside the source, to leading and next-to-leading order in $\lambda\!\!\!^{-}/L_B$, the Ricci tensor (to linear order in h) vanishes, i.e.,

$$R^{(1)}_{\mu\nu} = 0 \tag{4.5}$$

which is,

$$\bar{D}^{\rho}\bar{D}_{\rho}\bar{h}_{\mu\nu} + 2\bar{R}_{\mu\rho\nu\sigma}\bar{h}^{\rho\sigma} - \bar{R}_{\mu\rho}\bar{h}^{\rho}_{\nu} - \bar{R}_{\nu\rho}\bar{h}^{\rho}_{\mu} = 0 \tag{4.6}$$

[2] We will later see that the galaxy lenses are the dominant strong lenses.

[3] That is, we are considering a small ripple in the background spacetime.

[4] In source-free spacetime, they are of same order, i.e.,

$$h \sim \lambda\!\!\!^{-}/L_B \tag{4.3}$$

, because the curvature is produced by the ripple itself. In the presence of the source, however, the background curvature is dominated by the source (Eq. 4.2).

Note that,

$$\bar{R}_{\mu\rho\nu\sigma}\bar{h}^{\rho\sigma} = \mathcal{O}(h/L_B^2) \tag{4.7}$$

While,

$$\bar{D}^\rho \bar{D}_\rho \bar{h}_{\mu\nu} = \mathcal{O}(h/\lambda\!\!\!^{-2}) \tag{4.8}$$

We thus see that the quantity in Eq. 4.7 is smaller than the one in Eq. 4.8 by a factor $\mathcal{O}(\lambda\!\!\!^{-2}/L_B^2)$. Since we restrict ourselves to only next-to-leading term in $\lambda\!\!\!^{-}/L_B$, this implies,

$$\bar{D}^\rho \bar{D}_\rho \bar{h}_{\mu\nu} = 0 \tag{4.9}$$

This equation along with the gauge condition, Eq. 4.4 represent the propagation of the gravitational waves in the curved spacetime, provided $\lambda\!\!\!^{-} \ll L_B$ [5].

[5] It is this requirement that allows us to decompose the spacetime metric into a background metric and a fluctuating part of the metric, $h_{\mu\nu}$ (Eq. 4.1). Otherwise, we would not know how to proceed.

4.2 *Eikonal Approximation*

We can solve the Eq. 4.9 using what is called *eikonal approximation* [6], where we make following ansatz,

$$\bar{h}_{\mu\nu}(x) = [A_{\mu\nu}(x) + \epsilon B_{\mu\nu}(x) + \cdots]\mathrm{e}^{i\theta(x)/\epsilon} \tag{4.10}$$

[6] It assumes that the the phase θ of the perturbation changes on the scale $\lambda\!\!\!^{-}$, while the amplitude changes on the scale L_B. In other words, the phase changes much faster than the amplitude.

Here ϵ is just a book-keeping parameter, which will be later set to unity. It is just there to remind us that a term before ϵ^n is of order $(\lambda\!\!\!^{-}/L_B)^n$. The wave vector is defined by $k^\mu = \partial_\mu\theta$. We write the gravitational wave amplitude in terms of the polarization tensors $e_{\mu\nu}$ as, $A_{\mu\nu} = Ae_{\mu\nu}$, where A is the scalar amplitude. Plugging the Eq. 4.10 in Eq. 4.4 and keeping only the lowest order in ϵ, gives us [7]

[7] Using also the fact that the change in the amplitude over length $\lambda\!\!\!^{-}$ is negligible.

$$k^\mu e_{\mu\nu} = 0 \tag{4.11}$$

From the Eq. 4.9, we get

$$k^\mu k_\nu = 0 \tag{4.12}$$

Using this equation we can show that,

$$k_\mu \bar{D}^\mu k_\nu = 0 \tag{4.13}$$

This says that the gravitons travel along the null geodesics of the background spacetime metric $\bar{g}_{\mu\nu}$ [8]. We further find that, to next-to-leading order in ϵ, Eq. 4.9 gives

$$k^\rho \bar{D}_\rho e_{\mu\nu} = 0. \tag{4.14}$$

The Eq. 4.11 and Eq. 4.14 imply that the polarisation tensor is transverse and parallelly transported along the null geodesic.

[8] More appropriately, the curves normal to the surfaces of the constant phase (called 'rays' in geometric optics limit) travel along the null geodesics of the background spacetime metric $\bar{g}_{\mu\nu}$

4.3 *Gravitational Lensing: Wave Optics*

We just showed that the polarisation tensor does not change during the propagation. We can thus treat the propagating gravitational waves as scalar waves times the polarization tensor as follows:

$$h_{\mu\nu} = \phi\, e_{\mu\nu} \tag{4.15}$$

where ϕ is a scalar wave. Then the propagation equation, Eq. 4.9 becomes,

$$\partial_\mu\big(\sqrt{-\bar{g}}\,\bar{g}^{\mu\nu}\,\partial_\nu\phi\big) = 0 \tag{4.16}$$

Let us assume that the background metric is given by

$$ds^2 = -(1+2U)dt^2 + (1+2U)d\boldsymbol{r}^2 = \bar{g}_{\mu\nu}dx^\mu dx^\nu \tag{4.17}$$

where $U(\boldsymbol{r})(\ll 1)$ is the gravitational potential of the lens object. The Eq. 4.16 in frequency domain $\tilde{\phi}(f,\boldsymbol{r})$ takes the form,

$$(\nabla^2 + \omega^2)\tilde{\phi} = 4\omega^2 U\tilde{\phi} \tag{4.18}$$

where $\omega = 2\pi f$. Now this is the equation that we need to solve to get the lensing effect on the gravitational waves. These kinds of equations are solved using Kirchhoff integral theorem. The amplification

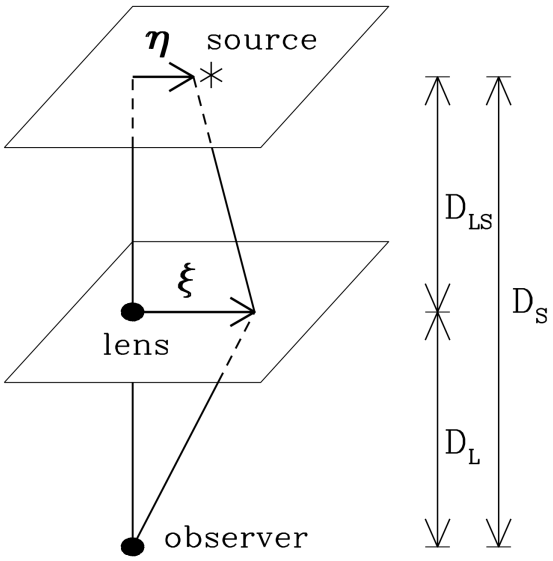

Figure 4.1: Gravitational lens geometry for the source, the lens and the observer. D_l,D_s and D_{ls} are the distances between them. $\boldsymbol{\eta}$ is a displacement of the source and $\boldsymbol{\xi}$ is an impact parameter. We use the thin lens approximation in which the gravitational waves are scattered in the thin lens plane. [Takahashi et al (2003)]

factor is defined as

$$F(f) = \tilde{\phi}^L(f)/\tilde{\phi}(f) \tag{4.19}$$

where $\tilde{\phi}^L(f)$ represents the lensed scalar waves [9] while $\tilde{\phi}(f)$ represents the unlensed scalar waves (i.e., $U = 0$).

[9] Or the gravitational waves.

To solve for $F(f)$, we need to first specify the gravitational lens geometry of the source, the lens and the observer (see, Fig. 4.1). In Fig. 4.1, D_s and D_l represent the distance to the source and the lens from the observer, respectively. While D_{ls} denotes the distance between the lens and the source. $\boldsymbol{\eta}$ is the position vector of the source in the source plane and $\boldsymbol{\xi}$ is the impact parameter in the lens plane. We assume that our lens can be characterized by its surface mass density $\Sigma(\boldsymbol{\xi})$. This is called 'thin lens approximation'. This is a valid approximation if the distances are much larger compared to the size of the lens, which is true for astrophysical lenses. For this configuration, the solution to the Eq. 4.18, i.e., the amplification factor is given by

$$F(f) = -i\frac{D_s}{D_l D_{ls}}\frac{\xi_0^2}{D_{ls}} f \int d^2\boldsymbol{x}\, \exp\left[2\pi i f t_d(\boldsymbol{x},\boldsymbol{y})\right] \tag{4.20}$$

where $\boldsymbol{x} = \boldsymbol{\xi}/\xi_0$ and $\boldsymbol{y} = \boldsymbol{\eta}/\xi_0$. ξ_0 is an arbitrary normalization constant with a dimension of length. t_d denotes the time taken by a

ray originating from the source to reach the observer (i.e., the arrival time). Note that $|F| = 1$, if $U = 0$, i.e., in the case of no lensing.

To take into account of the cosmological expansion, all we need to do is to use angular diameter distances and replace f by $f(1 + z_l)$, where the z_l is the lens redshift. That is,

$$F(f) = -i\frac{D_s\xi_0^2(1+z_l)}{D_l D_{ls}} f \int d^2\boldsymbol{x} \exp\left[2\pi i f t_d(\boldsymbol{x},\boldsymbol{y})\right] \tag{4.21}$$

but now D_s, D_l and D_{ls} represent the angular diameter distances.

The arrival time t_d at the observer from the source at $\boldsymbol{\eta}$ with an impact position $\boldsymbol{\xi}$ in the lens plane is given by

$$t_d(\boldsymbol{x},\boldsymbol{y}) = \frac{D_s\xi_0^2}{D_l D_{ls}}(1+z_l)\left[\frac{1}{2}|\boldsymbol{x}-\boldsymbol{y}|^2 - \psi(\boldsymbol{x}) + \phi_m(\boldsymbol{y})\right] \tag{4.22}$$

where $\psi(\boldsymbol{x})$ is called the deflection potential and is given by

$$\nabla_x^2\psi = 2\Sigma/\Sigma_{cr} \tag{4.23}$$

where ∇_x^2 denotes the two dimensional Laplacian with respect to $\boldsymbol{x}$ and $\Sigma_{cr} = D_s/4\pi D_l D_{ls}$ is called the critical surface mass density. Note that, by definition the deflection potential is dimensionless. We choose $\phi_m(\boldsymbol{y})$ such that the minimum value of the arrival time becomes zero. The dimensionless mass density Σ/Σ_{cr} is called the convergence and is denoted by κ.

4·4 *Geometric optics limit*

The geometric optics limit is approached when $f \gg t_d^{-1}$, i.e., $T_{GW} \ll t_d$ [10]. In this limit, only the stationary points of the $t_d(\boldsymbol{x},\boldsymbol{y})$ contribute to the integral of Eq. 4.21 [11], i.e., the image positions $\boldsymbol{x}_j$ are determined by

$$\partial t_d(\boldsymbol{x},\boldsymbol{y})/\partial\boldsymbol{x} = 0 \tag{4.24}$$

This gives what is called the lens equation,

$$\boldsymbol{y} = \boldsymbol{x} - \boldsymbol{\alpha}(\boldsymbol{x}) \tag{4.25}$$

[10] We will later see that t_d is actually proportional to the redshifted mass of the lens.

[11] This is essentially the Fermat's principle.

where $\boldsymbol{\alpha}(\boldsymbol{x}) = \nabla\psi(\boldsymbol{x})$ is called the deflection angle. The integral of the Eq. 4.21 is then given by the sum over these images $\boldsymbol{x}_j$,

$$F(f) = \sum_j |\mu_j|^{1/2} \exp[2\pi i f t_{d,j} - i\pi n_j] \tag{4.26}$$

where $\mu_j = 1/\det(\partial\boldsymbol{y}/\partial\boldsymbol{x}_j)$ is the magnification of the j-th image, $t_{d,j} = t_d(\boldsymbol{x}_j, \boldsymbol{y})$ and $n_j = 0, 1/2, 1$ when x_j is a minimum, saddle, maximum point of $t_d(\boldsymbol{x}, \boldsymbol{y})$.

4·5 *Point Mass Lens*

The surface mass density for a point mass lens is described by $\Sigma(\boldsymbol{\xi}) = M_L\delta^2(\boldsymbol{\xi})$, where M_L is the mass of the lens. We choose the normalisation constant as $\xi_0 = \sqrt{4M_L D_l D_{ls}/D_s}$. The deflection potential for this system (Eq. 4.23) is $\psi(\boldsymbol{x}) = \ln x$, where $x = |\boldsymbol{x}|$. In this case, it is possible to find an analytical expression of the Eq. 4.21. This is,

$$F(f) = \exp\left[\frac{\pi\omega}{4} + i\frac{\omega}{2}\left(\ln\left(\frac{\omega}{2}\right) - 2\phi_m(y)\right)\right]\Gamma\left(1 - \frac{i}{2}\omega\right)\,{}_1F_1\left(\frac{i}{2}\omega, 1; \frac{i}{2}\omega y^2\right) \tag{4.27}$$

where $w = 8\pi M_{Lz} f$, $\phi_m(y) = (x_m - y)^2/2 - \ln x_m$ with $x_m = (y + \sqrt{y^2+4})/2$, $M_{Lz} = M_L(1+z_l)$ is the redshifted mass of the lens and ${}_1F_1$ is the confluent hypergeometric function. We can see that the amplification factor depends on just two lens parameters; the redshifted mass of the lens M_L and the source position y. In geometric optics limit, i.e., $T_{GW} \ll t_d$ or $f \gg M_{Lz}^{-1}$, Eq. 4.27 reduces to,

$$F(f) = |\mu_+|^{1/2} - i|\mu_-|^{1/2}\, e^{2\pi i f \Delta t_d} \tag{4.28}$$

where $\mu_\pm$ represent the magnifications of the images, $\mu_\pm = 1/2 \pm (y^2+2)/(2y\sqrt{y^2+4})$ and the time delay between the double images is, $\Delta t_d = 4M_{Lz}\left[y\sqrt{y^2+4}/2 + \ln\left((\sqrt{y^2+4}+4)/(\sqrt{y^2+4}-y)\right)\right]$. The typical time delay expected is $\Delta t_d \sim 4M_{Lz} = 2\times10^3 \text{ sec } M_{Lz}/(10^8 M_\odot)$. For galaxy lenses with the mass between $10^7 M_\odot - 10^{12} M_\odot$, we thus expect the typical time delay to vary from a few minutes to a few months.

4.6 Singular Isothermal Sphere Lens Model

This is most widely used model for the astrophysical lenses, e.g., galaxy lenses. If we consider the galaxies as the self-gravitating spherically symmetric concentration of stars which behave like an ideal gas in thermal and hydrostatic equilibrium, then a density profile satisfying this condition is

$$\rho(r) = \frac{\sigma_v^2}{2\pi r^2} \tag{4.29}$$

where σ_v is the velocity dispersion of the "gas" particles and r is the distance from the center of the sphere. The surface mass density is found by projecting $\rho(r)$ along the line of sight

$$\begin{aligned} \Sigma(\boldsymbol{\xi}) &= 2\frac{\sigma_v^2}{2\pi}\int_0^\infty \frac{dz}{\xi^2 + z^2} \\ &= \frac{\sigma_v^2}{2\xi} \end{aligned} \tag{4.30}$$

We see that the surface density diverges at the center. This is the reason they are called singular isothermal [12] sphere (SIS) lens. Nevertheless, this model has been used to describe the matter distribution in galaxies, especially because it can reproduce the flat rotation curves of spiral galaxies.

[12] Isothermal just means that the surface mass density asymptotically decreases as 1/distance.

Let us choose $\xi_0 = 4\pi\sigma_v^2 D_l D_{ls}/D_s$ as a length scale on th lens plane. The deflection potential for such a surface density is given by, $\psi(\boldsymbol{x}) = x$. In this case, there is no analytical expression for the Eq. 4.21. In the geometric optics limit, however, the lens equation, Eq. 4.25, reduces to a 1-d equation (due to the spherical symmetry of the lens mass distribution),

$$y = x - \frac{x}{|x|} \tag{4.31}$$

For $y < 1$, this has two solutions: at $x = y + 1$ and $x = y - 1$, on opposite sides of the centre of the lens. We can express these solutions in terms of the angular variables by dividing with the corresponding

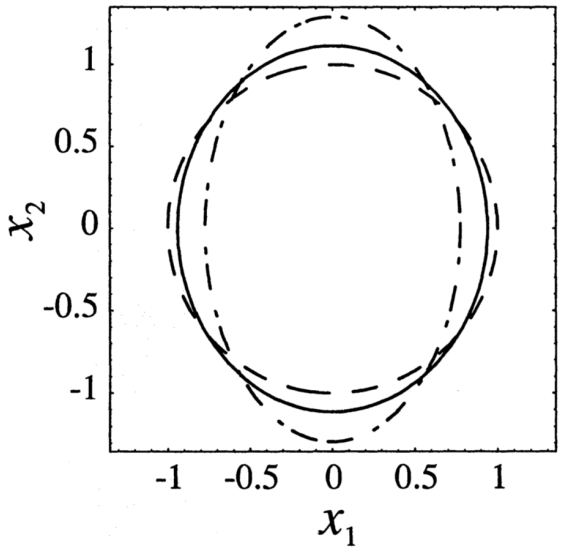

Figure 4.2: Iso-density contours for the SIS (dashed) and the SIE (dash-dotted) with $f = 0.6$ for the same value of κ in both cases. The solid line represents the contour of the deflection potential ψ. We see that the contour of ψ looks much rounder than corresponding iso-density contour. [Astron. Astrophys. 284, 285-299 (1994)]

angular diameter distances. We find,

$$\theta_{\pm} = \beta \pm \theta_E \tag{4.32}$$

where β is the angular position of the source in the source plane and θ_E is called the Einstein radius, defined as,

$$\theta_E = \sqrt{4M_L(\theta_E)\frac{D_{ls}}{D_l D_s}} \tag{4.33}$$

where $M_L(\theta_E)$ is the mass within the Einstein radius. We see that the angular separation between the images is $\Delta\theta = 2\theta_E$. Thus the Einstein radius defines a typical scale for the angular separation between the images. The time delay between the images is $\Delta t_d = 8M_{Lz}(\theta_E)y$.

The magnifications of these images are

$$\mu_+ = 1 + \frac{1}{y} \quad ; \quad \mu_- = 1 - \frac{1}{y} \tag{4.34}$$

For $y \to 1$, the magnification of the second image becomes weaker and weaker until it disappears at $y = 1$. This is in agreement with the fact that for $y > 1$, we have only one image.

4.7 Singular Isothermal Elliptical Lens Model

A more realistic lens model for the galaxies is given by singular isothermal ellipsoid (SIE), i.e., the surface mass density is described by

$$\Sigma(\boldsymbol{\xi}) = \sqrt{q}\,\frac{\sigma_v^2}{2\zeta} \tag{4.35}$$

where $\zeta := \sqrt{\xi_1^2 + q^2\xi_2^2}$ and q is called the axis ratio (or ellipticity). Note that $q = 1$ reproduces the spherical mass surface density with ζ becoming the actual radial coordinate ξ. The $\sqrt{q}$ factor makes sure that the mass inside an elliptical iso-density contour (see, Fig. 4.2) for a given value of density (Σ) is independent of q.

We choose the length scale ξ_0 same as the SIS model. The dimensionless surface density in polar coordinates is

$$\kappa(x, \varphi) = \frac{\sqrt{q}}{2x\Delta(\varphi)} \tag{4.36}$$

where $\Delta(\varphi) = \sqrt{\cos^2\varphi + q^2\sin^2\varphi}$, since $\xi_1 = x\cos\varphi$ and $\xi_2 = x\sin\varphi$. The lens equation takes the form

$$\boldsymbol{y} = \boldsymbol{x} - \frac{\sqrt{q}}{q'}\left[\operatorname{arcsinh}\left(\frac{q'}{q}\cos\varphi\right)\boldsymbol{e}_1 + \arcsin(q'\sin\varphi)\boldsymbol{e}_2\right] \tag{4.37}$$

where $q' := \sqrt{1-q^2}$ and $\boldsymbol{e}_i$ is the unit vector in the direction of x_i.

The magnification is found from the Jacobian $A = \partial\boldsymbol{y}/\partial\boldsymbol{x}$, also called the distortion matrix. The trace free part of this matrix is antisymmetric and called a shear matrix. The eigenvalues of the shear matrix represent the amount of the shear produced in the images. While the trace of the distortion matrix, which is $2(1-\kappa)$, produces isotropic changes in the images, i.e., the images are only rescaled by a constant factor in all directions. The Jacobian is found to be,

$$A = \begin{bmatrix} 1 - 2\kappa\sin^2\varphi & \kappa\sin(2\varphi) \\ \kappa\sin(2\varphi) & 1 - 2\kappa\cos^2\varphi \end{bmatrix} \tag{4.38}$$

The magnification is defined as, $\mu = 1/\det(A) = 1/(1-2\kappa(x))$. We

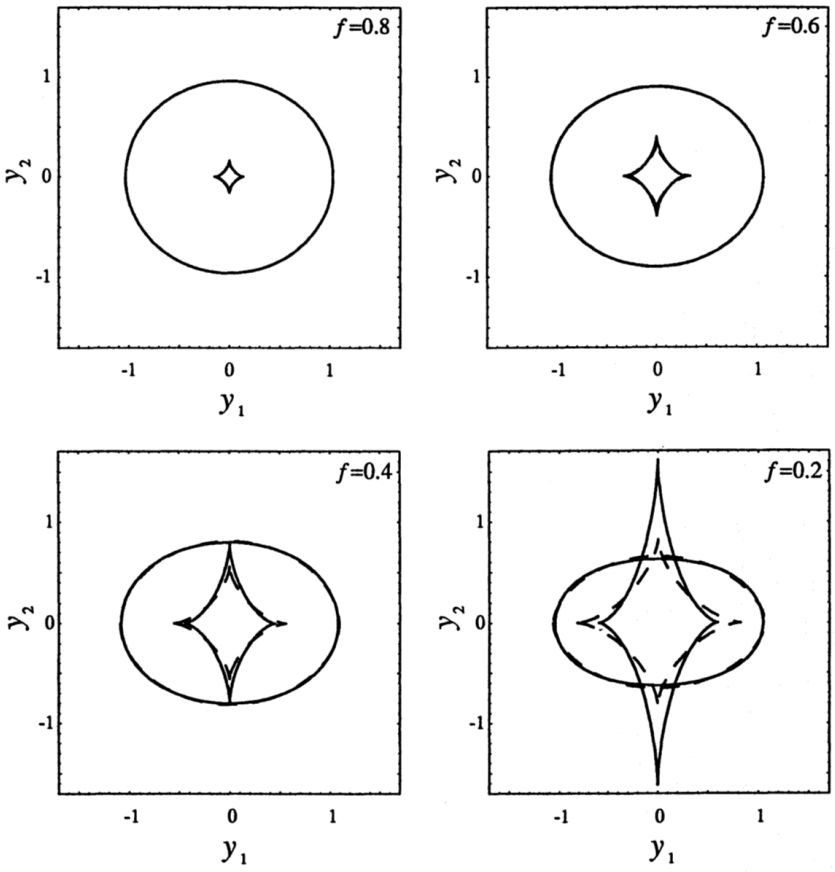

Figure 4.3: Cut and caustics of the SIE for different values of the axis ratio. The curves with the cusps are the caustics. The high axis ratio means that we are closer to the case of the SIS. In SIS, the caustic degenerates to a point (top left plot). The dashed lines have to be ignored here. [Astron. Astrophys. 284, 285-299 (1994)]

see that the magnification of an image just depends on the value of dimensionless mass density at its position in the lens plane.

One interesting aspect would be to ask about the set of points in the source plane that will be associated with the multiple images. It turns out that these points lie within the curves known as caustics, i.e., the points outside the caustics have only one image. We discuss this here in detail.

Critical curves are the curves on the lens plane that separate the multiple images. This is given by the condition, $\det(A) = 0$, i.e., a critical curve is the locus of the points on the lens plane with infinite magnifications. The images inside the critical curves have negative magnifications while those lying outside have positive magnifications. The mapping of the critical curves to the source plane through the lens equation gives the caustic curves. For our case (i.e.,

SIE),

$$\det(A) = 0 \Rightarrow \kappa = \frac{1}{2}, \quad \text{or,} \quad x = \frac{\sqrt{q}}{\Delta(\varphi)} \tag{4.39}$$

Inserting this in the lens equation, Eq. 4.37, gives us the parametrised equation for the caustics,

$$\begin{aligned} y_1 &= \frac{\sqrt{q}}{\Delta}\cos\varphi - \frac{\sqrt{q}}{q'}\text{arcsinh}\Big(\frac{q'}{q}\cos\varphi\Big) \\ y_2 &= \frac{\sqrt{q}}{\Delta}\sin\varphi - \frac{\sqrt{q}}{q'}\arcsin\Big(q'\sin\varphi\Big) \end{aligned} \tag{4.40}$$

There is an another important curve known as *cut*, which is the locus of the points on the source plane with one and only one image, at the center of the lens. This image is "infinitely faint" because the convergence is infinite at the center and since, $\mu = 1/(1-2\kappa)$. Thus we can get this curve by setting $x = 0$,

$$\begin{aligned} \boldsymbol{y}(\varphi) &= \lim_{x\to 0}\boldsymbol{y}(x,\varphi) = -\boldsymbol{\alpha}(\varphi) \\ &= -\frac{\sqrt{q}}{q'}\Big[\text{arcsinh}\Big(\frac{q'}{q}\cos\varphi\Big)\boldsymbol{e}_1 + \arcsin(q'\sin\varphi)\boldsymbol{e}_2\Big] \end{aligned} \tag{4.41}$$

The existence of the cut is due to the singular nature of the surface density. If we make the core of the lens smooth by putting some matter, i.e., if we introduce a finite core radius, then the cut will transform into a caustic and consequently, the image at the centre of the lens splits into a pair of images separated by the corresponding critical curve. Fig. 4.3 shows the cuts and caustics of the SIE for different values of the axis ratio. The positions of the cusps are computed from the intersections of the caustics with the axes,

$$\begin{aligned} y_1 &= \pm(s_1 - \sqrt{q}) \quad \text{with} \quad s_1 = \frac{\sqrt{q}}{q'}\,\text{arccosh}\,\frac{1}{q} \\ y_2 &= \mp\Big(s_2 - \frac{1}{\sqrt{q}}\Big) \quad \text{with} \quad s_2 = \frac{\sqrt{q}}{q'}\arccos q \end{aligned} \tag{4.42}$$

Similarly, for the cut, we find

$$y_1 = \pm s_1 \qquad \text{and} \qquad y_2 = \pm s_2 \tag{4.43}$$

From the Fig. 4.3, we see that the cusps on y_2 axis can be inside and

outside the region surrounded by the cut. We find that the cusps are inside if $q > q_0$, where q_0 is the solution to the transcendental equation, $2q_0 \arccos q_0 = \sqrt{1-q_0^2}$. The numerical solution gives $q_0 = 0.3942\cdots$.

Finally we would like to solve the lens equation, Eq. 4.37, so that we can find the positions of the images in the lens plane for a given source position. However, it seems almost impossible to invert this equation. Nevertheless, we can reduce this to a one-dimensional equation as follows: the two components of the lens equation are

$$\begin{aligned} y_1 &= x\cos\varphi - \frac{\sqrt{q}}{q'}\operatorname{arcsinh}\left(\frac{q'}{q}\cos\varphi\right) \\ y_2 &= x\sin\varphi - \frac{\sqrt{q}}{q'}\arcsin(q'\sin\varphi) \end{aligned} \tag{4.44}$$

where we have used usual polar coordinates for $x_1 = x\cos\varphi$ and $x_2 = x\sin\varphi$. Now, if we multiply the first component of the above equation by $\cos\varphi$ and the second component by the $\sin\varphi$, we find that,

$$\begin{aligned} x = y_1\cos\varphi + y_2\sin\varphi + \frac{\sqrt{q}}{q'}\Big[\sin\varphi\arcsin(q'\sin\varphi) + \\ \cos\varphi\operatorname{arcsinh}\Big(\frac{q'}{q}\cos\varphi\Big)\Big] \end{aligned} \tag{4.45}$$

If we insert x back in the lens equation (Eq. 4.37), we find a one-dimensional equation for φ,

$$\Big[y_1 + \frac{\sqrt{q}}{q'}\operatorname{arcsinh}\Big(\frac{q'}{q}\cos\varphi\Big)\Big]\sin\varphi - \Big[y_2 + \frac{\sqrt{q}}{q'}\arcsin(q'\sin\varphi)\Big]\cos\varphi = 0 \tag{4.46}$$

This can now be solved numerically. Eq. 4.45 and Eq. 4.46 together provide the positions of the images for a given source position. The time delay between the images can be computed by finding the difference between their arrival times t_d using the Eq. 4.22.

The numerical solution to the Eq. 4.46 provides the following information: a source outside the cut [13] has only one image with small positive magnification and lies outside the corresponding crit-

[13] Just for the sake of example; we are dealing with the case where the source crosses the cut first and then the caustic. This will be true when $q \geq q_0$.

ical curve. As soon as it crosses the cut, a second image appears inside the critical curve and has very small negative magnification. This is because the second image forms near the center of the lens where the convergence (κ) is very high. When it crosses the caustic, two new images are formed which of course have to be separated by the associated critical curve [14], i.e., one of them lies within the critical curve having negative magnification and other lies outside the critical curve having positive magnification. We find that we always have an even number of the images. This is a property of lenses with singular surface mass densities.

[14] Note that, cut and caustic both have critical curves.

A source close to, but inside the caustic has two images close to. This fact is universal in the nature, i.e., irrespective of the lens system, if the caustic exists then a source close to the caustic will always have two images close to each other [15]. Furthermore, these images have very high and similar magnifications. The calculation shows that the magnification is given by

[15] Note, however, that this is not true near the cusps of the caustics.

$$|\mu| = \frac{4\sqrt{q}\Delta}{q'^2|\sin(2\varphi)|}\frac{1}{\delta x} \tag{4.47}$$

and the time delay between them is given by

$$c\delta t_d = 2\pi^2(1+z_l)\frac{\sigma_v^4}{c^4}\frac{D_l D_{ls}}{D_s}\frac{q'^2|\sin(2\varphi)|}{\sqrt{q}\Delta}(\delta x)^3 \tag{4.48}$$

where δx is the separation between the images in the dimensionless units. If we take typical values of the parameter appearing in these equations, e.g., $\sigma_v = 220\,\mathrm{km/s}$, $z_l = 0.5$ and $z_s = 2$ in an Einstein-de Sitter universe with Hubble constant $H_0 = 100h\,\mathrm{km/(s\,Mpc)}$ with the axis ratio $f = 0.8$ at $\varphi = \pi/4$, we find the approximate relations as

$$|\mu| \simeq \frac{7''.2}{\delta\theta} \tag{4.49}$$

and,

$$\delta t_d \simeq \frac{15}{h}\left(\frac{\delta\theta}{0''.8}\right)^3 \text{ hours} \tag{4.50}$$

where $\delta\theta$ is the angular separation between the images. For $h =$

0.5, two images with magnification $|\mu| = 20$ would have roughly an angular separation of $0''.36$ and the time delay δt_d of roughly three hours.

5 Identifying Strongly Lensed gravitational Wave Signals From Binary Black Hole Mergers

Arthur Eddington's 1919 observation of the gravitational bending of light was the first observational test that heralded the remarkable success of general relativity (GR) [71]. Recent observations of gravitational waves (GWs) by LIGO [8] and Virgo [25] have vindicated one of the most famous astrophysical predictions of GR [11, 12, 14, 15, 16, 17]. While gravitational lensing (of electromagnetic waves) has been well established as a powerful astronomical tool (see, e.g., [35] for a review), GW observations are opening up an emerging branch of observational astronomy (see, e.g., [118] for a review).

GWs are gravitationally lensed by intervening mass concentrations along the line of sight from the source to the observer, in a manner similar to electromagnetic waves. Several previous papers in the literature have considered the resulting phenomenology for GWs from a variety of compact object mergers [148, 131, 130, 121, 119, 120, 114, 42, 60, 68]. Recent estimates of the lensing rates have shown that at upgraded sensitivities of Advanced LIGO, a small fraction ($< 1\%$) of the detected GW signals from stellar–mass binary black hole mergers can be strongly lensed by intervening galaxies and clusters (see, e.g., [109]). These mergers would produce multiple "images" at different times, with significantly different intrinsic masses and redshifts [61, 109, 127, 97]. It has even been sug-

gested that a significant fraction of the detected merger population was strongly lensed [47], which would require a strong redshift evolution of the intrinsic merger rate. In the standard case, the lensed fraction is expected to be small, but LIGO and Virgo are expected to detect hundreds of binary black hole mergers over the next few years [9]; thus it is quite likely that some of the detected signals will be strongly lensed. Identification of strongly lensed GW signals would be rewarding. On the one hand, we will be verifying a fundamental prediction of GR using a messenger entirely different from electromagnetic radiation [98, 72]. In addition, such a detection can potentially enable astrophysical studies of the lens galaxy and the host galaxy [125].

In this chapter, we consider the problem of observationally identifying a pair of lensed signals coming from a single merger among hundreds of unrelated merger signals. From the perspective of the observer, these lensed images would appear as different GW signals that are separated by time delays of minutes to weeks. The observed gravitational waveform depends on the zenith angle and the azimuth of the merger relative to the detectors, which will be different for each image. Moreover, each image will be observed against a different realization of the detector noise. This makes it difficult to compare multiple images at the waveform level, and necessitates a comparison in the space of the estimated intrinsic parameters.

We work in the geometric optics limit, which applies when the wavelength of the GW signal is small compared to the Schwarzschild radius of the lens mass ($\lambda_{\rm GW} \ll 2GM_{\rm lens}/c^2$). This approximation can fail to model the lensing of GW signals from supermassive black holes lensed by intervening supermassive black holes or dark matter halos with masses $\sim 10^8 M_\odot$ (which leads to interesting wave effects that could be observed by LISA [131, 130]), or of GW signals from stellar mass black holes lensed by intermediate mass black holes or compact halo objects with masses $\sim 10^3 M_\odot$ (which can lead to interesting wave effects observable by LIGO [95, 88]). However, the

geometric optics approximation is adequate to model the GW signals from stellar–mass black holes observed in LIGO/Virgo that are lensed by galaxies. In this regime, lensing will magnify/de-magnify the GW signal without affecting its shape. Since the parameters of the merging binary are estimated by comparing the data with theoretical templates of the expected signals (see, e.g, [10]), the estimated parameters (barring the estimated luminosity distance, which is degenerate with the magnification and hence will be biased) of these different signals will be mutually consistent.

We develop a Bayesian formalism for identifying strongly lensed and multiply imaged GW signals from binary black hole merger events among hundreds of unrelated merger signals. From each pair of GW signals, we compute the Bayesian odds ratio between two hypotheses: 1) that they are the lensed images of the same merger event, 2) that they are two unrelated events. Using simulated GW events (lensed as well as unlensed), we show that this odds ratio is a powerful discriminator that will allow us to identify strongly lensed signals. Our method can be easily integrated with the standard Bayesian parameter estimation pipelines that are used to analyze LIGO and Virgo data [146].

The material presented in this chapter is based on the articles [82] and [83].

5.1 *Bayesian model selection of strongly lensed GW signals from binary black hole mergers*

Consider a data stream $d(t)$ of a GW detector containing a signal $h(t, \boldsymbol{\theta})$ described by a set of parameters $\boldsymbol{\theta}$ and some stochastic noise $n(t)$:

$$d(t) = n(t) + h(t, \boldsymbol{\theta}). \tag{5.1}$$

For binary black holes in quasi-circular orbits, the GW signals $h(t, \boldsymbol{\theta})$ are described by a set of parameters $\boldsymbol{\theta}$ that consists of the redshifted masses $(m^z{}_1, m^z{}_2)$, the dimensionless spin vectors $(\boldsymbol{\chi}_1, \boldsymbol{\chi}_2)$, the time

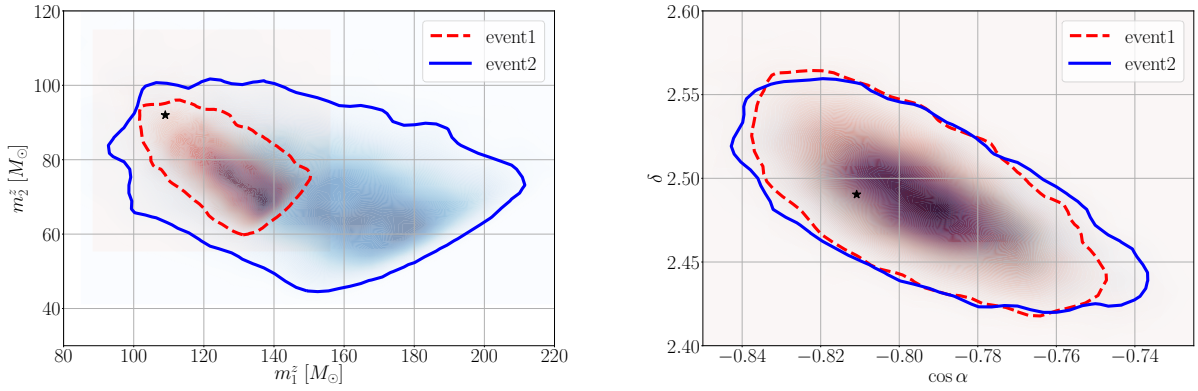

Figure 5.1: 95% credible regions of the marginalized posteriors of the redshifted masses m_1^z, m_2^z (left) and sky location $\cos\alpha, \delta$ (right) of lensed images of a sample binary black hole merger event. Black stars show the actual injected parameters.

of coalescence t_0 and the phase at coalescence φ_0, sky location (α, δ), the inclination ι of the binary, the polarization angle ψ and the luminosity distance d_L to the source. The posterior distribution of the set of parameters $\boldsymbol{\theta}$ can be computed from the data using the Bayes theorem as follows:

$$P(\boldsymbol{\theta}|d) = \frac{P(\boldsymbol{\theta})\, P(d|\boldsymbol{\theta})}{P(d)}, \tag{5.2}$$

where $P(\boldsymbol{\theta})$ denotes the prior distribution of $\boldsymbol{\theta}$, $P(d|\boldsymbol{\theta})$ is the likelihood of the data d assuming the signal $h(t, \boldsymbol{\theta})$ and

$$P(d) := \int d\boldsymbol{\theta}\, P(\boldsymbol{\theta})\, P(d|\boldsymbol{\theta}) \tag{5.3}$$

is called the marginalized likelihood. If $n(t)$ can be well approximated by a stationary Gaussian process with mean zero and a one-sided power spectral density $S_n(f)$, then the likelihood is given by

$$P(d|\boldsymbol{\theta}) = \mathcal{N}\ \exp\left\{-\frac{1}{2}\langle d-h \mid d-h\rangle\right\}, \tag{5.4}$$

where $\mathcal{N}$ is a normalization constant and $\langle .|. \rangle$ denotes the following noise-weighted inner product:

$$\langle a|b\rangle := 2\int_{f_{\text{low}}}^{f_{\text{upp}}} df\, \frac{\tilde{a}^*(f)\tilde{b}(f) + \tilde{a}(f)\tilde{b}^*(f)}{S_n(f)}. \tag{5.5}$$

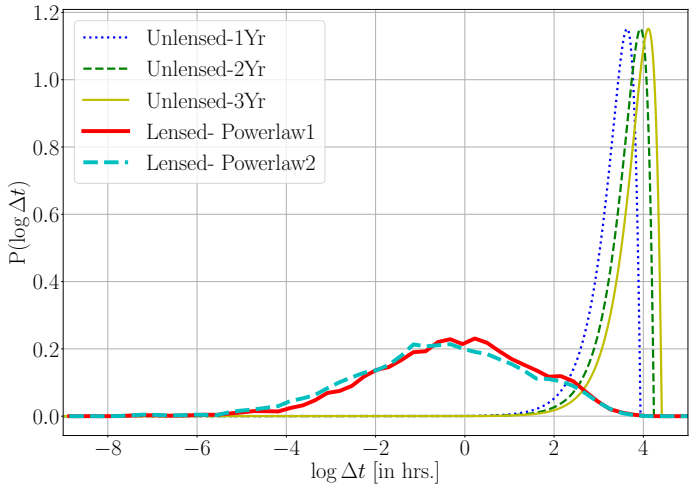

Figure 5.2: Distribution of the log of the time delay between lensed event pairs detected by the Advanced LIGO-Virgo network, along with the distribution from unlensed event pairs. The simulated binary black hole populations have their component masses (source-frame) distributed according to two power laws (see text); however, note that the time delays are practically insensitive to the specific form of the mass distribution. The redshifts of the mergers are sampled with the distribution obtained in . We consider strong lensing produced by intervening galaxies. In order to compute the distribution of the time delay between *unlensed* events, we assume that they follow a Poisson distribution with a rate of 10 mergers per month. The time delay distributions of unlensed event pairs get skewed towards larger values as we increase the observation time.

Above, $f_{\rm low}$ and $f_{\rm upp}$ denote the lower and upper cutoff frequencies of the detector's bandwidth, $\tilde{a}(f)$ denotes the Fourier transform of $a(t)$ and a * denotes complex conjugation.

If we have two data streams d_1 and d_2 containing GW signals from binary black holes, there is a small probability that these signals are lensed versions of a single merger event. In the geometric optics approximation, lensing does not affect the frequency profile of the signal. As a result, the lensed signals would correspond to the same set of parameters $\boldsymbol{\theta}$ (except the estimated luminosity distance, which will be biased due to the unknown magnification). In order to determine whether d_1 and d_2 contain lensed signals from the same binary black hole merger, we compute the *odds* ratio between two hypotheses:

- $\mathcal{H}_{\rm l}$: The data set $\{d_1, d_2\}$ contain lensed signals from a single binary black hole merger event with parameters $\boldsymbol{\theta}_1 = \boldsymbol{\theta}_2 = \boldsymbol{\theta}$.

- $\mathcal{H}_{\rm u}$: The data set $\{d_1, d_2\}$ contain signals from two independent binary black hole merger events with parameters $\boldsymbol{\theta}_1$ and $\boldsymbol{\theta}_2$.

The odds ratio between $\mathcal{H}_{\rm l}$ and $\mathcal{H}_{\rm u}$ is the ratio of the posterior prob-

abilities of the two hypotheses. That is,

$$\mathcal{O}^{\mathrm{l}}_{\mathrm{u}} = \frac{P(\mathcal{H}_{\mathrm{l}}|\{d_1, d_2\})}{P(\mathcal{H}_{\mathrm{u}}|\{d_1, d_2\})} \,, \tag{5.6}$$

Using Bayes theorem we can rewrite the odds ratio as

$$\mathcal{O}^{\mathrm{l}}_{\mathrm{u}} = \frac{P(\mathcal{H}_{\mathrm{l}})}{P(\mathcal{H}_{\mathrm{u}})} \, \frac{P(\{d_1, d_2\}|\mathcal{H}_{\mathrm{l}})}{P(\{d_1, d_2\}|\mathcal{H}_{\mathrm{u}})} = \mathcal{P}^{\mathrm{l}}_{\mathrm{u}} \, \mathcal{B}^{\mathrm{l}}_{\mathrm{u}} \tag{5.7}$$

Here $\mathcal{P}^{\mathrm{l}}_{\mathrm{u}} := \frac{P(\mathcal{H}_{\mathrm{l}})}{P(\mathcal{H}_{\mathrm{u}})}$ is the ratio of prior odds of the two hypotheses while the Bayes factor $\mathcal{B}^{\mathrm{l}}_{\mathrm{u}} := \mathcal{Z}_{\mathrm{l}}/\mathcal{Z}_{\mathrm{u}}$ is the ratio of the marginalized likelihoods, where the marginal likelihood of the hypothesis A is $\mathcal{Z}_A := P(\{d_1, d_2\}|\mathcal{H}_A)$ with $A \in \{\mathrm{L}, \mathrm{U}\}$. Under the assumption of d_1 and d_2 being independent, the marginal likelihood of the "null" hypothesis equals the product of the marginal likelihoods from individual events, i.e.,

$$\mathcal{Z}_{\mathrm{u}} = P(d_1)\, P(d_2), \tag{5.8}$$

where $P(d_i)$ is the marginal likelihood from event i, defined in Eq. (5.3). Now, we rewrite the marginal likelihood of the lensing hypothesis in terms of the likelihoods of d_1 and d_2 as

$$\mathcal{Z}_{\mathrm{l}} = \int d\boldsymbol{\theta}\; P(\boldsymbol{\theta})\; P(d_1|\boldsymbol{\theta})\; P(d_2|\boldsymbol{\theta}) \,. \tag{5.9}$$

Using Eq. (5.2), we can rewrite this as

$$\mathcal{Z}_{\mathrm{l}} = P(d_1)\, P(d_2) \int d\boldsymbol{\theta}\; \frac{P(\boldsymbol{\theta}|d_1)\, P(\boldsymbol{\theta}|d_2)}{P(\boldsymbol{\theta})} \tag{5.10}$$

Combining Eqs. (5.8) and (5.10), we obtain the following expression for the Bayes factor:

$$\mathcal{B}^{\mathrm{l}}_{\mathrm{u}} := \frac{\mathcal{Z}_{\mathrm{l}}}{\mathcal{Z}_{\mathrm{u}}} = \int d\boldsymbol{\theta}\; \frac{P(\boldsymbol{\theta}|d_1)\; P(\boldsymbol{\theta}|d_2)}{P(\boldsymbol{\theta})} \,. \tag{5.11}$$

Thus, the Bayes factor is the inner product of the two posteriors that is inversely weighted by the prior. This has an intuitive explanation: if d_1 and d_2 correspond to lensed signals from a single binary black hole merger, the estimated posteriors on $\boldsymbol{\theta}$ would have a larger over-

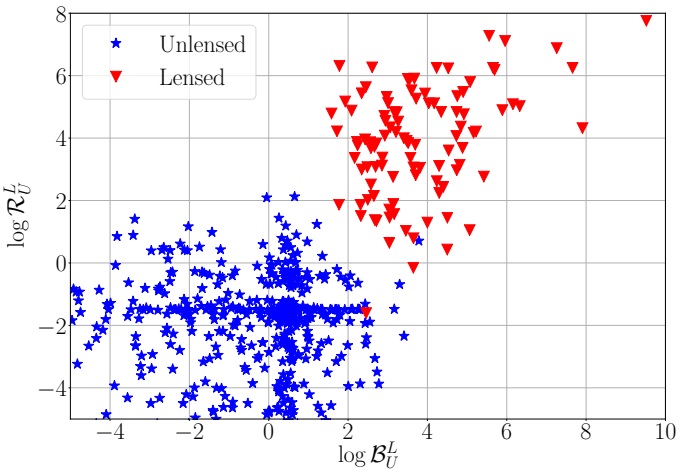

Figure 5.3: Scatter plot of the two Bayes factors $\mathcal{B}^{\rm l}_{\rm u}$ and $\mathcal{R}^{\rm l}_{\rm u}$ computed from the unlensed (blue stars) and lensed (red triangles) event pairs. The Bayes factors computed from the posterior distribution of the binary's parameters ($\mathcal{B}^{\rm l}_{\rm u}$) and that computed from the time delay distribution ($\mathcal{R}^{\rm l}_{\rm u}$) are in general correlated. However, they can be combined to improve our ability to distinguish lensed pairs from unlensed pairs. In this simulation, the component masses are distributed according to the second power law given in the text.

lap, favoring the lensing hypothesis (see, e.g., Fig. 5.1). The inverse weighting by the prior helps to down-weight the contribution to the inner product from regions in the parameter space that are strongly supported by the prior. The large overlap of the posteriors here is less likely to be due to the lensing but more likely due to the larger prior support to the individual posteriors.

While the odds ratio developed above checks for the consistency between the estimated parameters of two GW signals, the time delay between them can also be used to develop a potential discriminator between lensed and unlensed events. This however, would require certain assumptions on the distribution of lenses (i.e., galaxies) and the rate of binary mergers. If we assume that binary merger events follow a Poisson process with a rate of n events per month, one can compute the prior distribution $P(\Delta t|\mathcal{H}_{\rm u})$ of time delay between pairs of unlensed events (see Fig. 5.2). The prior distribution of the time delay between strongly lensed signals, $P(\Delta t|\mathcal{H}_{\rm l})$, would have a qualitatively different distribution, which can be computed using a reasonable distribution of the galaxies and a model of the compact binary mergers (see Sec. 5.2 for details). Following Eq.(5.3), the marginal likelihood for the lensed/unlensed hypothesis can be

computed from the time delay between two events d_1 and d_2 as

$$P_{\Delta t}(\{d_1, d_2\}|\mathcal{H}_A) = \int d\Delta t \, P(\Delta t|\mathcal{H}_A) \, P(\{d_1, d_2\}|\Delta t, \mathcal{H}_A), \quad (5.12)$$

where $A \in \{\text{L}, \text{U}\}$. Typical statistical errors in estimating the time of arrival of a GW signal at a detector are of the order of milliseconds — much smaller than the typical time delay between any pair of events. Thus, the likelihood function $P_{\Delta t}(\{d_1, d_2\}|\Delta t, \mathcal{H}_A)$ of the time delay can be well approximated by a Dirac delta function at the true value Δt_0. Thus, the Bayes factor between the lensed and unlensed hypotheses can be written as

$$\mathcal{R}^{\text{l}}_{\text{u}} = \frac{P(\Delta t_0|\mathcal{H}_{\text{l}})}{P(\Delta t_0|\mathcal{H}_{\text{u}})} \,, \quad (5.13)$$

where $P(\Delta t_0|\mathcal{H}_A)$ with $A \in \{\text{L}, \text{U}\}$ is the prior distribution of Δt (under lensed or unlensed hypothesis) evaluated at $\Delta t = \Delta t_0$. The prior distributions are shown in Fig. 5.2.

The Bayes factors $\mathcal{B}^{\text{l}}_{\text{u}}$ and $\mathcal{R}^{\text{l}}_{\text{u}}$ could be combined to improve the discriminatory power between lensed and unlensed events. Figure 5.3 shows a scatter plot of $\mathcal{B}^{\text{l}}_{\text{u}}$ and $\mathcal{R}^{\text{l}}_{\text{u}}$ computed from simulated pairs of lensed and unlensed events. As one can see, combining $\mathcal{B}^{\text{l}}_{\text{u}}$ and $\mathcal{R}^{\text{l}}_{\text{u}}$ improves the discriminatory power. Note that, since the fraction of binary black hole mergers that are expected to produce strongly lensed signals is very small, the ratio of prior odds $\mathcal{P}^{\text{l}}_{\text{u}}$ is a small number ($< 1\%$). Hence, we need large values for the Bayes factors to confidently identify strongly lensed pairs of signals.

5.2 *Testing the model selection*

In this section we test the efficacy of our Bayesian model selection method to identify strongly lensed GW signals from binary black hole merger events. We simulate a population of coalescing binary black holes and compute the effect of strong lensing on the GW signals that they radiate. The binary black hole mergers are distributed

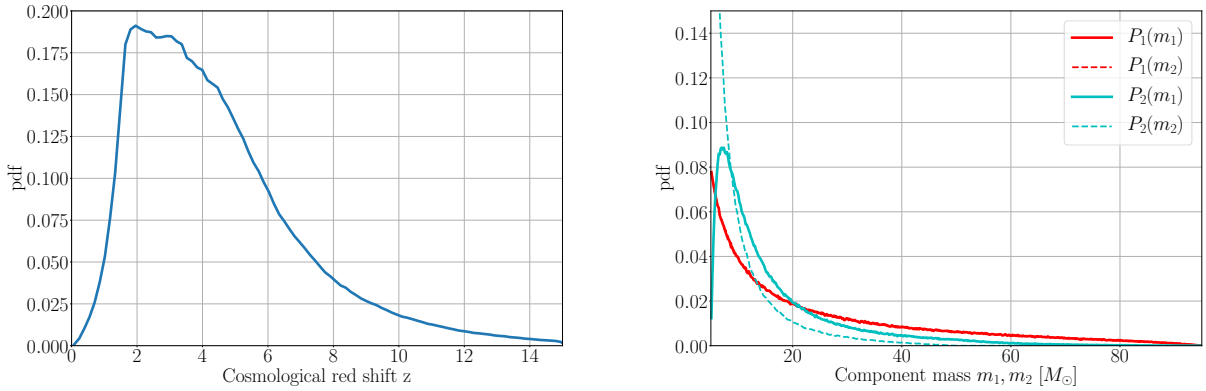

Figure 5.4: Probability distributions of the cosmological redshift (left) and component masses m_1, m_2 in the source frame (right) of the simulated binary black hole merger events.

according to the cosmological redshift distribution given in [69]. We use two different mass distributions proposed in [9] to sample component black hole masses m_1 and m_2:

1. Masses following a power-law $P_1(m_1, m_2) \sim \frac{1}{m_1}\frac{1}{m_2}$ with $m_1, m_2 \geq 5M_\odot$ and $m_1 + m_2 \leq 100M_\odot$.

2. Masses following a power-law $P_2(m_1) = m_1^{-2.35}$ on the mass of the larger black hole, with the smaller mass distributed uniformly in mass ratio m_1/m_2 and with $5M_\odot \leq m_1 + m_2 \leq 100M_\odot$.

Figure 5.4 shows the redshift and mass distributions of the injections. The spin magnitudes $\chi_1 := ||\chi_i||$ of component black holes are distributed uniformly between 0. and 0.99, with random directions with respect to the orbital angular momentum. The binaries are distributed uniformly in the sky (i.e., uniform in $\cos\alpha$ and δ), and the inclination and polarization angles are sampled uniformly from polarization sphere (i.e., uniform in $\cos\iota$ and ψ). Note that the GW signals will be redshifted due to the cosmological redshift, and we infer the redshifted masses $m^z_{1,2} := m_{1,2}(1+z)$ through parameter estimation.

Multiple images dominantly arise due to galaxy lenses [76]. We assume that the galaxy lenses are well modeled by singular isothermal ellipses [76, 92]. The lens parameters, namely velocity dispersion σ and axis-ratio q, are sampled from distributions modeled from the

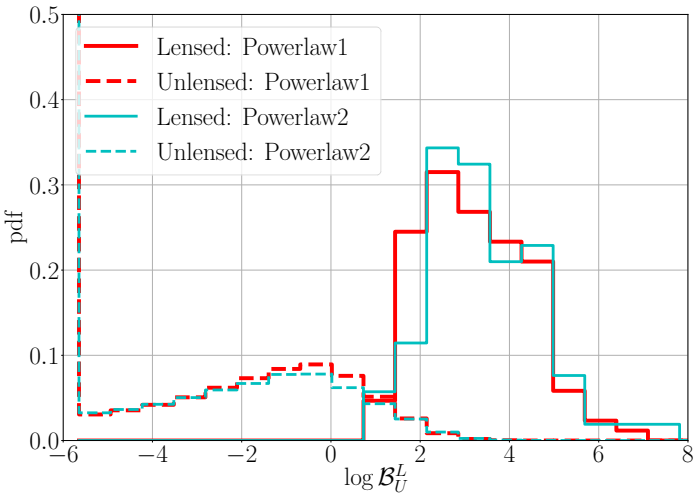

Figure 5.5: Distribution of the $\log_{10}$ Bayes factor $\mathcal{B}^{\mathrm{l}}_{\mathrm{u}}$ computed from the *unlensed* and *lensed* simulations with component masses sampled from power law 1 and power law 2. The Bayes factors are computed using the marginalized posteriors on parameter set $(m^z{}_1, m^z{}_2, \cos\alpha, \delta, \chi_1, \chi_2)$. It can be seen that the distributions are not strongly dependent on the specific mass distribution chosen.

SDSS population of galaxies [58]. A detailed account on the lensing probability, sampling of lens galaxies and computation of the magnification factor and time delays is provided in Appendix A.6. We simulate two populations of GW signals:

- *Lensed:* Pairs of events with same parameters $\boldsymbol{\theta}$, with parameter distributions as described above. We apply the lensing magnifications and time delays according to the prescription given in Appendix A.6.
- *Unlensed:* Pairs of events with random parameters $\boldsymbol{\theta}_1$ and $\boldsymbol{\theta}_2$, with parameter distributions as described above.

Figure 5.2 shows the distribution of time delays between pairs of lensed events as well as pairs of unlensed events from simulations assuming different distributions of source parameters. In the case of unlensed events, we compute the distribution of time delay assuming that the events follow a Poisson process with a rate of $n = 10$ events per month. Naturally the distribution of time delays between event pairs will depend only on the total observation time. The figure shows the time delay distributions from all pairs of events assuming observational runs of 1, 2 and 3 year duration.

To simulate GW observation coming from each population, we in-

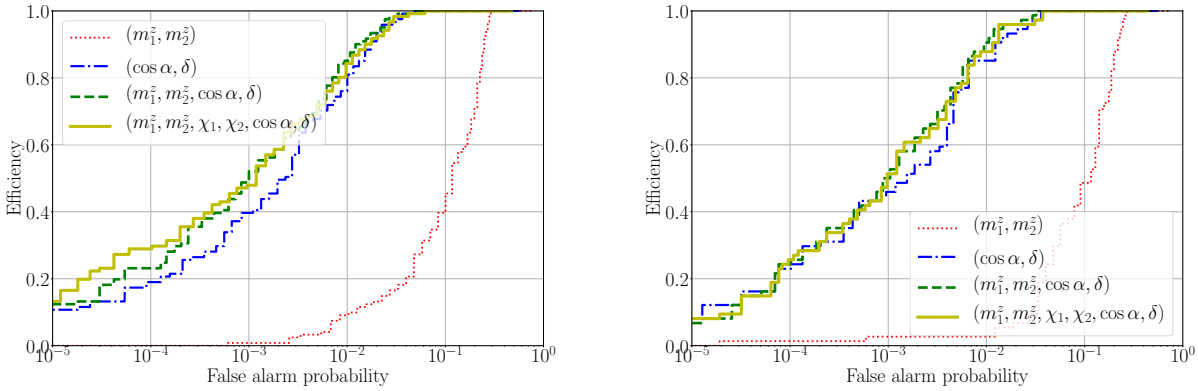

Figure 5.6: Receiver operating characteristic curves for the Bayes factor statistic $\mathcal{B}^{\rm l}_{\rm u}$ computed using the marginalized posteriors on parameter sets $(m^z{}_1, mz_2)$, $(\cos\alpha, \delta)$, $(m^z{}_1, m^z{}_2, \cos\alpha, \delta)$ and $(m^z{}_1, m^z{}_2, \chi_1, \chi_2 \cos\alpha, \delta)$ respectively with component masses sampled from power law 1 (left panel) and power law 2 (right panel). We observe that the performance of the statistic improves with with number of parameters. $\mathcal{B}^{\rm l}_{\rm u}$ computed with $(m^z{}_1, m^z{}_2, \chi_1, \chi_2 \cos\alpha, \delta)$ posteriors identifies $\sim 10-15\%$ of the lensed event pairs with a false alarm probability of 10^{-5}.

ject simulated GW signals from binary black holes in colored Gaussian noise with the design power spectrum of the three-detector Advanced LIGO-Virgo network [7, 6, 136]. The signals are modelled by the IMRPhenomPv2 waveform family [81, 84, 90] which describes GW signals from the inspiral, merger and ringdown of binary black holes with precessing spins in quasi-circular orbits [1].

From simulated events that cross a network signal-to-noise ratio (SNR) threshold of 8, we estimate the posterior distributions of the parameters using the LALInferenceNest code [146]. This code provides an implementation of the Nested Sampling algorithm [124] in the LALInference software package of the LIGO Algorithm Library LALSuite [2]. From each population of injections (lensed and unlensed), we draw random pairs from the simulated events and compute the Bayes factor $\mathcal{B}^{\rm l}_{\rm u}$ defined Eq. (5.11) by multiplying the kernel density estimates of the two posterior distributions and integrating them. Also we compute $\mathcal{R}^{\rm l}_{\rm u}$ using the time delay estimates between the event pairs. Figure 5.3 shows a scatter plot of the two Bayes factors $\mathcal{B}^{\rm l}_{\rm u}$ and $\mathcal{R}^{\rm l}_{\rm u}$ estimated from one set of simulated lensed and unlensed events.

Figure 5.5 shows the distributions of $\log \mathcal{B}^{\rm l}_{\rm u}$ for lensed and unlensed event pairs computed from the posteriors of $\{m^z_1, m^z_2, \cos\alpha, \delta, \chi_1, \chi_2\}$. Indeed, there is a small probability that two independent event pairs could have parameters that appear mutually consistent (accidentally)

[1] Note that, in this waveform, the spin effects modeled in terms of two effective spin parameters [81, 27].

[2] https://wiki.ligo.org/DASWG/LALSuite

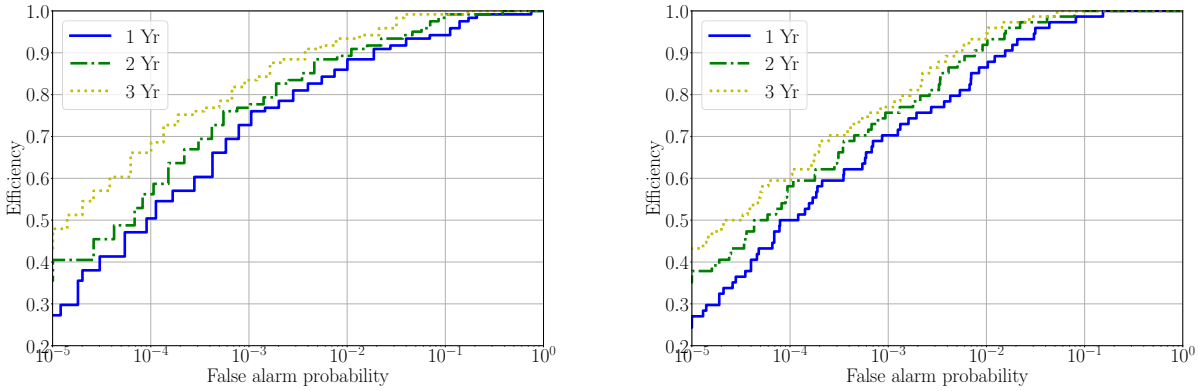

Figure 5.7: Receiver operating characteristic curves for the $\mathcal{R}^{l}_{u}$ statistic computed assuming a rate of 10 unlensed events per month and component masses sampled from power law 1 (left panel) and power law 2 (right panel). Three curves in each panel represent the ROC plots for $\mathcal{R}^{l}_{u}$ computed assuming 1, 2 and 3 years as the observation time.

and produce a large value for $\mathcal{B}^{l}_{u}$ ("false alarm"). Similarly, the statistic $\mathcal{B}^{l}_{u}$ computed for a truly lensed pair could sometimes attain small values (e.g., due to fluctuations in the detector noise), and reduce the efficiency for detecting truly lensed events. This causes the distributions of the Bayes factor computed from lensed and unlensed events to overlap; a good discriminator should minimize this overlap. Figure 5.6 shows this efficiency for correctly identifying truly lensed events, as a function of the false alarm probability (probability of wrongly identifying unlensed events as lensed events). We show such receiver operating characteristic (ROC) plots for $\mathcal{B}^{l}_{u}$ computed using different sets of parameters. We see that the discriminating efficiency of the Bayes factor increases when we add more signal parameters while computing the statistic. The source sky location parameters $(\cos\alpha, \delta)$ are the ones that most significantly improve the performance. However, considering the fact that the expected rate of lensed events is very small ($< 1\%$ of all events), the ROC curves indicate that $\mathcal{B}^{l}_{u}$, by itself, is not a very efficient statistic for identifying lensed events. The detection efficiency of $\mathcal{B}^{l}_{u}$ computed using 6 dimensional posteriors is $\sim 10 - 15\%$ for a false alarm probability of 10^{-5}.

Similarly, in Fig. 5.7 we plot the ROC curves for the time-delay Bayes factor $\mathcal{R}^{l}_{u}$ computed for the same simulated injected events with an average rate of 10 events per month as the binary black hole

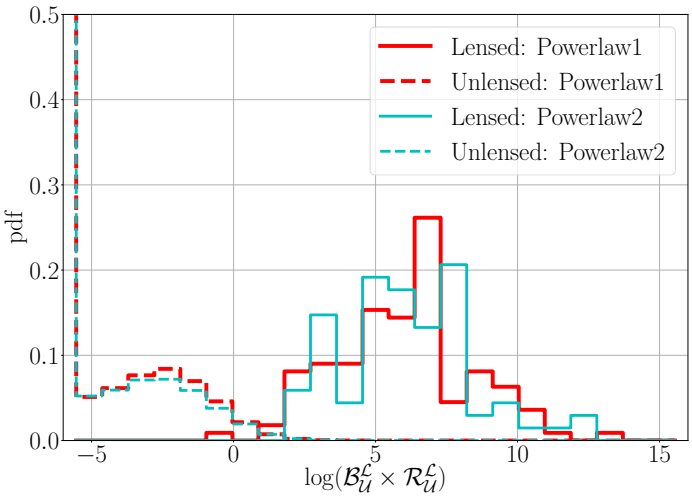

Figure 5.8: Distribution of the logarithm of the combined Bayes factor computed from the *unlensed* and *lensed* simulations with component masses sampled from power law 1 (solid) and power law 2 (dashed). The Bayes factors are computed using the marginalized posteriors on parameter set $(m^z{}_1, m^z{}_2, \cos\alpha, \delta, \chi_1, \chi_2)$. We use one year of unlensed events for the simulation.

detection rate. The three curves represent the ROC plots for $\mathcal{R}^{\mathrm{l}}_{\mathrm{u}}$ computed assuming 1, 2 and 3 years of observation time. The efficiency of $\mathcal{R}^{\mathrm{l}}_{\mathrm{u}}$ increases with the total length of the observation time included in the analysis. This is because the distribution of the time delay between unlensed event pairs becomes more and more skewed towards high values as the observation time increases (see Fig. 5.2). The performance of $\mathcal{R}^{\mathrm{l}}_{\mathrm{u}}$ is better than that of $\mathcal{B}^{\mathrm{l}}_{\mathrm{u}}$, with an efficiency of $\sim 45-50\%$ corresponding to a false alarm probability of 10^{-5} for an observation time of 3 years.

As one can see in the scatter plot of $\mathcal{B}^{\mathrm{l}}_{\mathrm{u}}$ and $\mathcal{R}^{\mathrm{l}}_{\mathrm{u}}$ of lensed/unlensed events pairs in Fig. 5.3, applying individual thresholds on $\mathcal{B}^{\mathrm{l}}_{\mathrm{u}}$ (vertical) and $\mathcal{R}^{\mathrm{l}}_{\mathrm{u}}$ (horizontal) are less effective in separating lensed pairs (red triangles) from unlensed pairs (blue stars). However, a combined threshold can improve the discriminatory power. Therefore, as described in Sec. 5.1, we combine $\mathcal{B}^{\mathrm{l}}_{\mathrm{u}}$ with $\mathcal{R}^{\mathrm{l}}_{\mathrm{u}}$ and define their product as a new statistic. Figure 5.8 shows the distributions of this combined statistic for lensed and unlensed event pairs with one year of observation time. Figure 5.9 shows the ROC plots for this combined statistic computed assuming 1 and 3 years of observations time. The results clearly demonstrate that the combined statistic has a significantly higher detection efficiency when compared to $\mathcal{B}^{\mathrm{l}}_{\mathrm{u}}$ and

$\mathcal{R}^{\mathrm{l}}_{\mathrm{u}}$. For a false alarm probability of 10^{-5}, the product statistic (computed using the six dimensional posteriors) identifies $\sim$ 80% of the lensed event pairs.

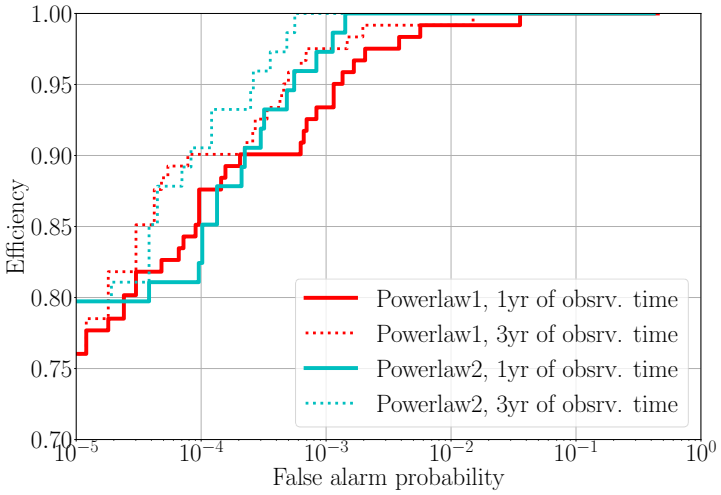

Figure 5.9: Receiver operating characteristic curves for the combined Bayes factor statistic computed using the marginalized posteriors on parameter set $(m^z{}_1, m^z{}_2, \chi_1, \chi_2 \cos\alpha, \delta)$ with component masses sampled from $P_1(m_1, m_2)$ (solid) and $P_2(m_1, m_2)$ (bashed). The statistic is able to correctly identify $\sim$ 80% of the lensed events with a false alarm probability of 10^{-5}.

5.3 *Search for lensing signatures in BBH events detected by LIGO and Virgo in their O1 and O2 runs*

During first and second observation runs of Advanced LIGO and Virgo, 10 BBH merger events were detected. We would like to see if any two events among the 45 pairs is strongly lensed images of the same merger event. We also explore the possibility of existence of at least one strongly lensed pair among the 45 pairs.

From each pair of binary black hole signals detected by LIGO and Virgo, we compute the ratio of the marginalized likelihoods (Bayes factor) of the competing hypotheses: 1) that, the pair of signals are strongly lensed images of a single binary black hole merger, 2) that, they are produced by two independent mergers. This Bayes factor can be computed using the Eq. 5.11, where $\boldsymbol{\theta}$ denotes the set of parameters that describes the signal (excluding the luminosity distance and arrival time), $P(\boldsymbol{\theta})$ denotes the prior probability distribution of $\boldsymbol{\theta}$, while $P(\boldsymbol{\theta}|d_1)$ and $P(\boldsymbol{\theta}|d_2)$ describe the posterior distributions of

$\boldsymbol{\theta}$ estimated from the data d_1 and d_2 containing the pair of signals under consideration.

The measured time delay Δt_0 between two signals can also be used to compute the likelihood ratio of the two hypotheses. The Bayes factor between the lensed and unlensed hypotheses can be computed using the Eq. 5.13, where $P(\Delta t_0|\mathcal{H}_A)$ with $A \in \{\text{L}, \text{U}\}$ is the prior distribution of Δt (under the lensed or unlensed hypothesis) evaluated at $\Delta t = \Delta t_0$. The prior $P(\Delta t_0|\mathcal{H}_\text{U})$ of the unlensed hypothesis is computed assuming that binary merger events follow a Poisson process. We use 714 days[3] as the observation time for computing $P(\Delta t_0|\mathcal{H}_\text{U})$. The prior distribution $P(\Delta t|\mathcal{H}_\text{L})$ of the time delay between strongly lensed signals is computed from an astrophysical simulation that employs reasonable distributions of galaxy lenses, mass function of binary black holes and redshift distribution of mergers, following.

[3] This is the total duration from the beginning of O1 to the end of O2. In reality, the data is not available for the entire 714 days due to the limited duty cycle of the Interferometers. We do not expect a significant change in the prior distribution even if we include this correction.

We compute $\mathcal{B}^\text{L}_\text{U}$ from a pair of binary black hole signals by integrating the posterior distributions of the binary's parameters released by the LIGO-Virgo Collaboration [18, 99]. These posteriors are estimated by the LALInferenceNest [146] code using the gravitational waveform family IMRPhenomPv2. We use the joint posterior distributions of the following parameters $\boldsymbol{\theta} := \{m_1^z, m_2^z, a_1, a_2, \cos\theta_{a1}, \cos\theta_{a2}, \alpha, \sin\delta, \theta_{J_N}\}$, where m_1^z, m_2^z are the redshifted component masses, a_1, a_2 are the dimensionless spin magnitudes, θ_{a1}, θ_{a2} are the polar angle of the spin orientations (with respect to the orbital angular momentum), $\alpha, \sin\delta$ denote the sky location, and θ_{J_N} is the orientation of the total angular momentum of the binary (with respect to the line of sight). [4] The Bayes factor in Eq.(5.11) is computed by numerically integrating the products of the Gaussian kernel density estimates of the posterior distributions of $\boldsymbol{\theta}$ from each pair of events, after marginalizing them over all other parameters using standard priors in the LIGO-Virgo parameter estimation [18].

[4] [62] have discovered that, if we neglect the effects of spin precession and non-quadrupole modes, multiple images are related to each other by specific phase shifts. Hence the consistency of the coalescence phase ϕ_c and polarization angle ψ, which is degenerate with ϕ_c can also be used to determine the consistency of multiple images. However, we are using a more general waveform family that include spin precession, where such a relationship does not hold. Hence we do not check the consistency of ϕ_0 and ψ.

Figure 5.10 presents a scatter plot of the Bayes factors $\mathcal{B}^\text{L}_\text{U}$ and $\mathcal{R}^\text{L}_\text{U}$ computed from binary black hole event pairs observed by LIGO and

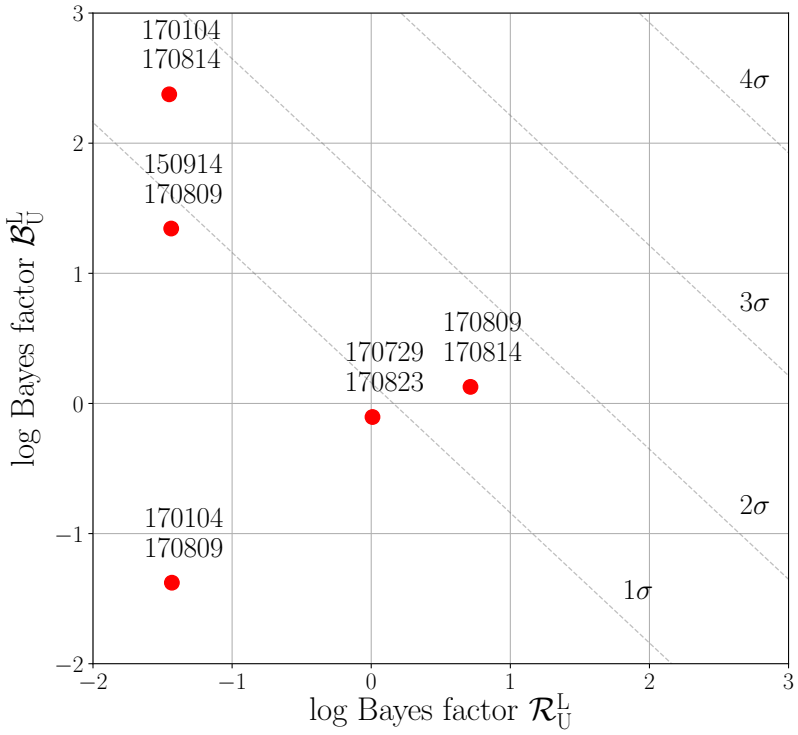

Figure 5.10: Scatter plot of the $\log_{10}$ Bayes factors $\mathcal{B}^{\mathrm{l}}_{\mathrm{u}}$ computed from the consistency of posteriors of signal parameters estimated from each pair of binary black holes events and Bayes factors $\mathcal{R}^{\mathrm{l}}_{\mathrm{u}}$ computed from the time delay between pairs of events. The significance of these Bayes factors is shown by dashed lines (in terms of Gaussian standard deviations). This is estimated by performing simulations of unlensed events in simulated Gaussian noise and estimating the probability of unlensed events producing Bayes factors of this value. In summary, we do not see any strong evidence for multiply lensed images in LIGO-Virgo binary black hole detections. Note that, out of 45 event pairs, only those pairs with $\log_{10}$ Bayes factors greater than -2 are shown in the plot. We have taken into account the effect of trials factor due the 45 event pairs.

Virgo during the first two observation runs. Since the $\mathcal{B}^{\mathrm{l}}_{\mathrm{u}}$ and $\mathcal{R}^{\mathrm{l}}_{\mathrm{u}}$ are computed using unrelated information, we can compute a joint Bayes factor by multiplying $\mathcal{B}^{\mathrm{l}}_{\mathrm{u}}$ and $\mathcal{R}^{\mathrm{l}}_{\mathrm{u}}$, which is used to determine the significance for each pair [83]. Figure 5.10 also shows the significance of these Bayes factor values, $\mathcal{B}^{\mathrm{l}}_{\mathrm{u}} \times \mathcal{R}^{\mathrm{l}}_{\mathrm{u}}$, in terms of Gaussian standard deviations. The significance is estimated from simulations of unlensed binary black hole events in Gaussian noise with power spectra of the Advanced LIGO-Virgo network with design sensitivity, presented in [83] [5]. In the estimation of the significance, we have taken into account the effect of the "trials factor" due to 45 event pairs produced by the 10 events — if p is the probability of an unlensed pair to have a Bayes factor greater than a given threshold (that we estimate from the simulations), the probability of at least one among N unlensed pairs to randomly cross this threshold is $1 - (1-p)^N \simeq Np$, assuming that each pair is independent.

The event pairs GW170104-GW170814 and GW150914-GW170809 show the highest Bayes factors $\mathcal{B}^{\mathrm{l}}_{\mathrm{u}} \sim 198$ and 29 — their posteriors

[5] The significance of lensed event pairs will be even lower if we used the actual O1-O2 noise spectra, due to the lower sensitivity. Hence this is an optimistic estimate of the significance of these Bayes factors.

overlap at a reasonable confidence level to suggest a possible explanation of them as double images of a single source based on waveform similarity (see Figs. 5.11 and 5.12). However, galaxy lenses are unlikely to produce time delays as long as 7 or 23 months between the images [83], resulting in a small $\mathcal{R}^{\rm l}_{\rm u} \sim 4 \times 10^{-3}$ and 10^{-4} for both pairs. If galaxy clusters were a viable lensing source, then one could expect time delays of a few months [129, 128]. However, the rate of strongly lensed binary black hole mergers by galaxy clusters at current sensitivity is around 10^{-5} per year [126], disfavoring this scenario. On the other hand, the time delay between GW170809 and GW170814 is consistent with galaxy lenses ($\mathcal{R}^{\rm l}_{\rm u} \sim 3.3$). While the projected 1-dimensional posterior of, e.g., chirp mass overlap within 90% confidence [48], this is mainly caused by correlation with other intrinsic parameters, e.g. effective spin. The posteriors in higher dimensions do not show similar overlap (see Fig. 5.13), implying that these waveforms can be discriminated from each other with reasonable confidence. Indeed, a full higher-dimensional consistency check between the estimated parameters from this pair does not significantly favor lensing ($\mathcal{B}^{\rm l}_{\rm u} \sim 1.2$). The joint Bayes factors $\mathcal{B}^{\rm l}_{\rm u} \times \mathcal{R}^{\rm l}_{\rm u}$ for these pairs are 0.9 (GW170104-GW170814), 4×10^{-3} (GW150914-GW170809) and 4 (GW170809-GW170814). In summary, we do not see any strong evidence for the hypothesis that any of the pairs of binary black hole signals are lensed images of the same merger event. We have also repeated the same calculation employing the waveform family SEOBNRv3 [113, 134, 34]. The Bayes factors that we obtain from this analysis are consistent with those presented in Fig. 5.10.

We also compute the Bayes factor of the hypothesis that there exists at least one multiply imaged event in the entire catalog of events observed by Advanced LIGO-Virgo in the first and second observing run (without specifically identifying that pair). Considering the fact that the probability for observing more than 2 lensed images of a single merger is negligible, the joint Bayes factor $\sum_{p \in \text{pairs}} \mathcal{B}^{\rm l}_{\rm u}(p)\mathcal{R}^{\rm l}_{\rm u}(p)$ is equal to 5.2, and is not highly significant.

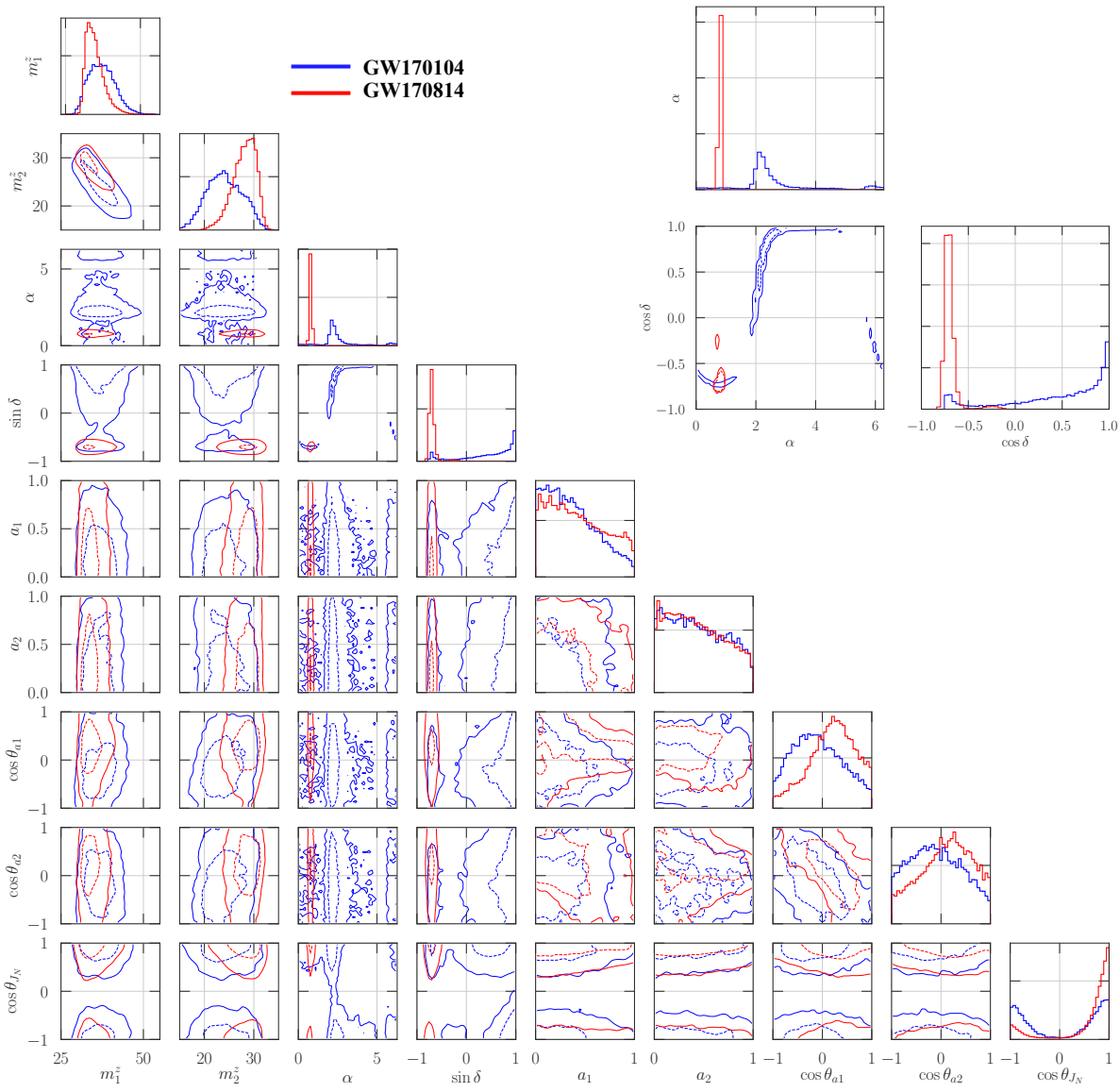

Figure 5.11: Marginalized 2D and 1D posterior distributions of the parameters that are included in the consistency test, for the event pair GW170104 (blue), GW170814(red). Here, m_1^z, m_2^z are the redshifted component masses, a_1, a_2 are the dimensionless spin magnitudes, θ_{a1}, θ_{a2} are the polar angle of the spin orientations (with respect to the orbital angular momentum), $\alpha, \sin\delta$ denote the sky location, and θ_{J_N} is the orientation of the total angular momentum of the binary (with respect to the line of sight). The solid (dashed) condors corrsponds to the 90%(50%) confidence levels of the 2D distributions. The inset plot shows the marginalized posterior distributions of the sky localization parameters for these events. Overall, the posteriors have some levels of overlap, thus resulting in a considerable Bayes factor of $\mathcal{B}^{\rm l}_{\rm u} \sim 198$ supporting the lensing hypothesis, purely based on parameter consistency. However, galaxy lenses are unlikely to produce time delay of 7 months between the images, resulting in a small Bayes factor $\mathcal{R}^{\rm l}_{\rm u} \sim 4 \times 10^{-3}$ based on time delay considerations.

5.4 *Detailed investigations of event pairs showing marginal evidence of lensing*

Here we present additional investigations on the event pairs that show marginal evidence of multiply-imaged lensing in the analysis presented in Sec. 5.3, providing a qualitative explanation of the Bayes factors presented in that section in terms of the overlap of the estimated posteriors from these event pairs. Figure 5.11 presents the 2D and 1D marginalized posterior distributions of the parameters that are included in the consistency test, for the event pair GW17014-

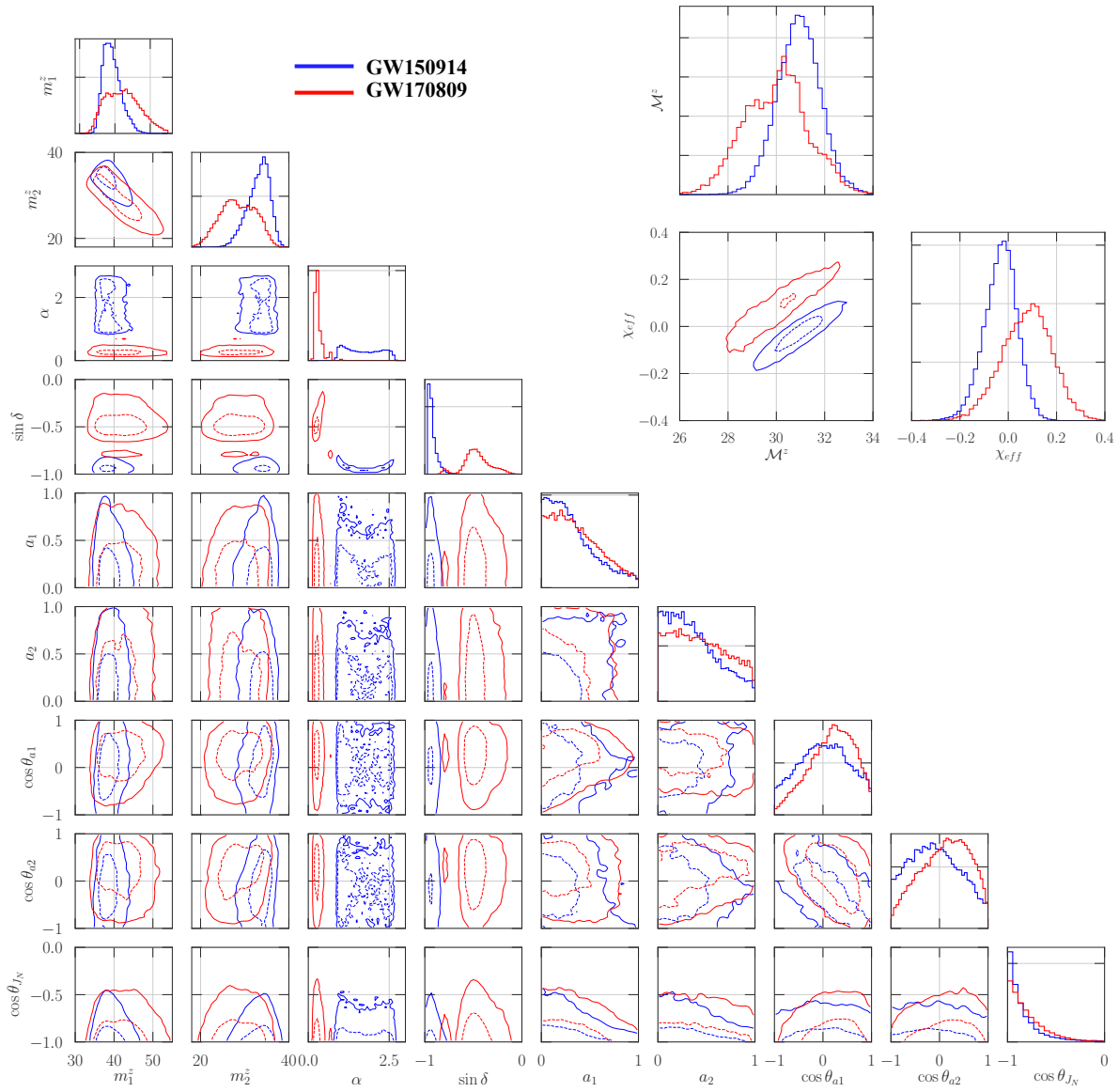

Figure 5.12: Same as Fig. 5.11, except that the figure corresponds to the 150914 (blue), GW170809 (red) event pair. The inset plot shows the marginalized posterior distributions of the redshifted chirp mass $\mathcal{M}^z$ and effective spin $\chi_{\rm eff}$ for these events. Marginalized 1D posteriors have some levels of overlap in many parameters; however 2D posteriors show good separation in many parameters, e.g., in $\mathcal{M}^z - \chi_{\rm eff}$. The resulting Bayes factor supporting the lensing hypothesis, based on parameter consistency is $\mathcal{B}^{\rm l}_{\rm u} \sim 29$. However, galaxy lenses are unlikely to produce time delay of 23 months between the images, resulting in a small Bayes factor $\mathcal{R}^{\rm l}_{\rm u} \sim \times 10^{-4}$ based on time delay considerations.

GW170814. Posteriors have appreciable levels of overlap in many parameters, thus resulting in a considerable Bayes factor of $\mathcal{B}^{\rm l}_{\rm u} \sim 198$ supporting the lensing hypothesis, purely based on parameter consistency. However, galaxy lenses are unlikely to produce time delay of 7 months between the images [83], resulting in a small Bayes factor $\mathcal{R}^{\rm l}_{\rm u} \sim 4 \times 10^{-3}$ based on time delay considerations.

Figure 5.12 shows similar plots for the event pair GW150914-GW170809. Although marginalized 1D posteriors have some levels of overlap in many parameters, 2D posteriors show good separation in many parameters, e.g., in $\mathcal{M}^z - \chi_{\rm eff}$. The resulting Bayes factor supporting

the lensing hypothesis, based on parameter consistency is $\mathcal{B}^{\rm l}_{\rm u} \sim 29$. However, galaxy lenses are unlikely to produce time delay of 23 months between the images, resulting in a small Bayes factor $\mathcal{R}^{\rm l}_{\rm u} \sim \times 10^{-4}$ based on time delay considerations. Figure 5.13 shows similar plots for the event pair GW170809-GW170814. Here also, the 2D posteriors of several parameters (e.g., in $\mathcal{M}^z - \chi_{\rm eff}$) show poor overlaps, suggesting that the full multidimensional posteriors do not have significant overlap. The resultant Bayes factor for parameter consistency is $\mathcal{B}^{\rm l}_{\rm u} \sim 1.2$, even though, the time delay between these events is consistent with galaxy lenses, producing a Bayes factor $\mathcal{R}^{\rm l}_{\rm u} \sim 3.3$ based on time delay.

5·5 *Summary and future work*

In this chapter we proposed a method for statistically identifying multiple images of strongly lensed binary black hole merger events from a population of GW detections by the LIGO-Virgo network. Recent estimates show that Advanced LIGO and Virgo, when they reach their design sensitivities, will detect several binary black hole mergers per year that are strongly lensed by intervening galaxies [109]. We will be able to observe multiple images of such GW signals, which are separated by time scales of minutes to weeks. In the case of GW signals from stellar mass black-hole binaries lensed by galaxies (for which $\lambda_{\rm GW} \ll 2GM_{\rm lens}/c^2$), the lensing will result in a magnification/de-magnification of the GW polarizations without affecting their frequency profile. Hence, the parameters of the binary that determine the frequency evolution of the signal (such as the redshifted masses and spins), which we extract from multiple images, will be mutually consistent [6]. In addition, since the deflection angle is small compared to the typical source-localization accuracies, the sky-location of multiple images will also be the same. In order to determine whether a pair of binary black hole signals are lensed images of the same merger, we check the consistency of extracted

[6] Note, however, that the luminosity distance that we extract using the parameter estimation using standard (unlensed) templates will be biased, due to the unknown magnification in the signal. Hence the inferred redshift and intrinsic masses will also be biased [61].

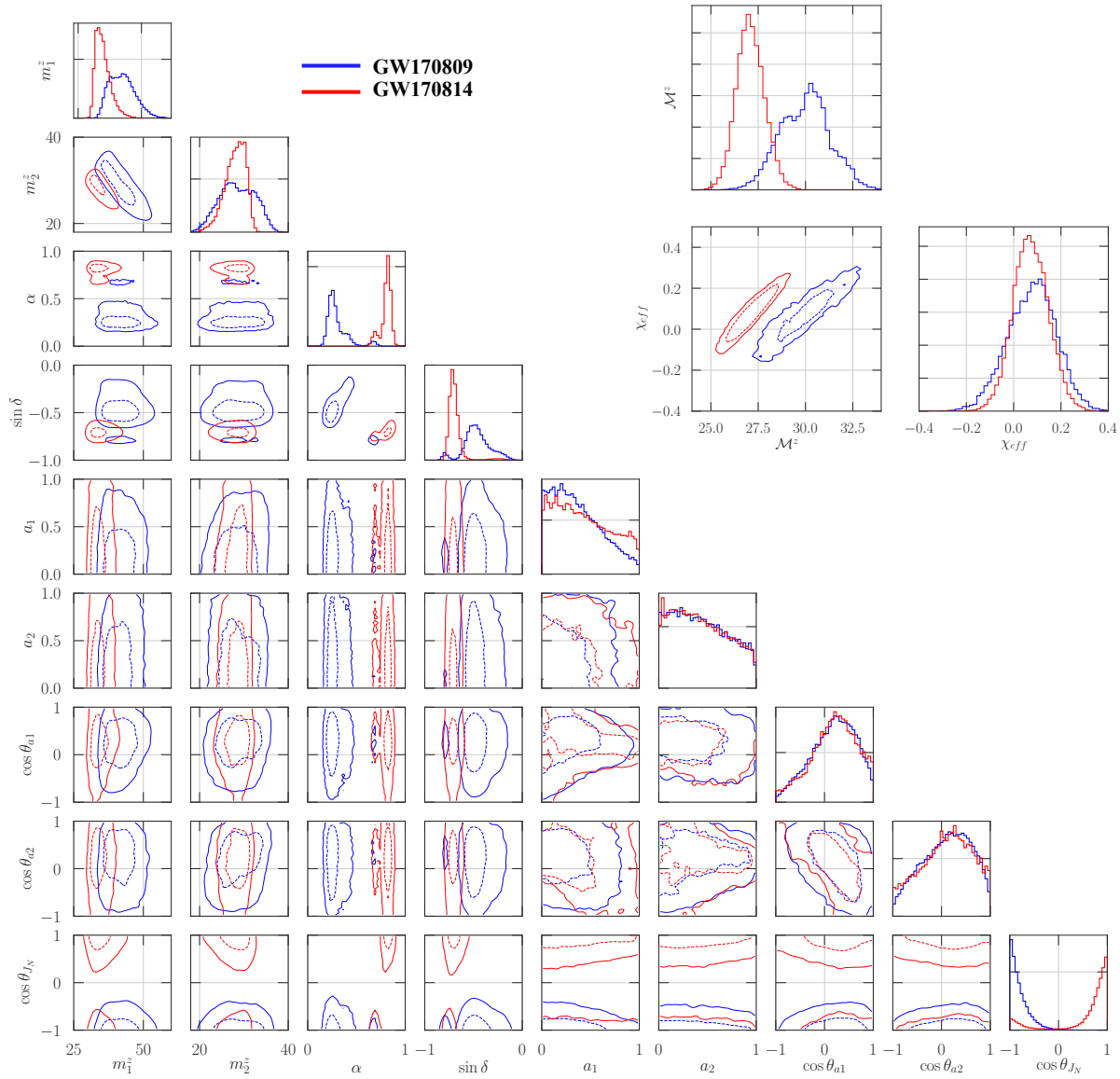

Figure 5.13: Same as Fig. 5.11, except that the figure corresponds to the GW170809 (blue), GW170814 (red) event pair. Marginalized 1D posteriors have some levels of overlap in many parameters; however 2D posteriors show good separation in many parameters, e.g., in $\mathcal{M}^z - \chi_{\rm eff}$. The resulting Bayes factor supporting the lensing hypothesis, based on parameter consistency is $\mathcal{B}^{\rm l}_{\rm u} \sim 1.2$.

parameters (except the luminosity distance) from the two signals. To be precise, we computed the odds ratio between two hypotheses 1) that they are the lensed images of the same merger event, 2) that they are two unrelated events. This odds ratio can be written in terms of the overlap of the posterior distributions of the extracted parameters from the two events, inversely weighted by the prior [see Eq. (5.11)]. In addition, we make use of the fact that the distribution of the time delays between a pair of lensed events will be different from that between a pair of random uncorrelated events (see Fig. 5.2). This allows us to define another odds ratio between the two hypotheses based on

the observed time delay between a pair of events [see Eq. (5.13)]. We combine these two different odds ratios to form a more sensitive discriminator between lensed and unlensed events.

We test the efficiency of the proposed statistic by simulating binary black hole merger events in the LIGO-Virgo network with design sensitivity. The simulations shows that the pipeline can distinguish images $\sim 80\%$ of strongly lensed merger events from unlensed events with a false alarm probability of 10^{-5} for three years of observation time.

There are possible ways of improving the discriminatory power of this statistic: one is by increasing the number of parameters that are used to test the consistency between estimated parameters of the two events (e.g., inclination angle, spin orientations, etc., if they are well measured). Secondly, one can use the property discovered by [62] that waveforms of different images are related by specific phase shifts. Thirdly, one could explore the possibility of using priors on the magnification ratios of multiple images (or the ratios of the SNRs of multiple images) in a way similar to the way we used the priors on time delays between multiple events to distinguish between lensed and unlensed pairs. We leave these as future work.

We looked for evidence of multiply imaged signals in the binary black hole observations by LIGO and Virgo during the observing runs O1 and O2. We found no strong evidence of strong gravitational lensing. However, in future, as the detector sensitivities improve further, we hope to observe more than one strongly lensed signal per year [109]. Apart from verifying a fundamental prediction of general relativity using a messenger that is different from electromagnetic waves, such an observation might enable precision localization of the merger when combined with optical observations of the lens galaxy. Since the fraction of lensed events will be small, we do not expect lensing to introduce significant biases in population analysis.

6 Acknowledgements

Firstly, I am extremely grateful to my advisor Prof. P. Ajith, for continuous support, both academically and non-academically during my doctoral study. I always felt very comfortable talking to him, whether it was sane or insane. I would simply like to say "Thank you" to him.

I am grateful to Prof. Bala Iyer for being very kind to me and giving me beautiful suggestions. I would like to thank Sumit, Rahul and Haris for helping me whenever I needed and also for being good friends to me with whom I could share anything. I also want to thank Gayathri for keeping us entertained through her beautiful singing and teaching me some bit of it. I owe thanks to my friends at ICTS with whom I have shared beautiful moments. My sincere thanks also go to my collaborators, from whom I have learned a lot. I am extremely grateful to ICTS for providing me an opportunity to do my work without having me to bother about anything.

The most important acknowledgement is of my father's encouragement that kept me sustained throughout and of my dearest mother's love which keeps me smiling.

"There is no alternative to hard work."

P. Ajith

7 Publications

Publications relevant to the thesis

- Ajit Kumar Mehta, Chandra Kant Mishra, Vijay Varma, P. Ajith; Accurate inspiral-merger-ringdown gravitational waveforms for non-spinning black-hole binaries including the effect of subdominant modes; Phys. Rev. D 96, 124010 (2017); arXiv:1708.03501 [gr-qc]

- Ajit Kumar Mehta, Praveer Tiwari, Nathan K. Johnson-McDaniel, Chandra Kant Mishra, Vijay Varma, Parameswaran Ajith; Including mode mixing in a higher-multipole model for gravitational waveforms from nonspinning black-hole binaries; Phys. Rev. D 100, 024032 (2019); arXiv:1902.02731 [gr-qc]

- Siddharth Dhanpal, Abhirup Ghosh, Ajit Kumar Mehta, P. Ajith, B. S. Sathyaprakash; A "no-hair" test for binary black holes; Phys. Rev. D 99, 104056 (2019); arXiv:1804.03297 [gr-qc]

- K. Haris, Ajit Kumar Mehta, Sumit Kumar, Tejaswi Venumadhav, Parameswaran Ajith; Identifying strongly lensed gravitational wave signals from binary black hole mergers; arXiv:1807.07062 (2018) [gr-qc]

- O.A. Hannuksela, K. Haris, K.K.Y. Ng, Sumit Kumar, Ajit Kumar Mehta, David Keitel, T.G.F. Li, Parameswaran Ajith; Search for gravitational lensing signatures in LIGO-Virgo binary black hole events; Astrophysical Journal Letters 874:L2 (2019); arXiv:1901.02674 [gr-qc]

Other Publications

- Tousif Islam, Ajit Kumar Mehta, Abhirup Ghosh, Parameswaran Ajith, B. S. Sathyaprakash; Testing the "no-hair" nature of binary black holes from higher modes of gravitational radiation, in preparation (2019).

- Apratim Ganguly, Soummyadip Basak, K. Haris, Shasvath Kapadia, Ajit Kumar Mehta, Parameswaran Ajith; First constraints on compact dark matter from gravitational-wave lensing, in preparation (2019).

A Appendix

A.1 *Padé summation on the post-Newtonian amplitude in the Fourier domain*

The PN expression for various mode amplitudes have a stationary point at high frequencies when higher order PN corrections are included. This makes it inconvenient to model the amplitude of the phenomenological waveforms as a factorized correction to the PN waveforms as shown in Eq.(2.9). In order to resolve this issue, and to generally improve the agreement of PN amplitude with that of the hybrid waveforms, we construct our inspiral amplitude model by performing Padé summation of these expressions. Padé summation of a given function involves finding a suitable rational function whose Taylor expansion to a given order matches exactly with the Taylor expression of the original function to the same order. For instance, Padé summation of a simple power series $\sum_{k=0}^{n} a_n x^n$ can be written as

$$P_q^p(x) = \frac{\sum_{k=0}^{p} b_k x^k}{\sum_{k=0}^{q} c_k x^k}, \tag{A.1}$$

where $p + q = n$. Each of these coefficients (b_k and c_k) then can readily be obtained by demanding that a Taylor expansion of the above to order n reproduces exactly the first n terms the given power series. Such rational functions are called Padé approximants (see App. A of Ref. [1] for a related discussion).

After comparing various Padé approximants corresponding to PN amplitude expressions for each mode we find the most suitable (i.e., an approximant with no point of inflection) approximant corresponds

[1] T. Damour, B R Iyer, and B S Sathyaprakash. Improved filters for gravitational waves from inspiraling compact binaries. *Phys. Rev. D*, 57:885–907, 1998

to the choice of rational functions associated with $p = 0$ and $q = n$, i.e., P^0_n. For instance for the $\ell = m = 2$ mode whose (normalized) amplitude is given by the series, $\sum_{k=0}^{7} \alpha_k v^k$, the Padé approximant we find most suitable for our purposes is given by

$$P^0_7(v) = \frac{\beta_0}{\sum_{k=0}^{7} \gamma_k v^k}\,. \tag{A.2}$$

Moreover by the virtue of the use of normalized amplitude expressions in constructing the Padé approximants we can choose (without any loss of generality), $\beta_0 = \gamma_0 = 1$, which leads to the following simple expression

$$P^0_7(v) = \frac{1}{1 + \sum_{k=1}^{7} \gamma_k v^k}\,. \tag{A.3}$$

Figure A.1 shows a comparison of the standard Taylor expanded 3.5PN (3PN) amplitude for 22 (21, 33, 44) with our corresponding resummed Padé function as well as the amplitude of the hybrid waveform in the Fourier domain. Explicit expressions for Padé approximants for modes we consider here are listed in Appendix A.2 below.

A.2 *Padé resummed frequency domain expressions for the inspiral amplitude*

As discussed above, occurrence of divergences in the PN amplitudes when including higher PN terms motivates us to find Padé resummed expressions of the PN amplitudes as our inspiral amplitude model. Here we provide, analytical expression for the complete inspiral model for each mode in the frequency domain which are constructed using the prescription listed in Ref. [141] and uses Stationary Phase Approximation. Resulting expression for each mode of the gravitational wave polarizations in the frequency domain take

the following general form

$$\tilde{h}_{\ell m}(f) = \frac{M^2}{D_L}\,\pi\,\sqrt{\frac{2\eta}{3}}\,v_f^{-7/2}\,e^{-\mathrm{i}\,m\,\Psi(v_f)}\,H_{\ell m}(v_f)\,. \tag{A.4}$$

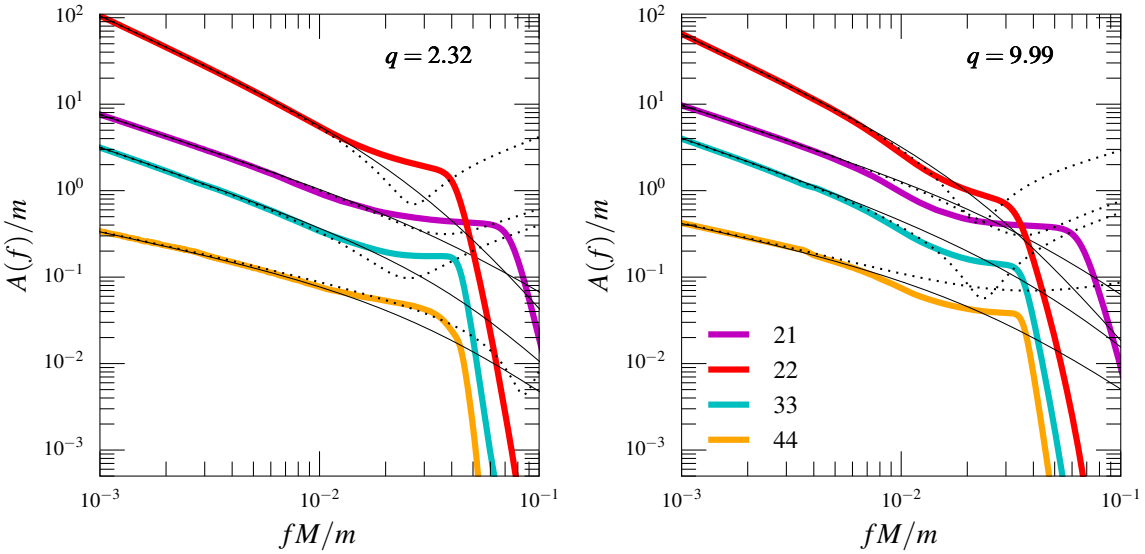

Figure A.1: Comparison of the Padé approximant of the PN inspiral amplitude (thin, solid lines) with regular Taylor expanded amplitude (thin, dotted lines) and the amplitude of the hybrid waveform (thick, solid lines) for different modes $\ell m = 21, 22, 33, 44$. The left panel corresponds to mass ratio $q = 2.32$ while the right panel corresponds to mass ratio $q \simeq 10$.

Here, M and η again denote the total mass and symmetric mass ratio parameter of the binary whereas D_L is the luminosity distance of the source. The quantity v_f is given by $v_f \equiv (2\,\pi M f/m)^{1/3}$ and $\Psi(v_f)$ represents the orbital phase of the binary computed using stationary phase approximation (see for instance Ref. [141] for a related discussion). Finally, $H_{\ell m}$ are the Padé resummed version of the inspiral amplitudes and takes following form for the modes whose complete models are presented in this study. They read

$$H_{22} = {}^{22}P_7^0(v_f) \tag{A.5a}$$

$$H_{21} = \mathrm{i}\,\frac{\sqrt{2}}{3}\,\delta\,[{}^{21}P_5^0(v_f)]\,v_f \tag{A.5b}$$

$$H_{33} = -\mathrm{i}\,\frac{3}{4}\sqrt{\frac{5}{7}}\delta\,[{}^{33}P_5^0(v_f)]\,v_f \tag{A.5c}$$

$$H_{44} = -\frac{4}{9}\sqrt{\frac{10}{7}}(1-3\,\eta)\,[{}^{44}P_4^0(v_f)]\,v_f^2 \tag{A.5d}$$

here, ${}^{\ell m}P_n^0(v_f)$ are Padé resummed expressions for (normalized) inspiral amplitudes corresponding to $p = 0$ and $q = n$ (see Appendix

A.1 for related discussions) and can be expressed in the following general form.

$$ {}^{\ell m}P_n^0(v) = \frac{1}{1 + \sum_{k=1}^{n} \gamma_k^{\ell m} v^k}\,, \tag{A.6} $$

where $\gamma^{\ell m}$ corresponding to each mode can be written in the follow-

ing form,

$$\gamma_1^{22} = 0 \tag{A.7a}$$

$$\gamma_2^{22} = \frac{323}{224} - \frac{451}{168}\eta \tag{A.7b}$$

$$\gamma_3^{22} = 0 \tag{A.7c}$$

$$\gamma_4^{22} = \frac{44213383}{8128512} - \frac{92437}{48384}\eta + \frac{483509}{169344}\eta^2 \tag{A.7d}$$

$$\gamma_5^{22} = \frac{85\pi}{64} + \left(24\,\mathrm{i} - \frac{85\pi}{16}\right)\eta \tag{A.7e}$$

$$\gamma_6^{22} = \frac{40919017211}{1226244096} - \frac{428\,\mathrm{i}\,\pi}{105} + \left(-\frac{1906061676931}{15021490176} + \frac{205\,\pi^2}{48}\right)\eta + \frac{6864704395}{1251790848}\eta^2 - \frac{48013667}{34771968}\eta^3 \tag{A.7f}$$

$$\gamma_7^{22} = \frac{633281\pi}{1161216} + \left(\frac{2357\,\mathrm{i}}{324} - \frac{21367\,\pi}{3456}\right)\eta + \left(-\frac{86519\,\mathrm{i}}{945} + \frac{496409\,\pi}{24192}\right)\eta^2 \tag{A.7g}$$

$$\gamma_1^{21} = 0 \tag{A.7h}$$

$$\gamma_2^{21} = -\frac{335}{672} - \frac{117}{56}\eta \tag{A.7i}$$

$$\gamma_3^{21} = \frac{\mathrm{i}}{2} + \pi + 2\,\mathrm{i}\ln 2 \tag{A.7j}$$

$$\gamma_4^{21} = \frac{2984407}{8128512} + \frac{62659}{12544}\eta + \frac{96847}{56448}\eta^2 \tag{A.7k}$$

$$\gamma_5^{21} = -\frac{335\mathrm{i}}{1344} + \frac{1115\pi}{1344} + \eta\left(\frac{1255\mathrm{i}}{112} - \frac{885\pi}{112} - \frac{145}{28}\mathrm{i}\ln 2\right) - \frac{335}{336}\mathrm{i}\ln 2 \tag{A.7l}$$

$$\gamma_1^{33} = 0 \tag{A.7m}$$

$$\gamma_2^{33} = \frac{1945}{672} - \frac{27}{8}\eta \tag{A.7n}$$

$$\gamma_3^{33} = \frac{2\,\mathrm{i}}{5} - \pi + 6\,\mathrm{i}\ln 2 - 6\,\mathrm{i}\ln 3 \tag{A.7o}$$

$$\gamma_4^{33} = \frac{4822859617}{447068160} - \frac{5571877}{887040}\eta + \frac{301321}{63360}\eta^2 \tag{A.7p}$$

$$\gamma_5^{33} = \frac{389\,\mathrm{i}}{32} - \frac{2105\pi}{1344} - \frac{1945\,\mathrm{i}}{112}\ln(3/2) + \eta\left(\frac{33079\,\mathrm{i}}{1944} - \frac{23\pi}{16} + \frac{93\,\mathrm{i}}{4}\ln(3/2)\right) \tag{A.7q}$$

$$\gamma_1^{44} = 0 \tag{A.7r}$$

$$\gamma_2^{44} = \frac{1}{1-3\eta}\left(-\frac{158383}{36960} + \frac{128221}{7392}\eta - \frac{1063}{88}\eta^2\right) \tag{A.7s}$$

$$\gamma_3^{44} = \frac{1}{1-3\eta}\left(-\frac{42\,\mathrm{i}}{5} + 2\pi + \eta\left(\frac{1193\,\mathrm{i}}{40} - 6\pi - 24\mathrm{i}\ln 2\right) + 8\,\mathrm{i}\ln 2\right) \tag{A.7t}$$

$$\gamma_4^{44} = \frac{1}{(1-3\eta)^2}\left(\frac{5783159561419}{319653734400} - \frac{6510652977943}{53275622400}\eta + \frac{8854729392203}{35517081600}\eta^2 - \frac{1326276157}{8456448}\eta^3 + \frac{63224063}{1006720}\eta^4\right). \tag{A.7u}$$

Finally, the orbital phase takes the following form in Fourier domain

$$\Psi(v_f) = 2\pi f t_0 - \pi/4 + \frac{3}{256\,\eta\, v_f^5}\left[\sum_{k=0}^{7}\psi_k v_f^k\right], \tag{A.8}$$

where, t_0 represents a reference time[2] and ψ_k denote the PN corrections to the leading order orbital phase. These read

[2] Note that we have set the phase at reference time to zero, since phase shifts can be introduced on the waveform by the spherical harmonic basis functions; see Eq.(A.16).

$$\psi_0 = 1, \tag{A.9a}$$

$$\psi_1 = 0, \tag{A.9b}$$

$$\psi_2 = \frac{3715}{756} + \frac{55}{9}\eta, \tag{A.9c}$$

$$\psi_3 = -16\,\pi, \tag{A.9d}$$

$$\psi_4 = \frac{15293365}{508032} + \frac{27145}{504}\eta + \frac{3085}{72}\eta^2, \tag{A.9e}$$

$$\psi_5 = \pi\left(\frac{38645}{756} - \frac{65}{9}\eta\right)(1 + 3\ln v_f), \tag{A.9f}$$

$$\begin{aligned}\psi_6 = {} & \frac{11583231236531}{4694215680} - \frac{6848\gamma_{\rm E}}{21} - \frac{640\pi^2}{3} \\ & + \left(-\frac{15737765635}{3048192} + \frac{2255\pi^2}{12}\right)\eta + \frac{76055}{1728}\eta^2 - \frac{127825}{1296}\eta^3 \\ & - \frac{6848}{21}\ln(4v_f),\end{aligned} \tag{A.9g}$$

$$\psi_7 = \frac{77096675\pi}{254016} + \frac{378515\pi}{1512}\eta - \frac{74045\pi}{756}\eta^2, \tag{A.9h}$$

where $\gamma_{\rm E}$ is the Euler's constant.

A.3 *Computing the + and × polarization waveforms from the spherical harmonic modes in the frequency domain*

The complex time-series, $h = h_+ - i\,h_\times$, can be decomposed into a sum of spherical harmonic modes as

$$h(t) = \sum_{\ell=2}^{+\infty}\sum_{m=-\ell}^{\ell} h_{\ell m}(t)\, Y^{\ell m}_{-2}(\iota, \varphi_0)\,, \tag{A.10}$$

where $Y^{\ell m}_{-2}$'s (the spin-weighted spherical harmonics of weight -2) are functions of the spherical angles (ι, φ_0) defining the binary's ori-

entation, and are given as

$$Y^{\ell m}_{-2} = \sqrt{\frac{2\ell+1}{4\pi}}\, d^{\ell m}_{2}(\iota)\, e^{i\,m\,\varphi_0}, \tag{A.11}$$

where $d^{\ell m}_{2}(\iota)$ are the Wigner d functions (e.g., [149]). The spherical harmonic modes of the waveform in time-domain have the following generic form

$$h_{\ell m}(t) = A_{\ell m}(t)\, e^{i\,\varphi_{\ell m}(t)} \tag{A.12}$$

Further, $m < 0$ modes are related to $m > 0$ modes as $h_{\ell,-m}(t) = (-)^{\ell} h^{*}_{\ell m}(t)$ [91]. Using Eq. (A.11) and Eq. (A.12) in Eq. (A.10) and making use of the above property we can write expressions for the real and imaginary part as

$$h_{+}(t) = \sum_{\ell=2}^{+\infty}\sum_{m=1}^{\ell}\sqrt{\frac{2\ell+1}{4\pi}}\left[(-)^{\ell} d^{\ell,-m}_{2}(\iota) + d^{\ell m}_{2}(\iota)\right] A_{\ell m}(t)\,\cos[\varphi_{\ell m}(t) + m\varphi_0], \tag{A.13a}$$

$$h_{\times}(t) = \sum_{\ell=2}^{+\infty}\sum_{m=1}^{\ell}\sqrt{\frac{2\ell+1}{4\pi}}\left[(-)^{\ell} d^{\ell,-m}_{2}(\iota) - d^{\ell m}_{2}(\iota)\right] A_{\ell m}(t)\,\sin[\varphi_{\ell m}(t) + m\varphi_0]. \tag{A.13b}$$

The frequency domain $+$ and $\times$ waveforms can now be obtained simply by taking Fourier Transform of $h_{+}(t)$ and $h_{\times}(t)$, respectively

$$\tilde{h}_{+}(f) = \sum_{\ell=2}^{+\infty}\sum_{m=1}^{\ell}\sqrt{\frac{2\ell+1}{4\pi}}\left[(-)^{\ell} d^{\ell,-m}_{2}(\iota) + d^{\ell m}_{2}(\iota)\right]\left\{\cos(m\varphi_0)\,\tilde{h}^{\mathrm{R}}_{\ell m}(f) - \sin(m\varphi_0)\,\tilde{h}^{\mathrm{I}}_{\ell m}(f)\right\}, \tag{A.14a}$$

$$\tilde{h}_{\times}(f) = \sum_{\ell=2}^{+\infty}\sum_{m=1}^{\ell}\sqrt{\frac{2\ell+1}{4\pi}}\left[(-)^{\ell} d^{\ell,-m}_{2}(\iota) - d^{\ell m}_{2}(\iota)\right]\left\{\sin(m\varphi_0)\,\tilde{h}^{\mathrm{R}}_{\ell m}(f) + \cos(m\varphi_0)\,\tilde{h}^{\mathrm{I}}_{\ell m}(f)\right\}. \tag{A.14b}$$

where $\tilde{h}^{\mathrm{R}}_{\ell m}(f)$ and $\tilde{h}^{\mathrm{I}}_{\ell m}(f)$ are the Fourier transforms of the real and imaginary parts of $h_{\ell m}(t)$.

$$\tilde{h}^{\mathrm{R}}_{\ell m}(f) = \int_{-\infty}^{\infty} e^{2\pi i f t} A_{\ell m}(t)\cos\varphi_{\ell m}(t)\,dt, \tag{A.15a}$$

$$\tilde{h}^{\mathrm{I}}_{\ell m}(f) = \int_{-\infty}^{\infty} e^{2\pi i f t} A_{\ell m}(t)\sin\varphi_{\ell m}(t)\,dt. \tag{A.15b}$$

We know that for non-spinning binaries (as well as for non-precessing binaries), $\tilde{h}^{\rm I}_{\ell m}(f) = -i\tilde{h}^{\rm R}_{\ell m}(f)$. This allows us to write Eq. (A.14) as

$$\tilde{h}_+(f) = \sum_{\ell=2}^{+\infty}\sum_{m=1}^{\ell}\left[(-)^{\ell}\frac{d^{\ell,-m}_2(\iota)}{d^{\ell m}_2(\iota)} + 1\right] Y^{\ell m}_{-2}(\iota,\varphi_0)\,\tilde{h}^{\rm R}_{\ell m}(f) \tag{A.16a}$$

$$\tilde{h}_\times(f) = -i\sum_{\ell=2}^{+\infty}\sum_{m=1}^{\ell}\left[(-)^{\ell}\frac{d^{\ell,-m}_2(\iota)}{d^{\ell m}_2(\iota)} - 1\right] Y^{\ell m}_{-2}(\iota,\varphi_0)\,\tilde{h}^{\rm R}_{\ell m}(f). \tag{A.16b}$$

Note that $\tilde{h}^{\rm R}_{\ell m}(f)$ can be written as

$$\tilde{h}^{\rm R}_{\ell m}(f) = A_{\ell m}(f)\, e^{i\,\Psi_{\ell m}(f)}. \tag{A.17}$$

The phenomenological model for the frequency domain amplitudes $A_{\ell m}(f)$ and phases $\Psi_{\ell m}(f)$ are obtained by fitting the FFT of hybrids.

The signal observed at a detector is a linear combination of the two polarizations h_+ and $h_\times$. The Fourier transform of the observed signal can be written in terms of the Fourier transform of the two polarizations as

$$\tilde{h}(f) = F_+(\theta,\phi,\psi)\,\tilde{h}_+(f) + F_\times(\theta,\phi,\psi)\,\tilde{h}_\times(f), \tag{A.18}$$

where the antenna pattern functions $F_+(\theta,\phi,\psi)$ and $F_\times(\theta,\phi,\psi)$ are functions of two angles (θ,ϕ) describing the location of the binary in the sky and the polarization angle ψ.

A.4 *Mode removal in frequency domain*

Here we detail the calculation of the spheroidal harmonic modes from spherical harmonic modes in the frequency domain, shown in Eq. (2.21). From Eq. (2.20), we have,

$${}^{\rm S}\!f_{320}(t) \simeq \frac{{}^{\rm Y}\!f_{32}(t) - {}^{\rm Y}\!f_{22}(t)\mu^*_{2320}/\mu^*_{2220}}{\mu^*_{2330}}, \tag{A.19}$$

Taking the real part gives us

$$
\begin{aligned}
{}^{\mathrm{S}}\hbar^{\mathrm{R}}_{320}(t) \simeq \frac{1}{|\mu_{2330}|^2}\Big[& {}^{\mathrm{Y}}\hbar^{\mathrm{R}}_{32}(t)\mu^{\mathrm{R}}_{2330} - {}^{\mathrm{Y}}\hbar^{\mathrm{I}}_{32}(t)\mu^{\mathrm{I}}_{2330} - {}^{\mathrm{Y}}\hbar^{\mathrm{R}}_{22}(t)\big(\rho^{\mathrm{R}}_{2320}\mu^{\mathrm{R}}_{2330} \\
& + \rho^{\mathrm{I}}_{2320}\mu^{\mathrm{I}}_{2330}\big) + {}^{\mathrm{Y}}\hbar^{\mathrm{I}}_{22}(t)\big(\rho^{\mathrm{R}}_{2320}\mu^{\mathrm{I}}_{2330} - \rho^{\mathrm{I}}_{2320}\mu^{\mathrm{R}}_{2330}\big)\Big] \\
= \frac{1}{|\mu_{2330}|^2}\Big[& \big({}^{\mathrm{Y}}\hbar^{\mathrm{R}}_{32}(t) - {}^{\mathrm{Y}}\hbar^{\mathrm{R}}_{22}(t)\rho^{\mathrm{R}}_{2320} - {}^{\mathrm{Y}}\hbar^{\mathrm{I}}_{22}(t)\rho^{\mathrm{I}}_{2320}\big)\mu^{\mathrm{R}}_{2330} \\
& - \big({}^{\mathrm{Y}}\hbar^{\mathrm{I}}_{32}(t) + {}^{\mathrm{Y}}\hbar^{\mathrm{R}}_{22}(t)\rho^{\mathrm{I}}_{2320} - {}^{\mathrm{Y}}\hbar^{\mathrm{I}}_{22}(t)\rho^{\mathrm{R}}_{2320}\big)\mu^{\mathrm{I}}_{2330}\Big].
\end{aligned}
\tag{A.20}
$$

In frequency domain, this takes the following form,

$$
\begin{aligned}
{}^{\mathrm{S}}\tilde{h}^{\mathrm{R}}_{320}(f) \simeq \frac{1}{|\mu_{2330}|^2}\Big[& \big({}^{\mathrm{Y}}\tilde{h}^{\mathrm{R}}_{32}(f) - {}^{\mathrm{Y}}\tilde{h}^{\mathrm{R}}_{22}(f)\rho^{\mathrm{R}}_{2320} - {}^{\mathrm{Y}}\tilde{h}^{\mathrm{I}}_{22}(f)\rho^{\mathrm{I}}_{2320}\big)\mu^{\mathrm{R}}_{2330} \\
& - \big({}^{\mathrm{Y}}\tilde{h}^{\mathrm{I}}_{32}(f) + {}^{\mathrm{Y}}\tilde{h}^{\mathrm{R}}_{22}(f)\rho^{\mathrm{I}}_{2320} - {}^{\mathrm{Y}}\tilde{h}^{\mathrm{I}}_{22}(f)\rho^{\mathrm{R}}_{2320}\big)\mu^{\mathrm{I}}_{2330}\Big],
\end{aligned}
\tag{A.21}
$$

or

$$
{}^{\mathrm{S}}\tilde{h}^{\mathrm{R}}_{320}(f) \simeq \frac{1}{|\mu_{2330}|^2}\Big(\alpha_1\mu^{\mathrm{R}}_{2330} - \alpha_2\mu^{\mathrm{I}}_{2330}\Big), \tag{A.22}
$$

where

$$
\begin{aligned}
\alpha_1 &:= {}^{\mathrm{Y}}\tilde{h}^{\mathrm{R}}_{32}(f) - \Big({}^{\mathrm{Y}}\tilde{h}^{\mathrm{R}}_{22}(f)\rho^{\mathrm{R}}_{2320} + {}^{\mathrm{Y}}\tilde{h}^{\mathrm{I}}_{22}(f)\rho^{\mathrm{I}}_{2320}\Big), \\
\alpha_2 &:= {}^{\mathrm{Y}}\tilde{h}^{\mathrm{I}}_{32}(f) + \Big({}^{\mathrm{Y}}\tilde{h}^{\mathrm{R}}_{22}(f)\rho^{\mathrm{I}}_{2320} - {}^{\mathrm{Y}}\tilde{h}^{\mathrm{I}}_{22}(f)\rho^{\mathrm{R}}_{2320}\Big).
\end{aligned}
\tag{A.23}
$$

Similarly, one can show for the imaginary part,

$$
{}^{\mathrm{S}}\tilde{h}^{\mathrm{I}}_{320}(f) \simeq \frac{1}{|\mu_{2330}|^2}\Big(\alpha_2\mu^{\mathrm{R}}_{2330} + \alpha_1\mu^{\mathrm{I}}_{2330}\Big). \tag{A.24}
$$

A.5 *Mode mixing removal for lower mass ratios*

We give analogs of Figs. 2.3 and 2.8 for a mass ratio of $q = 2.32$ in Figs. A.2 and A.3. The first of these figures illustrates that the mode mixing removal is still effective in improving the agreement of the instantaneous frequency with the expected QNM frequency, and in reducing the amplitude oscillations of the 32 mode. However, the mode mixing removal is less effective for $q \lesssim 3$, for reasons we do not fully understand. Nevertheless, the second figure shows that the

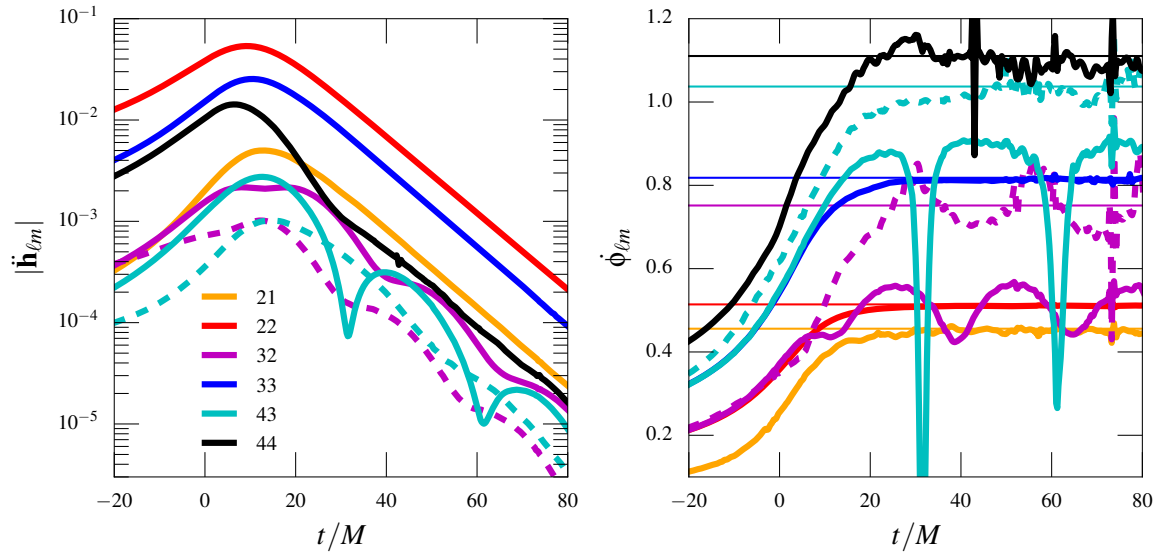

Figure A.2: This is the analog of Fig. 2.3 for mass ratio $q = 2.32$. The left-hand plot shows the mode mixing removal in the time domain amplitude of the second time derivatives of the modes and the right-hand plot shows the effects of the mode mixing removal on the instantaneous frequency of the second time derivatives of the modes. The solid lines show the spherical harmonic modes and the dashed lines show the unmixed spheroidal harmonic 320 and 430 modes constructed using the procedure in Sec. 2.3.1. We see that there are considerably larger oscillations in the instantaneous frequency of the 320 mode than in Fig. 2.3, particularly in the frequency. We also see some numerical noise in the frequency plots, which we find can be attributed to the extrapolation procedure used to obtain the waveform at infinity.

final model for the mixed modes still agrees well with the Fourier transform of the hybrid.

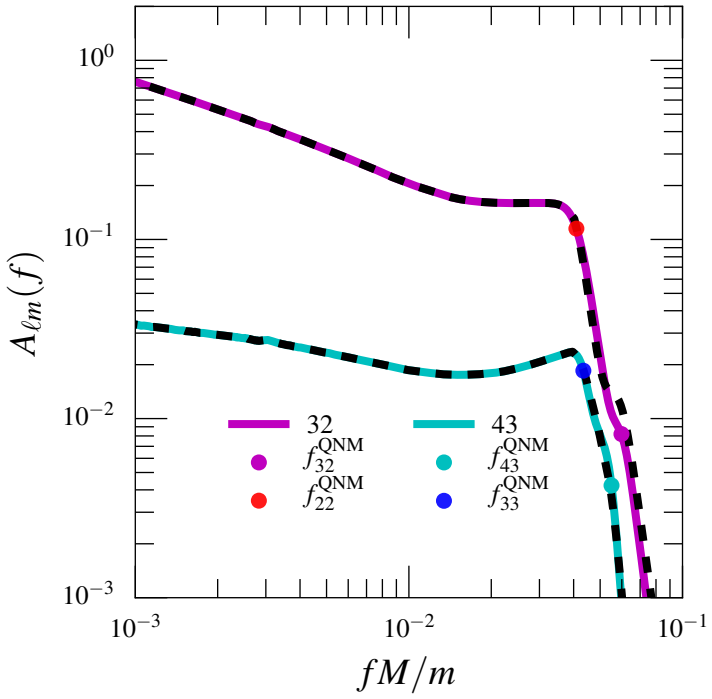

Figure A.3: This is the analog of Fig. 2.8 for mass ratio $q = 2.32$. The solid lines show the amplitude of the hybrid and the dashed lines show the amplitude of our analytical model for the mixed modes (32 and 43). We can see that the model is able to reproduce the hybrid modes quite well, even though our mode-mixing removal method for this mass ratio is less effective as compared to the same for higher mass ratios.

The numerical noise we find in the instantaneous frequency of the modes is reduced when considering the NR waveform with no extrapolation to infinity. Experimentation with the equal-mass non-

spinning Cauchy-characteristic extraction SXS waveform from [135] finds that this does not suffer from the numerical noise that is present in the instantaneous frequencies of the analogous finite radius or extrapolated equal-mass nonspinning SXS waveform modes.

A.6 *Generating samples of strongly lensed and multiply imaged binary mergers*

In this section, we outline our method for generating samples of strongly lensed and multiply imaged binary merger events. We will use results for strong lensing probabilities that have been derived earlier (see e.g., [92, 57]). Given below is a brief summary of our method and assumptions:

1. Given a source redshift, the bulk of the magnification probability describes cases with a single lensed image [132, 61]. We are interested in multiply imaged mergers, so we do not need to accurately model the cases with single images.

2. Multiple images dominantly arise due to galaxy lenses [76]. We model individual strong lenses as isothermal ellipses with nonzero ellipticity.

3. Singular isothermal ellipsoid (SIE) lens models have a surface mass density that diverges at the center. These lenses produce either two or four images [92].

4. The lens model has two parameters: velocity dispersion σ and axis-ratio q. We generate these parameters with distributions taken from the SDSS galaxy population [57]. The axis-ratio does not dramatically change the strong lensing cross section, so we can estimate overall rates in the manner of Ref. [150].

A.6.1 Probability of multiple imaging

Given the assumptions that are outlined above, the multiple imaging optical depth $\tau(z_s)$ to a given source redshift z_s is [150]:

$$\tau(z_s) = \int_0^{z_s} \frac{d\tau}{dz_l} dz_l, \tag{A.25}$$

where the differential optical depth per unit lens redshift z_l is

$$\frac{d\tau}{dz_l} = \int d\sigma\, n(z_l) \frac{dp}{d\sigma} (1+z_l)^3 \frac{cdt}{dz_l} \pi D_l(z_l)^2 \theta^2(\sigma, z_l, z_s). \tag{A.26}$$

Here, σ is the lens' velocity dispersion, $n(z_l)$ is the comoving number density of lenses, $dp/d\sigma$ is the PDF of the velocity dispersion σ, D_l is the angular diameter distance to the lens, and θ is the angular Einstein radius of a singular isothermal sphere (SIS) lens. We assume a constant number density and an unchanging PDF of the velocity dispersion, which are reasonable for galaxy lenses at relatively low redshifts [41].

Let us start with the parameters for the population of early-type galaxies from Ref. [56]: the number density $n = 8 \times 10^{-3} h^3 \mathrm{Mpc}^{-3}$, and the distribution of velocity dispersion (VDF) is

$$\frac{dp}{d\sigma} = \left(\frac{\sigma}{\sigma_*}\right)^{\alpha} \exp\left[-\left(\frac{\sigma}{\sigma_*}\right)^{\beta}\right] \frac{\beta}{\Gamma(\alpha/\beta)} \frac{1}{\sigma}, \tag{A.27}$$

where $\alpha = 2.32$, $\beta = 2.67$, and $\sigma_* = 161\,\mathrm{km\,s^{-1}}$. Substituting the Einstein radius for a SIS $\theta = 4\pi(\sigma^2/c^2) D_{ls}/D_s$ in Eq. (A.26), we get

$$\frac{d\tau}{dz_l} = 16\pi^3 (1+z_l)^2 \frac{c\,n}{H(z_l)} \left(\frac{D_l D_{ls}}{D_s}\right)^2 \left(\frac{\sigma_*}{c}\right)^4 \frac{\Gamma([4+\alpha]/\beta)}{\Gamma(\alpha/\beta)}. \tag{A.28}$$

The total multiple-imaging optical depth is

$$\begin{aligned}\tau(z_s) &= 16\pi^3 cn \left(\frac{\sigma_*}{c}\right)^4 \frac{\Gamma(\frac{4+\alpha}{\beta})}{\Gamma(\alpha/\beta)} \int_0^{z_s} dz_l (1+z_l)^2 \frac{1}{H(z_l)} \left(\frac{D_l D_{ls}}{D_s}\right)^2 \\ &= 16\pi^3 n \left(\frac{\sigma_*}{c}\right)^4 \frac{\Gamma(\frac{4+\alpha}{\beta})}{\Gamma(\alpha/\beta)} \int_0^{D_s^c} dD_l^c \, D_l^{c2} \left(1 - \frac{D_l^c}{D_s^c}\right)^2 \end{aligned} \tag{A.29}$$

$$\begin{aligned} &= 16\pi^3 \left(\frac{\sigma_*}{c}\right)^4 \frac{\Gamma(\frac{4+\alpha}{\beta})}{\Gamma(\alpha/\beta)} \frac{n D_s^{c3}}{30} \\ &= 4.17 \times 10^{-6} \left(\frac{D_s^c}{\mathrm{Gpc}}\right)^3 . \end{aligned} \tag{A.30}$$

In the last line, we have written the result in terms of the comoving distance $D^c(z) = \int_0^z dz' \, c/H(z')$, and used D_l^c and D_s^c to denote $D^c(z_l)$ and $D^c(z_s)$, respectively. For the simulations in this work, we use the following values for the cosmological parameters in the ΛCDM model: $H_0 = 70 \mathrm{Km\,s^{-1}Mpc^{-1}}$ and $\Omega_\Lambda = 0.7$.

Ref. [109] use a similar scaling as in Eq. (A.30) for the strong lensing optical depth. However, their normalization (as derived in Ref. [76]) is larger by a factor of 6.3. The difference arises because the number density and VDFs provided in Ref. [56] are fits to the SDSS population of early-type galaxies, which dominate the high velocity-dispersion end (and can be dominantly selected for in strong lensing surveys). Ref. [36] provide the number densities and VDFs for the entire galaxy population, and obtain a similar enhancement in the total characteristic number density n (and even larger characteristic velocity dispersions for early-type galaxies). The selection effects for GW lensing are very different from those for optical surveys (obscuration by the stellar light from the lens galaxy is not an issue), and hence, it is appropriate to use all lens galaxies when forward-modeling the population of lensed sources. However, this difference is immaterial for our study.

A.6.2 Method to generate samples of lensed events

In this section, we outline our method for drawing samples of strongly lensed mergers from a given source distribution.

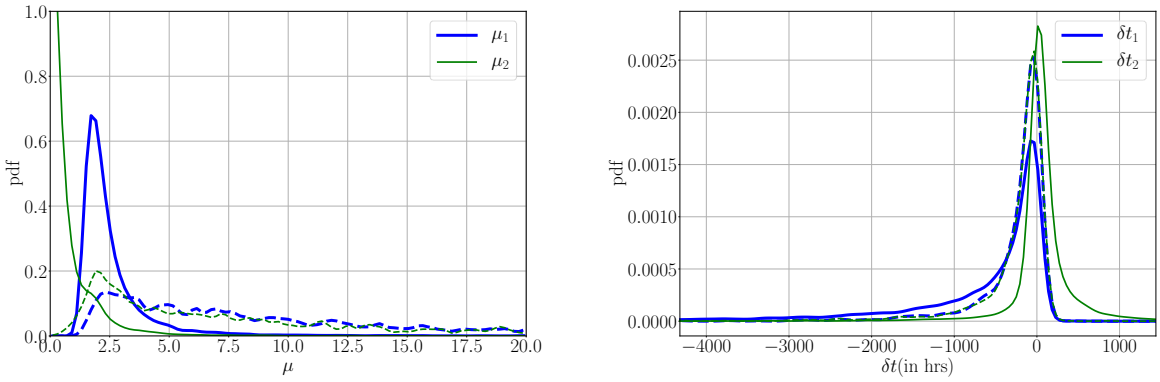

Figure A.4: Distributions of the magnifications μ_1, μ_2 (left) and the arrival times $\delta t_1, \delta t_2$ relative to unlensed arrival time (right) of the two dominant images for simulated events (See Eqs. A.41 ans A.42). Solid (dashed) traces show distributions before (after) applying the detection threshold SNR $\geq$ 8. The component masses of the simulated events are sampled from power law 1 distribution.

1. *Pick a source:* We start with a merger whose intrinsic parameters (total mass $M = m_1 + m_2$, symmetric mass ratio $\eta = m_1 m_2 / M^2$, and dimensionless spins χ_1 and χ_2) are drawn from given distributions. In addition, we randomly draw the angles (ι, ψ) associated with the binary's plane so that its orbital angular momentum is distributed uniformly over the sphere, and randomly draw its position $(\cos\alpha, \delta)$ so that the binaries are uniformly distributed in the sky. The redshift z_s is distributed as given in [69] (see, Fig. 5.4). See, Sec. 5.2 for more details.

2. *Accept/reject according to the multiple imaging probability*: Given the source redshift z_s, we read off the multiple–imaging probability $\tau(z_s)$ from (the enhanced version of) Eq. (A.30). If $\tau(z_s)$ is larger than a random number uniformly distributed between 0 and 1, we proceed to step 3. If not, we discard this source.

3. *Draw the lens redshift:* If the merger survives step 2, we draw a sample r from the PDF

$$p(x) = 30\, x^2 (1-x)^2, \qquad 0 < x < 1. \tag{A.31}$$

and compute a sample lens comoving distance using $D^c(z_l) = r\, D^c(z_s)$; we obtain the lens redshift z_l by inverting $D^c(z_l)$. Using Eq. (A.29), we see that if a source at z_s is multiply imaged, this procedure yields lens redshifts with the right posterior distribu-

tion.

4. *Draw the lens parameters:* We use the fits for the distribution of the lens parameters from Ref. [57]. We draw a parameter a from a generalized Gamma distribution

$$p(x) = x^{\alpha-1} \exp\left(-x^{\beta}\right) \frac{\beta}{\Gamma(\alpha/\beta)}, \tag{A.32}$$

where $\alpha = 2.32, \beta = 2.67$, and set $\sigma = 161\,\mathrm{km\,s^{-1}} \times a$. We next sample the distribution of the axis ratio of the lens. Given the above sample of a, we repeatedly draw parameter b from a Rayleigh distribution

$$g(x) = \frac{x}{s^2} \exp\left(-\frac{x^2}{2s^2}\right), \qquad 0 < x < \infty, \tag{A.33}$$

where,

$$s = 0.38 + 0.09177\,a, \tag{A.34}$$

until we get a sample $b < 0.8$. We then set the axis ratio $q = 1 - b$.

5. *Draw a source–plane location:* Given a lens with the above parameters, we then sample the source–plane location of the merger. Since we have already determined that it is multiply imaged, we only need to get the right posterior distribution of the source, which is a uniform distribution within the cut/caustics of the lens model. A complication is that we cannot analytically calculate the intersection of the two and four image regions for small values of the axis ratio. Our approach will be to use the results in Ref. [92], and draw with repetition. The idea is to repeatedly draw points (y_1, y_2) within a certain range, and solve the lens equation (as detailed in Step 6), until we obtain a location with multiple images.

Given axis ratio q, we draw coordinates y_1 and y_2 from uniform

distributions in the following ranges:

$$y_1 \in \left(0, \sqrt{\frac{q}{1-q^2}}\,\text{arccosh}\left[\frac{1}{q}\right]\right), \tag{A.35}$$

$$y_2 \in \begin{cases} \left(0, \sqrt{\frac{q}{1-q^2}}\,\arccos\left[q\right]\right), & \text{if } q > q_0 \\ \left(0, \sqrt{\frac{1}{q}} - \sqrt{\frac{q}{1-q^2}}\,\arccos\left[q\right]\right), & \text{if } q < q_0 \end{cases} \tag{A.36}$$

Here $q_0 = 0.3942$ is the numerical solution to the transcendental equation $2q_0 \arccos q_0 = \sqrt{1-q_0^2}$.

6. *Solve the lens equation:* Given y_1, y_2, and q, we numerically find all roots of the one-dimensional equation

$$\left[y_1 + \sqrt{\frac{q}{1-q^2}}\text{arcsinh}\left(\frac{\sqrt{1-q^2}}{q}\cos\phi\right)\right]\sin\phi - \left[y_2 + \sqrt{\frac{q}{1-q^2}}\arcsin\left(\sqrt{1-q^2}\sin\phi\right)\right]\cos\phi = 0 \tag{A.37}$$

in the interval $[0, 2\pi)$. Assuming that we get solutions $\{\phi_1, \phi_2, \cdots\}$, we only retain those ϕ_i that satisfy the condition

$$\left[y_1 + \sqrt{\frac{q}{1-q^2}}\text{arcsinh}\left(\frac{\sqrt{1-q^2}}{q}\cos\phi_i\right)\right]\cos\phi_i + \left[y_2 + \sqrt{\frac{q}{1-q^2}}\arcsin\left(\sqrt{1-q^2}\sin\phi_i\right)\right]\sin\phi_i > 0 \tag{A.38}$$

If the final list of solutions only contains one element, we go back to Step 5 and repeat until we get a case with a set $\{\phi_i\}$ with with multiple elements.

7. *Read off image magnifications and time delays:* The deflections are typically small relative to the GW localization uncertainties, so we ignore the differences between image positions on the sky while computing the GW signal. However, we need the positions to calculate the magnifications and time delays from the lens model.

   Given the list of solutions $\{\phi_1, \phi_2, \cdots\}$ from Step 6, and the source position (y_1, y_2) for each image, we compute the image positions

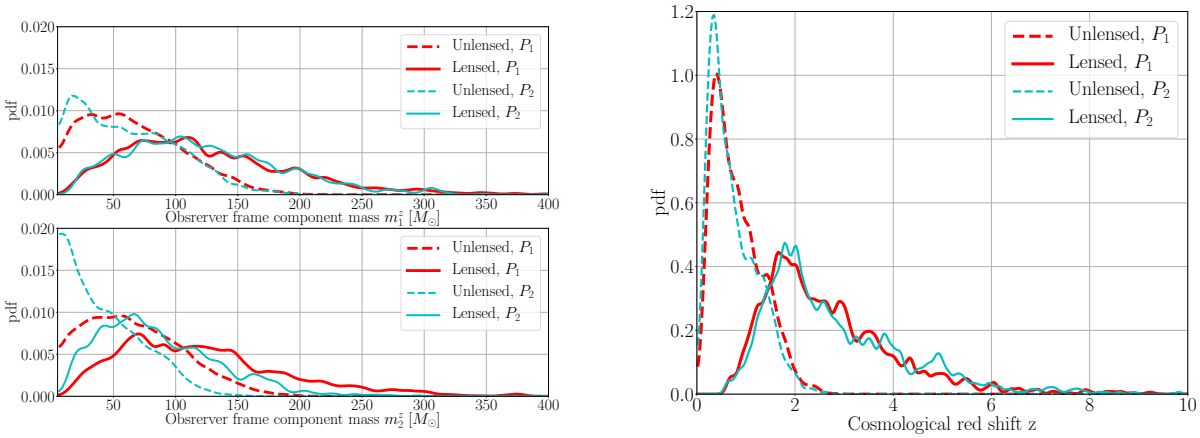

Figure A.5: *Left panel:* The distributions of red shifted component masses m_1^z and m_2^z for unlensed and lensed simulated events producing an SNR ≥ 8 in the Advanced LIGO-Virgo network. Solid and dashed curved correspond to the source frame mass distributions P_1 and P_2, respectively. *Right panel:* The red shift distributions of detectable (SNR ≥ 8) unlensed and lensed simulated events.

$(x_{1,i}, x_{2,i})$ as follows:

$$x_{1,i} = y_1 + \sqrt{\frac{q}{1-q^2}}\,\text{arcsinh}\left(\frac{\sqrt{1-q^2}}{q}\cos\phi_i\right), \tag{A.39}$$

$$x_{2,i} = y_2 + \sqrt{\frac{q}{1-q^2}}\,\arcsin\left(\sqrt{1-q^2}\,\sin\phi_i\right) \tag{A.40}$$

The magnifications of the images are given by

$$\mu_i = \left(1 - \sqrt{\frac{q}{x_{1,i}^2 + q^2 x_{2,i}^2}}\right)^{-1}. \tag{A.41}$$

The arrival times of the images relative to some common base time), are:

$$\begin{aligned}\delta t_i &= 16\pi^2 \frac{D^c(z_l)}{c}\left(\frac{\sigma}{c}\right)^4 \left[1 - \frac{D^c(z_l)}{D^c(z_s)}\right]\Phi_i \\ &= 1.35\times 10^6\,\text{s}\left(\frac{D^c(z_l)}{1\,\text{Gpc}}\right)\left(\frac{\sigma}{161\,\text{km s}^{-1}}\right)^4 \left[1 - \frac{D^c(z_l)}{D^c(z_s)}\right]\Phi_i,\end{aligned} \tag{A.42}$$

where

$$\begin{aligned}\Phi_i = \frac{1}{2}(\mathbf{x}_i - \mathbf{y})^2 - \sqrt{\frac{q(x_{1,i}^2 + x_{2,i}^2)}{1-q^2}}\ \times \\ \left[\sin\phi_i \arcsin\left(\sqrt{1-q^2}\sin\phi_i\right) + \cos\phi_i\,\text{arcsinh}\left(\frac{\sqrt{1-q^2}}{q}\cos\phi_i\right)\right],\end{aligned} \tag{A.43}$$

where σ is the velocity dispersion drawn in Step 4.

Figure A.4 shows the distributions of μ_i and δt_i corresponding to two prominent images for simulated events before and after applying the detection threshold (SNR=8) in LIGO-Virgo network.

A.6.3 Simulating GW observations

Appendix A.6.2 describes how we draw random samples of the binary's parameters. Strongly lensed events produced multiple values of the magnification $\{\mu_i\}$ and time delay $\{\delta t_i\}$. Multiply imaged GW signals can be generated by multiplying the original signal with the magnification factor and by applying the lensing time delay

$$h^{\rm lens}_{+,\times,i}(f;\boldsymbol{\lambda}) = \sqrt{\mu_i}\, \exp\left(\mathrm{i}\, 2\pi f \delta t_i\right)\, h_{+,\times}(f;\boldsymbol{\lambda}), \tag{A.44}$$

where $h_{+,\times}(f;\boldsymbol{\lambda})$ are the two polarizations of the original GW signal in Fourier domain corresponding to a set of parameters $\boldsymbol{\lambda}$, f is the Fourier frequency and $\mathrm{i} := \sqrt{-1}$. In practice, we compute different gravitational waveforms by rescaling the luminosity distance d_L by $1/\sqrt{\mu_i}$, at different times $t_0 + \delta t_i$, where t_0 is a fiducial reference time. We then project these polarizations on to the Advanced LIGO-Virgo network and compute the optimal signal-to-noise ratio

$$\rho^{\rm lens}_i = 2\left(\sum_D \int_{f_{\rm low}}^{\infty} \frac{h^{\rm lens}_{D,i}(f)^2}{S_D(f)} df\right)^{1/2}. \tag{A.45}$$

Above, the summation is over different detectors, $h^{\rm lens}_{D,i}(f) := F_{+,D}(\alpha,\delta,\psi)\, h^{\rm lens}_{+,i}(f) + F_{\times,D}(\alpha,\delta,\psi)\, h^{\rm lens}_{\times,i}(f)$ denote the observed signal in detector D whose noise has a one-sided power spectral density $S_D(f)$. The antenna patterns of the detector D is denoted as $F_{+,D}$ and $F_{\times,D}$, which are functions of the source position α, δ and polarization angle ψ. The low-frequency cutoff is chosen to be $f_{\rm low} = 20$ Hz. If at least two images have the network SNR ρ_i greater than a threshold of 8, we consider them as strong-lensing detections. In our simulation, the fraction of events with more than two detectable images is

negligible. We compute the Bayes factors described in Sec. 5.1 using pairs of lensed events as described in Sec. 5.2. Figure A.5 shows the mass and red shift distributions of detectable events.

List of Figures

List of Tables

B Bibliography

[1] M. Boyle (private communication).

[2] URL https://wiki.ligo.org/DASWG/LALSuite.

[3] URL http://www.black-holes.org/waveforms/. SXS Gravitational Waveform Database.

[4] Advanced LIGO anticipated sensitivity curves. URL https://dcc.ligo.org/LIGO-T0900288/public. LIGO Document T0900288-v3.

[5] Updated Advanced LIGO sensitivity design curve, LIGO Document T1800044-v5, https://dcc.ligo.org/LIGO-T1800044/public.

[6] Advanced ligo reference design. Technical Report LIGO-M060056-v2, LIGO Document Control Center, April 2009. URL https://dcc.ligo.org/LIGO-M060056/public.

[7] The updated advanced ligo design curve. Technical Report LIGO-T1800044-v5, LIGO Document Control Center, April 2018. URL https://dcc.ligo.org/T1800044-v5.

[8] J. Aasi et al. Advanced LIGO. *Class. Quant. Grav.*, 32:074001, 2015. DOI: 10.1088/0264-9381/32/7/074001.

[9] B. P. Abbott et al. The Rate of Binary Black Hole Mergers Inferred from Advanced LIGO Observations Surrounding GW150914. *Astrophys. J.*, 833(1):L1, 2016. DOI: 10.3847/2041-8205/833/1/L1.

[10] B. P. Abbott et al. Properties of the Binary Black Hole Merger GW150914. *Phys. Rev. Lett.*, 116(24):241102, 2016. DOI: 10.1103/PhysRevLett.116.241102.

[11] B. P. Abbott et al. Observation of gravitational waves from a binary black hole merger. *Phys. Rev. Lett.*, 116:061102, Feb 2016. DOI: 10.1103/PhysRevLett.116.061102. URL http://link.aps.org/doi/10.1103/PhysRevLett.116.061102.

[12] B. P. Abbott et al. Gw151226: Observation of gravitational waves from a 22-solar-mass binary black hole coalescence. *Phys. Rev. Lett.*, 116:241103, Jun 2016. DOI: 10.1103/PhysRevLett.116.241103. URL http://link.aps.org/doi/10.1103/PhysRevLett.116.241103.

[13] B. P. Abbott et al. Gw170104: Observation of a 50-solar-mass binary black hole coalescence at redshift 0.2. *Phys. Rev. Lett.*, 118:221101, Jun 2017. DOI: 10.1103/PhysRevLett.118.221101. URL https://link.aps.org/doi/10.1103/PhysRevLett.118.221101.

[14] B. P. Abbott et al. Gw170104: Observation of a 50-solar-mass binary black hole coalescence at redshift 0.2. *Phys. Rev. Lett.*, 118:221101, Jun 2017. DOI: 10.1103/PhysRevLett.118.221101. URL https://link.aps.org/doi/10.1103/PhysRevLett.118.221101.

[15] B.. P.. Abbott et al. GW170608: Observation of a 19-solar-mass Binary Black Hole Coalescence. *Astrophys. J.*, 851(2):L35, 2017. DOI: 10.3847/2041-8213/aa9f0c.

[16] B. P. Abbott et al. Gw170814: A three-detector observation of gravitational waves from a binary black hole coalescence. *Phys. Rev. Lett.*, 119:141101, Oct 2017. DOI: 10.1103/PhysRevLett.119.141101. URL https://link.aps.org/doi/10.1103/PhysRevLett.119.141101.

[17] B. P. Abbott et al. Gw170817: Observation of gravitational waves from a binary neutron star inspiral. *Phys. Rev. Lett.*, 119:161101, Oct 2017. DOI: 10.1103/PhysRevLett.119.161101. URL https://link.aps.org/doi/10.1103/PhysRevLett.119.161101.

[18] B. P. Abbott et al. GWTC-1: A Gravitational-Wave Transient Catalog of Compact Binary Mergers Observed by LIGO and Virgo during the First and Second Observing Runs. 2018.

[19] B. P. Abbott et al. Tests of General Relativity with the Binary Black Hole Signals from the LIGO-Virgo Catalog GWTC-1. 2019.

[20] Benjamin P. Abbott et al. Effects of waveform model systematics on the interpretation of GW150914. *Class. Quant. Grav.*, 34 (10):104002, 2017. DOI: 10.1088/1361-6382/aa6854.

[21] B. P. Abbott et al. Binary black hole mergers in the first advanced ligo observing run. *Phys. Rev. X*, 6:041015, Oct 2016. DOI: 10.1103/PhysRevX.6.041015. URL http://link.aps.org/doi/10.1103/PhysRevX.6.041015.

[22] B. P. Abbott et al. Observation of gravitational waves from a binary black hole merger. *Phys. Rev. Lett.*, 116:061102, Feb 2016. DOI: 10.1103/PhysRevLett.116.061102. URL http://link.aps.org/doi/10.1103/PhysRevLett.116.061102.

[23] B. P. Abbott et al. Tests of general relativity with gw150914. *Phys. Rev. Lett.*, 116:221101, May 2016. DOI: 10.1103/PhysRevLett.116.221101. URL http://link.aps.org/doi/10.1103/PhysRevLett.116.221101.

[24] B. P. Abbott et al. (LIGO Scientific Collaboration). The Rate of Binary Black Hole Mergers Inferred from Advanced LIGO Observations Surrounding GW150914. *ArXiv e-prints*, February 2016.

[25] F. Acernese et al. Advanced Virgo: a second-generation interferometric gravitational wave detector. *Class. Quant. Grav.*, 32 (2):024001, 2015. DOI: 10.1088/0264-9381/32/2/024001.

[26] P. Ajith. Gravitational-wave data analysis using binary black-hole waveforms. *Class. Quant. Grav.*, 25:114033, 2008. DOI: 10.1088/0264-9381/25/11/114033.

[27] P. Ajith, M. Hannam, S. Husa, Y. Chen, B. Brügmann, N. Dorband, D. Müller, F. Ohme, D. Pollney, C. Reisswig, L. Santamaría, and J. Seiler. Inspiral-merger-ringdown waveforms for black-hole binaries with nonprecessing spins. *Phys. Rev. Lett.*, 106(24):241101, Jun 2011. DOI: 10.1103/PhysRevLett.106.241101.

[28] P. Ajith et al. Data formats for numerical relativity waves. September 2007.

[29] P. Ajith et al. A template bank for gravitational waveforms from coalescing binary black holes: I. non-spinning binaries. *Phys. Rev. D*, 77:104017, 2008. DOI: 10.1103/PhysRevD.77.104017.

[30] Parameswaran Ajith et al. Phenomenological template family for black-hole coalescence waveforms. *Class. Quant. Grav.*, 24: S689–S699, 2007.

[31] K. G. Arun, Luc Blanchet, Bala R. Iyer, and Moh'd S. S. Qusailah. The 2.5PN gravitational wave polarisations from inspiralling compact binaries in circular orbits. *Class. Quant. Grav.*, 21:3771–3802, 2004. DOI: 10.1088/0264-9381/21/15/010. [Erratum: Class. Quant. Grav.22,3115(2005)].

[32] K. G. Arun et al. Massive Black Hole Binary Inspirals: Results from the LISA Parameter Estimation Taskforce. *Class. Quant. Grav.*, 26:094027, 2009. DOI: 10.1088/0264-9381/26/9/094027.

[33] K.G. Arun, Bala R. Iyer, B.S. Sathyaprakash, Siddhartha Sinha, and Chris Van Den Broeck. Higher signal harmonics, LISA's angular resolution and dark energy. *Phys.Rev.*, D76:104016, 2007. DOI: 10.1103/PhysRevD.76.129903, 10.1103/PhysRevD.76.104016.

[34] Stanislav Babak, Andrea Taracchini, and Alessandra Buonanno. Validating the effective-one-body model of spinning, precessing binary black holes against numerical relativity. *Phys. Rev. D*, 95(2):024010, 2017. DOI: 10.1103/PhysRevD.95.024010.

[35] Matthias Bartelmann. Gravitational Lensing. *Class. Quant. Grav.*, 27:233001, 2010. DOI: 10.1088/0264-9381/27/23/233001.

[36] M. Bernardi, F. Shankar, J. B. Hyde, S. Mei, F. Marulli, and R. K. Sheth. Galaxy luminosities, stellar masses, sizes, velocity dispersions as a function of morphological type. *Monthly Notices of the Royal Astronomical Society*, 404:2087–2122, June 2010. DOI: 10.1111/j.1365-2966.2010.16425.x.

[37] Emanuele Berti and Antoine Klein. Mixing of spherical and spheroidal modes in perturbed Kerr black holes. *Phys. Rev.*, D90(6):064012, 2014. DOI: 10.1103/PhysRevD.90.064012.

[38] Emanuele Berti, Vitor Cardoso, and Marc Casals. Eigenvalues and eigenfunctions of spin-weighted spheroidal harmonics in four and higher dimensions. *Phys. Rev. D*, 73:024013, 2006. DOI: 10.1103/PhysRevD.73.109902. **73**, 109902(E) (2006).

[39] Emanuele Berti, Vitor Cardoso, and Andrei O. Starinets. Quasinormal modes of black holes and black branes. *Class. Quant. Grav.*, 26:163001, 2009. DOI: 10.1088/0264-9381/26/16/163001.

[40] Emanuele Berti, Alberto Sesana, Enrico Barausse, Vitor Cardoso, and Krzysztof Belczynski. Spectroscopy of Kerr

black holes with Earth- and space-based interferometers. *Phys. Rev. Lett.*, 117(10):101102, 2016. DOI: 10.1103/PhysRevLett.117.101102.

[41] R. Bezanson, P. G. van Dokkum, M. Franx, G. B. Brammer, J. Brinchmann, M. Kriek, I. Labbé, R. F. Quadri, H.-W. Rix, J. van de Sande, K. E. Whitaker, and R. J. Williams. Redshift Evolution of the Galaxy Velocity Dispersion Function. *apjl*, 737: L31, August 2011. DOI: 10.1088/2041-8205/737/2/L31.

[42] M. Biesiada, X. Ding, A. Piórkowska, and Z.-H. Zhu. Strong gravitational lensing of gravitational waves from double compact binariesmdashperspectives for the Einstein Telescope. *Journal of Cosmology and Astroparticle Physics*, 10:080, October 2014. DOI: 10.1088/1475-7516/2014/10/080.

[43] Luc Blanchet, Bala R. Iyer, Clifford M. Will, and Alan G. Wiseman. Gravitational wave forms from inspiralling compact binaries to second postNewtonian order. *Class. Quant. Grav.*, 13: 575–584, 1996. DOI: 10.1088/0264-9381/13/4/002.

[44] Luc Blanchet, Thibault Damour, Gilles Esposito-Farese, and Bala R. Iyer. Gravitational radiation from inspiralling compact binaries completed at the third post-Newtonian order. *Phys. Rev. Lett.*, 93:091101, 2004. DOI: 10.1103/PhysRevLett.93.091101.

[45] Luc Blanchet, Guillaume Faye, Bala R. Iyer, and Siddhartha Sinha. The Third post-Newtonian gravitational wave polarisations and associated spherical harmonic modes for inspiralling compact binaries in quasi-circular orbits. *Class.Quant.Grav.*, 25:165003, 2008. DOI: 10.1088/0264-9381/25/16/165003, 10.1088/0264-9381/29/23/239501.

[46] Alejandro BohÃl′ et al. Improved effective-one-body model of spinning, nonprecessing binary black holes for the era

of gravitational-wave astrophysics with advanced detectors. *Phys. Rev.*, D95(4):044028, 2017. DOI: 10.1103/PhysRevD.95.044028.

[47] T. Broadhurst, J. M. Diego, and G. Smoot, III. Reinterpreting Low Frequency LIGO/Virgo Events as Magnified Stellar-Mass Black Holes at Cosmological Distances. *ArXiv e-prints*, February 2018.

[48] Tom Broadhurst, Jose M. Diego, and George F. Smoot. Twin LIGO/Virgo Detections of a Viable Gravitationally-Lensed Black Hole Merger. 2019.

[49] A. Buonanno and T. Damour. Effective one-body approach to general relativistic two-body dynamics. *Phys. Rev.*, D59:084006, 1999. DOI: 10.1103/PhysRevD.59.084006.

[50] Alessandra Buonanno and Thibault Damour. Transition from inspiral to plunge in binary black hole coalescences. *Phys. Rev.*, D62:064015, 2000. DOI: 10.1103/PhysRevD.62.064015.

[51] Alessandra Buonanno, Gregory B. Cook, and Frans Pretorius. Inspiral, merger and ring-down of equal-mass black-hole binaries. *Phys. Rev.*, D75:124018, 2007. DOI: 10.1103/PhysRevD.75.124018.

[52] Juan Calderón Bustillo, Sascha Husa, Alicia M. Sintes, and Michael Pürrer. Impact of gravitational radiation higher order modes on single aligned-spin gravitational wave searches for binary black holes. *Phys. Rev. D*, 93:084019, Apr 2016. DOI: 10.1103/PhysRevD.93.084019. URL `http://link.aps.org/doi/10.1103/PhysRevD.93.084019`.

[53] Juan CalderÃşn Bustillo, Alejandro BohÃl', Sascha Husa, Alicia M. Sintes, Mark Hannam, and Michael PÃijrrer. Comparison of subdominant gravitational wave harmonics between post-Newtonian and numerical relativity calculations and construction of multi-mode hybrids. 2015.

[54] B. Carter. Axisymmetric black hole has only two degrees of freedom. *Phys. Rev. Lett.*, 26:331–333, Feb 1971. DOI: 10.1103/PhysRevLett.26.331. URL https://link.aps.org/doi/10.1103/PhysRevLett.26.331.

[55] S. Chandrasekhar and Steven L. Detweiler. The quasi-normal modes of the Schwarzschild black hole. *Proc. Roy. Soc. Lond.*, A344:441–452, 1975. DOI: 10.1098/rspa.1975.0112.

[56] Y.-Y. Choi, C. Park, and M. S. Vogeley. Internal and Collective Properties of Galaxies in the Sloan Digital Sky Survey. *apj*, 658: 884–897, April 2007. DOI: 10.1086/511060.

[57] T. E. Collett. The Population of Galaxy-Galaxy Strong Lenses in Forthcoming Optical Imaging Surveys. *apj*, 811:20, September 2015. DOI: 10.1088/0004-637X/811/1/20.

[58] Thomas E. Collett. The population of galaxyâĂŞgalaxy strong lenses in forthcoming optical imaging surveys. *The Astrophysical Journal*, 811(1):20, 2015. URL http://stacks.iop.org/0004-637X/811/i=1/a=20.

[59] Roberto Cotesta, Alessandra Buonanno, Alejandro Bohé, Andrea Taracchini, Ian Hinder, and Serguei Ossokine. Enriching the Symphony of Gravitational Waves from Binary Black Holes by Tuning Higher Harmonics. *Phys. Rev. D*, 98(8):084028, 2018. DOI: 10.1103/PhysRevD.98.084028.

[60] L. Dai and T. Venumadhav. On the waveforms of gravitationally lensed gravitational waves. *ArXiv e-prints*, February 2017.

[61] L. Dai, T. Venumadhav, and K. Sigurdson. Effect of lensing magnification on the apparent distribution of black hole mergers. *prd*, 95(4):044011, February 2017. DOI: 10.1103/PhysRevD.95.044011.

[62] Liang Dai and Tejaswi Venumadhav. On the waveforms of gravitationally lensed gravitational waves. 2017.

[63] T. Damour, B R Iyer, and B S Sathyaprakash. Improved filters for gravitational waves from inspiraling compact binaries. *Phys. Rev. D*, 57:885–907, 1998.

[64] Thibault Damour and Alessandro Nagar. An improved analytical description of inspiralling and coalescing black-hole binaries. *Phys. Rev. D*, 79:081503, 2009. DOI: 10.1103/PhysRevD.79.081503.

[65] Thibault Damour, Bala R. Iyer, and Alessandro Nagar. Improved resummation of post-Newtonian multipolar waveforms from circularized compact binaries. *Phys. Rev.*, D79: 064004, 2009. DOI: 10.1103/PhysRevD.79.064004.

[66] Thibault Damour, Alessandro Nagar, and Sebastiano Bernuzzi. Improved effective-one-body description of coalescing nonspinning black-hole binaries and its numerical-relativity completion. *Phys. Rev.*, D87(8):084035, 2013. DOI: 10.1103/PhysRevD.87.084035.

[67] Siddharth Dhanpal, Abhirup Ghosh, Ajit Kumar Mehta, Parameswaran Ajith, and B. S. Sathyaprakash. A no-hair test for binary black holes. *Phys. Rev. D*, 99(10):104056, 2019. DOI: 10.1103/PhysRevD.99.104056.

[68] X. Ding, M. Biesiada, and Z.-H. Zhu. Strongly lensed gravitational waves from intrinsically faint double compact binariesmdashprediction for the Einstein Telescope. *Journal of Cosmology and Astroparticle Physics*, 12:006, December 2015. DOI: 10.1088/1475-7516/2015/12/006.

[69] Michal Dominik, Krzysztof Belczynski, Christopher Fryer, Daniel E. Holz, Emanuele Berti, Tomasz Bulik, Ilya Mandel, and Richard O'Shaughnessy. Double Compact Objects II: Cosmological Merger Rates. *Astrophys. J.*, 779:72, 2013. DOI: 10.1088/0004-637X/779/1/72.

[70] Olaf Dreyer, Bernard J. Kelly, Badri Krishnan, Lee Samuel Finn, David Garrison, and Ramon Lopez-Aleman. Black hole spectroscopy: Testing general relativity through gravitational wave observations. *Class. Quant. Grav.*, 21:787–804, 2004. DOI: 10.1088/0264-9381/21/4/003.

[71] F. W. Dyson, A. S. Eddington, and C. Davidson. A Determination of the Deflection of Light by the Sun's Gravitational Field, from Observations Made at the Total Eclipse of May 29, 1919. *Philosophical Transactions of the Royal Society of London Series A*, 220:291–333, 1920. DOI: 10.1098/rsta.1920.0009.

[72] Xi-Long Fan, Kai Liao, Marek Biesiada, Aleksandra Piorkowska-Kurpas, and Zong-Hong Zhu. Speed of Gravitational Waves from Strongly Lensed Gravitational Waves and Electromagnetic Signals. *Phys. Rev. Lett.*, 118(9):091102, 2017. DOI: 10.1103/physrevlett.118.091102, 10.1103/PhysRevLett.118.091102.

[73] Marc Favata. The gravitational-wave memory effect. *Class. Quant. Grav.*, 27:084036, 2010. DOI: 10.1088/0264-9381/27/8/084036.

[74] Guillaume Faye, Sylvain Marsat, Luc Blanchet, and Bala R. Iyer. The third and a half post-Newtonian gravitational wave quadrupole mode for quasi-circular inspiralling compact binaries. *Class. Quant. Grav.*, 29:175004, 2012. DOI: 10.1088/0264-9381/29/17/175004.

[75] Daniel Foreman-Mackey, David W Hogg, Dustin Lang, and Jonathan Goodman. emcee: the mcmc hammer. *Publications of the Astronomical Society of the Pacific*, 125(925):306, 2013.

[76] M. Fukugita and E. L. Turner. Gravitational lensing frequencies - Galaxy cross-sections and selection effects. *Monthly Notices of the Royal Astronomical Society*, 253:99–106, November 1991. DOI: 10.1093/mnras/253.1.99.

[77] Abhirup Ghosh, Nathan K. Johnson-McDaniel, Archisman Ghosh, Chandra Kant Mishra, Parameswaran Ajith, Walter Del Pozzo, Christopher P. L. Berry, Alex B. Nielsen, and Lionel London. Testing general relativity using gravitational wave signals from the inspiral, merger and ringdown of binary black holes. *Classical Quantum Gravity*, 35(1):014002, 2018. DOI: 10.1088/1361-6382/aa972e.

[78] Jonathan Goodman and Jonathan Weare. Ensemble samplers with affine invariance. *Communications in applied mathematics and computational science*, 5(1):65–80, 2010.

[79] S. Gossan, J. Veitch, and B. S. Sathyaprakash. Bayesian model selection for testing the no-hair theorem with black hole ringdowns. *Phys. Rev.*, D85:124056, 2012. DOI: 10.1103/PhysRevD.85.124056.

[80] Philip B. Graff, Alessandra Buonanno, and B. S. Sathyaprakash. Missing Link: Bayesian detection and measurement of intermediate-mass black-hole binaries. *Phys. Rev.*, D92(2):022002, 2015. DOI: 10.1103/PhysRevD.92.022002.

[81] Mark Hannam, Patricia Schmidt, Alejandro BohÃl', LeÃńla Haegel, Sascha Husa, Frank Ohme, Geraint Pratten, and Michael PÃijrrer. Simple Model of Complete Precessing Black-Hole-Binary Gravitational Waveforms. *Phys. Rev. Lett.*, 113(15): 151101, 2014. DOI: 10.1103/PhysRevLett.113.151101.

[82] O. A. Hannuksela, K. Haris, K. K. Y. Ng, S. Kumar, A. K. Mehta, D. Keitel, T. G. F. Li, and P. Ajith. Search for gravitational lensing signatures in LIGO-Virgo binary black hole events. *Astrophys. J.*, 874(1):L2, 2019. DOI: 10.3847/2041-8213/abocof. [Astrophys. J. Lett.874,L2(2019)].

[83] K. Haris, Ajit Kumar Mehta, Sumit Kumar, Tejaswi Venumadhav, and Parameswaran Ajith. Identifying strongly lensed

gravitational wave signals from binary black hole mergers. *arXiv: 1807.07062*, 2018.

[84] Sascha Husa, Sebastian Khan, Mark Hannam, Michael Pürrer, Frank Ohme, Xisco Jiménez Forteza, and Alejandro Bohé. Frequency-domain gravitational waves from nonprecessing black-hole binaries. i. new numerical waveforms and anatomy of the signal. *Phys. Rev. D*, 93:044006, Feb 2016. DOI: 10.1103/PhysRevD.93.044006. URL http://link.aps.org/doi/10.1103/PhysRevD.93.044006.

[85] Werner Israel. Event horizons in static vacuum space-times. *Phys. Rev.*, 164:1776–1779, Dec 1967. DOI: 10.1103/PhysRev.164.1776. URL https://link.aps.org/doi/10.1103/PhysRev.164.1776.

[86] Werner Israel. Event horizons in static electrovac space-times. *Communications in Mathematical Physics*, 8(3):245–260, Sep 1968. ISSN 1432-0916. DOI: 10.1007/BF01645859. URL https://doi.org/10.1007/BF01645859.

[87] Warren G. Anderson Jolien D. E. Creighton. *Gravitational-Wave Physics and Astronomy: An Introduction to Theory, Experiment and Data Analysis*. Wiley-VCH, 2011.

[88] Sunghoon Jung and Chang Sub Shin. Gravitational-Wave Lensing Fringes by Compact Dark Matter at LIGO. 2017.

[89] Bernard J. Kelly and John G. Baker. Decoding mode mixing in black-hole merger ringdown. *Phys. Rev. D*, 87(8):084004, 2013. DOI: 10.1103/PhysRevD.87.084004.

[90] Sebastian Khan, Sascha Husa, Mark Hannam, Frank Ohme, Michael Pürrer, Xisco Jiménez Forteza, and Alejandro Bohé. Frequency-domain gravitational waves from nonprecessing black-hole binaries. ii. a phenomenological model for the advanced detector era. *Phys. Rev. D*, 93:044007, Feb 2016.

DOI: 10.1103/PhysRevD.93.044007. URL http://link.aps.org/doi/10.1103/PhysRevD.93.044007.

[91] Lawrence E. Kidder. Using full information when computing modes of post-Newtonian waveforms from inspiralling compact binaries in circular orbit. *Phys. Rev.*, D77:044016, 2008. DOI: 10.1103/PhysRevD.77.044016.

[92] R. Kormann, P. Schneider, and M. Bartelmann. Isothermal elliptical gravitational lens models. *Astronomy and Astrophysics*, 284:285–299, April 1994.

[93] N. V. Krishnendu, K. G. Arun, and Chandra Kant Mishra. Testing the binary black hole nature of a compact binary coalescence. 2017.

[94] Ajit Kumar Mehta, Praveer Tiwari, Nathan K. Johnson-McDaniel, Chandra Kant Mishra, Vijay Varma, and Parameswaran Ajith. Including mode mixing in a higher-multipole model for gravitational waveforms from nonspinning black-hole binaries. *Phys. Rev.*, D100(2):024032, 2019. DOI: 10.1103/PhysRevD.100.024032.

[95] Kwun-Hang Lai, Otto A. Hannuksela, Antonio Herrera-MartÃ■n, Jose M. Diego, Tom Broadhurst, and Tjonnie G. F. Li. Discovering intermediate-mass black hole lenses through gravitational wave lensing. 2018.

[96] Jacob Lange et al. A Parameter Estimation Method that Directly Compares Gravitational Wave Observations to Numerical Relativity. 2017.

[97] S.-S. Li, S. Mao, Y. Zhao, and Y. Lu. Gravitational lensing of gravitational waves: a statistical perspective. *Monthly Notices of the Royal Astronomical Society*, 476:2220–2229, May 2018. DOI: 10.1093/mnras/sty411.

[98] Kai Liao, Xi-Long Fan, Xu-Heng Ding, Marek Biesiada, and Zong-Hong Zhu. Precision cosmology from future lensed gravitational wave and electromagnetic signals. *Nature Commun.*, 8(1):1148, 2017. DOI: 10.1038/s41467-017-01152-9, 10.1038/s41467-017-02135-6. [Erratum: Nature Commun.8,no.1,2136(2017)].

[99] LIGO Scientific Collaboration. Parameter estimation sample release for gwtc-1, 2018. URL `https://dcc.ligo.org/LIGO-P1800370/public`.

[100] L. London and E. Fauchon-Jones. On modeling for Kerr black holes: Basis learning, QNM frequencies, and spherical-spheroidal mixing coefficients. 2018.

[101] Lionel London, Sebastian Khan, Edward Fauchon-Jones, Xisco JimÃľnez Forteza, Mark Hannam, Sascha Husa, Chinmay Kalaghatgi, Frank Ohme, and Francesco Pannarale. First higher-multipole model of gravitational waves from spinning and coalescing black-hole binaries. 2017.

[102] Lionel London et al. First higher-multipole model of spinning binary-black-hole gravitational waveforms. 2017. LIGO-P1700203-v2.

[103] Michele Maggiore. *Gravitational Waves: Volume 1: Theory and Experiments*. OUP Oxford, 2007.

[104] Ajit Kumar Mehta, Chandra Kant Mishra, Vijay Varma, and Parameswaran Ajith. Accurate inspiral-merger-ringdown gravitational waveforms for nonspinning black-hole binaries including the effect of subdominant modes. *Phys. Rev.*, D96 (12):124010, 2017. DOI: 10.1103/PhysRevD.96.124010.

[105] J. Meidam, M. Agathos, C. Van Den Broeck, J. Veitch, and B. S. Sathyaprakash. Testing the no-hair theorem with black hole ringdowns using TIGER. *Phys. Rev.*, D90(6):064009, 2014. DOI: 10.1103/PhysRevD.90.064009.

[106] Jeroen Meidam et al. Parametrized tests of the strong-field dynamics of general relativity using gravitational wave signals from coalescing binary black holes: Fast likelihood calculations and sensitivity of the method. *Phys. Rev. D*, 97(4):044033, 2018. DOI: 10.1103/PhysRevD.97.044033.

[107] C. Messick, K. Blackburn, P. Brady, P. Brockill, K. Cannon, R. Cariou, S. Caudill, S. J. Chamberlin, J. D. E. Creighton, R. Everett, C. Hanna, D. Keppel, R. N. Lang, T. G. F. Li, D. Meacher, A. Nielsen, C. Pankow, S. Privitera, H. Qi, S. Sachdev, L. Sadeghian, L. Singer, E. G. Thomas, L. Wade, M. Wade, A. Weinstein, and K. Wiesner. Analysis framework for the prompt discovery of compact binary mergers in gravitational-wave data. *prd*, 95(4):042001, February 2017. DOI: 10.1103/PhysRevD.95.042001.

[108] Chandra Kant Mishra, K. G. Arun, Bala R. Iyer, and B. S. Sathyaprakash. Parametrized tests of post-Newtonian theory using Advanced LIGO and Einstein Telescope. *Phys. Rev.*, D82: 064010, 2010. DOI: 10.1103/PhysRevD.82.064010.

[109] Ken K. Y. Ng, Kaze W. K. Wong, Tom Broadhurst, and Tjonnie G. F. Li. Precise LIGO Lensing Rate Predictions for Binary Black Holes. *Phys. Rev.*, D97(2):023012, 2018. DOI: 10.1103/PhysRevD.97.023012.

[110] Richard O'Shaughnessy, Jonathan Blackman, and Scott E. Field. An architecture for efficient gravitational wave parameter estimation with multimodal linear surrogate models. 2017.

[111] Yi Pan, Alessandra Buonanno, Michael Boyle, Luisa T. Buchman, Lawrence E. Kidder, et al. Inspiral-merger-ringdown multipolar waveforms of nonspinning black-hole binaries using the effective-one-body formalism. *Phys. Rev. D*, 84:124052, 2011. DOI: 10.1103/PhysRevD.84.124052.

[112] Yi Pan, Alessandra Buonanno, Ryuichi Fujita, Etienne Racine,

and Hideyuki Tagoshi. Post-Newtonian factorized multipolar waveforms for spinning, non-precessing black-hole binaries. *Phys. Rev.*, D83:064003, 2011. DOI: 10.1103/PhysRevD.83.064003, 10.1103/PhysRevD.87.109901. [Erratum: Phys. Rev.D87,no.10,109901(2013)].

[113] Yi Pan, Alessandra Buonanno, Andrea Taracchini, Lawrence E. Kidder, Abdul H. MrouÃľ, Harald P. Pfeiffer, Mark A. Scheel, and BÃľla SzilÃągyi. Inspiral-merger-ringdown waveforms of spinning, precessing black-hole binaries in the effective-one-body formalism. *Phys. Rev.*, D89(8):084006, 2014. DOI: 10.1103/PhysRevD.89.084006.

[114] A. Piórkowska, M. Biesiada, and Z.-H. Zhu. Strong gravitational lensing of gravitational waves in Einstein Telescope. *Journal of Cosmology and Astroparticle Physics*, 10:022, October 2013. DOI: 10.1088/1475-7516/2013/10/022.

[115] Denis Pollney and Christian Reisswig. Gravitational memory in binary black hole mergers. *Astrophys. J.*, 732:L13, 2011. DOI: 10.1088/2041-8205/732/1/L13.

[116] William H. Press. Long Wave Trains of Gravitational Waves from a Vibrating Black Hole. *Astrophys. J.*, 170:L105–L108, 1971. DOI: 10.1086/180849.

[117] L. Santamaria et al. Matching post-Newtonian and numerical relativity waveforms: systematic errors and a new phenomenological model for non-precessing black hole binaries. *Phys. Rev.*, D82:064016, 2010. DOI: 10.1103/PhysRevD.82.064016.

[118] B. S. Sathyaprakash and B. F. Schutz. Physics, Astrophysics and Cosmology with Gravitational Waves. *Living Rev. Rel.*, 12: 2, 2009. DOI: 10.12942/lrr-2009-2.

[119] M. Sereno, A. Sesana, A. Bleuler, P. Jetzer, M. Volonteri, and M. C. Begelman. Strong Lensing of Gravitational Waves as

Seen by LISA. *Physical Review Letters*, 105(25):251101, December 2010. DOI: 10.1103/PhysRevLett.105.251101.

[120] M. Sereno, P. Jetzer, A. Sesana, and M. Volonteri. Cosmography with strong lensing of LISA gravitational wave sources. *Monthly Notices of the Royal Astronomical Society*, 415:2773–2781, August 2011. DOI: 10.1111/j.1365-2966.2011.18895.x.

[121] N. Seto. Strong gravitational lensing and localization of merging massive black hole binaries with LISA. *prd*, 69(2):022002, January 2004. DOI: 10.1103/PhysRevD.69.022002.

[122] D. Shoemaker. Advanced ligo anticipated sensitivity curves. *LIGO Document T0900288-v3*, 2010. URL `https://dcc.ligo.org/LIGO-T0900288/public`.

[123] Alicia M. Sintes and Alberto Vecchio. Detection of gravitational waves from inspiraling compact binaries using nonrestricted postNewtonian approximations. In *Proceedings, 34th Rencontres de Moriond gravitational waves and experimental gravity: Les Arcs, France, Jan 23-30, 1999*, pages 73–78, 2000. URL `http://alice.cern.ch/format/showfull?sysnb=2187848`.

[124] John Skilling. Nested sampling for general bayesian computation. *Bayesian Anal.*, 1(4):833–859, 12 2006. DOI: 10.1214/06-BA127. URL `https://doi.org/10.1214/06-BA127`.

[125] G. P. Smith, M. Bianconi, M. Jauzac, J. Richard, A. Robertson, C. P. L. Berry, R. Massey, K. Sharon, W. M. Farr, and J. Veitch. Deep and rapid observations of strong-lensing galaxy clusters within the sky localisation of GW170814. 2018.

[126] G. P. Smith, M. Bianconi, M. Jauzac, J. Richard, A. Robertson, C. P. L. Berry, R. Massey, K. Sharon, W. M. Farr, and J. Veitch. Deep and rapid observations of strong-lensing galaxy clusters within the sky localisation of GW170814. 2018.

[127] G. P. Smith, M. Jauzac, J. Veitch, W. M. Farr, R. Massey, and J. Richard. What if LIGO's gravitational wave detections are strongly lensed by massive galaxy clusters? *Monthly Notices of the Royal Astronomical Society*, 475:3823–3828, April 2018. DOI: 10.1093/mnras/sty031.

[128] Graham P Smith, CPL Berry, Matteo Bianconi, Will M Farr, Mathilde Jauzac, RJ Massey, Johan Richard, Andrew Robertson, Keren Sharon, Alberto Vecchio, et al. Strong-lensing of gravitational waves by galaxy clusters. *arXiv preprint arXiv:1803.07851*, 2018.

[129] Graham P. Smith, Mathilde Jauzac, John Veitch, Will M. Farr, Richard Massey, and Johan Richard. What if LIGOâĂŹs gravitational wave detections are strongly lensed by massive galaxy clusters? *Mon. Not. Roy. Astron. Soc.*, 475(3):3823–3828, 2018. DOI: 10.1093/mnras/sty031.

[130] R. Takahashi. Quasi-geometrical optics approximation in gravitational lensing. *Astronomy and Astrophysics*, 423:787–792, September 2004. DOI: 10.1051/0004-6361:20040212.

[131] R. Takahashi and T. Nakamura. Wave Effects in the Gravitational Lensing of Gravitational Waves from Chirping Binaries. *apj*, 595:1039–1051, October 2003. DOI: 10.1086/377430.

[132] R. Takahashi, M. Oguri, M. Sato, and T. Hamana. Probability Distribution Functions of Cosmological Lensing: Convergence, Shear, and Magnification. *apj*, 742:15, November 2011. DOI: 10.1088/0004-637X/742/1/15.

[133] Ryuichi Takahashi and Takashi Nakamura. Wave effects in gravitational lensing of gravitational waves from chirping binaries. *Astrophys. J.*, 595:1039–1051, 2003. DOI: 10.1086/377430.

[134] Andrea Taracchini et al. Effective-one-body model for black-hole binaries with generic mass ratios and spins. *Phys. Rev.*, D89(6):061502, 2014. DOI: 10.1103/PhysRevD.89.061502.

[135] Nicholas W. Taylor, Michael Boyle, Christian Reisswig, Mark A. Scheel, Tony Chu, Lawrence E. Kidder, and BÃl'la Szilágyi. Comparing Gravitational Waveform Extrapolation to Cauchy-Characteristic Extraction in Binary Black Hole Simulations. *Phys. Rev. D*, 88(12):124010, 2013. DOI: 10.1103/PhysRevD.88.124010.

[136] The Virgo Collaboration. Advanced Virgo Baseline Design. Technical Report VIR-0027A-09, Virgo Collaboration, August 2009. URL `https://tds.virgo-gw.eu/ql/?c=6589`.

[137] Praveer Tiwari. Gravitational waves from binary black hole coalescence: A study on the effect of non-quadrupole modes. Master's thesis, Indian Institute of Science, 2016.

[138] Miquel Trias and Alicia M. Sintes. LISA parameter estimation of supermassive black holes. *Class. Quant. Grav.*, 25:184032, 2008. DOI: 10.1088/0264-9381/25/18/184032.

[139] Samantha A. Usman et al. The PyCBC search for gravitational waves from compact binary coalescence. *Class. Quant. Grav.*, 33(21):215004, 2016. DOI: 10.1088/0264-9381/33/21/215004.

[140] Chris Van Den Broeck and Anand S. Sengupta. Binary black hole spectroscopy. *Class. Quant. Grav.*, 24:1089–1114, 2007. DOI: 10.1088/0264-9381/24/5/005.

[141] Chris Van Den Broeck and Anand S. Sengupta. Phenomenology of amplitude-corrected post-Newtonian gravitational waveforms for compact binary inspiral. I. Signal-to-noise ratios. *Class.Quant.Grav.*, 24:155–176, 2007. DOI: 10.1088/0264-9381/24/1/009.

[142] Vijay Varma and Parameswaran Ajith. Effects of non-quadrupole modes in the detection and parameter estimation of black hole binaries with nonprecessing spins. 2016.

[143] Vijay Varma, Ryuichi Fujita, Ashok Choudhary, and Bala R. Iyer. Comparison of post-Newtonian templates for extreme mass ratio inspirals. *Phys. Rev.*, D88(2):024038, 2013. DOI: 10.1103/PhysRevD.88.024038.

[144] Vijay Varma, Parameswaran Ajith, Sascha Husa, Juan Calderon Bustillo, Mark Hannam, and Michael Pürrer. Gravitational-wave observations of binary black holes: Effect of nonquadrupole modes. *Phys. Rev. D*, 90: 124004, Dec 2014. DOI: 10.1103/PhysRevD.90.124004. URL `http://link.aps.org/doi/10.1103/PhysRevD.90.124004`.

[145] J. Veitch and A. Vecchio. Bayesian coherent analysis of in-spiral gravitational wave signals with a detector network. *Phys. Rev. D*, 81, 2010. DOI: 10.1103/PhysRevD.81.062003.

[146] J. Veitch et al. Parameter estimation for compact binaries with ground-based gravitational-wave observations using the LALInference software library. *Phys. Rev.*, D91(4):042003, 2015. DOI: 10.1103/PhysRevD.91.042003.

[147] C. V. Vishveshwara. Scattering of Gravitational Radiation by a Schwarzschild Black-hole. *Nature*, 227:936–938, 1970. DOI: 10.1038/227936a0.

[148] Y. Wang, A. Stebbins, and E. L. Turner. Gravitational Lensing of Gravitational Waves from Merging Neutron Star Binaries. *Physical Review Letters*, 77:2875–2878, September 1996. DOI: 10.1103/PhysRevLett.77.2875.

[149] Yves Wiaux, L. Jacques, and P. Vandergheynst. Fast spin +-2 spherical harmonics transforms. *J. Comput. Phys.*, 226:2359–2371, 2007. DOI: 10.1016/j.jcp.2007.07.005.

[150] J. S. B. Wyithe, H. Yan, R. A. Windhorst, and S. Mao. A distortion of very-high-redshift galaxy number counts by gravitational lensing. *nat*, 469:181–184, January 2011. DOI: 10.1038/nature09619.